

KU LEUVEN

ARENBERG DOCTORAL SCHOOL
Faculty of Science



Institute of Theoretical and
Computational Physics

Cloud formation in 3D exoplanet atmospheres

Sven Kiefer

September 2024

Sven KIEFER, BSc MSc

Cloud formation in 3D exoplanet atmospheres

Doctoral Thesis

to achieve the university degree of
Doktor der Naturwissenschaften

submitted to
Graz University of Technology.

Supervisors:
Univ.-Prof. Dr.rer.nat. Christiane Helling
Institute of Theoretical and Computational Physics, Graz University of Technology
and
Prof. Dr. Leen Decin
Institute of Astronomy, KU Leuven

Graz, September 2024

Cloud formation in 3D exoplanet atmospheres

Sven KIEFER

Dissertation presented in partial fulfillment of the requirements for
the degree of Doctor of Science (PhD): Astronomy and Astrophysics

Doctoral Thesis to achieve the university degree of Doktor der
Naturwissenschaften submitted to Graz University of Technology.

Examination committee:

Chair: Prof. Dr. Patrick Wagner (KU Leuven)

Supervisor: Prof. Dr. Leen Decin (KU Leuven)

Supervisor: Prof. Dr. Christiane Helling (TU Graz)

Co-Supervisor: Dr. Ludmila Carone (OEWAW IWF)

Assessor: Prof. Dr. Denis Defrère (KU Leuven)

Assessor: Prof. Dr. Hans Gerd Evertz (TU Graz)

Referee: Dr. Kaustubh Hakim (KU Leuven)

Referee: Prof. Dr. Paul Palmer (University of Edinburgh)

Funding acknowledgement: Sven Kiefer is part of the CHAMELEON MC ITN EJD which received funding from the European Union's Horizon 2020 research and innovation programme under the Marie Skłodowska-Curie grant agreement no. 860470.

© 2024 Sven Kiefer

Alle rechten voorbehouden. Niets uit deze uitgave mag worden vermenigvuldigd en/of openbaar gemaakt worden door middel van druk, fotokopie, microfilm, elektronisch of op welke andere wijze ook zonder voorafgaande schriftelijke toestemming van de uitgever.

All rights reserved. No part of the publication may be reproduced in any form by print, photoprint, microfilm, electronic or any other means without written permission from the publisher.

Cover image by Vanessa Sennrich

For those who dare to dream

Acknowledgments

I was always wondering how it would feel to have completed a PhD thesis. Thinking back on the journey makes me realize how much I have learned and how much I have grown. Curiosity has always been my biggest motivator. I needed to know how the world works, and when I learned that there are other worlds in our universe, I knew I had to understand them too. From then on, I knew what I had to do and started working on the skills I would need to explore these distant planets. When I look at this thesis now, I feel proud of everything I have achieved. This would not have been possible without the people who supported me along the way and I would like to thank everyone who made this journey possible.

To my supervisors, Leen, Christiane, Ludmila, and David. Thank you for the opportunity to tackle exciting scientific questions and for your guidance and support throughout my PhD. Thanks to you, I was able to live out my curiosity and dive into the atmospheres of exoplanets (figuratively, of course). Leen, thank you for our thought provoking scientific discussions, which provided a new perspective and showed me the value of my research in the bigger picture. Christiane, thank you for all the times we revisited and explored fundamental physical concepts and for encouraging me to face even the most difficult challenges. Ludmila, thank you for all the time and energy you invested in me. Our weekly meetings were intriguing, incredibly helpful and gave me energy for the week ahead. I have always appreciated your honest and practical support. David, thank you for your mentorship and motivation when I needed it most. Starting my PhD during a pandemic was difficult and your constant encouragement has helped me achieve so much in the first years of my PhD.

To the CHAMELEON early stage researchers. It has been a great joy to share the four years of my PhD with all of you. You are a colorful assortment of spirited and talented researchers. To Helena, from government-assigned cuddle buddies to the Steyergasse-Gang, I am truly grateful that I had the pleasure to share so much of my PhD with you and I am already looking forward to our

next adventures. To Till, few can match my early mornings but you did your best and our daily morning meetings were an uplifting start into the day. To Nanna, you have always been a most wonderful host; never give up on your dreams to become a dragon ninja warrior. To Thorsten, thank you for making Graz come to life by organizing countless events. To Jayatee, Beatriz, Marrick, Linus, and Flavia, it was great sharing time at the same institute with you even though it was much shorter than I would have liked. To Pieter and Oriel, your energy is unmatched and I am grateful for everything you dragged me into.

To my colleagues and collaborators. Having the opportunity to conduct research at two institutes allowed me to meet twice as many brilliant researchers and good friends. Thank you to everyone at the IvS with whom I spent many afternoons playing beach volleyball and evenings at Metafoor. Thank you Thomas, Joline, Silke, and Olivier for putting in the extra effort to make Belgium feel like home, even in the middle of a pandemic. To the people in Graz, thank you for all the hikes, travels, movie nights, game afternoons and many more adventures. Thank you Nidhi, Kundan, David, Dominic, Sierk, Patrick, JP, and Cyril for making the IWF so much more than a workplace. To Jayatee and Nidhi, it was a pleasure sharing an office and my questionable taste in music with you. Lastly, a special thanks to the righteous crowd who never left.

To my friends and family, thank you for always believing in me. Knowing that you are always there for me when I need it most made the biggest steps in my life so much easier. To my parents Claudia and Thomas, you always encouraged me to find my own path and the only thing that matters is that I am happy. Your unwavering support, love, and patience for my curiosity have made me the person I am today. To Gabi and Hans-Jörg, you were always there for me and taught me so much. Thank you for all the wonderful days spent hiking in the mountains. To my siblings Severin and Leoni, after we decided to no longer annoy our parents, our shared love for music, memes, games, and ridiculous questions has turned us into close friends. I appreciate all the time and effort you put in to make our discord hangouts feel like we are all still living under the same roof. To Roger, Kuchler, Sonja, and Peter, we all became friends because you stuck around and refused to leave. I am ever grateful that the same spirit remained once I left Switzerland and I am certain this will not change no matter where my next steps will take me.

To Vanessa, thank you for embarking on this adventurous journey with me. It has been a roller coaster ride through which you stuck by me. It's times like these that show me I can do anything with you by my side. And no matter whether we travel two, three or five times around the world or if we stay forever, I know you are flying inside thinking about our next adventure, and truth be told, I've got to say, I do so too.

One day

I will walk among the stars

gazing into the unknown

knowing I belong

for I am no traveler

just stardust

returning home

Abstract

The atmospheres of exoplanets are the key to answering numerous open science questions about atmospheric processes. In the near future, advanced telescopes like JWST, PLATO, ARIEL, and ELT will provide new insights which require extensive atmospheric modeling. To support these efforts, the goal of this thesis is to provide a detailed understanding of how clouds in gas-giant exoplanets affect and are affected by the interplay of cloud formation, gas-phase chemistry, and global climate.

To study fully time-dependent cloud formation, we couple kinetic gas-phase chemistry, kinetic nucleation, condensation, and cloud particle surface reactions. Our results show that non-equilibrium effects are most relevant in low density environments. Thermal non-equilibrium can increase or decrease cloud formation if larger clusters are cooler or hotter than the surrounding gas-phase, respectively. Surface reactions on cloud particles lead to an SiO-SiO₂ catalytic cycle which dissociates molecular hydrogen to atomic hydrogen ($H_2 \rightarrow 2H$). The composition of clouds forming in exoplanet atmospheres can be considerably heterogeneous which leads to complex optical properties. We investigate five different cloud particle mixing treatments and 21 commonly considered cloud particle materials. Our results show that different cloud particle morphologies lead to observable differences in the transmission spectra of exoplanets. Well-mixed cloud particles lead to broad spectral features whereas non-mixed cloud particles retain the spectral features of their components. Especially iron-bearing species and carbon are cloud particle materials that can dominate optical properties even if they make up less than 1% of the volume. To analyze how the opacities of cloud particles affect the climate of exoplanets, we implement cloud opacities into a general circulation model (GCM) and simulate the atmosphere of HATS-6b. We find that after iterating five times between a micro-physical cloud model and a GCM the differences in the atmospheric structures fall below the observational accuracy of JWST NIRSpec prism and MIRI LRS. Our results show that HATS-6b has a global but not uniform cloud structure which leads to a temperature inversion in the upper atmosphere ($p_{\text{gas}} \approx 10^{-3}$ bar) and cooling deeper down

($p_{\text{gas}} \approx 1 \text{ bar}$). The changes in the temperature structure lead to a narrower and faster equatorial wind jet.

The research conducted in this thesis demonstrates the significance of clouds within exoplanet atmospheres. For a detailed picture of atmospheric processes, it is crucial to consider the interplay of clouds, gas-phase chemistry, and climate. Future observations carry the potential to directly and indirectly detect cloud particle properties and their effect on the gas-phase chemistry and climate. In particular, observations of fully cloudy planets like HATS-6b or partially cloudy planets like WASP-76b enable such investigations.

Beknopte Samenvatting

De atmosferen van exoplaneten zijn cruciaal voor het beantwoorden van talloze wetenschappelijke vragen over atmosferische processen. In de nabije toekomst zullen geavanceerde telescopen zoals JWST, PLATO, ARIEL en ELT nieuwe inzichten opleveren die uitgebreide atmosferische modellering vereisen. Het doel van dit proefschrift is om een gedetailleerd inzicht te verschaffen in de manier waarop wolken in de atmosferen van gasreuzen de wisselwerking tussen wolkenvorming, gasfasechemie en het globale klimaat beïnvloeden en erdoor worden beïnvloed.

Om volledig tijdsafhankelijke wolkenvorming te bestuderen, koppelen we de kinetische gasfasechemie, kinetische vorming van nuclei, condensatie en oppervlaktereacties van wolkendeeltjes. Onze resultaten laten zien dat niet-evenwichtseffecten het meest relevant zijn in omgevingen met lage dichtheid. Thermisch niet-evenwicht kan de vorming van wolken vergroten of afremmen wanneer grotere clusters respectievelijk koeler of warmer zijn dan het omringende gas. Oppervlaktereacties op wolkendeeltjes leiden tot een SiO-SiO₂ katalytische cyclus die molecuair waterstof dissociert tot atomair waterstof ($H_2 \rightarrow 2H$).

De samenstelling van wolken die zich vormen in de atmosfeer van exoplaneten kan aanzienlijk heterogeen zijn, wat kan leiden tot complexe optische eigenschappen. We onderzoeken vijf verschillende manieren voor het mengen wolkendeeltjes en 21 welgekende materialen voor wolkendeeltjes. Onze resultaten tonen aan dat verschillende morfologieën van wolkendeeltjes leiden tot waarneembare verschillen in de transmissiespectra van exoplaneten. Goed gemengde wolkendeeltjes leiden tot brede spectrale kenmerken, terwijl niet-gemengde wolkendeeltjes de spectrale kenmerken van hun componenten behouden. Vooral ijzerhoudende soorten en koolstof zijn materialen van wolkendeeltjes die de optische eigenschappen kunnen domineren, zelfs als ze minder dan 1% van het volume uitmaken.

Om te analyseren hoe wolkendeeltjes het klimaat van exoplaneten beïnvloedt,

implementeren we de opaciteit van wolken in een globaal circulatiemodel (GCM) en simuleren we de atmosfeer van HATS-6b. We ontdekken dat, na vijf keer itereren tussen een microfysisch wolkenmodel en een GCM, de verschillen in de atmosferische structuren lager dan de waarnemingsnauwkeurigheid van het JWST NIRSpec-prisma en MIRI LRS vallen. Onze resultaten laten zien dat HATS-6b een globale maar niet uniforme wolkenstructuur heeft die leidt tot een temperatuurinversie in de bovenste lagen van de atmosfeer ($p_{\text{gas}} \approx 10^{-3}$ bar) en een afkoeling dieper naar onder ($p_{\text{gas}} \approx 1$ bar). De veranderingen in de temperatuurstructuur leiden tot een smallere en snellere equatoriale windstraal.

Het onderzoek dat in dit proefschrift wordt uitgevoerd, toont het belang aan van wolken in de atmosfeer van exoplaneten. Voor een gedetailleerd beeld van atmosferische processen is het van cruciaal belang om rekening te houden met de wisselwerking tussen de wolken, de gasfasechemie en het klimaat. Toekomstige waarnemingen hebben het potentieel om de eigenschappen van wolkendeeltjes en hun effect op de gasfasechemie en het klimaat te detecteren, zowel direct als indirect. Observaties van volledig bewolkte planeten, zoals HATS-6b, of gedeeltelijk bewolkte planeten, zoals WASP-76b, maken dergelijk onderzoek mogelijk.

Zusammenfassung

Die Atmosphären von Exoplaneten sind der Schlüssel zur Beantwortung zahlreicher offener wissenschaftlicher Fragen zu atmosphärischen Prozessen. In naher Zukunft werden fortschrittliche Teleskope wie JWST, PLATO, ARIEL und ELT neue Beobachtungen liefern, die eine umfassende Atmosphärenmodellierung erfordern. Das Ziel dieser Arbeit besteht darin, diese Bemühungen zu unterstützen indem ein detailliertes Verständnis über die Interaktionen von Wolkenbildung, Gasphasenchemie und globalem Klima erarbeitet wird.

Um die vollständig, zeitabhängige Wolkenbildung zu untersuchen, koppeln wir kinetische Gasphasenchemie, kinetische Keimbildung, Kondensation und Wolkenpartikeloberflächenreaktionen. Unsere Ergebnisse zeigen, dass Nichtgleichgewichteffekte in Umgebungen mit geringer Dichte am relevantesten sind. Ein thermisches Ungleichgewicht kann die Wolkenkeimbildung erhöhen (oder reduzieren) falls jeweils größere Cluster kühler (oder heißer) als die umgebende Gasphase sind. Oberflächenreaktionen an Wolkenpartikeln führen zu einem SiO-SiO₂-Katalysezyklus, der molekularen Wasserstoff in atomaren Wasserstoff ($H_2 \rightarrow 2H$) dissoziert. Die Zusammensetzung der Wolken, die sich in der Atmosphäre von Exoplaneten bilden, kann sehr heterogen sein, was zu komplexen optischen Eigenschaften führt. Wir untersuchen fünf verschiedene Wolkenpartikel-Mischverfahren und 21 häufig berücksichtigte Stoffe, aus denen Wolkenpartikel bestehen können. Unsere Ergebnisse zeigen, dass unterschiedliche Wolkenpartikelmorphologien zu beobachtbaren Unterschieden in den Transmissionsspektren von Exoplaneten führen. Gut gemischte Wolkenpartikel führen zu breiten spektralen Signaturen, während nicht gemischte Wolkenpartikel die spektralen Signaturen ihrer Komponenten beibehalten. Insbesondere eisenhaltige Teilchen und Kohlenstoff sind Wolkenpartikelmaterialien, die die optischen Eigenschaften dominieren können, selbst wenn sie weniger als 1% des Volumens ausmachen. Um zu analysieren, wie sich die Opazität von Wolkenpartikeln auf das Klima von Exoplaneten auswirkt, implementieren wir die Opazität von Wolkenpartikeln in ein globales Klimamodell (General Circulation Model, kurz GCM) und

simulieren die Atmosphäre von HATS-6b. Wir stellen fest, dass nach fünf Iterationen zwischen einem mikrophysikalischen Wolkenmodell und einem GCM die Unterschiede in den atmosphärischen Strukturen unter die Beobachtungsgenauigkeit von JWST NIRSpec Prisma und MIRI LRS fallen. Unsere Ergebnisse zeigen, dass HATS-6b eine globale, aber nicht gleichmäßige, Wolkenstruktur aufweist, die zu einer Temperaturinversion in der oberen Atmosphäre ($p_{\text{Gas}} \approx 10^{-3}$ bar) und einer Abkühlung in tieferen Schichten führt ($p_{\text{Gas}} \approx 1$ bar). Die Veränderungen in der Temperaturstruktur führen zu einem schmaleren und schnelleren äquatorialen Jetstream.

Die in dieser Dissertation durchgeführte Forschung zeigt die Bedeutung von Wolken in der Atmosphäre von Exoplaneten. Für ein detailliertes Verständnis der atmosphärischen Prozesse ist es entscheidend, das Zusammenspiel von Wolken, Gasphasenchemie und Klima zu berücksichtigen. Zukünftige Beobachtungen haben das Potenzial, die Eigenschaften von Wolkenpartikeln und deren Auswirkungen auf die Gasphasenchemie und das Klima direkt und indirekt zu erfassen. Insbesondere Beobachtungen vollständig bewölkter Planeten wie HATS-6b oder teilweise bewölkter Planeten wie WASP-76b ermöglichen solche Untersuchungen.

List of Abbreviations

ADI	Angular Differential Imaging
AGB	Asymptotic Giant Branch
BAS	Batch Approximation of Spheres
CCN	Cloud Condensation Nuclei
CIA	Collision-induced absorption
CNT	Classical Nucleation Theory
EMT	Effective Medium Theory
GCM	General Circulation Model
HPE	Hydrostatic Primitive Equations
HST	Hubble Space Telescope
ISM	Interstellar Medium
JWST	James Webb Space Telescope
LECR	Low Energy Cosmic Rays
LLL	Landau-Lifshitz-Looyenga
MCNT	Modified Classical Nucleation Theory
ODE	Ordinary Differential Equation
PGR	Phase Equilibrium for a Given Bulk Growth Reaction
PSF	Point Spread Function
RNr	Reaction number
RV	Radial Velocity
SDI	Spectral Differential Imaging
SED	spectral energy distribution
SEP	Stellar Energetic Particle
SSA	System of Spheres Approximation
TCM	Temperature-Weighted Centre of Mass
WR	Wolf-Rayet

Contents

Abstract	vii
Beknopte Samenvatting	ix
Zusammenfassung	xi
List of Abbreviations	xiii
Contents	xv
1 The Hitchhiker's Guide to Exoplanets	1
1.1 Discovery and classification	2
1.1.1 Finding exoplanets	2
1.1.2 Demographics	6
1.1.3 Probing atmospheres	10
1.2 Atmospheres	12
1.2.1 Atmospheric composition	12
1.2.2 Clouds	13
1.2.3 Climate and weather	15
1.3 Goals and outline	16
1.3.1 Research questions	16
1.3.2 Outline	19
2 Theory and Modeling of Exoplanet Atmospheres	21
2.1 Atmospheric chemistry	21
2.1.1 Equilibrium chemistry	22
2.1.2 Chemical kinetics	24
2.2 Clouds in gaseous exoplanets	28
2.2.1 Nucleation	28
2.2.2 Moment method	34
2.2.3 Bulk growth	35

2.2.4	Advection, settling and diffusion	38
2.2.5	The master equation	40
2.3	Three dimensional atmospheres of exoplanets	40
2.3.1	Fluid dynamics of exoplanet atmospheres	40
2.3.2	The general circulation model expeRT/MITgcm	45
2.3.3	The climate of hot Jupiters	48
2.4	Opacities	51
2.4.1	Radiative transfer	51
2.4.2	Gas-phase species	52
2.4.3	Cloud particle opacities	53
3	The Effect of Thermal Non-Equilibrium on Kinetic Nucleation	57
3.1	Introduction	59
3.2	Kinetic nucleation model	61
3.2.1	Kinetic reactions	61
3.2.2	Two-particle speed distribution	63
3.2.3	Forward reaction rate	65
3.2.4	Association and dissociation of small clusters	65
3.2.5	Backward reaction rate	66
3.3	Cooling and heating processes	70
3.3.1	Kinetic temperature	70
3.3.2	Internal temperature	72
3.4	Kinetic nucleation in thermal non-equilibrium	75
3.4.1	Kinetic nucleation in thermal equilibrium	76
3.4.2	Effect of thermal non-equilibrium	78
3.4.3	Thermal equilibrium versus non-equilibrium	81
3.5	Conclusion	82
4	Cloud Formation from a Non-Equilibrium Gas-Phase	85
4.1	Introduction	87
4.2	Model	89
4.2.1	Gas-phase chemistry	89
4.2.2	Nucleation	90
4.2.3	Three-body reactions for cluster formation	91
4.2.4	Bulk growth	92
4.2.5	Reaction supersaturation	95
4.2.6	Formation rate of CCNs	100
4.3	Exploring kinetic chemistry and nucleation	101
4.3.1	A chemical network for kinetic cloud formation	102
4.3.2	SiO-SiO ₂ cycle	105
4.3.3	Kinetic nucleation of TiO ₂	107
4.4	The time evolution of cloud formation in HD 209458b	110
4.4.1	Time evolution of cloud formation	115

4.4.2	Comparison to dynamical processes	116
4.5	Summary	118
5	Optical Properties of Heterogeneous Cloud Particles	121
5.1	Introduction	123
5.2	Theoretical Basis	128
5.2.1	Cloud particle opacities	129
5.2.2	Mie Theory	129
5.2.3	Effective medium theory	130
5.2.4	Non-mixed treatments of cloud particles	132
5.3	Approach	134
5.3.1	Cloud opacity calculation	134
5.3.2	Cloud modelling	135
5.3.3	Transmission spectrum	136
5.4	Mixing behaviour of cloud particle materials	137
5.4.1	Effective refractive index from EMTs	138
5.4.2	Effective refractive index for clouds in hot Jupiter	144
5.4.3	Effective refractive index for clouds in temperate atmospheres	145
5.4.4	Non-mixed versus EMT	145
5.5	Heterogeneous clouds on exoplanets	149
5.5.1	Pressure dependent cloud optical properties of WASP-39b	152
5.5.2	Transmission spectrum	155
5.5.3	Iron-bearing cloud particle materials in WASP-76b	157
5.5.4	Cloud detections in WASP-107b	159
5.6	Discussion	161
5.6.1	Comparing mixing treatments	161
5.6.2	How do assumptions about heterogeneous cloud particles affect predicted observables?	162
5.6.3	Iron-bearing species and carbon require precise modelling	164
5.7	Conclusion	164
6	The Cloudy Climate of HATS-6b	167
6.1	Introduction	169
6.2	Approach	172
6.2.1	3D atmosphere	173
6.2.2	Cloud Structure	174
6.2.3	Stopping the step-wise iteration	178
6.2.4	Disequilibrium gas-phase chemistry	179
6.2.5	Transmission radiative transfer	181
6.3	Evaluation of the combined model	181
6.3.1	Cloud-free GCM and post-processed clouds	184
6.3.2	Impact of clouds on the atmospheric structure	188

6.3.3	Disequilibrium chemistry	190
6.3.4	Observable differences between iterations	191
6.4	The combined 3D model for the warm Saturn HATS-6b that orbits an M-dwarf	192
6.4.1	The atmospheric structure of HATS-6b	194
6.4.2	Transmission spectra	196
6.5	Discussion	197
6.5.1	Anti-greenhouse effect	198
6.5.2	Dynamics of the terminator regions	199
6.5.3	Comparison to other models	201
6.6	Conclusion	202
7	Conclusions and Outlook	205
7.1	Conclusion	205
7.2	Outlook	209
A	Cluster data	211
B	Chemical network	215
B.1	Numerical solver	215
B.2	GGchem	216
B.3	Al ₂ O ₃ nucleation	217
B.4	Comparing chemical networks	218
B.4.1	Gobrecht versus Vulcan	218
B.4.2	Vulcan	220
B.5	Data and additional plots	221
B.6	Additional plots	222
C	Cloud particle optical properties	231
C.1	Mie Theory	231
C.2	CaSiO ₃ opacity treatment	232
C.3	Data	234
C.4	Additional figures	234
D	HATS-6b	251
D.1	Additional cloud structure plots	251
D.2	GCM convergence tests	251
D.3	Input SED for ARGO	251
Bibliography		255
List of Publications		285

Chapter 1

The Hitchhiker's Guide to Exoplanets

Planets have been studied throughout the history of humankind. Babylon astronomers discovered Mercury, Venus, Mars, Jupiter, and Saturn more than 2500 years ago (Sachs 1974). Some astronomers at that time already proposed that planets orbit the Sun rather than following the traditional belief that the Earth is the center of the universe (Russell 2004). After these first five planets, it took over 2000 years before the next planets were discovered: Uranus in the 18th century (Herschel & Watson 1781) and Neptune in the 19th century (Airy 1846). The last Solar System "planet" Pluto was discovered in 1930 (Tombaugh 1946). Unfortunately, after it became apparent that Pluto failed to clear its orbit from debris, it was demoted to a dwarf-planet (Green 2006). There is evidence for an additional "Planet Nine" (Batygin et al. 2019) which has not yet been discovered. So far only indirect evidence has been collected and it remains to be seen if a planet has once more successfully hidden from our observations.

Once we learned how our Solar System works and discovered our neighboring planets, the next question naturally arose: do stars have planets as well? And if so, what do these planets look like? For centuries, the answers to these questions were outside the reach of human investigations. Only since the late 20th century are we finally able to search for planets outside the Solar System. These planets are called exoplanets.

1.1 Discovery and classification

The first planet outside the Solar System was detected in 1992 around the millisecond pulsar PSR1257+12 (Wolszczan & Frail 1992). While fascinating, this discovery did not yet answer the question if stars like our Sun have planets as well. That discovery came three years later when Mayor & Queloz (1995) detected the planet 51 Pegasi b which orbits a sun-like star. This planet has roughly half the mass of Jupiter and has an orbital period of 4.2 days. 51 Pegasi b proved two things right from the start: other stars can have planets and not all planetary systems are similar to the Solar System. Since then, thousands of exoplanets have been discovered using methods like high contrast imaging, radial velocity, or transit measurements (Sect. 1.1.1). Many of the exoplanets found do not have Solar System analogs and new classes of planets needed to be defined (Sect. 1.1.2). While the mass and radius of an exoplanet can be determined from the detection methods themselves, investigating their atmospheres requires spectral information (Sect. 1.1.3). These observations allow for more insights but they are much more difficult to conduct and thus only some planets are characterized in detail.

1.1.1 Finding exoplanets

High contrast imaging

Discovering exoplanets has been, and continues to be, a challenging task. The luminosity of planets is between 10^4 to 10^{10} times lower than the luminosity of stars (Follette 2023). To overcome this challenge, high contrast imaging instruments were developed that specialize in filtering out the stellar light. A core part of these instruments are coronagraphs which block parts of the stellar light using different types of apertures (Guyon et al. 2006; Galicher & Mazoyer 2023). However, the final images are still dominated by the residuals of the stellar point spread function (PSF). To detect planets, post processing techniques like Angular Differential Imaging (ADI) or Spectral Differential Imaging (SDI) are needed (Marois et al. 2006; Kiefer et al. 2021). These techniques create a model of the stellar PSF with ideally no contributions of the planetary companions. The PSF model can then be used to remove the remaining stellar light from the images. An image of Beta Pictoris b where all these techniques were applied with the post-processing pipeline PynPoint (Amara & Quanz 2012; Amara et al. 2015; Stolker et al. 2019; Kiefer et al. 2021) can be seen in Fig. 1.1.

High contrast imaging has been used to discover multiple planets and planetary systems. One of the most famous detections is the system HR 8799 where four

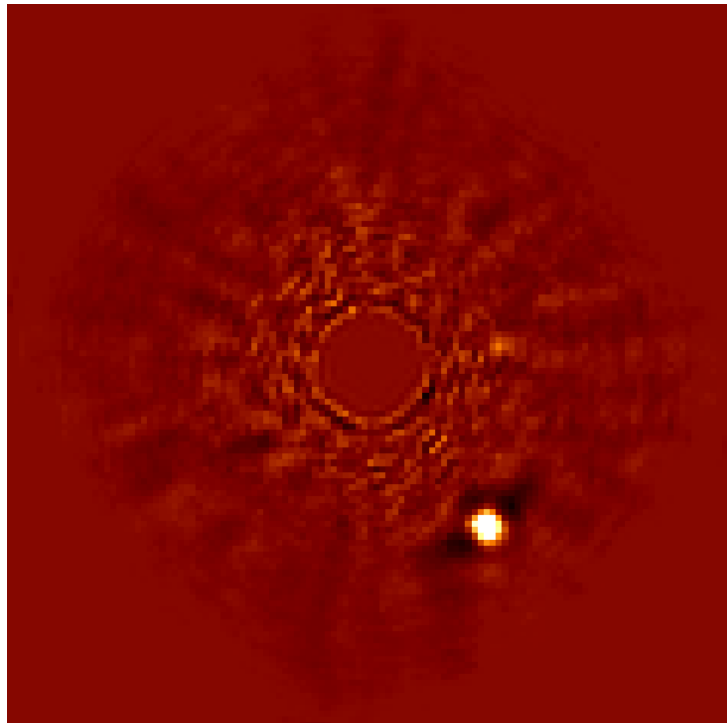


Figure 1.1: High contrast imaging of the planet Beta Pictoris b. Observations were conducted with SPHERE/IFS (PI: J. Beuzit; ESO ID: 096.C-0241(B)).

planets have been detected (Marois et al. 2008, 2010). By observing this system over many years, it was possible to observe the orbital motion of these planets. Because high contrast imaging favors luminous planets on large orbits, many planets were found in young stellar systems. These planets still carry residual heat from their formation process, making them more luminous and thus easier to detect.

Radial velocity method

Rather than directly detecting an exoplanet, the Radial Velocity (RV) method is based on the Doppler effect. Due to the mutual gravitational pull between the two bodies, the star will orbit around the system center of mass, which is very close to the center of the star because it is more massive. We can measure the RV component by measuring the instantaneous Doppler shift which is induced

by the gravitational influence of the orbiting planet on the many absorption lines that comprise the stellar spectrum of the host star. The velocity of this induced motion on the star is given by the velocity of the planet v_{planet} [m s⁻¹] and the ratio between the stellar mass M_{star} [kg] and the planetary mass M_{planet} [kg]. For a spherical orbit this is:

$$v_{\text{star}}^{\text{obs}} = v_{\text{star}} \sin(i) \approx v_{\text{planet}} \frac{M_{\text{planet}}}{M_{\text{star}}} \sin(i) \approx \sqrt{\frac{M_{\text{star}} G}{r}} \frac{M_{\text{planet}}}{M_{\text{star}}} \sin(i) \quad (1.1)$$

where $v_{\text{star}}^{\text{obs}}$ [m s⁻¹] is the observed stellar velocity, v_{star} [m s⁻¹] is the actual stellar velocity, i is the inclination of the planets orbit, r [m] is the distance between the star and the planet, and $G = 6.6743 \times 10^{-11}$ m³ kg⁻¹ s⁻² is the gravitational constant.

The observed stellar velocity differs from the actual stellar velocity because of the inclination of the planetary orbit. The signal is maximized if the orbit of the planet is aligned with the line of sight of the observer. The more inclined the orbit is, the weaker the observed signal gets. Hence, it is only possible to measure the lower limit of the planetary mass $M_{\text{planet}}^{\text{min}}$ [kg] which relates to the actual mass M_{planet} by:

$$M_{\text{planet}}^{\text{min}} = M_{\text{planet}} \sin(i) \quad (1.2)$$

The more massive a planet is and the closer it is to its host star, the larger the velocity of the star. Giant planets on short orbits are therefore more easily detectable using the RV method.

Using the RV method, Mayor & Queloz (1995) detected the first exoplanet around a sun-like star. Since then, hundreds of exoplanets have been found using the RV method. Especially exoplanet surveys like HARPS (Mayor et al. 2003; Rupprecht et al. 2004; Lovis et al. 2006) have contributed to the success of the RV method. In addition to detecting planets, RV measurements are often used to follow up transit detections to determine the mass of the exoplanets.

Transit method

Another way of indirectly detecting exoplanets is the transit method. A planetary transit occurs when a planet's orbital plane is aligned with the line of sight of the observer. The planet then regularly passes in front of its host star, causing an attenuation in brightness. The difference in flux ΔF [J s⁻¹ m⁻²] during a transit compared to the stellar flux F_s [J s⁻¹ m⁻²] outside of a transit is called transit depth. It can be related to the ratio between the stellar radius

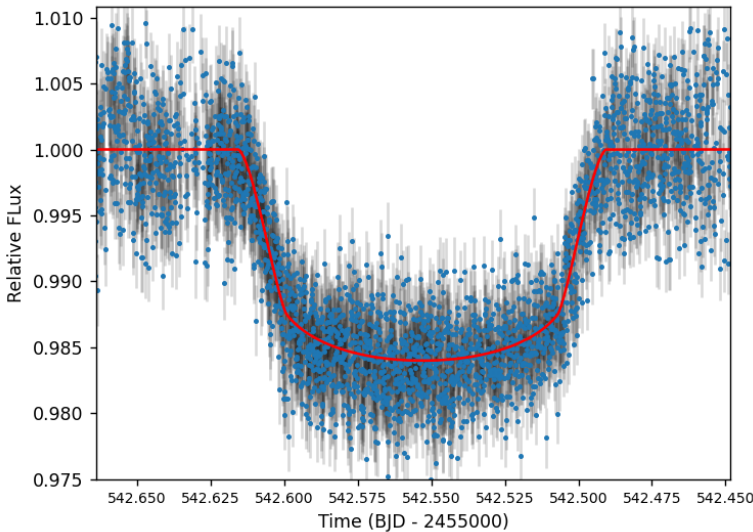


Figure 1.2: Transit detection of WASP-12b. Observations were conducted with the Copernico telescope at the Asiago Observatory on the night of 2010-12-22. Data taken from Leonardi et al. (2024).

R_s [m] and the radius of the planet R_p [m]:

$$\frac{\Delta F}{F_s} = \left(\frac{R_p}{R_s} \right)^2 \quad (1.3)$$

Larger planets cover more of the stellar light and thus are easier to observe. Hence, the transit method has a bias towards large exoplanets. An example of WASP-12b as observed with the Copernico telescope at the Asiago Observatory on the night of 2010-12-22 is shown in Fig. 1.2.

A single transit event does not prove the presence of an exoplanet. The star has to be observed until a second transit event occurs. With two consecutive transits, the orbital period of the planet can be determined and a prediction on the timing of the third transit can be made. Only after a third transit event has been measured at the predicted time does the exoplanet count as confirmed. Hence, it takes 2 to 3 years to confirm an exoplanet on an Earth like orbit. The transit method therefore has a bias towards short orbit planets.

For a transit to occur, the orbit of the planet has to be nearly perfectly aligned

with the observer. The probability P_t of an exoplanet transit assuming a circular orbit is given by (Beatty & Seager 2010):

$$P_t \approx \frac{R_s}{r} \quad (1.4)$$

where r [m] is distance between the star and the planet. For an Earth-like exoplanet, this would only be $P_t = 0.47\%$. It is therefore not always possible to follow up RV detections with transit measurements to determine the radius of the exoplanet.

The first exoplanet detected using the transit method is HD 209548b (Charbonneau et al. 2000; Henry et al. 2000). This detection was a follow-up study of a previous RV discovery. Since then multiple ground and space based surveys using the transit method have been conducted. So far, the Kepler space mission (Borucki 2016) has been the most successful survey, in number of exoplanets detected, at 2774 confirmed exoplanets¹. These efforts are followed up with other space based missions like TESS (Ricker et al. 2010) and CHEOPS (Broeg et al. 2013; Fortier et al. 2014).

1.1.2 Demographics

The discovery of thousands of exoplanets allows to analyze their demographics. Such studies most often use the radius, mass, or orbital period to classify exoplanets. It is common to express the mass of planets in Jupiter masses ($M_J = 1.89813 \times 10^{27}$ kg), the radius in Jupiter radii ($R_J = 6.9911 \times 10^7$ m) and the orbital period in days. As we have seen in Sect. 1.1.1, the radius of a planet can be determined by the transit method, the mass of a planet by the RV method, and the orbital period by both. Other parameters that can be derived from these quantities are the semi-major axis and bulk density. The known exoplanets as well as our Solar System planets are shown in Fig. 1.3. However, before analyzing exoplanet demographics, it is important to understand observational biases.

Observational bias

Most exoplanets have been detected using either the transit or the RV method. Both detection methods favor large exoplanets on short orbits. Most discovered planets therefore have an orbital period of less than 100 days and many of them have masses similar to or heavier than Jupiter. Only high contrast imaging has

¹As of 03.06.2024 according to the NASA exoplanet archive.

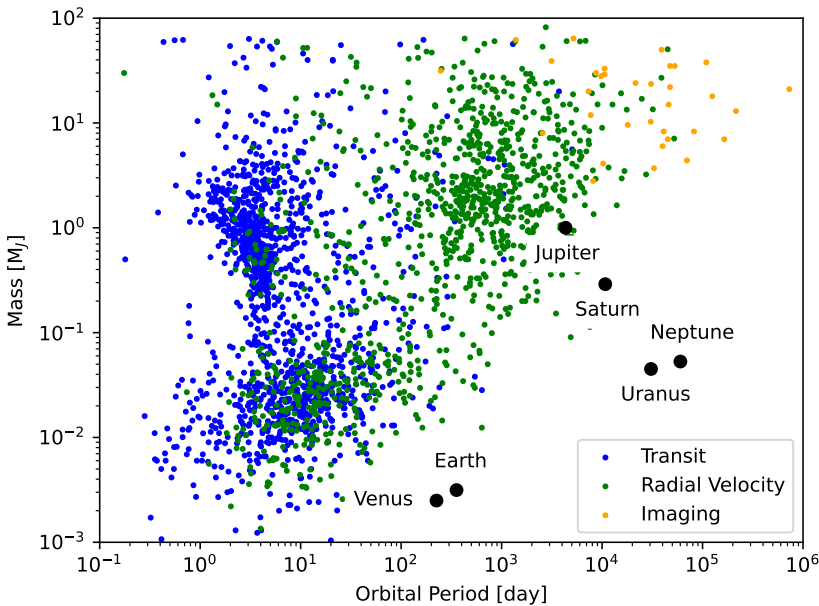


Figure 1.3: Solar System planets and all known exoplanets as of 13.05.2024 that were discovered with either the transit, RV, or direct imaging method. This plot was made using the database exoplanet.eu and pyExoplaneteu.

a bias towards wide orbit planets. Because imaging favors luminous planets, it is biased towards large, young planets. As a result of these biases, most planets found so far are not similar to any Solar System planets (see Figure 1.3). Long-term and large-scale surveys like PLATO (Rauer et al. 2014) are designed to help counteract this biases by finding smaller planets on wider orbits.

Another important bias in the detection of exoplanets are their host stars. The Kepler survey focused on stars with roughly the same mass as our Sun. Since Kepler detected a majority of the currently known exoplanets, most known planets therefore orbit either an F-, G-, or K-star. Exoplanets around other stellar types can be more difficult to observe. A-stars are rapidly rotating, which make detections via RV difficult. More active stars, like M-dwarfs, have variable brightness due to stellar activity which complicates both RV and transit measurements (Czesla et al. 2009; Boisse et al. 2011). However, the lower number of discovered planets around these stars is not entirely due to observational biases. Investigations have shown that planets around A-stars

might occur less frequently (Sabotta et al. 2019). Extremely massive O- and B-stars are too luminous to allow for efficient planet formation, and thus less planets are expected to form (Pinilla et al. 2022).

Temperature

An important quantity to classify exoplanets by is the temperature. Even though the thermal structure of a planet is complex, for classification purposes it is often useful to define a single global temperature. One way to calculate such a global temperature is by considering the energy balance of incoming stellar radiation and the emitted radiation of the planet. Assuming that the planet and the star emit like a blackbody, the equilibrium temperature T_{eq} [K] is:

$$T_{\text{eq}} = T_{\text{star}} \sqrt{\frac{R_{\text{star}}}{r}} \sqrt[4]{f(1 - A_B)} \quad (1.5)$$

where T_{star} [K] is the temperature of the star, R_{star} [m] is the radius of the star, r [m] is the distance between the star and the planet, and A_B is the Bond albedo of the planet. The variable f describes the heat redistribution of the planet which can range from 1/4 for a fully efficient heat transfer to 2/3 for no heat transfer (Hansen 2008) and it depends on the rotational period, semi-major axis, and atmospheric composition. Oftentimes the atmospheric structure is more complex than these two corner cases (see e.g. Mol Lous et al. 2022; Innes et al. 2023).

Another global temperature is the effective temperature T_{eff} [K]. In addition to the equilibrium temperature, it considers the intrinsic temperature T_{int} [K] of a planet:

$$T_{\text{eff}}^4 = T_{\text{eq}}^4 + T_{\text{int}}^4 \quad (1.6)$$

The intrinsic temperature T_{int} of a planet describes the heat flux coming from the planet's deep interior. For hot Jupiters T_{int} can range from 100 K to 700 K (Thorngren et al. 2019).

While defining a single temperature is desirable for classification, the atmospheric structure of exoplanets is complex and can cover a wide temperature range (see Sect. 2.3.3). Especially close-in planets are known to have large temperature differences between day- and night-side which neither the equilibrium temperature nor the effective temperature can fully capture.

Hot Jupiters and the Neptunian desert

Already the first detection of an exoplanet defined a new class of planets: hot Jupiters. These gas-giant planets have masses similar to Jupiter ($\sim 0.3 M_J$ to $\sim 13 M_J$) but are on orbits with periods of days. Due to the close proximity of these planets to their host stars, tidal forces slow down the rotation of the planet until the rotational period is equal to the orbital period (Showman et al. 2020). In this state, a planet is called tidally locked. Hot Jupiters therefore receive all irradiation on one-side of the planet, called the day-side, and none on the other, called the night-side. Day-side temperatures are typically between 1000 K to 2000 K. If the temperature reaches above 2200 K, the planet is classified as an ultra-hot Jupiter. If the temperatures are below 800 K, the planet can be called a warm Jupiter. A planet with a mass between $\sim 0.1 M_J$ and $\sim 0.5 M_J$ is sometimes also classified as a hot or warm Saturn. The extreme temperature differences between day and night side of these planets lead to unique climates (see Sect. 1.2.3). While hot Jupiters are one of the most detected types of exoplanets, this is mainly due to observational biases. Population studies found that hot Jupiters occur only around 0.4% of all A, F, and G stars (Beleznay & Kunimoto 2022).

The exoplanet demographic plot in Fig. 1.3 shows a clear absence of planets with masses between $0.1 M_J$ to $1 M_J$ with orbital periods of less than 4 days. This is called the Neptunian or sub-Jovian desert. Studies have shown that the origin of this desert can be explained by high eccentricity migration and photo-evaporation of the planetary atmosphere (Matsakos & Königl 2016; Owen & Lai 2018). If a planet has more than $1 M_J$, its gravity is large enough to retain the atmosphere despite the strong irradiation. However, if a gas-giant is less massive than $1 M_J$, it is likely to loose all of its atmosphere leaving behind a barren core.

Sub-Neptunes and terrestrial planets

The most common type of exoplanets discovered so far are planets with a radius between 1 to 4 Earth radii (Batalha et al. 2013; Morton & Swift 2014; Petigura et al. 2018; Zhu & Dong 2021). If the bulk density of these planets is closer to that of a gaseous planet, they are classified as sub-Neptunes. If the bulk density is closer to terrestrial planets, they are classified as super Earths. Even when accounting for observational biases, they are more abundant than earth-sized planets. However, as we have discussed before, it is possible that many of the super Earths are stripped cores from previously gaseous planets (Neil & Rogers 2020).

The existence of life is one of the big questions of exoplanet research. Hence, terrestrial planets that can harbor liquid water are of special interest. While water is no guarantee for life on a planet, it is essential for all life forms on Earth. A planet is defined as habitable if its distance from the star allows liquid water to occur on its surface. Trappist-1 is one of the most famous planetary systems because it contains seven terrestrial planets, three of which are in the habitable zone (Gillon et al. 2017). Because the host star is an M-dwarf, which is much dimmer than our Sun, the habitable zone is closer to the star. First attempts at detecting the atmosphere of the Trappist-1 planets were not successful (Ih et al. 2023; Greene et al. 2023).

1.1.3 Probing atmospheres

The mass, orbital period, and radius of an exoplanet can be derived directly from detection methods. However, to measure the atmospheric composition, spectral information is required. The two most common techniques to probe exoplanet atmospheres are transit spectroscopy and measuring absorption features in the thermal emission of a planet.

Transmission spectroscopy

Transmission spectroscopy measures the transit depth at multiple wavelengths (see Fig. 1.4). It is important to note that the observed radius of a planet is not a physical radius, but rather the radius of a circular disk that would absorb the same amount of light as the planet. Let's imagine a planet with a rocky core and no atmosphere. In this case, the observed radius is the same for all wavelengths and equal to the actual radius of the planet. However, if the planet has an atmosphere, certain wavelengths will be absorbed more than others, leading to different observed radii. Because the opacity of gas-phase species is highly wavelength dependent (see Sect. 2.4.2), light traveling through the atmosphere will carry the fingerprints of the atmospheric composition.

The differences in transit depth caused by the atmosphere are typically less than 1% for hot Jupiters and 0.1% for terrestrial planets. Observing such small differences is difficult and further complicated by stellar activity (Ballerini et al. 2012; Genest et al. 2022). Therefore, state-of-the-art instrumentation is required to probe the composition of exoplanet atmospheres. Gas-phase molecules have successfully been detected in many different exoplanets using, for example, space telescopes like Spitzer (Deming & Knutson 2020; Spake et al. 2021) or JWST (Tsai et al. 2023; Dyrek et al. 2023; Alderson et al. 2023; Feinstein et al. 2023)

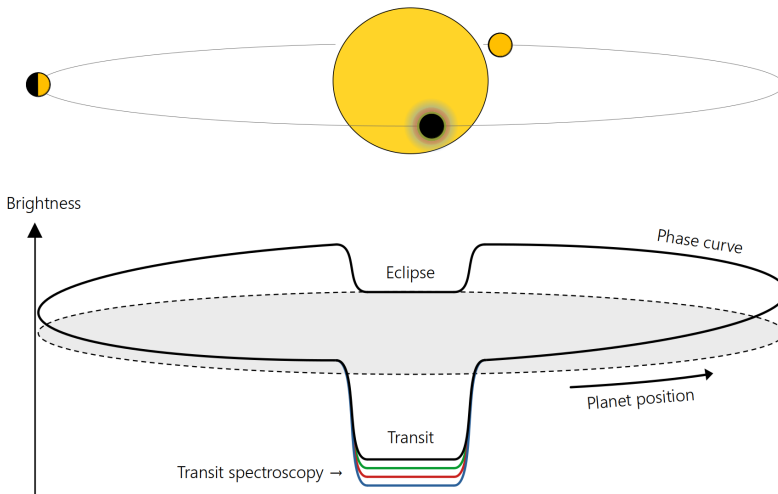


Figure 1.4: Illustration of the transit method, transit spectroscopy, phase curve, and secondary eclipse. The phase curve is tilted due to the hot spot offset of the planet (see Sect. 2.3.3). Image adapted from ESA illustration for phase curves.

and ground based telescopes like HARPS (Hoeijmakers et al. 2020; Stangret et al. 2022) or MAROON-X (Kasper et al. 2021; Pelletier et al. 2023).

Transmission spectroscopy can also be used to study inhomogeneities in the structure of exoplanets. During the beginning and end of a transit, only half of the planet is in front of the star. The transit depth is therefore determined by the side of the planet which currently covers the star (Paris et al. 2016; Savel et al. 2023). While such observations are more challenging, they were successfully conducted and resulted in new insights into the inhomogeneous structure of exoplanet atmospheres (Prineth et al. 2022).

Planetary emission and phase curves

The flux of a planet is much lower than the flux of its host star but it is still observable. As discussed in Sect. 1.1.1, high contrast imaging uses the thermal emission of planets for detections. This technique is also suitable for spectroscopic observations (see e.g. Samland et al. 2017; Nasedkin et al. 2024). Similar to transmission spectroscopy, the thermal radiation from a planet passes through the atmosphere where it is wavelength dependently absorbed. The thermal emission thus also carries the fingerprints of the atmosphere. Directly

imaged planets are great targets to study the atmosphere of young planets since most planets detected with this technique are young objects which are still hot from their formation. These observations are most fruitful in wavelengths where the contrast between planet and star is most favorable. From Wien's law, we know that the peak in emission of a blackbody happens at the wavelength:

$$\lambda^{\text{Wien}} = \frac{2898 \mu\text{m K}}{T_{\text{obj}}} \quad (1.7)$$

where T_{obj} [K] is the blackbody temperature of the light emitting object. Taking the example of a hot Jupiter ($T_{\text{planet}} \approx 1000$ K, $\lambda_{\text{planet}}^{\text{Wien}} \approx 2.9 \mu\text{m}$) around a G-star ($T_{\text{star}} \approx 5500$ K, $\lambda_{\text{star}}^{\text{Wien}} \approx 0.52 \mu\text{m}$), we see that observing in the near infrared results in a favorable contrast.

The emission of a planet can also be measured for close-in planets. By observing the full orbit of an exoplanet around its host star, the contribution of the planet to the total brightness can be measured (see Fig. 1.4). This is called a phase curve. The disappearance of the planet behind the star is called the secondary eclipse. Because the hottest point of a close-in exoplanet is oftentimes offset from the sub-stellar point, the maximum contribution of the planet is shortly before the secondary eclipse. Similar to transit spectroscopy and high contrast imaging, observations of phase curves can also be used to study the spectral features of an exoplanet to gain insights into its atmosphere (see e.g. Deming & Knutson 2020; Greene et al. 2023; Zieba et al. 2023).

1.2 Atmospheres

Understanding the atmosphere of exoplanets is the key to many open questions about planet formation, planetary evolutions, and habitability. Thanks to space telescopes like Spitzer, HST, and JWST, we are able to research the atmospheres of exoplanets and learn more about their composition, clouds, and climate.

1.2.1 Atmospheric composition

From Solar System planets, it is known that planets can have vastly different atmospheric compositions. Earth's atmosphere consists mainly of nitrogen (78%) and oxygen (21%) (Schubert & Walterscheid 2002). The atmospheres of Venus and Mars on the other hand are dominated by CO₂ (Marcq et al. 2017; Trainer et al. 2019). For the gas-giants Jupiter, Saturn, Uranus, and Neptune, hydrogen and helium make up the bulk of the observable atmosphere (Atreya et al. 2020). The exact composition of a planet depends on its formation history

and can vary notably between planets (Turrini et al. 2015; Mordasini et al. 2016; Mollière et al. 2022). For exoplanets, measuring the precise atmospheric composition is difficult (see Sect. 1.1.3).

The dominant gas-phase species in the atmosphere of gas-giant exoplanets are hydrogen and helium. Observations have also confirmed the presence of many other molecules and atoms like H₂O, CO₂, CO, TiO, CH₄ Na, and K (Sing et al. 2011; Žák et al. 2019; Guilluy et al. 2019; Prinot et al. 2022; Rustamkulov et al. 2023). Unfortunately, measuring precise abundances for a wide range of gas-phase species is difficult. Chemical models of exoplanet atmospheres therefore rely on assumptions about their composition. A common starting point is to assume solar abundances (Asplund et al. 2009). However, what can be inferred from observations is the metallicity [Fe/H] which is defined as the logarithm of the ratio between the fraction of elements heavier than hydrogen and helium in the planet compared to our sun. In astrophysics, these heavier elements are commonly called metals. The metallicity of an exoplanet can be estimated based on its mass, radius, and evolution history (Miller & Fortney 2011; Thorngren et al. 2016; Müller et al. 2020). Another important quantity for exoplanets is the carbon to oxygen (C/O) ratio. This ratio is used, for example, to identify formation and evolution history of planets (Öberg et al. 2011; Helling et al. 2014; Öberg & Bergin 2016; Mollière et al. 2022; Tabone et al. 2023). Solar abundances have a C/O ratio of ~ 0.5 which corresponds to an oxygen rich environment. For exoplanets, the C/O ratio is often inferred from H₂O and CO measurements assuming all carbon is in CO and all the oxygen in H₂O and CO (see e.g. Hood et al. 2024).

1.2.2 Clouds

On Earth, cloud formation starts with small solid particles that are lifted from the surface into the atmosphere. They can originate from, for example, deserts, volcanic activity, forest fires, or man-made pollution (Boucher 2015). These particles are called aerosols and they are the precursors of cloud formation. If an atmospheric parcel loses pressure or if it cools down, it can hold less water vapor and water can become supersaturated. It then condenses onto the aerosols, forming a cloud. If the cloud particle becomes large enough, they will fall as rain to the ground. After the water accumulates to rivers, lakes, and oceans, it can again evaporate into the atmosphere. This forms the water and cloud formation cycle of Earth.

The cloud formation on Venus and Mars can also start with aerosols originating from their surface onto which other materials can condense. Mars has water ice clouds similar to Earth's cirrus clouds (Whiteway et al. 2009). Venus on

the other hand has higher atmospheric pressures, higher temperatures, and a different atmospheric composition than Earth. Clouds are therefore made not from water but from sulfuric acid (H_2SO_4) and extend from 40 km up to 80 km above the surface (Titov et al. 2018). For gas-giant planets, aerosols have to form directly from the gas phase and are called Cloud Condensation Nuclei (CCNs). This can happen through nucleation which describes the process of gas-phase species growing to larger clusters. In the Solar System, gas-giant planets are further away from the Sun than terrestrial planets and are therefore colder. Jupiter has a temperature around 165 K. Its clouds are made from ammonia (NH_3) and ammonia hydrosulfide (NH_4SH) (Ragent et al. 1998). It is also possible that there are water clouds further down in the atmosphere but so far no observation could reach deep enough to confirm them (Wong et al. 2023). Uranus and Neptune are even colder at 76 K and 72 K, respectively. Both have layers of methane clouds (CH_4) and they show evidence of lower hydrogen sulfide clouds (H_2S) (Hueso & Sánchez-Lavega 2019). It is also possible that Uranus and Neptune have ammonia hydrosulfide and water clouds deeper in their atmosphere.

Compared to Solar System planets, exoplanets span over a large range of temperatures and pressures, allowing many different materials to form clouds. The atmosphere of terrestrial planets is especially difficult to constrain because they span a wide range of possible compositions (Forget & Leconte 2014). While water clouds are a possibility, so are clouds similar to what we know from Venus. For hotter terrestrial exoplanets, materials like KCl and ZnS are discussed as cloud materials (Gao & Benneke 2018). So far, most observations of terrestrial atmospheres have resulted in flat transmission spectra. It is unclear if this is caused by clouds or the absence of an atmosphere (Bean et al. 2010; Kreidberg et al. 2014; Libby-Roberts et al. 2022; Ridden-Harper et al. 2023).

In hot Jupiters, the temperatures are high enough for silicate-, iron-, and magnesium-bearing species to form clouds (Hellings et al. 2001; Hellings & Woitke 2006; Gao et al. 2020; Hellings et al. 2020). At these temperatures CCNs are formed from species like TiO_2 , SiO , or V_2O_5 (Bromley et al. 2016; Sindel et al. 2022; Lecoq-Molinos et al. 2024). These clouds are made from solid materials and have large opacities. While many aspects of clouds in gas-giant exoplanets can only be studied through theoretical modeling, the first detections of silicate clouds on hot Jupiters were recently possible (Grant et al. 2023; Dyrek et al. 2023). However, some measurements of potentially cloudy atmospheres result in a simple flat transmission spectra (Espinoza et al. 2019; Spyros et al. 2021).

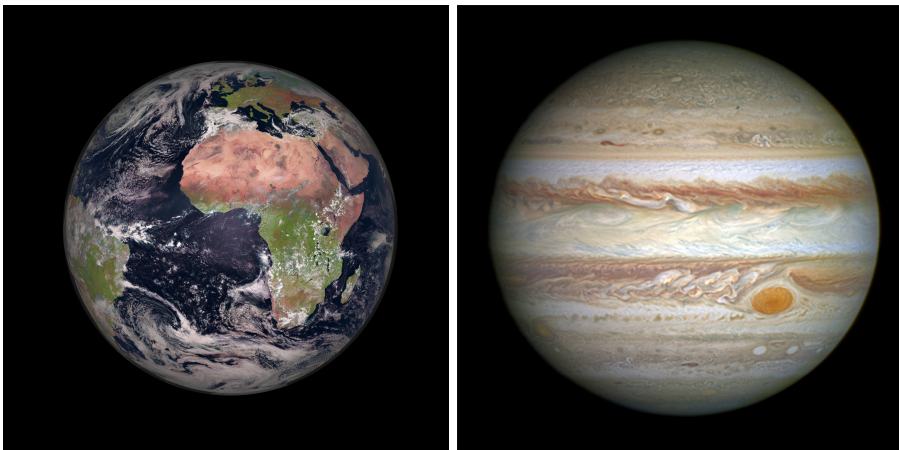


Figure 1.5: Satellite images of Earth (EUMETSAT/ESA) and Jupiter (NASA, ESA, and A. Simon).

1.2.3 Climate and weather

The range of planetary climates already becomes apparent when comparing Earth and Jupiter (see Fig 1.5). Earth has three main atmospheric cells (Hadley, Farrel, and Polar; Goosse et al. 2010), which lead to strong rainfall at the equator, the Sahara desert and jet streams at the border of the cells. Jupiter on the other hand has multiple "stripes" from the north to south pole (Young et al. 2019) and a red spot which is a storm going on for more than a century (Simon et al. 2018).

The diversity of exoplanets naturally leads to a diversity of climates. Baeyens et al. (2021) analyzed a large range of possible exoplanets and found that cooler planets ($T_{\text{eq}} < 1000$ K) have a more uniform chemical structure whereas hotter planets ($T_{\text{eq}} > 1800$ K) exhibit strong longitudinal differences. Based on these climate simulations, Helling et al. (2023) calculated cloud structures. They found three categories of climates which exhibit different cloud structures: cool planets ($T_{\text{eq}} < 1200$ K), intermediate temperature planets ($1400 \text{ K} < T_{\text{eq}} < 1800$ K), and ultra hot planets ($T_{\text{eq}} > 2000$ K). Cool planets have a global cloud coverage, intermediate temperature planets have an asymmetric day-side cloud coverage, and hot planets have no clouds on the day side. The general circulation of hot Jupiters is discussed in more detail in Sect. 2.3.3.

While the climate describes the time averaged structure of an atmosphere, weather describes the short term changes. On Earth, we are well aware that the

weather of a planet is not static. Cloud coverage, winds, and temperatures can change daily, or even hourly. It is therefore not unreasonable to expect that the climate of exoplanets is variable as well (Crossfield 2015; Cooke et al. 2023; Lee et al. 2024). Unfortunately, it is difficult to observationally distinguish between variability in an exoplanet atmosphere and stellar activity (Lally & Vanderburg 2022).

1.3 Goals and outline

Through theoretical studies (Helling et al. 2016; Gao & Powell 2021; Helling et al. 2023) and observations (Grant et al. 2023; Dyrek et al. 2023), we know that clouds can be expected to be present in most exoplanets. Studying cloud formation in exoplanet atmospheres using detailed micro-physical modeling and analyzing the interplay of clouds with the atmospheric structure is therefore crucial to gain insights into exoplanet atmospheres. In this thesis, we study the details of the interplay of chemistry, clouds, and climate within exoplanet atmospheres to understand how cloud formation shapes the structure of an exoplanet atmosphere and to support characterization efforts.

1.3.1 Research questions

The interplay of atmospheric processes is complex in nature and computationally expensive to model. To advance our understanding of how clouds affect and are affected by the thermal and chemical structure of an exoplanet, the following three research questions are addressed:

How do thermal and chemical non-equilibria interact with cloud formation?

The atmospheres of exoplanets are known to be affected by chemical disequilibrium drivers like quenching and photo-chemistry (Moses et al. 2011; Moses 2014; Rimmer & Helling 2016; Zamyatina et al. 2022; Tsai et al. 2023). Furthermore, recent theoretical studies (Plane & Robertson 2022) and observations (Fonfría et al. 2008, 2017, 2021) found that some gas-phase species in low density environments are not in thermal equilibrium with the surrounding gas phase. Cloud formation therefore might happen in environments that are not necessarily in chemical or thermal equilibrium.

Cloud formation is a chemical process and is therefore systematically coupled to gas-phase chemistry. The first steps of cloud formation, e.g. nucleation, are often calculated under the assumption of either chemical equilibrium (see e.g.

Helling & Fomins 2013; Powell et al. 2018; Lee 2023) or monomeric growth (see e.g. Lee et al. 2015; Sindel et al. 2022; Lecoq-Molinos et al. 2024). While Patzer et al. (1998) already defined a theoretical framework that lifts these assumptions, few studies have used it so far to study nucleation (Boulangier et al. 2019b; Köhn et al. 2021). A study coupling kinetic nucleation to the bulk growth of other cloud particle materials has not yet been conducted. Furthermore, while some studies highlight the possible impact of thermal non-equilibrium on cloud formation (Patzer et al. 1998; Helling & Woitke 2006; Köhn et al. 2021), no study has been conducted evaluating kinetic nucleation in thermal non-equilibrium.

To understand how cloud formation is affected by thermal and chemical non-equilibria a detailed look at the kinetic theory of cloud formation is needed. This is particularly the case for the nucleation process because it provides the bridge between gas-phase and solid cloud particles. Thermal non-equilibrium can impact the stability of clusters and thus affect the formation of CCNs. Because nucleation competes with bulk growth for gas-phase species, small changes in the timescales of either can lead to significant change in the cloud structure. This competition for material depends on the timescale of the individual processes and can also impact the gas-phase chemistry. Studying gas-phase chemistry, kinetic nucleation, and bulk growth together, each in its full complexity, is therefore crucial to understand their interplay.

What are the optical properties of heterogeneous cloud particles?

Cloud particles have a large opacity compared to gas-phase molecules. Some observations of exoplanet atmospheres using the transit method have resulted in flat transmission spectra which was attributed to the presence of clouds (Bean et al. 2010; Kreidberg et al. 2014; Espinoza et al. 2019; Spyros et al. 2021; Libby-Roberts et al. 2022). Only through recent observations with JWST was it possible to measure the spectral features of cloud particle materials, thus proving the presence of clouds in exoplanet atmospheres (Grant et al. 2023; Dyrek et al. 2023). Such studies require a detailed understanding of the optical properties of cloud particles.

In contrast to water clouds on Earth, clouds in hot Jupiters might be considerably heterogeneous (Helling et al. 2008b; Min et al. 2020; Helling et al. 2021; Komacek et al. 2022; Helling et al. 2023). While the optical properties of homogeneous cloud particle materials have been studied in detail (Wakeford & Sing 2015; Kitzmann & Heng 2018; Potapov & Bouwman 2022), heterogeneous particles are more complex. In the most general case, their opacity depends on the composition, shape, and material distribution of the cloud particle (see e.g. Bohren & Huffman 1983; Draine & Flatau 1994; Min et al. 2003; Lodge et al.

2023). While these properties can be measured on Earth (see e.g. Unga et al. 2018; McGrory et al. 2022), they need to be approximated for cloud particles in exoplanet atmospheres. The three most common assumptions for the cloud particle morphology are either that materials are well-mixed (e.g. Min et al. 2020; Dyrek et al. 2023; Lee 2023), that they consist of two materials where one material forms a shell around the other (Wong et al. 2020; Gao & Powell 2021; Komacek et al. 2022), or that each material forms homogeneously (Powell et al. 2019; Roman et al. 2021; Christie et al. 2022).

To support the characterization efforts of clouds in exoplanet atmospheres, the optical properties of heterogeneous cloud particles will be studied in detail. Firstly, it is important to determine which cloud particle materials influence the observations, even if they are only a minor component. If small amounts of a material can change the overall opacity of a cloud particle, it is crucial to accurately model that species. Secondly, the effect of different assumptions on the cloud particle morphology will be investigated. Being able to differentiate between well-mixed and non-mixed particles within observations would allow to gain further insights into cloud particle properties within exoplanet atmospheres.

How do clouds affect the climate of warm Saturns?

The day-side of (ultra) hot Jupiters can be hot enough to inhibit cloud formation. However, to achieve such high temperatures, the planet needs to be very close to its host star (Helling et al. 2019a,b). Planets that are further away are more temperate. Already warm exoplanets with equilibrium temperatures between 500 K to 1000 K are expected to have a global cloud coverage (Helling et al. 2023). Understanding the climate, chemistry, and cloud coverage of these planets is the next step towards smaller and colder exoplanets.

HATS-6b, which was discovered by Hartman et al. (2015), is an especially interesting target to study for multiple reasons. Firstly, it is a warm Saturn type exoplanet with an equilibrium temperature around 700 K. Global cloud coverage can thus be expected which will impact the climate and observations. Secondly, HATS-6b has an M-dwarf host star. These stars are known for their high magnetic activity and consequently the high number of stellar energetic particles they emit. This will affect the chemistry of their planets. Furthermore, the comparably small radius of M-dwarfs compared to other stars results in high transit depths making such planets ideal for atmospheric characterization.

1.3.2 Outline

The theoretical background for this thesis is presented in Chapter 2. This includes atmospheric chemistry, cloud formation, 3D climate modeling, and opacity sources within exoplanet atmospheres. In Chapter 3, the effect of thermal non-equilibrium on kinetic nucleation is examined. The developed theory is applied to the nucleation of TiO₂. In Chapter 4, the interplay between a non-equilibrium gas-phase and cloud formation is investigated. This includes the study of polymeric TiO₂ nucleation, the catalytic potential of cloud particle surface reactions, and determining cloud formation timescales. In Chapter 5, we explore the opacity of heterogeneous cloud particles. The impact of cloud particle composition and structure on the transmission spectra are studied to determine the observability of cloud particle properties. In Chapter 6, we present the atmospheric modeling of HATS-6b, a warm Saturn around an M-dwarf host star. To model the atmospheric structure, an iterative approach between a micro-physical cloud model and a 3D climate model is used. Finally, in Chapter 7, we summarize the results of this thesis, draw conclusions and provide an outlook for future work.

Chapter 2

Theory and Modeling of Exoplanet Atmospheres

The atmospheres of exoplanets are complex environments where many physical processes take place. This work focuses on warm to hot gas-giant atmospheres where the atmospheric layers of interest for this thesis have temperatures from 300 K to 3000 K and pressures from 10^{-5} bar to 10^3 bar. Reproducing these conditions on Earth is difficult and insights from observations are limited. Therefore, in order to study the structure of exoplanet atmospheres, a detailed understanding of the underlying physical processes is required. This chapter covers the theory of atmospheric chemistry (Section 2.1), cloud formation in hot Jupiters (Section 2.2), climate modeling of exoplanet atmospheres (Section 2.3), and optical properties of cloud particles and the gas-phase (Section 2.4).

2.1 Atmospheric chemistry

The wide range of temperatures and pressures within exoplanet atmospheres allows the study of chemistry in environments that do not exist in our Solar System and are difficult to reproduce in laboratory environments. However, this means that there is little experimental data on the chemical reactions occurring in these environments. We therefore rely on theoretical studies to describe the chemistry of exoplanets. In its most general form, a chemical reaction can be

described by a set of reactants \mathcal{R} being transformed into a set of products \mathcal{P} :



where ν_R and ν_P are the stoichiometric coefficients of the reactants and products, respectively. An example reaction would be:



The law of mass action states that the rate of a chemical reaction $R_r^+ [\text{cm}^{-3} \text{s}^{-1}]$ is proportional to the number densities $n_i [\text{cm}^{-3}]$ of its reactants. In the case of our example, this is:

$$R_r^+ = k_r^+ n_{\text{H}_2\text{O}} n_{\text{CO}} \quad (2.3)$$

where $k_r^+ [\text{cm}^3 \text{s}^{-1}]$ is the forward rate coefficient. A chemical reaction can also happen in reverse. The rate of the reverse reaction $R_r^- [\text{cm}^{-3} \text{s}^{-1}]$ is also given by the law of mass action. For our example, this is:

$$R_r^- = k_r^- n_{\text{H}_2} n_{\text{CO}_2} \quad (2.4)$$

where $k_r^- [\text{cm}^3 \text{s}^{-1}]$ is the backward rate coefficient. In this section, the two most common approaches used to model the chemistry of exoplanet atmospheres are described: equilibrium chemistry and chemical kinetics.

2.1.1 Equilibrium chemistry

Chemical equilibrium of a gas-phase describes the state where the net change in number densities of all gas-phase species is zero. The forward and backward rates of each chemical reaction must therefore be equal:

$$R_r^+ = k_r^+ \dot{n}_{\text{H}_2\text{O}} \dot{n}_{\text{CO}} = k_r^- \dot{n}_{\text{H}_2} \dot{n}_{\text{CO}_2} = R_r^- \quad (2.5)$$

where $\dot{n}_i [\text{cm}^{-3}]$ is the number density of species i in chemical equilibrium. The ratio of the reaction rate coefficients is therefore equal to the ratio of the equilibrium number densities of the reactants and products:

$$\frac{k_r^+}{k_r^-} = \frac{\dot{n}_{\text{H}_2} \dot{n}_{\text{CO}_2}}{\dot{n}_{\text{H}_2\text{O}} \dot{n}_{\text{CO}}} \quad (2.6)$$

Calculating chemical equilibrium number densities

Chemical reactions either produce (exothermic) or require (endothermic) energy which they exchange with the surrounding gas-phase through heat. From the

second law of thermodynamics, we know that during any process that exchanges heat δQ [erg] at a temperature T_{gas} [K], the change in entropy dS_{gas} [erg K⁻¹] is at least:

$$dS_{\text{gas}} \geq \frac{\delta Q}{T_{\text{gas}}} \quad (2.7)$$

Over time, an atmosphere therefore progresses towards a state of maximum entropy. From the first law of thermodynamics, we know that heat added to a system is equal to the work done on the system $p_{\text{gas}}dV_{\text{gas}}$ [erg] and the change in internal energy dU_{gas} [erg]:

$$\delta Q = dU_{\text{gas}} + p_{\text{gas}}dV_{\text{gas}} \quad (2.8)$$

where p_{gas} [bar] is the gas pressure and V_{gas} [cm³] is the atmospheric volume. Using the definition of the Gibbs free energy G_{gas} [erg], we find that the change in Gibbs free energy dG_{gas} caused by chemical reactions must be negative:

$$dG_{\text{gas}} = dU_{\text{gas}} + p_{\text{gas}}dV_{\text{gas}} - T_{\text{gas}}dS_{\text{gas}} = \delta Q - T_{\text{gas}}dS_{\text{gas}} \leq 0 \quad (2.9)$$

Therefore, to find the state of maximum entropy, the Gibbs free energy needs to be minimized. The total Gibbs free energy $G_{\text{tot,gas}}$ [erg] of a gas made from multiple gas-phase species is given by:

$$G_{\text{tot}}(T_{\text{gas}}, p_{\text{gas}}) = \sum_i \left[N_i \Delta_f G_i(T_{\text{gas}}) + N_i R T_{\text{gas}} \ln \left(\frac{N_i R T_{\text{gas}}}{p_{\text{gas}} V_{\text{gas}}} \right) \right] \quad (2.10)$$

where $\Delta_f G_i$ [erg mol⁻¹] is the Gibbs free energy of formation of the i -th gas-phase species, N_i [mol] the number of i gas-phase species, and $R = 8.314 \times 10^7$ erg K⁻¹ mol⁻¹ is the gas constant. Minimizing Eq. 2.10 for N_i results in:

$$\frac{dG_{\text{tot}}}{dN_i} = \Delta_f G_i(T_{\text{gas}}) + RT_{\text{gas}} \ln \left(\frac{\dot{N}_i R T_{\text{gas}}}{p_{\text{gas}} V_{\text{gas}}} \right) = 0 \quad (2.11)$$

where \dot{N}_i is the number of i particles in chemical equilibrium. Using Eq. 2.11, the ratio between the equilibrium number densities can be derived. For the example reaction from Eq. 2.2, the ratio of the chemical equilibrium abundances are therefore:

$$\frac{\dot{n}_{\text{H}_2} \dot{n}_{\text{CO}_2}}{\dot{n}_{\text{H}_2\text{O}} \dot{n}_{\text{CO}}} = \exp \left(- \frac{\Delta_f G_{\text{H}_2} + \Delta_f G_{\text{CO}_2} - \Delta_f G_{\text{H}_2\text{O}} - \Delta_f G_{\text{CO}}}{RT_{\text{gas}}} \right) \quad (2.12)$$

Using the equivalent relation for all gas-phase species considered, the equilibrium abundances can be determined.

Where is chemical equilibrium a good assumption?

Chemical equilibrium is a suitable assumption for collision-dominated environments where the timescales of chemical reactions are fast compared to processes driving the abundances out of equilibrium. This is the case in hot and dense environments such as the deep atmosphere of gas-giant exoplanets (Moses et al. 2011; Moses 2014). At low pressures or in cold environments, the timescales of dynamical mixing can be faster than the chemical timescales. In these atmospheric layers the vertical mixing of gas-phase species is faster than chemical equilibrium can be established. This process is called "quenching" which can lead to atmospheric layers resembling the atmospheric composition of deeper layers that are collision-dominated (Cooper & Showman 2006; Moses et al. 2011; Baeyens et al. 2021; Zamyatina et al. 2022). Another process known to bring atmospheres out of equilibrium is photochemistry which is most relevant in the upper atmosphere (Moses et al. 2011; Hu 2021; Baeyens et al. 2022). The further the radiation of the star penetrates the atmosphere, the more it is absorbed. Once most of the irradiation is absorbed by higher up layers, the effect of photochemical reactions becomes negligible.

Multiple numerical implementations have been developed which efficiently solve for chemical equilibrium (e.g. Stock et al. 2018, 2022; Woitke et al. 2018; Woitke & Helling 2021). Besides modeling the chemistry of collision-dominated environments, these tools are often used to determine the starting abundances for chemical kinetics networks.

2.1.2 Chemical kinetics

If chemical abundances are affected by disequilibrium processes, like quenching or photo-chemistry, the time-dependence of chemical reactions needs to be considered. In the most general case, the time-dependent change in number density n_i of each gas-phase species caused by chemical reactions is given by:

$$\frac{dn_i}{dt} = \sum_{r \in F_i} \left(\nu_{i,r} k_r \prod_{j \in E_r} n_j \right) - \sum_{r \in D_i} \left(\nu_{i,r} k_r \prod_{j \in E_r} n_j \right) \quad (2.13)$$

where F_i is the set of reactions r that have i as product, D_i is the set of reactions r that have i as reactant, E_r is the set of reactants of reactions r , $\nu_{i,r}$ is the stoichiometric coefficient, and n_j [cm^{-3}] are the number densities of the reactants of reaction r . To evaluate this system of Ordinary Differential Equations (ODEs) the reaction rate coefficients k_r have to be known.

Reaction rates

The rate of chemical reactions can depend on many factors like temperature, pressure, or radiation. The exact dependencies vary between reactions. A common type of reactions considered within atmospheres are bi-molecular reactions ($A + B \rightarrow C + D$). Their reaction rate coefficients are often described with only a temperature dependence using the modified Arrhenius form (Arrhenius 1889):

$$k_r(T_{\text{gas}}) = \alpha_r T_{\text{gas}}^{\beta_r} \exp\left(-\frac{\gamma_r}{T_{\text{gas}}}\right) \quad (2.14)$$

where α_r [$\text{s}^{-1} \text{cm}^{3(q_r-1)} \text{K}^{-\beta_r}$], β_r , and γ_r [K] are reaction specific parameters¹. Reaction rates given in the Arrhenius form can be found in many chemical reaction networks for exoplanet atmospheres (see e.g. Venot et al. 2012; Rimmer & Helling 2016; Tsai et al. 2017).

If the reaction rate coefficient depends on pressure, the Arrhenius form alone is no longer sufficient. This is the case for association reactions ($A + B + M \rightarrow AB + M$). These reactions require a third body M that removes the released bond energy which would otherwise increase the chance of an immediate dissociation. Pressure dependent reactions can be described with the Lindemann approach (Lindemann et al. 1922). Assuming that any gas-phase species can act as third body M, the reaction rate is given by:

$$k(T_{\text{gas}}, p_{\text{gas}}) = \frac{k_0 p_{\text{gas}}}{k_B T_{\text{gas}} + \frac{k_0 p_{\text{gas}}}{k_\infty}} F \quad (2.15)$$

where $k_B = 1.380649 \times 10^{-16}$ erg K⁻¹ is the Boltzmann constant, k_0 [$\text{s}^{-1} \text{cm}^{3q_r}$] is the reaction rate in the low pressure limit, and k_∞ [$\text{s}^{-1} \text{cm}^{3(q_r-1)}$] is the reaction rate in the high pressure limit². Both k_0 and k_∞ can be given in the Arrhenius form. F is an additional factor that can be used to modify the equation. In the Lindemann form, F is equal to 1. In other descriptions F can be a function of temperature and pressure (e.g. Troe form; Gilbert et al. 1983). An example of an association reaction which is often considered in chemical kinetics networks for exoplanet atmospheres is the association of molecular hydrogen: $H + H + M \leftrightarrow H_2 + M$ (see e.g. Venot et al. 2012; Tsai et al. 2017).

Often, only the forward rate of a chemical reaction is known. In this case, the principle of detailed balance can be used to derive the backward rate. This principle states that in local thermodynamic equilibrium, each forward rate is equal to the corresponding backward rate. Using chemical equilibrium as the

¹The variable q_r is the number of reactants in reaction r .

²The third body is not counted within q_r .

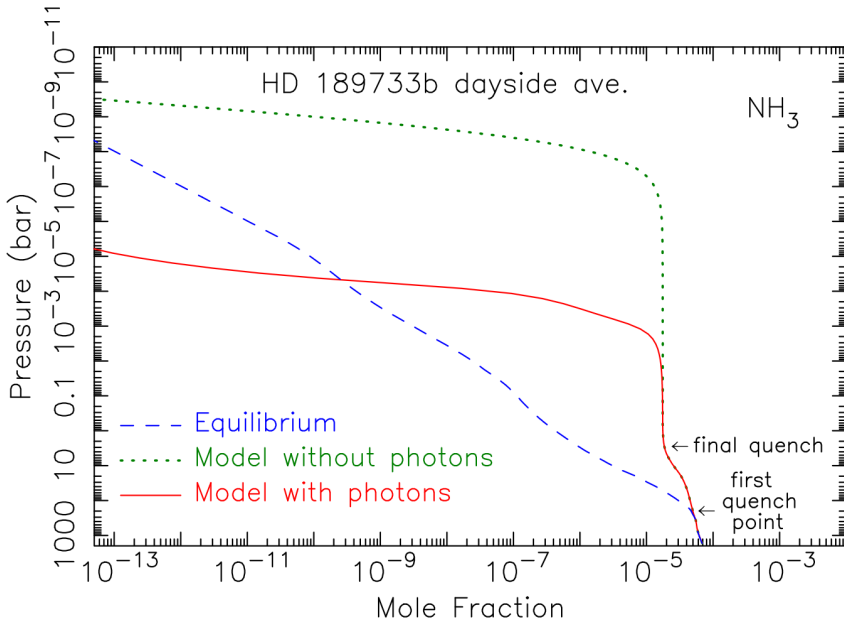


Figure 2.1: One dimensional chemical structure of the day-side of HD 189733b as predicted by chemical equilibrium and chemical kinetics. Figure taken from Moses et al. (2011). © AAS. Reproduced with permission.

reference state, the backward rate can be derived from the forward rate and the ratio of chemical equilibrium abundances (see Eq. 2.6). Furthermore, Eq. 2.12 links the ratio of equilibrium abundances to the Gibbs free energy of formation of the reactants and the products. Combining both equations for the example reaction from Eq. 2.2 leads to the following expression for the backward rate k_r^- :

$$k_r^- = k_r^+ \exp \left(\frac{1}{RT_{\text{gas}}} [\Delta_f G_{\text{H}_2} + \Delta_f G_{\text{CO}_2} - \Delta_f G_{\text{H}_2\text{O}} - \Delta_f G_{\text{CO}}] \right) \quad (2.16)$$

Chemical kinetics in exoplanet atmospheres

The most common drivers of chemical disequilibrium are quenching (Baeyens et al. 2021; Zamyatina et al. 2022) and photo-chemistry (Baeyens et al. 2022; Tsai et al. 2023). A good example for both effects is the day-side of HD 189733b. Its chemical composition was studied in detail by Moses et al. (2011). Take the

example of NH₃ (Fig. 2.1). Chemical equilibrium predicts a steadily increasing abundance with decreasing height (blue dashed line). If vertical mixing is included, the number densities start to deviate from equilibrium number densities (green dotted line). For pressures between 10⁻⁷ bar and 1 bar, chemical equilibrium cannot be established due to the fast mixing of chemical species from deeper layers. In these layers, the NH₃ number densities are constant and resemble deeper layers. Between 1 bar and 100 bar, the chemical timescale of NH₃ and the vertical mixing timescale are similar. Therefore, chemical equilibrium number densities cannot be established, nor are the number densities constant. Considering photo-chemistry changes the number densities of NH₃ once more. For pressures below 0.01 bar (higher in the atmosphere), photo-dissociation of NH₃ lowers the abundance. Photo-chemistry becomes less important deeper in the atmosphere because most of the stellar radiation is already absorbed higher in the atmosphere. While quenching leads to higher and photochemistry to lower NH₃ number densities on the day-side of HD 189733b, this can be the other way around for other chemical species or other planets (Chapman 1930; Tsai et al. 2021). Recently, photochemistry in exoplanet atmospheres has been confirmed observationally by detecting SO₂ that cannot be explained with equilibrium chemistry or quenching (Tsai et al. 2023).

The atmospheres of exoplanets are chemically rich. This is best demonstrated by chemical equilibrium calculations which consider hundreds of gas-phase species (Lodders & Fegley 2002; Woitke et al. 2018; Woitke & Helling 2021; Stock et al. 2018, 2022). Considering a chemical reaction network including all these molecules and all possible reactions between them is not feasible. Firstly, not all reaction rates are known. Secondly, the evaluation of such an enormous chemical network would be extremely computationally expensive. Detailed chemical networks considering only H, C, N, and O bearing molecules can already include hundreds or even thousands of reactions (see e.g. Moses et al. 2011; Venot et al. 2012; Rimmer & Helling 2016; Tsai et al. 2017). Reducing the number of reactions in chemical networks while ensuring an accurate prediction of the gas-phase chemistry is a complex task. Some studies reduce the number of reactions by carefully analyzing which reactions can be ignored without causing observable changes to the gas-phase (e.g. Venot et al. 2019). Other studies use net-reactions which summarize multiple chemical reactions into one reaction (Moses 2014; Tsai et al. 2022). Chemical kinetics networks are also actively being extended. Of particular interest are species like TiO and VO which can cause thermal inversions (Fortney et al. 2008; Piette et al. 2020) and sulfur species which are known to be affected by photo-chemistry (Polman et al. 2023). Reaction rates for these species are actively being researched and added to chemical reaction networks (Boulanger et al. 2019a; Hobbs et al. 2021).

To solve chemical kinetics networks, numerical tools are required. At its core,

a chemical kinetics network is a set of ODEs. However, the vastly different timescales of chemical reactions make these ODEs stiff. To evaluate them, a solver for stiff differential equations is required. DLSODES from the FORTRAN package ODEPACK (Hindmarsh 1983; Radhakrishnan & Hindmarsh 1993) is one of the most popular solvers for chemical kinetics networks (e.g. Agundez et al. 2014; Grassi et al. 2014; Rimmer & Helling 2016; Zamyatina et al. 2022; Kiefer et al. 2024). Alternatively, chemical kinetics networks can be evaluated using machine learning techniques (e.g. Hendrix et al. 2023; Maes et al. 2024). These techniques allow for a fast evaluation once the model is trained, but they require large training datasets.

2.2 Clouds in gaseous exoplanets

Clouds are present in all gas-giant planets of the Solar System and are present in exoplanet gas-giants as well. However, hot Jupiters do not have Solar System analogs. Detailed micro-physical models are therefore required to understand cloud formation for hot Jupiters (Fig. 2.2).

Cloud formation in gaseous exoplanets starts with the formation of CCNs through nucleation (Sect. 2.2.1). Because cloud particles of various sizes have to be considered, it is useful to express the equations using volume moments rather than size bins (Sect. 2.2.2). After CCNs are present in the atmosphere, other cloud particle materials that might not be able to nucleate themselves can grow onto CCNs. This can happen either through condensation or more complex surface reactions (Sect 2.2.3). While growing, cloud particles will gravitationally settle. Because the deep atmosphere of gas-giant exoplanets becomes increasingly hotter, the cloud particle materials will become thermally unstable and evaporate. Through advective and diffusive processes, cloud particle materials are brought up from the deeper atmosphere which replenishes the cloud forming layers of the atmosphere (Sect. 2.2.4). All these processes can be described within the master equation for cloud formation (Sect 2.2.5).

2.2.1 Nucleation

Nucleation describes the transition from gas-phase molecules to solid particles. These intermediate sized particles are called clusters. Sizes of clusters can be described by the number of monomeric units N and are therefore also called N -mers. For example the cluster $(\text{TiO}_2)_{10}$ is made from 10 TiO_2 monomers and is called a 10-mer. An N -mer can grow to an $N+M$ -mer through an association reaction with an M -mer. Reversely, an $N+M$ -mer can dissociate to an N -mer

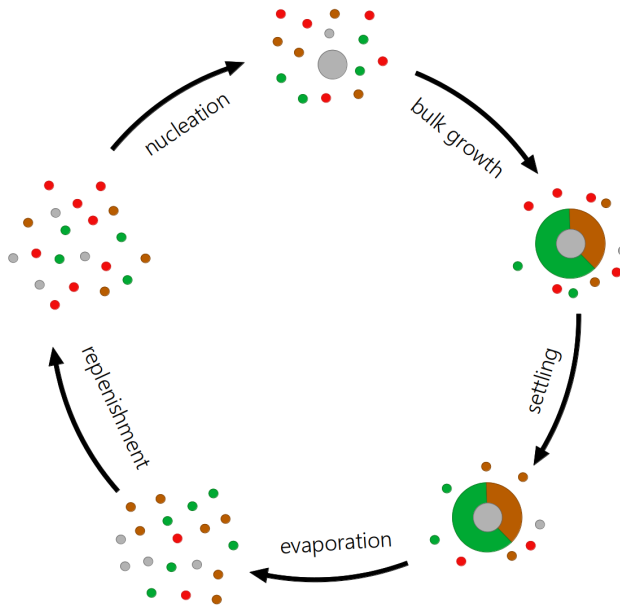


Figure 2.2: Illustration of the cloud cycle in gaseous exoplanet atmospheres.

and an M-mer. Once a cluster is large enough for other species to condense onto, it is called a CCN. There exist multiple formation pathways to go from a monomer to a CCN. If one particular formation pathway is faster than all the others, the overall nucleation rate is limited by the slowest step within this fastest pathway (Gail & Sedlmayr 2013; Helling & Fomins 2013). The cluster size of this slowest step in the fastest nucleation pathway is called the critical cluster size N_* . To calculate nucleation rates, multiple approaches exist.

(Modified) classical nucleation theory

Classical Nucleation Theory (CNT) calculates the nucleation rate J_* [$\text{cm}^{-3} \text{ s}^{-1}$] under the following assumptions³:

- The gas-phase and the clusters are in chemical equilibrium.
- Clusters grow only by addition of monomers.

³A detailed derivation can be found in Gail & Sedlmayr (2013).

- The thermodynamic properties of clusters can be approximated by the surface tension σ_∞ [erg cm⁻²] which describes the energy needed to increase the surface area of a solid, for example by cutting it. This definition requires that interior and surface atoms can be distinguished which might not be the case for small clusters (Donn 1978; Donn & Nuth 1985; Gail & Sedlmayr 2013).

Under these assumptions, the stationary nucleation rate is given by (Gail & Sedlmayr 2013; Lee et al. 2015; Sindel et al. 2022):

$$J_* = \frac{\dot{n}_1}{\tau_{\text{gr}}(N_*, T_{\text{gas}})} Z(N_*) \exp \left((N_* - 1) \ln(S(T_{\text{gas}})) - \frac{\Delta G(N_*)}{RT_{\text{gas}}} \right) \quad (2.17)$$

where \dot{n}_1 [cm⁻³] is the chemical equilibrium number density of the monomer, and $S(T_{\text{gas}})$ is the supersaturation ratio of the monomer which is given by:

$$S(T_{\text{gas}}) = \frac{\dot{n} k_B T_{\text{gas}}}{p_1^{\text{vap}}} \quad (2.18)$$

where p_1^{vap} [bar] is the vapor pressure of the monomer. The growth rate $\tau_{\text{gr}}(N, T_{\text{gas}})$ [s] for monomeric growth from an N-mer to an N+1-mer is given by:

$$\tau_{\text{gr}}^{-1}(N, T_{\text{gas}}) = \alpha(N, T_{\text{gas}}) A(N) v_{\text{rel}}(N, T_{\text{gas}}) \dot{n}_1 \quad (2.19)$$

where $\alpha(N, T_{\text{gas}})$ is the sticking coefficient, $A(N)$ [cm²] is the reaction surface area, $v_{\text{rel}}(N, T_{\text{gas}})$ [cm s⁻¹] is the relative velocity. Assuming spherical particles, the reaction surface is:

$$A(N) = 4\pi a_0^2 N^{2/3} \quad (2.20)$$

where a_0 [cm] is the radius of the monomer. The relative velocity between an N-mer and a monomer is:

$$v^{\text{rel}}(N, T_{\text{gas}}) = \sqrt{\frac{k_B T_{\text{gas}}}{2\pi} \frac{m_N + m_1}{m_N m_1}} \approx \sqrt{\frac{k_B T_{\text{gas}}}{2\pi m_1}} \quad (2.21)$$

where m_1 [g] is the mass of the monomer and m_N [g] the mass of an N-mer. The Zeldovich factor $Z(N_*)$ describes the probability of the critical cluster to grow rather than to dissociate (Vehkamäki et al. 2007):

$$Z(N_*) = \sqrt{\frac{\theta_\infty}{9\pi(N_* - 1)^{4/3}}} \quad (2.22)$$

$$\theta_\infty = \frac{4\pi a_0^2 \sigma_\infty}{k_B T_{\text{gas}}} \quad (2.23)$$

where the critical cluster size is given by:

$$N_* = \frac{1}{8} \left(\frac{2}{3} \frac{\theta_\infty}{\ln(S(T_{\text{gas}}))} \right)^3 + 1 \quad (2.24)$$

It is important to note that the critical cluster size can only be calculated if the supersaturation ratio $S(T_{\text{gas}})$ is positive. If $S(T_{\text{gas}})$ is smaller than 1, no nucleation takes place. Lastly, using modified classical nucleation theory (MCNT), the Gibbs free energy can be approximated by:

$$\frac{\Delta G(N_*)}{RT_{\text{gas}}} = \theta_\infty (N_* - 1)^{2/3} \quad (2.25)$$

CNT is useful to calculate nucleation in cases where there is little thermodynamic data of clusters available. However, it is important to note that it represents an approximation and does not account for the detailed thermodynamic properties of clusters.

Non-classical nucleation theory

If thermodynamic data of clusters are available, the surface tension approximation can be dropped. If one keeps the assumption of monomeric growth and chemical equilibrium, the Becker-Döring method can be used (Becker & Döring 1935; Gail & Sedlmayr 2013). In this case, the nucleation rate is given by:

$$\frac{1}{J_*} = \sum_{N=1}^{N_{\text{max}}} \left(\frac{\tau_{\text{gr}}(N)}{\dot{n}_N} \right) \quad (2.26)$$

where N_{max} is the largest cluster size considered. The chemical equilibrium number density of the N -mers \dot{n}_N are calculated with the thermodynamic data available:

$$\dot{n}_N = \frac{p^\ominus}{k_B T_{\text{gas}}} \left(\frac{\dot{p}_1}{p^\ominus} \right)^N \exp \left(-\frac{\Delta_f^\ominus G(N) - N \Delta_f^\ominus G(1)}{RT_{\text{gas}}} \right) \quad (2.27)$$

where $p^\ominus = 1$ bar is the standard pressure at which the thermodynamic properties have been measured, \dot{p}_1 [bar] is the partial pressure of the monomer, and $\Delta_f^\ominus G(N)$ [erg mol⁻¹] the Gibbs free energy of formation of the N -mer at standard pressure.

Non-classical nucleation theory (see e.g. Gail & Sedlmayr 2013; Helling & Fomins 2013) has been used to study the nucleating properties of species like TiO₂ (Lee

et al. 2015; Sindel et al. 2022) and V₂O₅ (Lecoq-Molinos et al. 2024). However, one needs to be aware that this method is limited by the largest cluster for which thermodynamic data is available which ideally should be larger than the critical cluster size N_{*}.

Kinetic nucleation networks

Patzer et al. (1998) further generalize the nucleation description by dropping the assumption of chemical equilibrium and monomeric growth. Here, we summarize their formalism. The time-dependent change of the cluster number densities n_N(t) in the most general form can be described with the following equation:

$$\frac{dn_N(t)}{dt} = \sum_{i=1}^I J_i^C(N, t) - \sum_{i=1}^I J_i^C(N + i, t) \quad (2.28)$$

$$J_i^C(N, t) = \sum_{m_i=1}^{M_i} \left(\frac{n_{N-i}(t)}{\tau_{gr}(m_i, N - i, t)} - \frac{n_N(t)}{\tau_{ev}(m_i, N, t)} \right) \quad (2.29)$$

where I is the maximum I-mer that contributes to the growth of a cluster. The effective transition rate J_i^C(N, t) [cm⁻³ s⁻¹] describes the rate at which (N-i)-mers transition to N-mers. The variable M_i is the set of all chemical reactions m_i which have an i-mer as reactant. The growth rate τ_{gr}(m_i, N - i, t) [s] and evaporation rate τ_{ev}(m_i, N, t) [s] for these reactions are given by:

$$\tau_{gr}^{-1}(m_i, N, t) = \alpha(m_i, N) A(N) v^{rel}(n_f(m_i), N) n_f(m_i, t) \quad (2.30)$$

$$\tau_{ev}^{-1}(m_i, N, t) = \beta(m_i, N) A(N) v^{rel}(n_r(m_i), N) n_r(m_i, t) \quad (2.31)$$

where n_f [cm⁻³] and n_r [cm⁻³] are the particle densities of the forward and backward reactant of reaction m_i, respectively. The variable α(m_i, N) is the sticking coefficient and β(m_i, N) is the efficiency of the reverse reaction. The reaction surface A(N) and the relative velocity v^{rel}(n_f(m_i), N) are the same as in Eq. 2.20 and Eq. 2.21, respectively.

For association reactions, where two clusters form a single, larger cluster (e.g. (TiO₂)₃ + (TiO₂)₂ → (TiO₂)₅), the corresponding dissociation reaction (e.g. (TiO₂)₅ → (TiO₂)₃ + (TiO₂)₂) is a spontaneous process. To calculate the dissociation rate, the reference state where the clusters are in local thermodynamic equilibrium with the gas-phase can be used (Patzer et al. 1998). In this state, the principle of detailed balance holds which states that each forward rate is equal to the corresponding backward rate. This allows the

derivation of the backward rate:

$$\tau_{ev}^{-1}(m_i, N, t) = \tau_{gr}^{-1}(m_i, N, t) \frac{1}{n_i(t)} \frac{\dot{n}_{N-i} \dot{n}_i}{\dot{n}_N} \quad (2.32)$$

The ratio between the cluster number densities in chemical equilibrium can be calculated from the thermodynamic properties of the reactants and the products using Eq. 2.27:

$$\frac{\dot{n}_{N-i} \dot{n}_i}{\dot{n}_N} = \frac{p^\ominus}{k_B T_{\text{gas}}} \exp \left(\frac{\Delta_f^\ominus G(N) - \Delta_f^\ominus G(N-i) - \Delta_f^\ominus G(n_i)}{RT_{\text{gas}}} \right) \quad (2.33)$$

We are now able to describe the association and dissociation of clusters through various reactions. The particle flux through the cluster size space at any given cluster size N can then be estimated using:

$$J_*(N, t) = \sum_{i=1}^{N-1} \sum_{j=(N-i)}^{N-1} \sum_{m_j=1}^{M_j} \tau_{gr}^{-1}(m_j, i, t) n_i(t) \\ - \sum_{i=N}^{N_{\max}} \sum_{j=(N-i)+1}^{i-1} \sum_{m_j=1}^{M_j} \tau_{ev}^{-1}(m_j, i, t) n_i(t) \quad (2.34)$$

where N_{\max} is the maximum cluster size for which thermodynamic data is available. The first term on the right hand side of Eq. 2.34 describes the rate at which clusters smaller than N grow to or past size N . The second term describes the rate at which clusters of size N or greater dissociate to clusters smaller than N . If enough cluster data is available, N should be chosen larger than the critical cluster size N_* . If nucleation is fast compared to other processes, the nucleation rate will become stationary $J_*(N, t) = J_*(t)$.

Studying nucleation with a full kinetic network requires in-depth investigations of nucleation pathways. Such an investigation was conducted by Boulangier et al. (2019a), who used a fully kinetic nucleation network to study the cluster formation within Asymptotic Giant Branch (AGB) stars. They considered the polymeric nucleation of TiO_2 , MgO , and Al_2O_3 . However, due to data limitations, the maximum cluster sizes they could consider were $(\text{TiO}_2)_{10}$, $(\text{MgO})_9$, and $(\text{Al}_2\text{O}_3)_8$. Another study was conducted by Köhn et al. (2021), who investigated the formation of $(\text{TiO}_2)_{10}$ and compared it to a Monte Carlo approach.

Nucleating species in exoplanet atmospheres

For hot Jupiters, possible nucleation species are TiO_2 (Lee et al. 2015; Sindel et al. 2022; Köhn et al. 2021; Kiefer et al. 2023), SiO (Lee et al. 2015; Bromley

et al. 2016; Andersson et al. 2023), and V_2O_5 (Lecoq-Molinos et al. 2024). For even hotter environments like the outflows of AGB stars, Al_2O_3 nucleation can be considered as well (Gobrecht et al. 2022). For temperate exoplanets, KCl and NaCl are commonly assumed to be the dominant nucleating species (Gao & Benneke 2018; Lee et al. 2018). Which gas-phase species nucleates most efficiently depends on the stability of the species, the temperature, pressure, and the abundance of the nucleating species in the gas-phase.

While detailed kinetic nucleation networks describe nucleation most accurately, these calculations rely on thermodynamic data of clusters which is often missing. The derivation of the thermodynamic data is computationally extensive and becomes increasingly difficult for larger cluster sizes. For TiO_2 , the thermodynamic data of clusters up to size 15 has been calculated (Sindel et al. 2022) and for SiO up to cluster size 20 (Bromley et al. 2016). For most other species only the smallest cluster sizes are known, making a non-classical nucleation approach not feasible. Furthermore, some species are known to not nucleate homogeneously. Vanadium oxide clusters, for example, change between VO , V_2O , and V_2O_5 depending on the cluster size (Lecoq-Molinos et al. 2024). Therefore, the cluster data of several $(\text{VO})_N$, $(\text{VO}_2)_N$, and $(\text{V}_2\text{O}_5)_N$ clusters have to be known to calculate the nucleation rate of V_2O_5 .

2.2.2 Moment method

Cloud formation depends on the size of the cloud particles. One possibility to consider this size dependence is to define discrete size bins. However, this requires solving the cloud formation equations for each size bin individually, making it computationally expensive. To avoid binning, Gail & Sedlmayr (1988) developed the moment method which was later expanded by Dominik et al. (1993). Rather than using a discretization of cloud particle sizes, the moment method reformulates the cloud formation equations in terms of the moments L_j [cm^j/g] which are defined as:

$$\rho_{\text{gas}} L_j = \int_{V_l}^{\infty} f(V, \mathbf{x}, t) V^{j/3} dV \quad (2.35)$$

where ρ_{gas} [g cm^{-3}] is the gas density, V [cm^3] is the volume of the cloud particle, $f(V, \mathbf{x}, t)$ [cm^{-6}] is the size distribution of cloud particles in volume space, and V_l [cm^3] is the minimum volume of a cloud particle. The moments can be used to derive the cloud particle number density n_c [cm^{-3}], the mean cloud particle radius $\langle a \rangle$ [cm], the mean cloud particle surface area $\langle A \rangle$ [cm^2]

and the mean cloud particle volume $\langle V \rangle$ [cm³] (Helling et al. 2001):

$$n_c = \rho_{\text{gas}} L_0 \quad (2.36)$$

$$\langle a \rangle = \sqrt[3]{\frac{3}{4\pi} \frac{L_1}{L_0}} \quad (2.37)$$

$$\langle A \rangle = \sqrt[3]{36\pi} \frac{L_2}{L_0} \quad (2.38)$$

$$\langle V \rangle = \frac{L_3}{L_0} \quad (2.39)$$

How the cloud formation equations can be expressed with the moments L_j is shown in the following sections.

2.2.3 Bulk growth

Thermal stability

Once CCNs are present in the gas-phase, other species that might not be able to form CCNs themselves can grow onto them. For net growth, the rate at which particles are deposited has to be larger than the rate at which particles evaporate. This relation is expressed by the supersaturation ratio $S_i(T)$. If the condensing species $i = X_a Y_b$ exists in the gas-phase we find:

$$S_i(T_{\text{gas}}) = \frac{p_i^{\text{part}}}{p_i^{\text{vap}}} = \frac{n_i k_B T_{\text{gas}}}{p^\ominus} \exp\left(\frac{\Delta_f^\ominus G_i - \Delta_f^\ominus G_i^{\text{solid}}}{RT_{\text{gas}}}\right) \quad (2.40)$$

where p_i^{part} [bar] is the partial pressure of species i , p_i^{vap} [bar] is the vapor pressure of species i , and $\Delta_f^\ominus G_i^{\text{solid}}$ [erg mol⁻¹] is the Gibbs free energy of formation of species i in the solid phase at standard pressure. If the condensing species i does not exist in the gas-phase, the thermodynamic properties have to be linked to its elemental components. For the case of chemical equilibrium, Helling & Woitke (2006) found that the supersaturation ratio of a fictitious material $M = X_a Y_b$ is:

$$S_i(T_{\text{gas}}) = \frac{(\dot{n}_X)^a (\dot{n}_Y)^b}{(p^\ominus / k_B T_{\text{gas}})^{(a+b)}} \exp\left(-\frac{\Delta_f^\ominus G_{X_a Y_b} - a\Delta_f^\ominus G_X - b\Delta_f^\ominus G_Y}{RT_{\text{gas}}}\right) \quad (2.41)$$

The derivation for a gas-phase in chemical disequilibrium is given in Chapter 4.

When the supersaturation ratio is larger than 1, growth dominates over the evaporation. A cloud particle in a supersaturated environment will therefore

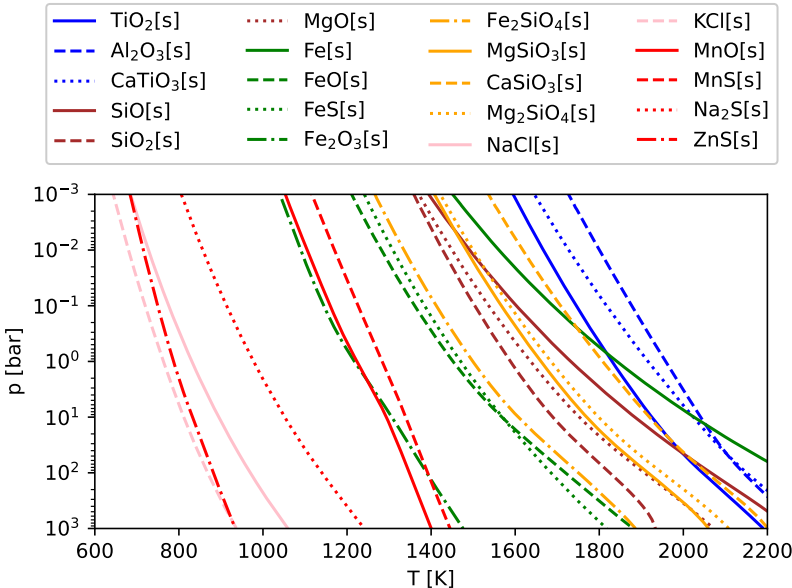


Figure 2.3: Thermal stability curves of possible cloud particle materials.

deplete the gas-phase until $S_i(T_{\text{gas}}) = 1$. If the supersaturation ratio is lower than 1, evaporation dominates. A cloud particle in an under-saturated area will therefore lose material. Thermal stability curves describe the temperatures and pressures at which the supersaturation ratio of a given material is 1 (see Fig. 2.3). These curves can be used as a first approximation to determine which cloud particle materials might form at a given temperature and pressure. For example, Savel et al. (2022) used thermal stability curves to study iron-bearing cloud species in the atmosphere of WASP-76b and Wakeford et al. (2017) used them to study high temperature condensates in ultra hot-Jupiters. However, thermal stability curves do not describe the formation process of clouds since the microphysics of cloud formation is missing.

Kinetic cloud formation

A kinetic description of cloud formation was derived by Helling & Woitke (2006). Each reaction r between the gas-phase particles and a cloud particle changes the volume of the cloud particle by ΔV_r [cm^3]. Therefore, it is useful to use the cloud particle size distribution $f(V)$ in volume space. The number of cloud particles of a given size $f(V)$ can increase through the growth of smaller

particles (\mathcal{A}) or through the evaporation of larger cloud particles (\mathcal{C}). On the other hand, the number can decrease if they grow to larger sizes (\mathcal{B}) or if they evaporate to smaller sizes (\mathcal{D}). In the most general form, the time-dependent change in $f(V)$ can therefore be described by (Helling & Woitke 2006):

$$\frac{df(V)}{dt} = \sum_r n_r v_r^{\text{rel}} \alpha_r \left(\underbrace{f(V - \Delta V_r) A_{\text{tot}}(V - \Delta V_r)}_{\mathcal{A}} - \underbrace{f(V) A_{\text{tot}}(V)}_{\mathcal{B}} \right) + \frac{\hat{n}_r \hat{v}_r^{\text{rel}} \hat{\alpha}_r}{b_s^{\text{surf}}} \left(\underbrace{f(V + \Delta V_r) A_{\text{tot}}(V)}_{\mathcal{C}} - \underbrace{f(V) A_{\text{tot}}(V - \Delta V_r)}_{\mathcal{D}} \right) \quad (2.42)$$

where n_r [cm⁻³] is the number density of the rate limiting reactant, α_r is the sticking coefficient, and $A_{\text{tot}}(V)$ [cm⁻²] is the cloud particle surface area. The variable $b_s^{\text{surf}} = A_{\text{tot}}/A_s$ is the inverse of the surface fraction of the cloud material s and can be related to the volume fraction assuming well-mixed particles $b_s^{\text{surf}} = V/V_s$, where V_s is the volume of the cloud particle species s within the cloud particle (Helling & Woitke 2006). The variables \hat{n}_r , \hat{v}_r^{rel} , $\hat{\alpha}_r$, refer to the state of chemical and phase equilibrium which are used to derive the evaporation rate. Assuming spherical particles and using the moment method, we find:

$$\frac{d}{dt} \rho_{\text{gas}} L_j = V_l^{j/3} J_* + \frac{j}{3} \chi^{\text{net}} \rho_{\text{gas}} L_{j-1} \quad (2.43)$$

$$\chi^{\text{net}} = \sqrt[3]{36\pi} \sum_s \sum_r \frac{\Delta V_r n_r v_r^{\text{rel}} \alpha_r}{\nu_r} \left(1 - \frac{1}{S_r} \frac{1}{b_s^{\text{surf}}} \right) \quad (2.44)$$

where χ^{net} [cm s⁻¹] is the net growth velocity and ν_r is the stoichiometric coefficient of the rate limiting reactant. The variable S_r is the reaction supersaturation which is discussed in Chapter 4.

Bulk growth species in exoplanet atmospheres

Cloud particles in exoplanet atmospheres are made from a diverse set of materials. In hot Jupiter atmospheres, clouds are made from solid materials which can be stable at high temperatures ($T_{\text{gas}} > 800$ K). At the upper temperature limit we have refractory materials like TiO₂[s], Al₂O₃[s], and CaTiO₃[s] (see Fig. 2.3). Only the day-side of (ultra) hot Jupiters is hot enough for these materials to evaporate (Helling et al. 2019b, 2023). It can therefore be expected that these three materials are forming cloud particles in almost all hot Jupiters. However, in an atmosphere with a solar-like composition the elements Fe, Mg and Si have higher elemental abundance than Ti and Al. Iron-bearing

($\text{Fe}[s]$, $\text{FeO}[s]$, $\text{Fe}_2\text{O}_3[s]$, $\text{Fe}_2\text{SiO}_4[s]$), silicon-bearing ($\text{SiO}[s]$, $\text{SiO}_2[s]$, $\text{MgSiO}_3[s]$, $\text{Mg}_2\text{SiO}_4[s]$), or magnesium-bearing ($\text{MgO}[s]$) species therefore dominate the cloud particle composition in atmospheric layers where temperatures and pressures are favorable for their formation. At lower temperatures, manganese-bearing ($\text{MnO}[s]$, $\text{MnS}[s]$), sulfur-bearing ($\text{ZnS}[s]$, $\text{Na}_2\text{S}[s]$), or chlorine-bearing ($\text{NaCl}[s]$, $\text{KCl}[s]$) species can condense in addition. However, similar to Ti and Al, the elemental abundances of Mn, Cl, Na, and Zn are expected to be lower than Si and Fe. Therefore, these species will only contribute significantly to the cloud particle composition if Si and Fe are not present in the atmosphere.

Species like TiO_2 and SiO are stable in the gas-phase and can directly condense onto CCNs. Other species like Mg_2SiO_4 however are not stable in the gas-phase but are stable in the solid phase. Therefore, they have to form through surface chemical reactions (see Helling & Woitke 2006). An example reaction would be:



These reactions are limited by the species with the lowest gas-phase abundance, in this case Mg. The abundance of the rate limiting species determines the bulk growth rate (see Eq. 2.43). A list of possible surface reactions can be found in Helling et al. (2019a).

2.2.4 Advection, settling and diffusion

The size distribution of cloud particles at a specific location in the atmosphere can change through the gravitational settling of cloud particles, the advection with winds, or turbulence. To account for the motion of cloud particles, Woitke et al. (2020) derived how the local cloud particle volume distribution is affected by advection, diffusion, and gravitational settling of the cloud particles. Their results are summarized here. In the most general form, the change in the cloud particle size distribution caused by advective and diffusive processes is given by:

$$\frac{d}{dt}f(V) = -\nabla \cdot [\mathbf{v}_c(V)f(V)dV] - \nabla \cdot \left[\rho_{\text{gas}}D_c \nabla \left(\frac{f(V)dV}{\rho_{\text{gas}}} \right) \right] \quad (2.46)$$

where $\mathbf{v}_c(V)$ [cm s^{-1}] is the cloud particle velocity and D_c [$\text{cm}^2 \text{ s}^{-1}$] is the diffusion constant of cloud particles.

Cloud particles are in most cases small enough to quickly adjust to the local gas-phase velocity \mathbf{v}_{gas} [cm s^{-1}] (Woitke & Helling 2003). For large cloud particles and low density environments, however, this assumption might not hold. In this case, the acceleration of cloud particles has to be considered. In addition to advection with the wind, a cloud particle also feels the gravitational pull of the

planet leading to a relative velocity \mathbf{v}_{dr} [cm s⁻¹] between the cloud particle and the gas-phase. This relative motion leads to friction. If the frictional force on the cloud particle is equal to the gravitational force, an analytic solution for \mathbf{v}_{dr} can be found. Assuming large Knudsen numbers and subsonic cloud particle velocities, the equilibrium drift velocity of a cloud particle is:

$$\mathbf{v}_{\text{dr}} = -\xi_{\text{dr}} a \mathbf{r} \quad (2.47)$$

$$\xi_{\text{dr}} = \frac{g\rho_c}{\rho_{\text{gas}}} \sqrt{\frac{\pi\mu}{8k_B T}} \quad (2.48)$$

where μ [g] is the mean molecular weight of the atmosphere, g [cm s⁻²] is the gravitational acceleration of the planet, ρ_c [g cm⁻³] is the cloud particle material density, a [cm] is the cloud particle radius, and \mathbf{r} the unit vector in the vertical direction. The cloud particle velocity is then given by:

$$\mathbf{v}_c = \mathbf{v}_{\text{gas}} - \xi_{\text{dr}} a \mathbf{r} \quad (2.49)$$

The turbulent motion of cloud particles caused by, for example, eddies lead to a diffusive effect. The diffusive constant D_c which describes these processes depends on the cloud particle properties as well as the gas-phase properties. A good example for this is the study by Schrapler & Henning (2004) of dust diffusion in protoplanetary disks. Here, we focus on the results of Woitke et al. (2020) and briefly summarize the results for the one dimensional atmosphere. In this case, the diffusion constant is given by:

$$D_c = \frac{\langle v_z \rangle H_p}{1 + \tau_{\text{fric}}/\tau_{\text{eddy}}} \quad (2.50)$$

where $\langle v_z \rangle$ [cm s⁻¹] is the root-mean-square average of vertical velocity fluctuations, and H_p [cm] is the pressure scale height. The frictional coupling timescale τ_{fric} [s] and the eddy diffusion timescale τ_{eddy} [s] are given by:

$$\tau_{\text{fric}} = \frac{a\rho_c}{\rho_{\text{gas}}} \sqrt{\frac{\pi\mu}{8k_B T_{\text{gas}}}} \quad (2.51)$$

$$\tau_{\text{eddy}} = \frac{H_p}{\langle v_z \rangle} \quad (2.52)$$

Since advection and diffusion also depend on the size of cloud particles, it is useful to express them using the moments from Sect. 2.2.2. This leads to the following change in the moments L_j due to advection and diffusion:

$$\frac{\partial}{\partial t}(\rho_{\text{gas}} L_j) + \nabla \cdot (\mathbf{v}_{\text{gas}} \rho_{\text{gas}} L_j) = \nabla \cdot (\xi_{\text{dr}} L_{j+1} \mathbf{r}) + \nabla \cdot (D_c \rho_{\text{gas}} \nabla L_j) \quad (2.53)$$

2.2.5 The master equation

Combining nucleation (Sect. 2.2.1), bulk growth (Sect. 2.2.3), advection, diffusion, and gravitational settling (Sect. 2.2.4) of cloud particles leads to the master equation of cloud formation (Woitke et al. 2020):

$$\begin{aligned} \frac{\partial}{\partial t}(\rho_{\text{gas}}L_j) + \nabla \cdot (\mathbf{v}_{\text{gas}}\rho_{\text{gas}}L_j) &= \underbrace{V_l^{j/3}(J_*)}_{\text{nucleation}} + \underbrace{\frac{j}{3}\chi^{\text{net}}\rho_{\text{gas}}L_{j-1}}_{\text{growth}} \\ &+ \underbrace{\nabla \cdot (\xi_{\text{dr}}L_{j+1}\mathbf{r})}_{\text{drift}} + \underbrace{\nabla \cdot (D_c\rho_{\text{gas}}\nabla L_j)}_{\text{diffusion}} \end{aligned} \quad (2.54)$$

Solving this equations for $j \in \{0, 1, 2, 3\}$ describes the cloud particle properties for an exoplanet atmosphere.

2.3 Three dimensional atmospheres of exoplanets

Exoplanets are inherently three dimensional objects. While one dimensional models can predict certain characteristics, the climate of exoplanets can only be captured in 3D. The core equations that describe the dynamics of the atmosphere are the fluid dynamics equations on a rotating sphere (Sect. 2.3.1). These equations are solved by General Circulation Models (GCMs) which deploy multiple numerical tricks to achieve a stable solution (Sect. 2.3.2). GCM modeling of hot Jupiter atmospheres has revealed common characteristics of these planets such as large temperature differences and equatorial wind jets (Sect. 2.3.3).

2.3.1 Fluid dynamics of exoplanet atmospheres

The general circulation of atmospheres is described by the fluid dynamics equations. At the core of these equations are conservation of mass, momentum and energy. Here, we will give an overview of their derivation.

Equation of state

Assuming that the gas of an exoplanet atmosphere is an ideal gas, which means that atomic and molecular interactions between gas-phase particles are negligible,

one can apply the equation of state:

$$p_{\text{gas}} = \rho_{\text{gas}} R_s T_{\text{gas}} = \frac{\rho_{\text{gas}} R T_{\text{gas}}}{\mu}, \quad (2.55)$$

where $R_s = R/\mu$ [$\text{J K}^{-1} \text{ kg}^{-1}$] is the specific gas constant and $R = 8.314 \text{ J K}^{-1} \text{ mol}^{-1}$ is the ideal gas constant. At very high pressures or very low temperatures, intermolecular forces between gas-phase species will become important and the ideal gas law will no longer be applicable. This happens for example in the interior of gaseous exoplanets where other equations of states have to be used (Stevenson 1982; Miguel et al. 2016). However, many climate studies exploring higher pressure regions of the atmosphere assume that the ideal gas law is valid until the lower boundary of exoplanet climate simulations which can be between 100 bar to 1000 bar (see e.g. Showman et al. 2009; Mayne et al. 2014; Schneider et al. 2022c).

Mass conservation

The mass conservation in geometric coordinates (x, y, z) can be described by the continuity equation of the gas-phase density ρ_{gas} in the Lagrangian reference frame:

$$\frac{D\rho_{\text{gas}}}{Dt} + \rho_{\text{gas}} \nabla \cdot \mathbf{v} = 0 \quad (2.56)$$

where $\mathbf{v} = (v_x, v_y, v_z)$ [m s^{-1}] is the three-dimensional velocity field. The Lagrangian frame can be transformed to the Eulerian frame using:

$$\frac{D}{Dt} = \frac{d}{dt} + \mathbf{v} \cdot \nabla \quad (2.57)$$

Fluid dynamics equations of atmospheres can be evaluated in isobaric coordinates (x, y, p) which expresses the vertical direction in pressure rather than height. In the case of hydrostatic equilibrium (see Eq. 2.67) the continuity equation then simplifies to⁴:

$$\nabla_p \cdot \mathbf{v} = 0 \quad (2.58)$$

where ∇_p is the divergence in isobaric coordinates defined as:

$$\nabla_p = \begin{pmatrix} d/dx \\ d/dy \\ d/dp \end{pmatrix} \quad (2.59)$$

⁴A detailed derivation can be found in the appendix of Baeyens (2021).

Momentum conservation

A gas parcel within an exoplanet atmosphere is accelerated by pressure differences ($\frac{1}{\rho_{\text{gas}}} \nabla p_{\text{gas}}$), gravity \mathbf{g}^* [m s^{-2}], and additional forces $\mathbf{F} = (F_u, F_v, F_w)$ [kg m s^{-2}]. In combination with the continuity equation of the momentum density in geometric coordinates (x, y, z) and the continuity equation of mass (Eq. 2.56), the momentum equation in the Lagrangian reference frame is given by:

$$\frac{D\mathbf{v}}{Dt} = \mathbf{g}^* - \frac{1}{\rho_{\text{gas}}} \nabla p_{\text{gas}} + \mathbf{F} \quad (2.60)$$

In some fluid dynamics problems, the kinematic viscosity ν [$\text{m}^2 \text{s}^{-1}$] of the medium can also impact the momentum ($\nu \nabla^2 \mathbf{v}$). However, the kinetic viscosity is typically low for planetary atmospheres in the pressure range considered in this thesis. For example, Earth at sea level has a kinematic viscosity of $\nu = 1.46 \times 10^{-5} \text{ m}^2 \text{s}^{-1}$ (Holton & Hakim 2013; Vallis 2017). Kinematic viscosity is therefore neglected in this work.

The reference frame of a planetary atmosphere is a rotating sphere with an angular velocity of $\boldsymbol{\Omega}$ [s^{-1}] and spherical coordinates $\mathbf{r} = (\phi, \varphi, r)$. Thus, when transforming the velocity \mathbf{v} into the co-rotating velocity $\mathbf{u} = (u, v, w)$, the rotation of the reference frame has to be considered:

$$\mathbf{u} = \mathbf{v} - \boldsymbol{\Omega} \times \mathbf{r} \quad (2.61)$$

Inserting Eq. 2.61 into the left hand side of Eq. 2.60 leads to two additional terms (Marshall & Plumb 2007):

$$\frac{D\mathbf{v}}{Dt} = \frac{D\mathbf{u}}{Dt} + \underbrace{2\boldsymbol{\Omega} \times \mathbf{r}}_{\text{Coriolis force}} + \underbrace{\boldsymbol{\Omega} \times \boldsymbol{\Omega} \times \mathbf{r}}_{\text{centrifugal force}} \quad (2.62)$$

The first additional term from this transformation is the Coriolis force. The second additional term is the centrifugal force which can be combined with the gravity and expressed as the modified geopotential height Φ [$\text{m}^2 \text{s}^{-2}$]:

$$-\nabla \Phi = -\nabla g z = \mathbf{g}^* + \boldsymbol{\Omega} \times \boldsymbol{\Omega} \times \mathbf{r} \quad (2.63)$$

where g [m s^{-2}] is the effective gravity. Using what we have derived so far, the momentum equation (Eq. 2.60) can be transformed into the co-rotating frame. A detailed account of the individual transformation steps can be found in Holton & Hakim (2013) and Vallis (2017). The individual components of \mathbf{u}

are then given by:

$$\frac{Du}{Dt} - \frac{uv \tan \varphi}{r} + \underbrace{\frac{uw}{r} + 2\Omega w \cos \varphi - 2\Omega v \sin \varphi}_{\text{Traditional}} + \frac{1}{\rho_{\text{gas}}} \frac{\partial p_{\text{gas}}}{\partial x} = F_u \quad (2.64)$$

$$\frac{Dv}{Dt} + \frac{u^2 \tan \varphi}{r} + \underbrace{\frac{vw}{r}}_{\text{Traditional}} + 2\Omega u \sin \varphi + \frac{1}{\rho_{\text{gas}}} \frac{\partial p_{\text{gas}}}{\partial y} = F_v \quad (2.65)$$

$$\frac{Dw}{Dt} - \underbrace{\frac{u^2 + v^2}{r} - 2\Omega u \cos \varphi}_{\text{Hydrostatic equilibrium}} + g + \frac{1}{\rho_{\text{gas}}} \frac{\partial p_{\text{gas}}}{\partial z} = F_w \quad (2.66)$$

While solving these equations in their full complexity is possible, it is also computationally intensive. To lower the complexity, several approximations can be made. A full discussion on the differences between approximations is given by Mayne et al. (2014). Here, we give a short overview of the most common assumptions.

To analyze which terms of the momentum equations might be simplified, it is useful to compare the vertical versus the horizontal extent of planetary atmospheres. The modeled part of an atmosphere is typically thin compared to the size of the planets. In the shallow-fluid approximation the radius r is therefore approximated by the radius of the planet ($r \approx R_{\text{pl}}$). Furthermore, the vertical velocities in hot Jupiter atmospheres are typically much smaller than the horizontal velocities. Therefore, in the traditional assumption the vertical velocity is not included and the underlined terms in Eq. 2.64 and Eq. 2.65 are neglected.

For a typical hot Jupiter atmosphere, the vertical wind acceleration, advection of the vertical winds, and the Coriolis terms are around three orders of magnitude smaller than the gravitational force (Showman et al. 2009; Baeyens 2021). Therefore, the underlined terms in Eq. 2.66 can be neglected, resulting in:

$$\frac{\partial p_{\text{gas}}}{\partial z} = -\rho_{\text{gas}} g \quad (2.67)$$

This approximation is called hydrostatic equilibrium. Combining the hydrostatic equilibrium, shallow-fluid, and traditional approximation results in the Hydrostatic Primitive Equations (HPE).

Thermal forcing

The internal energy U of a gas parcel can change if it either performs work through contraction and expansion ($p dV$) or through external heating and cooling (J). The heat capacity at constant volume c_V [$\text{J kg}^{-1} \text{ K}^{-1}$] links changes in the internal energy to temperature changes ($dU = c_V dT_{\text{gas}}$). Using the first law of thermodynamics (Eq. 2.8) we find:

$$c_V \frac{DT_{\text{gas}}}{Dt} = \frac{DU}{Dt} = J - p \frac{DV_{\text{gas}}}{Dt} \quad (2.68)$$

The work of a gas parcel can also be expressed in temperature and pressure changes using the ideal gas law (Marshall & Plumb 2007):

$$p_{\text{gas}} dV_{\text{gas}} = -\frac{p_{\text{gas}}}{\rho_{\text{gas}}^2} d\rho_{\text{gas}} = -\frac{1}{\rho_{\text{gas}}} dp_{\text{gas}} + R_s dT_{\text{gas}} \quad (2.69)$$

Inserting this equation into Eq. 2.68 and using the heat capacity at constant pressure $c_p = c_V + R_s$ [$\text{J kg}^{-1} \text{ K}^{-1}$] leads to:

$$c_p \frac{DT_{\text{gas}}}{Dt} = c_V \frac{DT_{\text{gas}}}{Dt} + R_s \frac{DT_{\text{gas}}}{Dt} = J + \frac{1}{\rho_{\text{gas}}} \frac{Dp_{\text{gas}}}{Dt} \quad (2.70)$$

Looking at Eq. 2.70, it becomes apparent that in the absence of external heating and cooling ($J = 0$), the temperature is affected by changes in pressure. This means that a gas parcel following the flow might not have a constant temperature. To express the temperature in terms of a constant quantity, we can define the potential temperature:

$$\theta = T_{\text{gas}} \left(\frac{p_0}{p_{\text{gas}}} \right)^{R/c_p}, \quad (2.71)$$

where p_0 [bar] is a reference pressure. The potential temperature describes the temperature a gas parcel would have if it would be moved adiabatically to the pressure layer p_0 . If the potential temperature increases with decreasing pressure ($\partial\theta/\partial p < 0$) any atmospheric parcel that is lifted up adiabatically will be colder and thus denser than the local environment. Consequently, it will fall down resulting in a stable atmosphere. If the potential temperature decreases with decreasing pressure ($\partial\theta/\partial p > 0$) any atmospheric parcel that is lifted up adiabatically will be hotter and therefore less dense. Such a parcel will continue to rise in the atmosphere leading to convective motion. Therefore, the potential temperature can be used to determine the stability of an atmosphere.

To rewrite Eq. 2.70 in terms of the potential temperature, we need the Lagrangian derivative which is:

$$\frac{D\theta}{Dt} = \frac{\theta}{T_{\text{gas}}} \frac{DT_{\text{gas}}}{Dt} - \frac{\theta}{T_{\text{gas}}} \frac{RT_{\text{gas}}}{c_p \rho_{\text{gas}}} \frac{Dp_{\text{gas}}}{Dt} \quad (2.72)$$

$$= \left(\frac{p_0}{p_{\text{gas}}} \right)^{R/c_p} \left(c_p \frac{DT_{\text{gas}}}{Dt} - \frac{1}{\rho_{\text{gas}}} \frac{Dp_{\text{gas}}}{Dt} \right) \quad (2.73)$$

Inserting this equation into Eq. 2.70 leads to:

$$c_p \left(\frac{p_{\text{gas}}}{p_0} \right)^{R/c_p} \frac{D\theta}{Dt} = J \quad (2.74)$$

This equation makes it apparent that in the absence of heating or cooling ($J = 0$), the potential temperature of a gas parcel is constant. Arguably the most important heating source for planetary atmospheres is stellar irradiation. Cooling and heating caused by radiation can be described by the net radiative flux F^{net} [W m^{-2}]:

$$J = g \frac{\partial F^{\text{net}}}{\partial p} \quad (2.75)$$

An in-depth description of the thermal forcing from radiation can be found in Schneider et al. (2022c) and Schneider (2024).

2.3.2 The general circulation model expeRT/MITgcm

To solve the fluid dynamics equations for a planetary atmosphere, General Circulation Models (GCMs) are used. Such models have first been developed to model Earth's atmosphere and oceans (see e.g. Phillips 1956; Manabe & Wetherald 1967; Meehl 1984; McWilliams 1996; Adcroft et al. 2004b; Staniforth & Wood 2003, 2008; Weart 2010). Through many efforts, these models were then adapted to the atmosphere of exoplanets (see e.g. Showman et al. 2009; Rauscher & Menou 2010; Mayne et al. 2014; Way et al. 2017; Carone et al. 2020). Building on the experience from these studies, GCMs are also being developed specifically for exoplanet atmospheres (see e.g. Mendonça et al. 2018; Deitrick et al. 2020).

For this work, expeRT/MITgcm was used (Carone et al. 2020; Schneider et al. 2022c). This model is based on the dynamical core of MITgcm (Marshall et al. 1997a,b; Adcroft et al. 2004b) which has already been used for a number of exoplanet studies (e.g. Showman et al. 2009; Carone et al. 2014; Kataria

et al. 2016; Komacek et al. 2019; Steinrueck et al. 2023; Tan et al. 2024). For expeRT/MITgcm, the radiative transfer scheme of petitRADTRANS (Mollière et al. 2019, 2020) was adopted into MITgcm.

Hydrostatic primitive equations

The dynamical core of MITgcm (Marshall et al. 1997a,b; Adcroft et al. 2004a) solves the Hydrostatic Primitive Equations (HPE⁵) (see Sect. 2.3.1). Since the vertical component of the grid is pressure, it is useful to express the HPE in pressure coordinates as well. The wind is therefore separated into horizontal winds $\mathbf{u}_h = (u, v, 0)$ [m s⁻¹] and the vertical wind ω [bar s⁻¹]. The equations solved by the MITgcm are thus:

$$\text{Mass continuity:} \quad \nabla_p \cdot \mathbf{u}_h + \frac{\partial \omega}{\partial p} = 0 \quad (2.76)$$

$$\text{Horizontal Momentum:} \quad \frac{D\mathbf{u}_h}{Dt} + 2\Omega \sin \varphi \hat{\mathbf{k}} \times \mathbf{u}_h + \nabla_p \Phi = F_{\mathbf{u}_h} \quad (2.77)$$

$$\text{Vertical Momentum:} \quad \frac{\partial \Phi}{\partial t} + \frac{1}{\rho_{\text{gas}}} = 0 \quad (2.78)$$

$$\text{Temperature:} \quad c_p \left(\frac{p_{\text{gas}}}{p_0} \right)^{R/c_p} \frac{D\theta}{Dt} = J \quad (2.79)$$

where $\hat{\mathbf{k}}$ is the unit vector in vertical direction and $F_{\mathbf{u}_h} = (F_u, F_v, 0)$ [kg m s⁻²] are additional horizontal forces. In the MITgcm, the horizontal winds are calculated using Eq. 2.77. The vertical velocity ω is calculated via the mass continuity equation (Eq. 2.76) and is therefore a diagnostic parameter calculated from the divergence of the horizontal winds. It is therefore not possible to model vertically propagating waves, like gravity or sound waves, using the HPE. The heating rate J of expeRT/MITgcm is determined by the net radiative flux which consists of the stellar irradiation and the planetary emission. The atmosphere is treated non-gray and plane parallel geometry is assumed⁶ for the radiative transfer calculations.

Studies have shown that solving the Navier-Stokes equation with fewer assumptions can impact the predicted atmospheric structure. Especially for smaller planets the HPE seem to be insufficient (see e.g. Tokano 2013; Mayne

⁵MITgcm can also solve the full Navier-Stokes equations. However for this work, only the HPE are used.

⁶A discussion on the validity of the plane parallel assumption for hot Jupiters can be found in Appendix A of Schneider et al. (2022c).

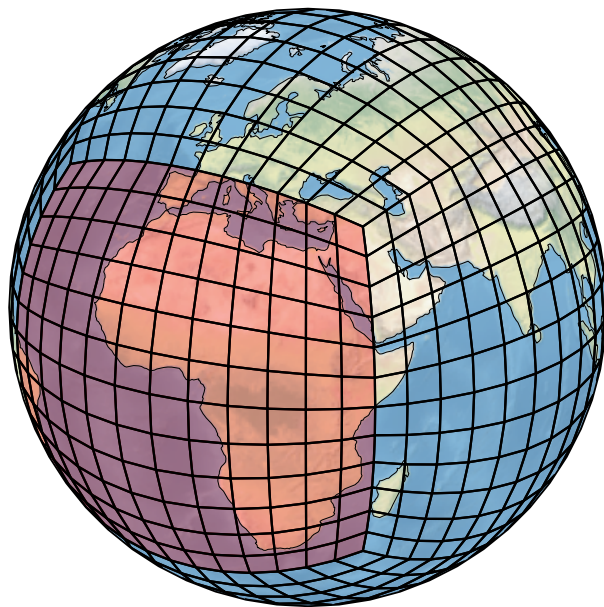


Figure 2.4: Visualization of a C12 cubed sphere grid. This image was created following the approach of Daniel Rothenberg.

et al. 2019). For hot Jupiters, Noti et al. (2023) found that differences increase for faster rotations, lower gravity, and higher irradiation temperatures.

Numerical Set-up

MITgcm solves the fluid dynamics equations on a staggered Arakawa-C grid (Arakawa & Lamb 1977), also called a cubed sphere grid (see Fig. 2.4). This grid has more evenly spaced cells than a longitude-latitude grid which has many smaller cells at the poles. Preventing this overcrowding is important to satisfy the Courant–Friedrichs–Lowy condition (Eq. 2.80). This condition states that the integration time step Δt [s] of an explicit solver is limited by the size of the

grid cells:

$$\Delta t < \left(\frac{\tilde{u}}{\Delta x} + \frac{\tilde{v}}{\Delta y} + \frac{\tilde{\omega}}{\Delta p} \right)^{-1} \quad (2.80)$$

where Δx [m], Δy [m], and Δp [bar] are the grid cell spacings and \tilde{u} [$m\ s^{-1}$], \tilde{v} [$m\ s^{-1}$], and $\tilde{\omega}$ [bar s^{-1}] are the magnitudes of the velocity. The overcrowding at the poles leads to small Δx and thus limits the time step Δt . Using a cubed sphere grid circumvents this problem because it has more evenly spaced grid cells. The grid used for this work consists of 32×32 grid cells on each of the 6 sides of the cubed sphere (called C32 grid).

GCMs are known to be impacted by numerical instabilities. A common problem are gravity waves at the upper boundary of the atmosphere. Many GCMs therefore include a sponge layer⁷ to ensure numerical stability by preventing non-physical boundary effects from affecting the solution (see e.g. Zalucha et al. 2013; Mendonça et al. 2018; Carone et al. 2020). In these layer, a Rayleigh friction term is added which dampens gravity waves. Another instability is caused by the edges of the cubed sphere grid which causes small scale perturbations. To reduce the impact of these perturbations, MITgcm uses a fourth-order Shapiro filter (Shapiro 1970).

2.3.3 The climate of hot Jupiters

Full 3D GCM modeling of hot Jupiters (see e.g. Showman et al. 2009; Parmentier et al. 2013; Kataria et al. 2015; Amundsen et al. 2016; Lee et al. 2016; Carone et al. 2020; Schneider et al. 2022b; Tan et al. 2024) is needed to support the current detailed observations with, for example, JWST, CHEOPS, HST, and VLT (see e.g. Kempton et al. 2023; Hammond et al. 2024; Bell et al. 2024). While there are differences in the atmospheric structure of hot Jupiters depending on the stellar type of the host star, distance to the host star, rotational period, gravity, or atmospheric composition, most hot Jupiters share several characteristics (Baeyens et al. 2021, 2022; Roth et al. 2024). In this section, we look at the example of WASP-107b. This exoplanet has a radius of $0.94 R_J$, a mass of $0.12 M_J$, and an orbital period of 5.72 days. The K-type host star has an effective temperature of 4420 K.

Because hot Jupiters are tidally locked, they receive all stellar irradiation, and thus the heating, on the day-side only. This leads to a strong temperature gradient between the day- and night-side. In Fig. 2.5, we show the temperature

⁷Grid cells at the boundaries of numerical simulations which ensure the numerical stability are also called ghost cells (see e.g. Peskin 1972; Frese 1987; Helling et al. 2004).

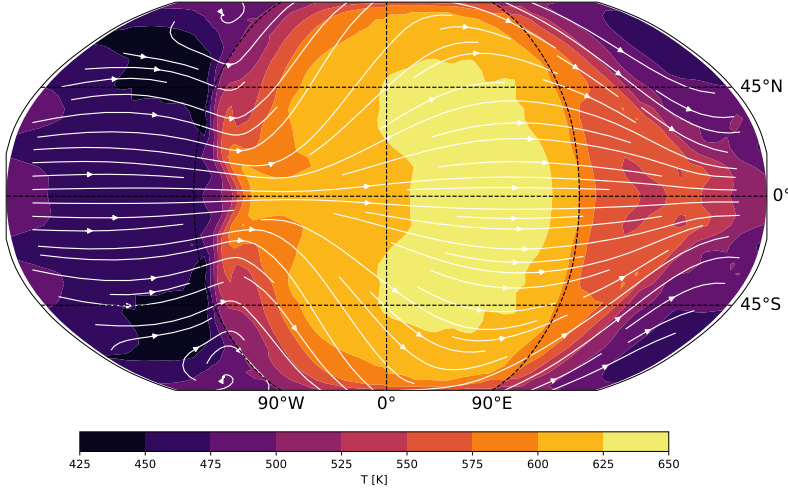


Figure 2.5: Temperature and horizontal wind structure of WASP-107b at the pressure level of 2×10^{-4} bar. This simulation was conducted with expeRT/MITgcm over 1600 simulation days.

and wind structure of WASP-107b at a pressure level of 2×10^{-4} bar. Here, the difference between day and night-side reaches up to 220 K. In other planets, the temperature differences between day- and night-side can reach over 1000 K (see e.g. HAT-P-7b; Helling et al. 2019b). Deeper in the atmosphere, most of the stellar irradiation is already absorbed by higher layers and interior heating starts to dominate. The exact structure of the interior of gas-giant exoplanets is difficult to determine and is the subject of ongoing research (see e.g. Spiegel et al. 2014; Bloot et al. 2023).

The strong temperature difference between day- and night-side leads to a unique wind pattern which is driven by standing planetary scale Rossby and Kelvin waves. Kelvin waves are latitudinally confined gravity waves which have an eastward group propagation (Holton & Hakim 2013). Rossby waves are caused by the conservation of vorticity (Vallis 2017) and have a westward group propagation around the equator (Matsuno 1966). The differences in the direction of the group propagation between Rossby and Kelvin waves leads to a northwest-to-southeast tilt of the height field in the northern hemisphere and a

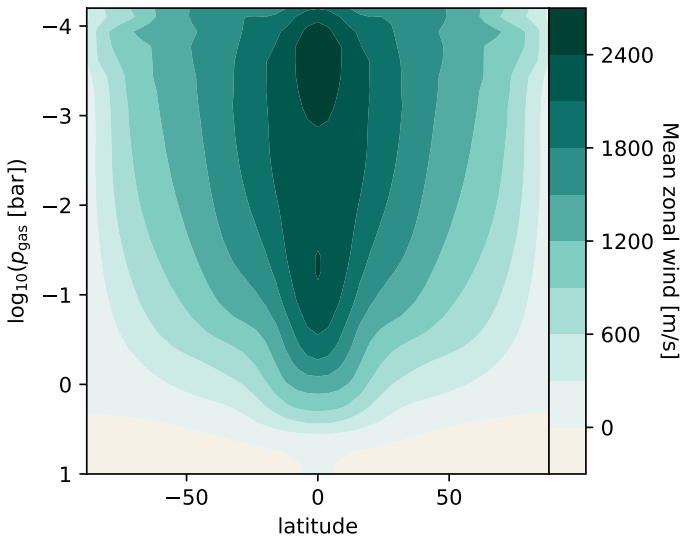


Figure 2.6: Zonal mean, which is the average of the wind velocities in eastward direction, wind of WASP-107b. The simulations were conducted with expeRT/MITgcm over 1600 simulation days.

southwest-to-northeast tilt in the southern hemisphere (Showman & Polvani 2011). Because of this tilt, eastward winds arrive at the equator faster than westward winds which leads to a transport of eastward momentum from the higher latitudes into the equator. This causes a strong equatorial wind jet (Showman & Polvani 2011).

This jet stream is best visualized in the zonal mean wind, which is the average of the winds in eastward direction. The zonal mean wind of WASP-107b can be seen in Fig. 2.6. The maximum speed of the wind jet is between 10^{-3} bar to 10^{-4} bar where the wind speeds reach up to 3000 m/s. These strong winds are the reason why the hot spot of hot Jupiters can be offset by several degrees in longitude. This offset can also be seen for WASP-107b in Fig. 2.5.

When an exoplanet is observed using transit spectroscopy, what is actually being measured are the morning (90° west of the sub-stellar point) and the evening (90° east of the sub-stellar point) terminators. Because the equatorial jet transports hot air from the day-side into the evening terminator and cold air from the night-side into the morning terminator, there can be a considerable

temperature, chemistry, or cloud structure differences between the two limbs. Normal transit spectroscopy would result in the average of both terminators. However, it is also possible to observe both limbs separately thus allowing further insights into the structure of exoplanet atmospheres (see e.g. Prineth et al. 2022; Maguire et al. 2024).

The differences in day and night-side temperatures is also reflected in the cloud coverage of hot Jupiters. While the day-side can be too hot for clouds to form, the night-side of nearly all (ultra) hot Jupiters is expected to have clouds (Helling et al. 2019a; Roman & Rauscher 2019; Gao & Powell 2021; Helling et al. 2023). For some planets, this results in a cloudy morning terminator and a cloudless evening terminator, making limb asymmetry studies all the more crucial (Roman & Rauscher 2019; Helling et al. 2019b). Clouds also affect the temperature structure of a planet by, for example, reflecting stellar light or by blocking outgoing thermal radiation. The feedback of clouds and climate is studied in more detail in Chapter 6.

2.4 Opacities

The atmosphere of exoplanets interacts with the radiation of the host star and the emission of the planet. As we have seen in Sect. 1.1.3, the absorption of light caused by gas-phase species can be used to detect them in exoplanet atmospheres. In this thesis, we study the effect of cloud particle opacities on transmission spectra (Chapter 5) and on the thermal structure of exoplanets (Chapter 6). Therefore, a short summary of the basic principles of radiative transfer (Sect. 2.4.1), gas-phase opacities (Sect. 2.4.2) and cloud particle opacities (Sect. 2.4.3) is given.

2.4.1 Radiative transfer

The change in spectral intensity I_ν [erg s⁻¹ cm⁻²] of light traveling along a straight line s through a medium can be described by the radiative transfer equation:

$$\frac{dI_\nu(s)}{ds} = \alpha_\nu (S_\nu(s) - I_\nu(s)) \quad (2.81)$$

where $\alpha_\nu = \kappa_\nu \rho$ [cm⁻¹] is the extinction coefficient and κ_ν [cm² g⁻¹] is the opacity⁸. The variable S_ν [erg s⁻¹ cm⁻²] is the source function which is defined

⁸Also called the mass attenuation coefficient.

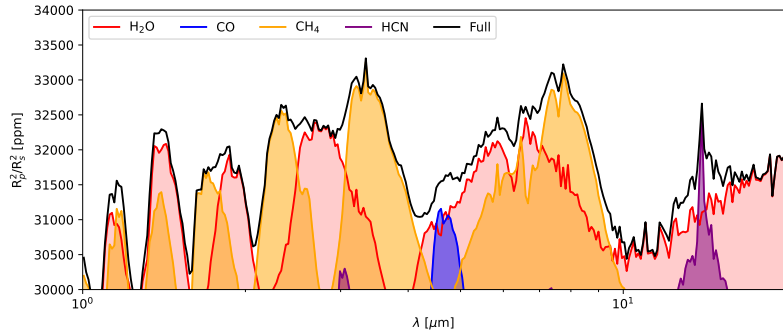


Figure 2.7: Gas-phase contributions of H_2O , CO , CH_4 , and HCN to the transmission spectrum of HATS-6b.

as:

$$S_\nu = \frac{j_\nu}{\alpha_\nu} \quad (2.82)$$

where j_ν [$\text{erg s}^{-1} \text{ cm}^{-3}$] is the emissivity which describes the light that is emitted along the path s . The solution of Eq. 2.81 form is given by:

$$I_\nu(s) = I_\nu(s_0)e^{-\tau_\nu(s_0, s)} + \int_{s_0}^s j_\nu(\tilde{s})e^{-\tau_\nu(\tilde{s}, s)}d\tilde{s} \quad (2.83)$$

where τ_ν is the optical depth which is defined as:

$$\tau_\nu(a, b) = \int_a^b \alpha_\nu ds \quad (2.84)$$

The first term on the right hand side of Eq. 2.83 describes how much light is absorbed by the medium from the original source. The second term describes the emitted light from the medium.

2.4.2 Gas-phase species

The opacity of gas-phase species depends on their vibrational, rotational, and electronic modes. Calculating precise values of these modes for gas-phase species is the subject of current research. Studies include molecules like CH_4 (Yurchenko & Tennyson 2014), CO_2 (Yurchenko et al. 2020), SiO_2 (Owens et al. 2020; Yurchenko et al. 2022), and TiO (McKemmish et al. 2019). In

particular the Exomol project (Tennyson & Yurchenko 2012) has resulted in a large database of optical properties for gas-phase species relevant for exoplanet atmospheres.

To illustrate how gas-phase species impact radiation passing through an atmosphere, we show the contributions of H₂O, CO, CH₄, and HCN to the spectrum of HATS-6b⁹ in Fig. 2.7. We can see that some species absorb over a large range of wavelengths (e.g. H₂O and CH₄) while others have clear peaks at specific wavelengths (e.g. HCN at 14 μm or CO at 4.7 μm). Both broad and narrow features can be used to detect the presence of gas-phase molecules in exoplanet atmospheres (Barman et al. 2015; Alderson et al. 2023; Tsai et al. 2023). However, it can be difficult to differentiate between gas-phase species when features overlap. A good example are H₂O and CH₄ which have overlapping feature around 1.4 μm . Observing only at this wavelength would make it difficult to differentiated between the two. Furthermore, species that are less abundant or that have generally lower opacities are more difficult to detect. Take for example the CO feature around 4.7 μm . While it still impacts the transit depth, very precise measurements are required to distinguish the CO feature within the broader H₂O feature.

When modeling exoplanet atmospheres it is important to consider all gas-phase species that impact the thermal structure of an exoplanet. This is best illustrated by Sodium (Na) and Potassium (K). Even though they are typically less abundant than other gas-phase species (Asplund et al. 2009; Nikolov et al. 2018), they still are an important opacity source in the optical wavelength range (Burrows & Volobuyev 2003; Burrows & Orton 2009; Seager 2011). How exactly gas-phase species impact the thermal structure depends on their optical properties. For example, the presence of molecules with large opacities in the optical (e.g. TiO, VO, AlO, CaO, NaH, or MgH) can lead to significant absorption of the stellar irradiation even at low pressures. This can lead to a temperature inversion in the upper atmosphere of ultra hot Jupiters (Fortney et al. 2008; Gandhi & Madhusudhan 2019). Another example are species with a large opacity in the infrared wavelength range (e.g. CO₂, CH₄, or H₂O; Kaltenegger et al. 2010). These species allow stellar light to pass through the atmosphere unhindered but block the thermal radiation from the planet. This causes the atmospheric heating known as the greenhouse effect.

2.4.3 Cloud particle opacities

Cloud particles are much larger than gas-phase species and thus are an important opacity source for exoplanet atmospheres. Their optical properties depend on

⁹HATS-6b will be discussed in detail in Chapter 6.

the composition, shape, size, and material distribution. In Chapter 5, the optical properties of heterogeneous cloud particles are investigated in detail. In this section, a brief overview of the optical properties of homogeneous cloud particles and how the extinction and scattering efficiency of a spherical particle can be calculated is given.

Mie theory

To understand the interaction between light and material, the Maxwell equations (Maxwell 1865) have to be solved. Mie theory (Mie 1908) presents such a solution for spherical particles with radius a and refractive index m_s in a medium with a refractive index m_m . Under these assumptions, the scattering and extinction efficiencies are given by:

$$Q_{\text{sca}}(\lambda, a) = \frac{C_{\text{sca}}}{\pi a^2} = \frac{2}{x^2} \sum_{n=1}^{\infty} (2n+1)(|a_n|^2 + |b_n|^2) \quad (2.85)$$

$$Q_{\text{ext}}(\lambda, a) = \frac{C_{\text{ext}}}{\pi a^2} = \frac{2}{x^2} \sum_{n=1}^{\infty} (2n+1)\Re(a_n + b_n) \quad (2.86)$$

where C_{sca} [cm²] is the scattering cross section, C_{ext} [cm²] is the extinction cross section, $x = 2\pi a/\lambda$ the size parameter, and λ [cm] is the wavelength in vacuum. The parameters a_n and b_n are the Lorenz-Mie coefficients:

$$a_n = \frac{\psi_n(xm_m)}{\zeta_n(xm_m)} \frac{m_m \frac{\psi'_n(xm_s)}{\psi_n(xm_s)} - m_s \frac{\psi'_n(m_m)}{\psi_n(m_m)}}{m_m \frac{\psi'_n(xm_s)}{\psi_n(xm_s)} - m_s \frac{\zeta'_n(xm_m)}{\zeta_n(xm_m)}} \quad (2.87)$$

$$b_n = \frac{\psi_n(xm_m)}{\zeta_n(xm_m)} \frac{m_s \frac{\psi'_n(xm_s)}{\psi_n(xm_s)} - m_m \frac{\psi'_n(xm_m)}{\psi_n(xm_m)}}{m_s \frac{\psi'_n(xm_s)}{\psi_n(xm_s)} - m_m \frac{\zeta'_n(xm_m)}{\zeta_n(xm_m)}} \quad (2.88)$$

These parameters depend on the Riccati-Bessel functions $\psi_n(z)$ and $\zeta_n(z)$, which in turn are derived from the Bessel functions $j_n(z)$, $y_n(z)$:

$$\psi_n(z) = z j_n(z) \quad (2.89)$$

$$\zeta_n(z) = z(j_n(z) - iy_n(z)) \quad (2.90)$$

The scattering and extinction coefficient directly relate to the absorption coefficient:

$$Q_{\text{abs}} = Q_{\text{ext}} - Q_{\text{sca}} \quad (2.91)$$

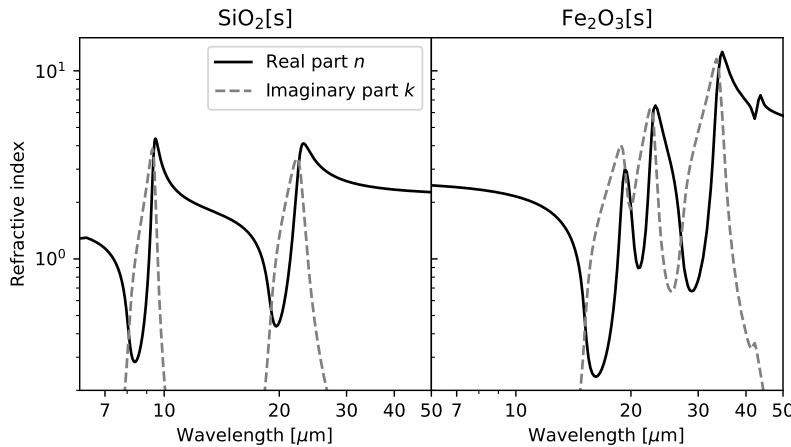


Figure 2.8: Real (solid) and imaginary (dashed) part of the refractive index of the cloud particle materials $\text{SiO}_2[\text{s}]$ and $\text{Fe}_2\text{O}_3[\text{s}]$.

Mie theory was first developed to describe the colors of colloidal gold which were studied by Zsigmondy (1898). Since then, the basic principles derived in the work of (Mie 1908) find many practical applications involving, for example, interstellar dust, near-field optics, or optical particle characterization. For more information on the historical aspects of Mie theory see Hergert & Wriedt (2012).

Optical properties of homogeneous cloud particle materials

The optical properties of homogeneous materials are described by their refractive index m :

$$m = n + ki \quad (2.92)$$

The real part n is the ratio of the speed of light and the phase velocity of light in the medium. Its values therefore strongly impact the scattering properties of the material. The imaginary part k describes the attenuation of the electromagnetic wave traveling through the medium. Its values therefore strongly impact the absorption of light by the material.

To give an example of refractive indices, the materials $\text{SiO}_2[\text{s}]$ and $\text{Fe}_2\text{O}_3[\text{s}]$ are shown in Fig. 2.8. Both materials have peaks in the imaginary and real part around and above 10 μm which are caused by vibrational mode features of the

Si-O and Fe-O bonds. In contrast to $\text{SiO}_2[\text{s}]$, $\text{Fe}_2\text{O}_3[\text{s}]$ has generally much larger k values. While cloud particles made from materials with a high k value do not necessarily have to have a high opacity, this is often the case (see e.g. Min et al. 2006). A list of studies investigating the optical properties of cloud particle materials can be found in Table C.2.

Using Mie theory, the opacities of cloud particles can be calculated and used within radiative transfer calculations. Cloud particles uniformly absorb short wavelength radiation ($< 5 \mu\text{m}$) because of their large sizes. Observations of cloudy planets at these wavelengths lead to characteristically flat spectra. Such flat spectra have been observed on several exoplanets and are often taken as an indication for clouds in their atmosphere (Bean et al. 2010; Kreidberg et al. 2014; Powell et al. 2019). For wavelengths around $10 \mu\text{m}$, the peaks in the refractive index of $\text{SiO}_2[\text{s}]$ and $\text{Fe}_2\text{O}_3[\text{s}]$ lead to peaks in the transit depth (see e.g. Helling et al. 2006; Wakeford & Sing 2015). Observing these features allows to gain insights into the cloud particle composition of exoplanet atmospheres (Grant et al. 2023; Dyrek et al. 2023).

Chapter 3

The Effect of Thermal Non-Equilibrium on Kinetic Nucleation

This chapter is based on the publication:

The effect of thermal non-equilibrium on kinetic nucleation

Sven Kiefer, David Gobrecht, Leen Decin, Christiane Helling

Astronomy & Astrophysics, Volume 671, March 2023, A169

Author contribution:

Sven Kiefer derived the equations, performed the simulations and analyses, and wrote the manuscript. David Gobrecht calculated the cluster data, derived the three-body reaction rates, and helped with the manuscript. Christiane Helling and Leen Decin contributed via discussions and advice.

Original abstract:

Nucleation is considered to be the first step in dust and cloud formation in the atmospheres of asymptotic giant branch (AGB) stars, exoplanets, and brown dwarfs. In these environments dust and cloud particles grow to macroscopic sizes when gas phase species condense onto cloud condensation nuclei (CCNs). Understanding the formation processes of CCNs and dust in AGB stars is important because the species that formed in their outflows enrich the interstellar medium. Although widely used, the validity of chemical and thermal equilibrium conditions is debatable in some of these highly dynamical astrophysical environments. We aim to derive a kinetic nucleation model that includes the effects of thermal non-equilibrium by adopting different temperatures for nucleating species, and to quantify the impact of thermal non-equilibrium on kinetic nucleation. Forward and backward rate coefficients are derived as part of a collisional kinetic nucleation theory ansatz. The endothermic backward rates are derived from the law of mass action in thermal non-equilibrium. We consider elastic collisions as thermal equilibrium drivers. For homogeneous TiO_2 nucleation and a gas temperature of 1250 K, we find that differences in the kinetic cluster temperatures as small as 20 K increase the formation of larger TiO_2 clusters by over an order of magnitude. Conversely, an increase in cluster temperature of around 20 K at gas temperatures of 1000 K can reduce the formation of a larger TiO_2 cluster by over an order of magnitude. Our results confirm and quantify the prediction of previous thermal non-equilibrium studies. Small thermal non-equilibria can cause a significant change in the synthesis of larger clusters. Therefore, it is important to use kinetic nucleation models that include thermal non-equilibrium to describe the formation of clusters in environments where even small thermal non-equilibria can be present.

3.1 Introduction

Signatures of active dust formation are present in many astrophysical environments. For example, asymptotic giant branch (AGB) and Wolf–Rayet (WR) stars have been studied as dust-producing environments (Williams et al. 1987; Winters et al. 1994, 1995; Woitke et al. 2000; Ferrarotti & Gail 2006; Höfner 2009; Gail 2010; Karovicova et al. 2013; Gobrecht et al. 2016; Gupta & Sahijpal 2020). Dust produced within these environments is ejected into the interstellar medium (ISM) by radiation pressure on dust particles and thus plays an important role in the chemical enrichment of the ISM (Matsuura et al. 2009; Ventura et al. 2020). In exoplanets, observations of mass-losing atmospheres (e.g. Lieshout et al. 2014) and exoplanet atmospheres (e.g. Kreidberg et al. 2014) have shown evidence of dust and clouds, respectively. Various models have been developed to describe the formation of cloud particles or their effects on exoplanet and brown dwarf atmospheres (e.g. Tsuji et al. 1996; Tsuji 2002, 2005; Allard et al. 2001, 2003; Ackerman & Marley 2001; Woitke & Helling 2003; Helling et al. 2008b). Because of the large cloud opacities in the optical wavelength regime, transmission spectra obtained from cloudy planets are typically featureless at those wavelengths (Pont et al. 2008, 2013; Bean et al. 2010; Crossfield et al. 2013; Knutson et al. 2014; Sing et al. 2015, 2016).

Nucleation describes the clustering of gas-phase species to cloud condensation nuclei (CCNs). One way of describing CCN formation is classical nucleation theory (CNT). This theory assumes chemical and thermal equilibrium of the gas phase, and that the Gibbs free energy of formation of the nucleating species can be approximated by macroscopic properties (see e.g. Helling & Fomins 2013). Modified classical nucleation theory (MCNT) extends CNT by connecting the surface tension with the Gibbs free energy of the nucleating cluster species (Draine & Salpeter 1977; Gail et al. 1984; Lee et al. 2018).

Recently, Tielens (2022) pointed out the importance of kinetics for dust formation in astrophysical environments. In order to study nucleation in chemical non-equilibrium, kinetic reaction networks including nucleation theory can be used (e.g. Girshick & Chiu 1990; Kalikmanov & van Dongen 1993; Patzer et al. 1998; Boulangier et al. 2019b; Gobrecht et al. 2022). Starting from the smallest entities of a substance corresponding to one stoichiometric formula unit (a monomer; e.g. TiO_2), these particles react to form larger (sub-)nanometre-sized structures (e.g. $\text{TiO}_2 + (\text{TiO}_2)_8 \rightarrow (\text{TiO}_2)_{10}$). These larger particles are subsequently referred to as clusters or N-mers. For small clusters the nucleation is likely to proceed as termolecular reactions involving a third body. Conversely, larger clusters can dissociate into smaller clusters or monomers at sufficiently high temperatures (e.g. $(\text{TiO}_2)_{10} \rightarrow \text{TiO}_2 + (\text{TiO}_2)_8$). In many cases, the dissociations are induced by collisions.

The Becker-Döring equations (Becker & Döring 1935; Burton 1977; Penrose & Lebowitz 1979) describe kinetic nucleation if cluster growth and dissociation happens solely via monomers and the same chemical species. Their framework was later extended to polymer nucleation (Ball & Carr 1990; Carr 1992; Carr & da Costa 1994). We note that the nucleation can also proceed via cluster stoichiometries that are different from the crystalline bulk (i.e. the mineral).

Constructing comprehensive chemical kinetic networks for modelling dust nucleation and growth in stellar outflows is a complex task (Gail & Sedlmayr 1998, 1999; Plane 2013; Gobrecht et al. 2016; Bromley et al. 2016; Gobrecht et al. 2022). In addition to the challenges in modelling chemical non-equilibrium, the assumption of thermal equilibrium has been criticised (Donn & Nuth 1985; Goeres 1996; Sedlmayr & Krüger 1997; Ferrarotti & Gail 2002). Recent observations of AGB stars (Fonfría et al. 2008, 2017, 2021) confirmed the presence of thermal non-equilibrium.

Plane & Robertson (2022) analysed the effect of vibrational non-equilibria on the dissociation rate of silicate clusters, OSi(OH)_2 , in stellar outflows. They found that the corresponding dissociation rate of OSi(OH)_2 is reduced by several orders of magnitude in vibrational non-equilibrium. Reactions of Ca, Fe, and Mg with OSi(OH)_2 might represent promising pathways to create metal silicon oxide clusters (e.g. CaSiO_3 , FeSiO_3 , and MgSiO_3). Combining the thermal non-equilibrium dissociation rate of OSi(OH)_2 with the chemical network of Plane (2013) showed that the reduced dissociation rate of OSi(OH)_2 increased the abundance of Ca-, Fe-, and Mg-bearing silicate clusters. This chemical network also includes TiO_2 which can form Ca, Fe, and Mg titanates via OTi(OH)_2 . The impact of thermal non-equilibrium on Ti- and Si-bearing nucleating species is considered to be important for dust formation (e.g. Waters et al. 1996; Gail & Sedlmayr 1999; Goumans & Bromley 2013; Lee et al. 2015; Gobrecht et al. 2016; Bromley et al. 2016; Boulanger et al. 2019b; Sindel et al. 2022).

Thermal non-equilibrium is not only important for small molecular dust precursors but also for larger clusters (Nuth et al. 1985). Nuth & Ferguson (2006) analysed the impact of vibrational non-equilibrium on the nucleation of SiO . They used the vibrational temperature of a single SiO molecule to approximate the vibrational temperatures of larger $(\text{SiO})_N$ clusters (Nuth & Donn 1981). Using this approximation, they analysed the applicability of CNT in circumstellar environments and found that the presence of vibrational disequilibrium enables SiO dust formation at higher kinetic temperatures. Although the authors conclude that CNT cannot be made to work in expanding circumstellar shells, CNT is used owing to the lack of a suitable alternative. Even though the importance of thermal non-equilibrium on titania and silica dust precursors has been shown, only a few modelling attempts have been made to include thermal non-equilibrium in kinetic nucleation models (Patzer

et al. 1998; Lazzati 2008; Köhn et al. 2021; Plane & Robertson 2022). These models start from thermal equilibrium conditions and include two different temperatures, one for the gas phase species and one for the clusters or dust.

In this study, we test and quantify the predicted importance of thermal non-equilibrium on kinetic nucleation. We prescribe different temperatures for each considered cluster size and we study the effect of different kinetic (translational) temperatures. We aim to address internal (vibrational and rotational) thermal non-equilibrium in more detail in a future study.

This chapter is organized as follows. We derive a kinetic nucleation framework from first principles including thermal and chemical non-equilibrium (Section 3.2). In Section 3.3, relaxation timescales for collisional and radiative cooling and heating processes are analysed in order to determine the importance of thermal non-equilibrium. We then use our model and recently published thermodynamic data to quantify the effects of thermal non-equilibrium on nucleation in Section 3.4. Lastly, we present our conclusions in Section 3.5.

3.2 Kinetic nucleation model

In this section we describe the kinetic nucleation model. In Section 3.2.1, the approach of Boulanger et al. (2019b) is used to show how the chemical reaction network formalism can be used to describe polymer nucleation. In Section 3.2.2, the derivation of the Maxwell-Boltzmann relative speed distribution in thermal non-equilibrium is made and in Section 3.2.3, 3.2.5, and 3.2.5 the forward and backward reaction rates are derived.

3.2.1 Kinetic reactions

Each cluster consists of N basic building blocks (e.g. TiO_2) that are linked by chemical bonds (e.g. $(\text{TiO}_2)_N$). The change in cluster number densities n_N [cm^{-3}] can be described by the following coupled ordinary differential equations (ODEs) (Eq. 1 of Boulanger et al. 2019b):

$$\frac{dn_N}{dt} = \sum_{j \in F_N} \left(k_j^+ \prod_{r \in R_j^+} n_r \right) - \sum_{j \in \mathcal{D}_N} \left(k_j^- \prod_{r \in R_j^-} n_r \right), \quad (3.1)$$

where F_N is the set of forward reactions (R_j^+) and \mathcal{D}_N is the set of backward reactions (R_j^-). In the following, R_j is defined as either R_j^+ or R_j^- and each

variable specific to reaction R_j has a j subscript. Similarly, k_j is either k_j^+ or k_j^- . The variable n_r [cm^{-3}] denotes the number densities of the cluster involved in reaction R_j and k_j [$\text{cm}^{3(J-1)}\text{s}^{-1}$] is the reaction rate for the reaction R_j , where J is the number of reactants in reaction R_j . For small cluster sizes and low densities, three-body association reactions are the dominant cluster nucleation process (see e.g. Bromley et al. 2016). The reaction rates for termolecular associations and their reverse collisional dissociation are discussed in Section 3.2.4. For larger clusters, two-body association reactions ($J=2$) are assumed to be the dominant forward reaction for which the reaction rate k_j^+ is the following (based on Peters 2017):

$$k_j^+ = \int_0^\infty \alpha_j(\nu_r) \sigma_j(\nu_r) \nu_r f(\nu_r) d\nu_r, \quad (3.2)$$

where $\alpha_j(\nu_r)$ is the sticking coefficient, $\sigma_j(\nu_r)$ [cm^2] the reaction cross section, ν_r [cm s^{-1}] the relative velocity of the colliding particles, and $f(\nu_r)$ the Maxwell-Boltzmann velocity distribution (see Sect. 3.2.2). Due to the lack of data on sticking coefficients for nucleating species, we set $\alpha_j(\nu_r) = 1$ for the rest of this chapter. Therefore, all reaction rates are upper limits. This is a frequently used approximation for the sticking coefficient (e.g. Lazzati 2008; Bromley et al. 2016; Boulanger et al. 2019b).

The cross section is a measure of the probability that a cluster reacts with other clusters¹. In the most general case, it can depend on the relative velocity ν_r . For small clusters, long-range interactions from electrostatic forces need to be taken into account² (Bromley & Zwijnenburg 2016; Köhn et al. 2021). We describe the cross section by a collision of two hard spheres:

$$\sigma_j = \pi(r_1 + r_2)^2, \quad (3.3)$$

where r_1 and r_2 [cm] are the interaction radii of the collision partners. We provide interaction radii for $(\text{TiO}_2)_N$ clusters (Table A.1), which are used in our reference nucleation case.

The goal of the present study is to assess the impact of thermal non-equilibrium on the kinetic formation of clusters. The gas is assumed to be in thermal equilibrium, but the clusters might not be. Clusters of a given size N are described by a kinetic cluster temperature (T_N^{kin}) and an internal cluster temperature (T_N^{int}) which can differ from each other and from the gas phase

¹In the case of kinetic chemistry, the cross section is a statistical property. Therefore, for non-spherical particles, the cross section σ has to be found by averaging the angle-dependent cross section $\sigma(\phi, \theta)$ over the azimuthal angles ϕ and polar angles θ .

²A comparison of van der Waals radii to geometric radii for TiO_2 can be found in Appendix A or in Köhn et al. (2021).

temperature T_{gas} . The internal temperature includes vibrational and rotational contributions which are not differentiated further in the present study.

An N -mer is composed of Nx_1 atoms, where x_1 is the number of atoms in a monomer unit. Therefore an N -mer has $3Nx_1$ degrees of freedom of which three describe translational movement and $D_N^f = 3Nx_1 - 3$ describe internal degrees of freedom (including three rotations and $3Nx_1 - 6$ vibrations). Using the equipartition theorem, we can define

$$E_N^{\text{tot}} = E_N^{\text{kin}} + E_N^{\text{int}} = \frac{3}{2}kT_N^{\text{kin}} + \frac{D_N^f}{2}kT_N^{\text{int}}, \quad (3.4)$$

where $k = 1.381 \times 10^{-16}$ erg K $^{-1}$ is the Boltzmann constant. In our model, each cluster size can be at a different kinetic temperature T_N^{kin} and at a different internal temperature T_N^{int} .

3.2.2 Two-particle speed distribution

To derive the relative speed distribution for two particle ensembles (P_1 and P_2) with different masses (m_1 and m_2) and temperatures (T_1 and T_2), we follow the derivation of Kusakabe et al. (2019). We use an adapted version of their centre of mass transformation, which we call the temperature-weighted centre of mass (TCM). We perform the TCM transformation as follows:

$$M_T \equiv \frac{m_1}{T_1^{\text{kin}}} + \frac{m_2}{T_2^{\text{kin}}} = \frac{m_1 T_2^{\text{kin}} + m_2 T_1^{\text{kin}}}{T_1^{\text{kin}} T_2^{\text{kin}}}, \quad (3.5)$$

$$\mu \equiv \frac{m_1 m_2}{m_1 + m_2}, \quad (3.6)$$

$$\mu_T \equiv \frac{\frac{m_1}{T_1^{\text{kin}}} \frac{m_2}{T_2^{\text{kin}}}}{\frac{m_1}{T_1^{\text{kin}}} + \frac{m_2}{T_2^{\text{kin}}}} = \frac{m_1 m_2}{m_1 T_2^{\text{kin}} + m_2 T_1^{\text{kin}}}, \quad (3.7)$$

$$\vec{\nu}_r \equiv \vec{\nu}_1 - \vec{\nu}_2, \quad (3.8)$$

$$\vec{\nu}_T \equiv \frac{\frac{m_1}{T_1^{\text{kin}}} \vec{\nu}_1 + \frac{m_2}{T_2^{\text{kin}}} \vec{\nu}_2}{\frac{m_1}{T_1^{\text{kin}}} + \frac{m_2}{T_2^{\text{kin}}}} = \frac{m_1 T_2^{\text{kin}} \vec{\nu}_1 + m_2 T_1^{\text{kin}} \vec{\nu}_2}{m_1 T_2^{\text{kin}} + m_2 T_1^{\text{kin}}}, \quad (3.9)$$

where m_1 , m_2 [g] are the masses of the particles within P_1 and P_2 , respectively. Furthermore, T_1^{kin} , T_2^{kin} [K] are their kinetic temperatures and $\vec{\nu}_1$, $\vec{\nu}_2$ [cm s $^{-1}$]

their velocity. In addition, M_T [g T⁻¹] is the temperature-weighted total mass, μ [g] the reduced mass, μ_T [g T⁻¹] the temperature-weighted reduced mass, \vec{v}_r [cm s⁻¹] the relative velocity, and \vec{v}_T [cm s⁻¹] the TCM velocity. Using these definitions, we can find the following relation:

$$\frac{m_1}{T_1^{\text{kin}}} \vec{v}_1^2 + \frac{m_2}{T_2^{\text{kin}}} \vec{v}_2^2 = M_T \vec{v}_T^2 + \mu_T \vec{v}_r^2. \quad (3.10)$$

From here, we assume that the velocity distribution of the clusters follows the Maxwell-Boltzmann velocity distribution for a particle of mass m [g]:

$$f(\vec{v}) d\vec{v} = \left(\frac{m}{2\pi k T} \right)^{3/2} \exp \left(-\frac{m \vec{v}^2}{2kT} \right) d\vec{v}. \quad (3.11)$$

The relative velocity distribution $f_r(v_r)$ can be found using an equivalent derivation³ as in Eq. 9 and 10 of Kusakabe et al. (2019):

$$\int_{\mathbb{R}^3} f_r(\vec{v}_r) d\vec{v}_r = \int_{\mathbb{R}^3} f(\vec{v}_1) d\vec{v}_1 \int_{\mathbb{R}^3} f(\vec{v}_2) d\vec{v}_2 \quad (3.12)$$

$$= \left(\frac{1}{2\pi k} \right)^3 \left(\frac{m_1 m_2}{T_1^{\text{kin}} T_2^{\text{kin}}} \right)^{3/2}$$

$$\int_{\mathbb{R}^3} \int_{\mathbb{R}^3} \exp \left(-\frac{M_T \vec{v}_T^2 + \mu_T \vec{v}_r^2}{2k} \right) d\vec{v}_r d\vec{v}_T \quad (3.13)$$

$$= \int_{\mathbb{R}^3} \left(\frac{\mu_T}{2\pi k} \right)^{3/2} \exp \left(-\frac{\mu_T \vec{v}_r^2}{2k} \right) d\vec{v}_r. \quad (3.14)$$

Assuming spherical symmetry ($d\vec{v}_r = 4\pi v_r^2 d\nu_r$), this leads to the following relative speed distribution:

$$f_r(\nu_r) d\nu_r = \left(\frac{\mu_T}{2\pi k} \right)^{3/2} 4\pi \nu_r^2 \exp \left(-\frac{\mu_T \nu_r^2}{2k} \right) d\nu_r, \quad (3.15)$$

which is similar to a Maxwell-Boltzmann distribution of the centre of mass frame, but the temperature-weighted reduced mass μ_T replaces the reduced mass. This distribution can be used to describe the relative velocity of two particle ensembles (e.g. a cluster of different sizes) at different temperatures.

For large temperature differences (e.g. $T_1^{\text{kin}} \gg T_2^{\text{kin}}$) or large mass differences (e.g. $m_1 \ll m_2$), μ_T becomes

$$\mu_T \approx \frac{m_1}{T_1^{\text{kin}}}, \quad (3.16)$$

³The relative speed distribution can be found by convolution of the velocity distributions of the collision partners: $f_r(\vec{v}_r) = \int d\vec{v}_1 \int d\vec{v}_2 f(\vec{v}_1) f(\vec{v}_2) \delta(|\vec{v}_r| - |\vec{v}_1 - \vec{v}_2|)$, where δ is the Dirac delta function.

which recovers the Maxwell-Boltzmann distribution for the particle ensemble P_1 . If the collision partners have the same kinetic temperature ($T_1^{\text{kin}} = T_2^{\text{kin}}$), we find

$$\mu_T = \frac{\mu}{T}, \quad (3.17)$$

which recovers the result for thermal equilibrium, defined as $T_{\text{gas}} = T_N^{\text{kin}} = T_N^{\text{int}}$ (Boulanger et al. 2019b).

3.2.3 Forward reaction rate

Combining Eq. 3.2, 3.3, and 3.15, we find a general expression for the forward reaction rate k_j^+ of a two-body collision between particles from P_1 (with m_1 and T_1) and particles from P_2 (with m_1 and T_1) for a sticking coefficient of $\alpha = 1$:

$$k_j^+ = \int_0^\infty \pi(r_1 + r_2)^2 \nu_r \left(\frac{\mu_T}{2\pi k} \right)^{3/2} 4\pi \nu_r^2 \exp \left(-\frac{\mu_T \nu_r^2}{2k} \right) d\nu_r \quad (3.18)$$

$$= \pi(r_1 + r_2)^2 \sqrt{\frac{8k}{\pi\mu_T}} = \pi(r_1 + r_2)^2 \langle \nu_r \rangle, \quad (3.19)$$

where $\langle \nu_r \rangle = \sqrt{8k/\pi\mu_T}$ is the average relative speed.

3.2.4 Association and dissociation of small clusters

For small cluster sizes (e.g. $N \leq 4$ for TiO_2) and gas densities $n_{\text{gas}} = 10^{12}\text{-}10^{14} \text{ cm}^{-3}$ considered in this study, termolecular associations ($A + B + M \rightarrow AB + M$) are the dominant cluster growth reactions, and they are favoured over bimolecular radiative associations ($A + B \rightarrow AB + h\nu$) (see e.g. Bromley et al. 2016). For the reverse collisional dissociation reactions ($AB + M \rightarrow A + B + M$), we use accurate CCSD(T)/6-311+G(2d,2p) single point energies to calculate the dissociation energy E_{AB} [erg mol⁻¹]. The dissociation rate is calculated as

$$k_{3B}^- = A \exp \left(\frac{-E_{AB}}{RT} \right). \quad (3.20)$$

The dissociation rates are adjusted for thermal non-equilibrium conditions by accounting for the different relative velocities of the gas particles M and the clusters:

$$k_{3B}^- = A \exp \left(\frac{-E_{AB}}{RT} \right) \sqrt{\frac{m_{\text{gas}} T_{AB}^{\text{kin}} + m_{AB} T_{\text{gas}}}{(m_{\text{gas}} + m_{AB}) T_{\text{gas}}}}. \quad (3.21)$$

We note that, in addition to the relative velocities, the clusters could have significantly cooler internal (vibrational) temperatures than the gas particles, which is not taken into account in the present study.

The corresponding three-body forward association reaction rates for TiO₂ are calculated using detailed balance as described in Section 3.2.5 with cluster partition functions derived in Sindel et al. (2022). For the pre-exponential rate constant A [cm³s⁻¹], a value of 1.4×10^{-9} cm³s⁻¹ is used. This approximated value is based on an upper limit of 2×10^{-9} cm³s⁻¹ that is still considered to be physical (see e.g. Gobrecht et al. 2022), and it is similar to the pre-exponential factors for collisional dissociations of aluminium oxide clusters (Catoire et al. 2003). The dissociation rate coefficients for TiO₂ are shown in Table A.2 and example values for the association reaction rate coefficients are shown in Table A.3. The detailed balance and equilibrium constant computations are approximated in kinetic-to-internal thermal equilibrium ($T_N^{\text{int}} = T_N^{\text{kin}} \neq T_{\text{gas}}$).

3.2.5 Backward reaction rate

Backward reactions are considered as spontaneous processes that cause larger clusters to fragment into smaller clusters. For kinetic nucleation, a general relation can be written as $A + B \rightleftharpoons C$. To determine the rate coefficients k_j^- of this process, we make use of the principle of detailed balance (Milne relation; Chapter 12.2.2 of Gail & Sedlmayr 2013) which assumes that, in detailed balance (e.g. chemical equilibrium), the ratio between the forward and backward rate of each reaction is the same. Therefore, in chemical equilibrium (marked with \circ), the species flux of each forward reaction is equivalent to the flux of the corresponding backward reaction:

$$k_j^+ \dot{n}_A \dot{n}_B = k_j^- \dot{n}_{A+B}, \quad (3.22)$$

where \dot{n}_A , \dot{n}_B , and \dot{n}_{A+B} [cm⁻³] are the number densities in chemical equilibrium. Eq. 3.22 can be rewritten as

$$k_j^- = k_j^+ \frac{\dot{n}_A \dot{n}_B}{\dot{n}_{A+B}}. \quad (3.23)$$

To find the number densities in chemical equilibrium, the total Gibbs free energy (including translational, rotational, and vibrational contributions) in thermal non-equilibrium $G^{\text{non-eq}}$ [erg] is minimized. The setup considered here can be described by nucleating clusters immersed in an ambient gas. We assume a single non-clustering gas species and a single clustering species to simplify notation, but the derivation also holds for multiple non-clustering and clustering

species. Furthermore, we assume that all clusters other than the monomer can be in thermal non-equilibrium (in the special case of thermal equilibrium, both temperatures are equal to the gas temperature: $T_{\text{gas}} = T_i^{\text{kin}} = T_i^{\text{int}}$) and each i -mer has a kinetic temperature T_i^{kin} and an internal temperature of T_i^{int} .

The Gibbs free energy of cluster⁴ where the internal cluster temperature T_i^{int} differs from the kinetic temperature T_i^{kin} can be written as follows:

$$G_i^{\text{non-eq}}(T_i^{\text{int}}, T_i^{\text{kin}}, p_i, N_i) = G_i(T_i^{\text{kin}}, p_i, N_i) + N_i \omega_i(T_i^{\text{kin}}, T_i^{\text{int}}), \quad (3.24)$$

where $G_i^{\text{non-eq}}(T_i^{\text{kin}}, T_i^{\text{int}}, p_i, N_i)$ is the i -mer's Gibbs free energy in kinetic-to-internal thermal non-equilibrium (defined as $T_i^{\text{kin}} \neq T_i^{\text{int}}$), p_i [dyn cm⁻²] is the partial pressure of the i -mer and N_i the number of i -mers. Furthermore, $\omega_i(T_i^{\text{kin}}, T_i^{\text{int}})$ [erg] is the difference in Gibbs free energy of a single i -mer in thermal equilibrium to the Gibbs free energy of a cluster in kinetic-to-internal thermal non-equilibrium. Because changes in the internal temperature do not affect the i -mer's partial pressure p_i , volume, or number densities of the gas, ω_i only depends on kinetic and internal temperature. Summing Eq. 3.24 for all clusters and gas species, the total Gibbs free energy can be written as follows:

$$\begin{aligned} G^{\text{non-eq}}(T_0^{\text{int}}, \dots, T_r^{\text{int}}, T_0^{\text{kin}}, \dots, T_r^{\text{kin}}, p_0, \dots, p_r, N_0, \dots, N_r) \\ = \sum_{i=0}^r G_i^{\text{non-eq}}(T_i^{\text{int}}, T_i^{\text{kin}}, p_i, N_i) \end{aligned} \quad (3.25)$$

$$= \sum_{i=0}^r G_i(T_i^{\text{kin}}, p_i, N_i) + N_i \omega_i(T_i^{\text{kin}}, T_i^{\text{int}}), \quad (3.26)$$

where the subscript 0 describes the gas ($T_{\text{gas}} = T_0^{\text{int}} = T_0^{\text{kin}}$ and $N_{\text{gas}} = N_0$), the subscript $i \geq 1$ represents the cluster sizes, and r denotes the largest cluster considered. Next, we need to convert the partial pressures p_i to the total pressure $p = \sum_{i=0}^r p_i$ [dyn cm⁻²]:

$$G_i(T_i^{\text{kin}}, p_i, N_i) = G_i(T_i^{\text{kin}}, p, N_i) + \int_p^{p_i} \frac{\partial G_i(T_i^{\text{kin}}, p', N_i)}{\partial p'} dp' \quad (3.27)$$

$$= G_i(T_i^{\text{kin}}, p, N_i) + \int_p^{p_i} \frac{N_i k T_i^{\text{kin}}}{p'} dp' \quad (3.28)$$

$$= G_i(T_i^{\text{kin}}, p, N_i) + N_i k T_i^{\text{kin}} \ln \left(\frac{N_i}{N} \right), \quad (3.29)$$

⁴We assume that each metastable cluster structure quickly relaxes to their global minimum after formation. Therefore, we can use the Gibbs free energies of the global minimum. For a detailed analysis of relaxation timescales of the potential energy surface, the reader is referred to Doye & Wales (1996).

where $N = \sum_{i=0}^r N_i$ is the total number of particles (gas and clusters). Combining Eq. 3.26 and 3.29 as well as the definition of the chemical potential μ ($G = N\mu$) leads to the Gibbs free energy of the mixture of gas and clusters:

$$\begin{aligned} G^{non-eq}(T_0^{\text{int}}, \dots, T_r^{\text{int}}, T_0^{\text{kin}}, \dots, T_r^{\text{kin}}, p, N_0, \dots, N_r) \\ = N_{\text{gas}}\mu_{\text{gas}}(T_{\text{gas}}, p) + N_{\text{gas}}kT_{\text{gas}} \ln \left(\frac{N_{\text{gas}}}{N} \right) + \sum_{i=1}^r N_i \mu_i(T_i^{\text{kin}}, p) \\ + N_i k T_i^{\text{kin}} \ln \left(\frac{N_i}{N} \right) + N_i \omega_i(T_i^{\text{kin}}, T_i^{\text{int}}), \end{aligned} \quad (3.30)$$

where $\mu_i(T_i^{\text{kin}}, p)$ [erg] is the chemical potential of the clusters and $\mu_{\text{gas}}(T_{\text{gas}}, p)$ [erg] the chemical potential of the gas species⁵. This equation describes the Gibbs free energy of a mixture of gas and clusters in thermal non-equilibrium.

To minimize the Gibbs free energy, the Lagrangian function can be used⁶. As an additional constraint, we assume that the number of basic building blocks (e.g. TiO₂) is conserved:

$$C = \sum_{i=1}^r i N_i. \quad (3.31)$$

Using Eq. 3.30 and Eq. 3.31, the Lagrangian function can be defined as

$$\begin{aligned} \mathcal{L} = N_{\text{gas}}\mu_{\text{gas}}(T_{\text{gas}}, p) + N_{\text{gas}}kT_{\text{gas}} \ln \left(\frac{N_{\text{gas}}}{N} \right) - \lambda C \\ + \sum_{i=1}^r N_i \mu_i(T_i^{\text{kin}}, p) + N_i k T_i^{\text{kin}} \ln \left(\frac{N_i}{N} \right) \\ + N_i \omega_i(T_i^{\text{kin}}, T_i^{\text{int}}) + \lambda i N_i. \end{aligned} \quad (3.32)$$

The number of clusters N_i are realistically much smaller than the total number of gas particles, such that

$$N_{\text{gas}} \gg \sum_{i=1}^r N_i. \quad (3.33)$$

⁵In the literature usually the molar Gibbs free energy G_{mol} is given, which is related to the chemical potential μ through the Avogadro constant N_A , such that $N_A\mu = G_{\text{mol}}$.

⁶The Lagrangian function is a tool for mathematical optimization problems in which equality constraints can be expressed using the Lagrangian multiplier λ .

Furthermore, we assume that the differences in temperature are small enough so as to not influence this approximation:

$$N_{\text{gas}} T_{\text{gas}} \gg \sum_{i=1}^r N_i T_i^{\text{kin}}. \quad (3.34)$$

Taking the partial derivatives of the Lagrangian with respect to N_1 , N_j (for $j \geq 2$) and λ and using the above approximations, we arrive at the following system of equations:

$$\begin{aligned} \frac{\partial \mathcal{L}}{\partial N_1} &= \mu_1(T_{\text{gas}}, p) + kT_{\text{gas}} \ln \left(\frac{N_1}{N} \right) \\ &+ \lambda + kT_{\text{gas}} \frac{N - N_1}{N} - \sum_{\substack{i=0 \\ i \neq 1}}^r \frac{N_i k T_i^{\text{kin}}}{N} \end{aligned} \quad (3.35)$$

$$\approx \mu_1(T_{\text{gas}}, p) + kT_{\text{gas}} \ln \left(\frac{N_1}{N} \right) + \lambda, \quad (3.36)$$

$$\begin{aligned} \frac{\partial \mathcal{L}}{\partial N_j} &= \mu_j(T_j^{\text{kin}}, p) + kT_j^{\text{kin}} \ln \left(\frac{N_j}{N} \right) + \omega_j(T_j^{\text{kin}}, T_j^{\text{int}}) \\ &+ \lambda j x_1 + kT_j^{\text{kin}} \frac{N - N_j}{N} - \sum_{\substack{i=0 \\ i \neq j}}^r \frac{N_i k T_i^{\text{kin}}}{N}, \end{aligned} \quad (3.37)$$

$$\begin{aligned} &\approx \mu_j(T_j^{\text{kin}}, p) + kT_j^{\text{kin}} \ln \left(\frac{N_j}{N} \right) + \omega_j(T_j^{\text{kin}}, T_j^{\text{int}}) \\ &+ \lambda j + k(T_j^{\text{kin}} - T_{\text{gas}}), \end{aligned} \quad (3.38)$$

$$(3.39)$$

where $j = \{2, 3, 4, \dots, r\}$. Minimizing the Lagrangian function with regard to N_j is equivalent to setting Eq. 3.38 to 0 and this represents the state of chemical equilibrium. Setting Eq. 3.38 to zero leads to

$$\begin{aligned} \frac{\dot{N}_j}{N_{\text{gas}}} &= \exp \left(\frac{-\mu_j(T_j^{\text{kin}}, p)}{kT_j^{\text{kin}}} \right) \\ &\exp \left(\frac{-k(T_j^{\text{kin}} - T_{\text{gas}}) - \omega_j(T_j^{\text{kin}}, T_j^{\text{int}}) - \lambda j}{kT_j^{\text{kin}}} \right). \end{aligned} \quad (3.40)$$

Using Eq. 3.40 for clusters of size A , B , and $A + B$ allows us to write the following:

$$\frac{\dot{N}_A \dot{N}_B}{\dot{N}_{A+B}} = N_{\text{gas}} \exp \left(\sum_{i \in \zeta} \frac{\delta(i)}{kT_i^{\text{kin}}} \mu_i(T_i^{\text{kin}}, p) \right) \exp \left(\sum_{i \in \zeta} \frac{\delta(i)}{kT_i^{\text{kin}}} [k(T_i^{\text{kin}} - T_{\text{gas}}) + \omega_i(T_i^{\text{kin}}, T_i^{\text{int}}) + \lambda i] \right), \quad (3.41)$$

where $\zeta = \{A, B, (A+B)\}$ defines the set of all involved cluster sizes and $\delta(i)$ is equal to 1 for products (here $A+B$) and -1 for the reactants (here A and B). To find the Lagrangian multiplier, we use Eq. 3.36 and find

$$\lambda = -\mu_1(T_{\text{gas}}, p) - kT_{\text{gas}} \ln \left(\frac{N_1}{N} \right). \quad (3.42)$$

Furthermore, it is convenient to express Eq. 3.42 in terms of the chemical potential ($\mu^\ominus(T_{\text{gas}}) = \mu_i(T_{\text{gas}}, p^\ominus)$) at standard pressure ($p^\ominus = 10^6 \text{ dyn cm}^{-2}$). Doing this and using Eq. 3.22, 3.41, and 3.42 leads to the following backward reaction rate:

$$k^- = \frac{k^+ p^\ominus}{kT_{\text{gas}}} \exp \left(\sum_{i \in \zeta} \frac{\delta(i)}{kT_i^{\text{kin}}} [\mu_i^\ominus(T_i^{\text{kin}}) - i\mu_1^\ominus(T_{\text{gas}}) + k(T_i^{\text{kin}} - T_{\text{gas}}) + \omega_i(T_i^{\text{kin}}, T_i^{\text{int}})] \right) \left(\frac{kT_{\text{gas}} \dot{n}_1}{p^\ominus} \right)^{-\sum_{i \in \zeta} \delta(i) i T_{\text{gas}} / T_i^{\text{kin}}}. \quad (3.43)$$

3.3 Cooling and heating processes

Collisional and radiative heating and cooling processes impact the cluster temperature. We first look at the collisional relaxation timescale of kinetic temperature T_N^{kin} to the gas temperature T_{gas} in Section 3.3.1. Afterwards, we investigate the timescale of changes in internal temperature T_N^{int} via collisions in section 3.3.2 and via radiative processes in section 3.3.2.

3.3.1 Kinetic temperature

To derive the collision-induced change in cluster kinetic temperature T_N^{kin} , we follow the derivation of Gail & Sedlmayr (2013). We assume that the energy

redistribution happens through elastic and isotropic collisions between gas particles and the clusters. Considering an elastic and isotropic collision of two particles P_1 (with mass m_1) and P_2 (with mass m_2), the average ratio between the energy before and after the collision is the following (Eq. 6.6 of Gail & Sedlmayr 2013):

$$\frac{E_1^{\text{after}} - E_2^{\text{after}}}{E_1^{\text{before}} - E_2^{\text{before}}} = 1 - \frac{8}{3} \frac{m_1 m_2}{(m_1 + m_2)^2}. \quad (3.44)$$

Every collision decreases the energy difference by that amount. The relaxation timescale is defined as the number of collisions K_{col} needed to reduce the kinetic energy of particles 1 with respect to particles 2 to $1/e$ of its initial value. Therefore, K_{col} is (Eq. 6.9 of Gail & Sedlmayr 2013)

$$K_{\text{col}} = -\ln \left(1 - \frac{8}{3} \frac{m_1 m_2}{(m_1 + m_2)^2} \right)^{-1} \approx \frac{3}{8} \frac{m_1}{m_2}, \quad (3.45)$$

where the approximation is the first term of a Taylor expansion and holds in the case of $m_1 \gg m_2$. This approximation holds for H_2 ($m = 2.02 \text{ u}$) gas, including TiO_2 clusters ($m = 79.87 \text{ u}$). To find the kinetic cooling timescale $\tau_{\text{gc}}^{\text{kin}}$ of elastic collisions, we multiply the number of collisions with $\langle t_{\text{gc}} \rangle$ being the average time for a cluster (e.g. TiO_2) to collide with a gas particle (e.g. H_2):

$$\langle t_{\text{gc}} \rangle = \frac{1}{n_{\text{gas}} \sigma_N \langle v_r \rangle} = \frac{1}{n_{\text{gas}} \pi r_N^2} \sqrt{\frac{\pi \mu T}{8k}}, \quad (3.46)$$

$$(\tau_{\text{gc}}^{\text{kin}})^{-1} = \frac{1}{K_{\text{col}} * \langle t_{\text{gc}} \rangle} \quad (3.47)$$

$$\approx \frac{8m_{\text{gas}}}{3m_N} n_{\text{gas}} \pi r_N^2 \sqrt{\frac{8kT_{\text{gas}}}{\pi m_{\text{gas}}}}, \quad (3.48)$$

where the approximation is justified for $m_{\text{gas}} \ll m_N$. Looking at the reference case of $(\text{TiO}_2)_2$ clusters in a gas as described in Table 3.1, we find a collisional cooling timescale for the $(\text{TiO}_2)_2$ kinetic temperature of $\tau_{\text{gc}}^{\text{kin}} = 0.018 \text{ s}$. We note that $\tau_{\text{gc}}^{\text{kin}}$ is inversely proportional to the gas number density n_{gas} . Therefore, clusters residing in low-density regions (where collisions are not efficient enough to maintain thermal equilibrium) might not be in kinetic-to-gas thermal equilibrium (defined as $T_N^{\text{kin}} = T_{\text{gas}}$).

Table 3.1: Summary of the quantities used for the $(\text{TiO}_2)_2$ cooling timescale examples.

gas species	H_2	Nucleating species	TiO_2
T_{gas} [K]	1000	T_{TiO_2} [K]	1000
n_{gas} [cm^{-3}]	10^{12}	n_{TiO_2} [cm^{-3}]	10^4
m_{gas} [u]	2.02	m_{TiO_2} [u]	79.87
		r_{TiO_2} [\AA]	2.32

3.3.2 Internal temperature

Collisional

Internal cooling or heating of clusters via elastic collisions with gas depends on the size ratio between cluster species and gas-phase molecules which is typically expressed with the Knudsen number (Woitke & Helling 2003):

$$Kn = \frac{\bar{l}}{2r_N}, \quad (3.49)$$

where $\bar{l} = (\sigma_N n_{\text{gas}})^{-1}$ [cm] is the mean free path of the gas and $2r_N$ is the diameter of the cluster (see also Table A.1).

Case 1: $Kn \gg 1$

In the high Knudsen number limit, the theory of Burke & Hollenbach (1983) is used. Here, the cooling rate per unit volume Λ_N [erg s⁻¹cm⁻³] of a cluster can be used to calculate the energy change for each particle per time (in the approximation $m_{\text{gas}} \ll m_N$):

$$\frac{dE^{\text{int}}}{dt} = \frac{\Lambda_N}{n_N} \approx \sqrt{\frac{8k^3}{\pi m_{\text{gas}}}} \bar{\alpha}_T \pi r_N^2 n_{\text{gas}} \sqrt{T_{\text{gas}}} (T_{\text{gas}} - T_N^{\text{int}}),$$

where $\bar{\alpha}_T$ is the average accommodation coefficient. The exact value of $\bar{\alpha}_T$ depends on the colliding species, the gas composition, and the temperature, but typically it is within 0.1 to 0.9 (Burke & Hollenbach 1983). To assess the timescales in orders of magnitude, we approximate the average accommodation coefficient as $\bar{\alpha}_T = 0.5$.

To calculate the collisional internal cooling timescale $\tau_{\text{gc}}^{\text{int}}$ towards the gas temperature, we need to relate the energy change of the cooling rate with the internal temperature change of the clusters. Using Eq. 3.4, we find the

following:

$$\frac{dT_N^{\text{int}}}{dt} = \frac{dT_N^{\text{int}}}{dE^{\text{int}}} \frac{dE^{\text{int}}}{dt} = (\tau_{\text{gc}}^{\text{int}})^{-1} (T_{\text{gas}} - T_N^{\text{int}}), \quad (3.50)$$

where $\tau_{\text{gc}}^{\text{int}}$ is given by

$$(\tau_{\text{gc}}^{\text{int}})^{-1} \approx \frac{2\bar{\alpha}_T}{D_f} n_{\text{gas}} r_N^2 \sqrt{\frac{8\pi k T_{\text{gas}}}{m_{\text{gas}}}}. \quad (3.51)$$

Assuming a constant gas temperature $T_{\text{gas}}(t) = T_{\text{gas}}$, this system can be solved and leads to the following temperature evolution for a cluster after collision:

$$T_N^{\text{int}}(t) = T_{\text{gas}} + (T_{N,0}^{\text{int}} - T_{\text{gas}}) \exp(-t/\tau_{\text{gc}}^{\text{int}}), \quad (3.52)$$

where $T_{N,0}^{\text{int}}$ [K] is the initial internal cluster temperature. Looking at our reference case of $(\text{TiO}_2)_2$ clusters in a gas as described in Table 3.1, we find a collisional cooling timescale for the $(\text{TiO}_2)_2$ internal temperature of $\tau_{\text{gc}}^{\text{int}} = 0.0059$ s. The kinetic cooling timescale is within an order of magnitude of the internal cooling timescale. This is not surprising, as Eq. 3.48 and Eq. 3.51 have the same n_{gas} , r_N , and $\langle \nu_r \rangle$ dependencies and only differ in their prefactor. This relation stems from the nature of collisional energy transfer. Kinetic energy is exchanged via elastic collisions of particles. The more often collisions occur and the more energy can be exchanged within one collision, the faster the kinetic temperature adjusts to the equilibrium temperature. Similarly, internal energy exchange can be described via collisions of gas particles with an internal 'spring' (vibration mode) of the cluster (see Burke & Hollenbach (1983)). Here, the timescale for thermal adjustment also depends on the collision rate and the energy amount exchange per collision.

Case 2: $Kn \ll 1$

For larger clusters, the Knudsen number becomes increasingly small. In this case, we use the definition of the isobaric-specific heat and of the heat flow (Eq. 15.19 and 17.1 of Tipler & Mosca 2015):

$$dQ = m_N c_p dT_N^{\text{int}}, \quad (3.53)$$

$$\frac{dQ}{dt} = \frac{k_c A_N}{\Delta x} (T_{\text{gas}} - T_N^{\text{int}}), \quad (3.54)$$

where c_p [erg g⁻¹K⁻¹] is the specific heat capacity for constant pressure, k_c [W cm⁻¹K⁻¹] is the thermal conductivity, and A_N [cm²] is the cluster surface area. We assume that the energy exchange between the cluster and the gas happens

over the mean free path of the gas ($\Delta x = \bar{l}$). The thermal conductivity k_c of an ideal gas is as follows (Eq. 10-25 of Sears & Salinger 1975):

$$k_c = \frac{1}{3} c_V \rho_{\text{gas}} \bar{l} \langle v \rangle, \quad (3.55)$$

where c_V [erg g⁻¹K⁻¹] is the isochoric-specific heat capacity. Using Eqs. 3.53, 3.54, and 3.55 leads to the following solution for the internal temperature:

$$\frac{dT^{\text{int}}}{dt} = \frac{k_c A}{\bar{l} m_N c_p} (T_{\text{gas}} - T_N^{\text{int}}) \quad (3.56)$$

$$\approx \frac{c_V \rho_{\text{gas}} \pi r_N^2}{3c_p m_N} \sqrt{\frac{8kT_{\text{gas}}}{\pi m_{\text{gas}}}} (T_{\text{gas}} - T_N^{\text{int}}), \quad (3.57)$$

$$T_N^{\text{int}}(t) = T_{\text{gas}} + (T_N^{\text{int}}(0) - T_{\text{gas}}) \exp(-t/\tau_{\text{gc}}^{\text{int}}), \quad (3.58)$$

$$(\tau_{\text{gc}}^{\text{int}})^{-1} \approx \frac{c_V m_{\text{gas}}}{3c_p m_N} n_{\text{gas}} r_N^2 \sqrt{\frac{8\pi k T_{\text{gas}}}{m_{\text{gas}}}}. \quad (3.59)$$

Radiative

Radiative cooling is especially important for a cluster with large dipole moments in regions where the gas density is low and collisional cooling processes become inefficient (Woitke et al. 1996; Plane & Robertson 2022). Because of their intermediate size, small clusters are not well described as black bodies, but rather they radiate via discrete de-excitation (i.e. relaxation) of rotationally, vibrationally, and electronically excited states (Woitke et al. 2009; Coppola et al. 2011; Ferrari et al. 2019). Each cluster size i has discrete energy levels E_i^a [erg] with $a \geq 1$ and the ground state is denoted with G ($E_i^1 = E_i^G$). The energy levels have a number density of n_i^a [cm⁻³] which follow the Boltzmann distribution at the specific temperature T_N^{int} ,

$$\frac{n_i^a}{n_i^G} = \frac{g_{i,a}}{g_{i,G}} \exp\left(\frac{-(E_i^a - E_i^G)}{kT_i^{\text{int}}}\right), \quad (3.60)$$

$$n_i^G = n_i \left(\sum_{a=1}^{\infty} \frac{g_{i,a}}{g_{i,G}} \exp\left(\frac{-(E_i^a - E_i^G)}{kT_N^{\text{int}}}\right) \right)^{-1}, \quad (3.61)$$

where $n_i = \sum_{a=1}^{\infty} n_i^a$ is the total number density of the i -mer and $g_{i,a}$ is the degeneracy of state a of an i -mer. A relaxation from an upper level a to a lower

level b of an N -mer changes the internal cluster energy E_i^{int} by

$$\frac{dE_i^{\text{int}}}{dt} \Big|_{ab} = -A_i^{ab}(E_i^a - E_i^b) \frac{n_i^a}{n_i}, \quad (3.62)$$

where $A_{i,ab}$ [s⁻¹] is the Einstein coefficient. The internal temperature change is then given as the sum over all changes in energy levels:

$$\begin{aligned} \frac{dT_i^{\text{int}}}{dt} &= \sum_{a=2}^{\infty} \sum_{b=1}^{a-1} \frac{dT_i^{\text{int}}}{dE_i^{\text{int}}} \frac{dE_i^{\text{int}}}{dt} \Big|_{ab} \\ &= \frac{-2}{kD_i^f} \sum_{a=2}^{\infty} \sum_{b=1}^{a-1} A_i^{ab}(E_i^a - E_i^b) \frac{n_i^a}{n_i} \\ &= \frac{-2}{kD_i^f} \frac{n_i^G}{n_i} \sum_{a=2}^{\infty} \sum_{b=1}^{a-1} A_i^{ab}(E_i^a - E_i^b) \frac{g_{i,a}}{g_{i,G}} \exp\left(\frac{-(E_i^a - E_i^G)}{kT_i^{\text{int}}}\right). \end{aligned} \quad (3.63)$$

The investigation of spontaneous and stimulated radiative emissions of clusters, that is to say their Einstein coefficients, is challenging. Previous studies used strong assumptions to approximate the thermal non-equilibrium caused by radiative processes (Nuth & Donn 1981; Nuth & Ferguson 2006). Recently, a more detailed investigation was done by Plane & Robertson (2022). They calculated the Einstein coefficients of the potentially dust-forming silicate OSi(OH)₂ at the B3LYP/6-311+g(2d,p) level of theory assuming that harmonic vibrations and Einstein coefficients remain constant in each of the vibration modes. They found that for gas densities below 10¹² cm⁻³ at $T_{\text{gas}} = 1583$ K, the vibrational (internal) non-equilibrium can reach as large as $T_{\text{gas}} - T_{\text{OSi(OH)}_2}^{\text{vib}} \approx 900$ K. The corresponding dissociation rate is reduced by several orders of magnitude. We note, however, that clusters can show significant anharmonic vibrations and temperature dependencies which further complicate the exact descriptions of radiative emissions (Guiu et al. 2021). Owing to these complications we do not explicitly derive master equations in internal non-equilibrium, but account for its effect by adopting different internal cluster temperatures.

3.4 Kinetic nucleation in thermal non-equilibrium

To test our equations in thermal equilibrium, a comparison to the work of Lee et al. (2015) and Boulanger et al. (2019b) is presented in Section 3.4.1. In Section 3.4.2, different temperature non-equilibria and their impact on

kinetic cluster nucleation are analysed. In Section 3.4.3, we compare the effect of thermal non-equilibrium with thermal equilibrium on the cluster number densities.

3.4.1 Kinetic nucleation in thermal equilibrium

First we compare our model to that of Boulangier et al. (2019b). Similar to their analysis, we use $(\text{TiO}_2)_N$ clusters up to a size of $N = 10$ and evolve the chemical network for a period of $t = 1$ yr. Instead of number densities, they used mass densities of the total gas, which is related to the gas number densities by the mean molecular weight. Furthermore, they assumed in their closed nucleation model that all Ti is bound in TiO_2 . To reproduce their results, we calculated the initial TiO_2 number density using the molecular weight of Ti ($m_{\text{Ti}} = 47,867 \text{ u} \approx 8 \times 10^{-23} \text{ g}$) and the Ti mass fraction ($\chi_{\text{Ti}} = 2.84 \times 10^{-6}$). We assume thermal equilibrium between the gas and all clusters ($T = T_{\text{gas}} = T_i^{\text{int}} = T_i^{\text{kin}}$ for all cluster sizes i). Using this conversion⁷, we calculated the relative $(\text{TiO}_2)_{10}$ abundance, defined as

$$\xi_{(\text{TiO}_2)_{10}} = \frac{n_{(\text{TiO}_2)_{10}}}{\sum_{i=1}^{10} n_{(\text{TiO}_2)_i}}, \quad (3.64)$$

after 10^5 seconds for a temperature range of 500 K to 3000 K and a number density range of roughly $5.08 \times 10^3 \text{ cm}^{-3}$ to $5.08 \times 10^7 \text{ cm}^{-3}$ (values taken from Boulangier et al. (2019b)). Our result can be seen in the top panel of Fig. 3.1. Overall, our $(\text{TiO}_2)_{10}$ abundances match the results from Boulangier et al. (2019b) which was expected because both use the same underlying assumptions and the same setup for the nucleation network.

Next, we compare our network to the nucleation model of Lee et al. (2015). In their study, the nucleation rate is calculated for homo-molecular monomer nucleation. They consider clusters of sizes up to $(\text{TiO}_2)_{10}$. Since our work also uses polymer nucleation, we calculate the nucleation rate by instantly dissociating⁸ all $(\text{TiO}_2)_{10}$ clusters into ten monomers ($10 \times \text{TiO}_2$). This leads to a constant nucleation flux. Our results are shown in the bottom of Fig. 3.1. Above 600 K, our nucleation network (Eq. 3.1) produces comparable nucleation rates as the non-classical nucleation rate of Lee et al. (2015). Below 600 K, they found a steep decrease in the nucleation rate which is not reproduced by our model showing a constant rate of roughly $J = 1 \times 10^6 \text{ s}^{-1} \text{ cm}^{-1}$. Comparing the results of Lee et al. (2015) with Boulangier et al. (2019b) shows that both predict a lack of $(\text{TiO}_2)_{10}$ for homo-molecular monomer nucleation. Polymer

⁷The conversion is given by $n_{\text{TiO}_2} = \rho_{\text{gas}} \chi_{\text{Ti}} / m_{\text{Ti}} \approx 3.6 \times 10^{20} \text{ g}^{-1} \rho_{\text{gas}}$.

⁸This process is also known as a Maxwell-Demon.

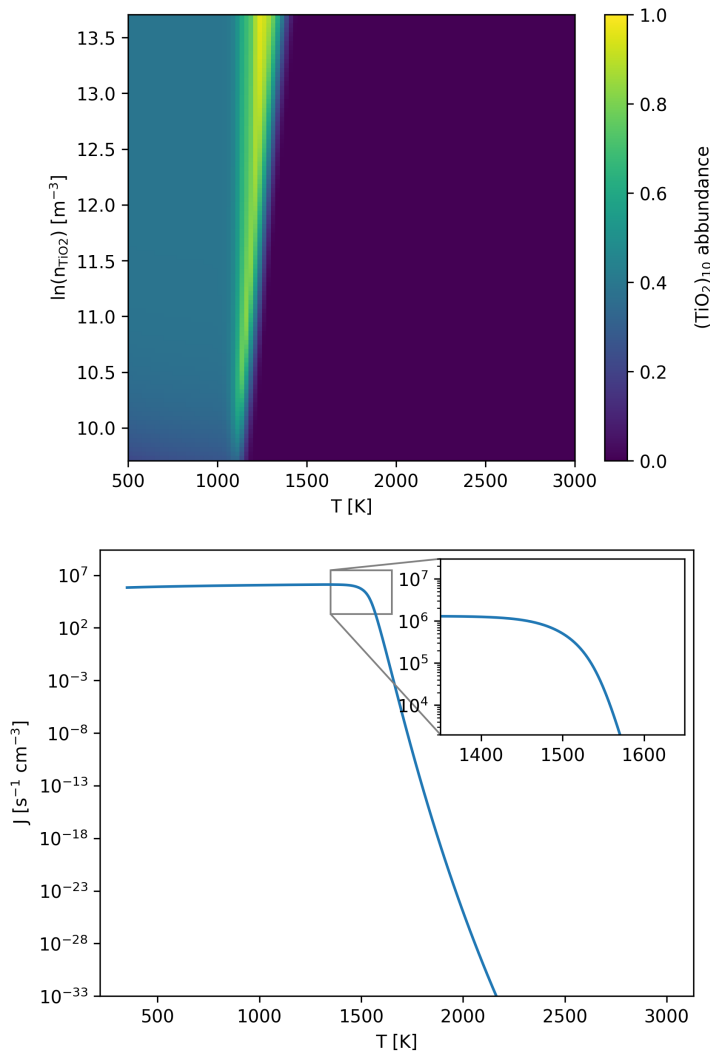


Figure 3.1: Comparison to previous studies. **Top:** $(\text{TiO}_2)_{10}$ abundance after 1 year with respect to the total number density of all clusters $\sum_{i=1}^{10} n_{(\text{TiO}_2)_i}$. This graph was made to be compared with the results of Boulanger et al. (2019b). **Bottom:** Nucleation rate of TiO_2 . The simulation was conducted for an initial uniform cluster number density of $n_{(\text{TiO}_2)_N} = 10^9$ cm⁻³ and evaluated after $t = 10^5$ s. This graph was made to be compared with the results of Lee et al. (2015).

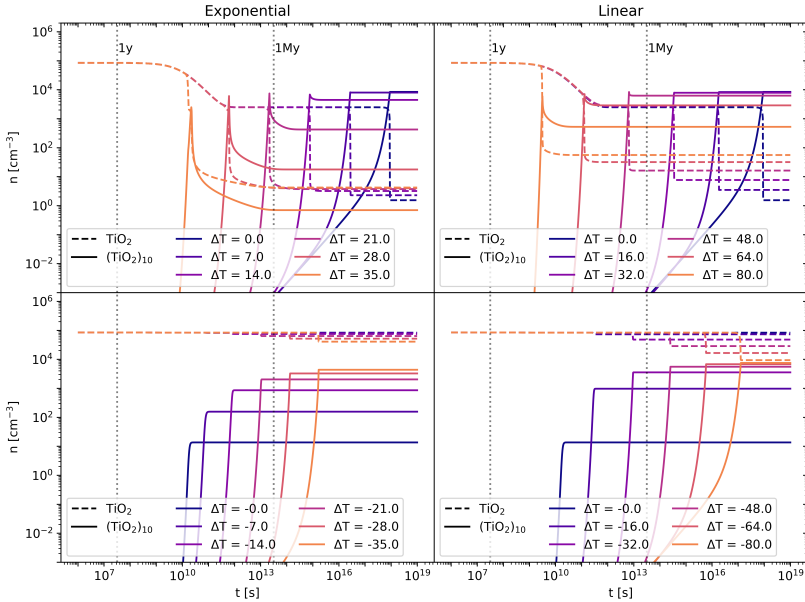


Figure 3.2: $(\text{TiO}_2)_N$ cluster number densities as a function of time under kinetic-to-gas thermal offsets ($T_N^{\text{kin}} = T_N^{\text{int}} \neq T_{\text{gas}}$). The initial TiO_2 number density is $n_{\text{TiO}_2} = 10^4 \text{ cm}^{-3}$ in a H_2 gas in thermal equilibrium. **Top left:** Exponential temperature offsets (see Eq. 3.69) at $T_{\text{gas}} = 1000 \text{ K}$. **Bottom left:** Exponential temperature offsets at $T_{\text{gas}} = 1250 \text{ K}$. **Top right:** Linear temperature offsets (see Eq. 3.70) at $T_{\text{gas}} = 1000 \text{ K}$. **Bottom right:** Linear temperature offsets at $T_{\text{gas}} = 1250 \text{ K}$.

nucleation, on the other hand (as implemented in our network and the one from Boulanger et al. (2019b)), showed non-negligible $(\text{TiO}_2)_{10}$ abundances below 1000 K.

3.4.2 Effect of thermal non-equilibrium

Thermal non-equilibrium affects the kinetic nucleation network in two ways: firstly, via the relative velocity distribution $f_r(\nu_r)$. If the velocity distribution of the colliding cluster is a Maxwell-Boltzmann distribution, the temperature dependence is given within the TCM-reduced mass μ_T . In the general case, the velocity distribution can depend on the type of non-equilibrium present. For this section, we assume the velocity distribution of all clusters to be a Maxwell-

Boltzmann distribution. Secondly, the backward rates (Eq. 3.43) depend on the kinetic and internal temperatures of the clusters. The dependencies can be divided as follows:

$$k^- = k^+ \frac{p^\ominus}{kT_{\text{gas}}} A B C, \quad (3.65)$$

$$A = \exp \left(\sum_{i \in \zeta} \frac{\delta(i)}{kT_i^{\text{kin}}} \left[\mu_i^\ominus(T_{\text{gas}}) - i\mu_1^\ominus(T_i^{\text{kin}}) + k(T_i^{\text{kin}} - T_{\text{gas}}) \right] \right), \quad (3.66)$$

$$B = \exp \left(\sum_{i \in \zeta} \frac{\delta(i)}{kT_i^{\text{kin}}} \omega_i(T_i^{\text{kin}}, T_i^{\text{int}}) \right), \quad (3.67)$$

$$C = \left(\frac{kT_{\text{gas}} \dot{n}_{\text{TiO}_2}}{p^\ominus} \right)^{-\sum_{i \in \zeta} \delta(i) i \frac{T_{\text{gas}}}{T_i^{\text{kin}}}}, \quad (3.68)$$

where A is the correction term due to kinetic-to-gas thermal non-equilibrium, B the correction term due to kinetic-to-internal thermal non-equilibrium, and C the correction due to the Lagrangian multiplier.

The correction term C depends on the equilibrium number density of the monomer \dot{n}_{TiO_2} , which in turn depends on the reaction rates. To decouple this dependency, we start by assuming $C = 1$. Afterwards, we calculate the maximum offset to check if this assumption holds. The correction term A only depends on the difference between kinetic temperature and gas temperature. If the clusters are in kinetic-to-gas thermal equilibrium ($T_N^{\text{kin}} = T_{\text{gas}}$), A becomes the exponent of the backward reaction rate for thermal equilibrium (as in e.g. Boulangier et al. (2019b)). The correction term B does not depend on the temperature of the gas phase, but rather on the thermal difference between internal and kinetic temperature. As long as N-mers are in kinetic-to-internal thermal equilibrium ($T_N^{\text{kin}} = T_N^{\text{int}}$), the correction term B is equal to 1.

In this section we assume kinetic-to-internal thermal equilibrium for all clusters to study thermal non-equilibrium between gas phase and dust. This assumption is similar to the thermal non-equilibrium considered in the model of Patzer et al. (1998), Helling & Woitke (2006), and Köhn et al. (2021). Our TiO_2 reference case therefore allows for the importance of thermal non-equilibrium for their models to be estimated. Studying the effect kinetic-to-internal non-equilibrium, similar to Plane & Robertson (2022), would also be interesting. Unfortunately, this requires evaluating the Gibbs free energy of clusters in kinetic-to-internal non-equilibrium which is outside of the scope of this chapter and will be dealt with in a separate study.

To investigate the effect of the correction terms A , we use four different simulations. We assume kinetic-to-internal thermal equilibrium ($T_N^{\text{int}} = T_N^{\text{kin}} \neq T_{\text{gas}}$) and use two temperature structures each:

$$\text{Exponential:} \quad T_N^{\text{kin}} = T_{\text{gas}} + \frac{e^{N-1} - 1}{e^9 - 1} \Delta T, \quad (3.69)$$

$$\text{Linear:} \quad T_N^{\text{kin}} = T_{\text{gas}} + \frac{(N-1)}{9} \Delta T, \quad (3.70)$$

where ΔT is a free parameter quantifying the kinetic thermal non-equilibrium between the monomer ($n=1$) and the decamer ($n=10$). The definitions were chosen so that $\Delta T = T_{(\text{TiO}_2)_{10}}^{\text{kin}} - T_{\text{TiO}_2}^{\text{kin}}$ holds in all cases. Both offsets are toy models to show the effect of different offsets on the resulting number densities.

The simulations use TiO_2 as nucleating species with an initial monomer density $n_{\text{TiO}_2} = 10^4 \text{ cm}^{-3}$ in a H_2 gas with a density of $n_{\text{gas}} = 10^{12} \text{ cm}^{-3}$ at $T_{\text{gas}} = 1000 \text{ K}$. Clusters of size $N \leq 4$ are considered to associate and disassociate via an additional collision partner M. We used temperature offsets in the range of $0 \text{ K} \leq \Delta T \leq 35 \text{ K}$ for the exponential offset (top-left panel of Fig. 3.2) and $0 \text{ K} \leq \Delta T \leq 80 \text{ K}$ for the linear offset (top-right panel of Fig. 3.2). The simulations show a decrease in $(\text{TiO}_2)_{10}$ number density with increased temperature offsets. This decrease is stronger for the exponential offset than for the linear offset. Therefore, not only does the general temperature increase, but the type of non-equilibrium also affects the resulting number densities. For $T_{\text{gas}}=1000 \text{ K}$, $(\text{TiO}_2)_{10}$ does not represent the most abundant cluster in all cases. As such, $(\text{TiO}_2)_8$ becomes the most abundant cluster size for exponential offsets of $\Delta T = 21 \text{ K}$ and for linear offsets of $\Delta T = 80 \text{ K}$. The peaks and declines in $(\text{TiO}_2)_{10}$ number density for increased thermal offsets are caused by the initially efficient growth reactions due to the high abundance of small cluster and the enhanced dissociation rate, respectively. A similar overshoot can be seen in Köhn et al. (2021) who analysed different evaporation efficiencies for TiO_2 nucleation.

We also considered the reverse temperature offset for both simulations. For this, we repeated the simulation with $T_{\text{gas}} = 1250 \text{ K}$ where, in thermal equilibrium, the $(\text{TiO}_2)_{10}$ number density is significantly lower than at $T_{\text{gas}} = 1000 \text{ K}$. The results for exponential offsets can be seen in the bottom-left panel of Fig. 3.2. The results for linear offsets can be seen in the bottom-right panel of Fig. 3.2. In both simulations, the $(\text{TiO}_2)_{10}$ number density increases with decreased kinetic temperatures. Overall, we find that for TiO_2 around 1000 to 1250 K lower kinetic temperatures favour nucleation and higher kinetic temperatures hamper nucleation.

To evaluate the assumption that $C \approx 1$, we compare C to the uncertainty factors F_k of the reaction rates (Baulch et al. 1992; Dobrijevic & Parisot 1998). The upper and lower limit for C throughout all simulations are $0.962 < C \leq 1.0$, which corresponds to a correction factor of $F_C = 1.04$. Typical uncertainty factors of hydrocarbon reactions at $T_{\text{gas}} < 300$ K exceed 1.5. (Dobrijevic & Parisot 1998; Dobrijevic et al. 2003; Hébrard et al. 2006). Hébrard et al. (2015) extrapolate the uncertainty factor to temperatures up to 1000 K and estimate that the uncertainty factors exceed 1.26 for bi-molecular reactions. Therefore, the assumption of $C \approx 1$ is justified.

In all simulations, thermal non-equilibrium can change the $(\text{TiO}_2)_{10}$ number density by several orders of magnitude. The exact change in the abundance of the largest cluster depends on the gas temperature T_{gas} , the clustering species, the cluster number densities n_N , and the type of thermal non-equilibrium present.

3.4.3 Thermal equilibrium versus non-equilibrium

In Section 3.4.2, we have shown that positive cluster temperature offsets can lead to lower $(\text{TiO}_2)_{10}$ number densities and negative cluster temperature offsets can lead to higher $(\text{TiO}_2)_{10}$ number densities. Since this behaviour is also expected for thermal equilibrium, we compare the change in $(\text{TiO}_2)_{10}$ number density for thermal equilibrium to thermal non-equilibrium. We choose an H_2 gas with a density of $n_{\text{gas}} = 10^{12} \text{ cm}^{-3}$, an initial TiO_2 monomer density $n_{\text{TiO}_2} = 10^4 \text{ cm}^{-3}$, and assume exponential temperature offsets (see Eq. 3.69).

The first simulation is done in thermal non-equilibrium using a gas temperature of $T_{\text{gas}} = 1000$ K and a temperature offset⁹ of $\Delta T = 35$ K for the clusters (see Section 3.4.2). The second simulation is done assuming thermal equilibrium ($\Delta T = 0$ K) at $T_{\text{gas}} = T_N^{\text{kin}} = T_N^{\text{int}} = 1035$ K. The results can be seen in Fig. 3.3.

Even though the $(\text{TiO}_2)_{10}$ clusters are at the same temperature, the $(\text{TiO}_2)_{10}$ number densities are 4 orders of magnitude smaller if thermal non-equilibrium is present. We tested additional gas temperatures assuming thermal equilibrium and found that to reach a similar $(\text{TiO}_2)_{10}$ number density as in the thermal non-equilibrium case, the gas temperature has to be around $T_{\text{gas}} = T_N^{\text{kin}} = T_N^{\text{int}} = 1258$ K.

⁹ $\Delta T = 35$ K was chosen because it showed a clear impact on the $(\text{TiO}_2)_{10}$ number density.

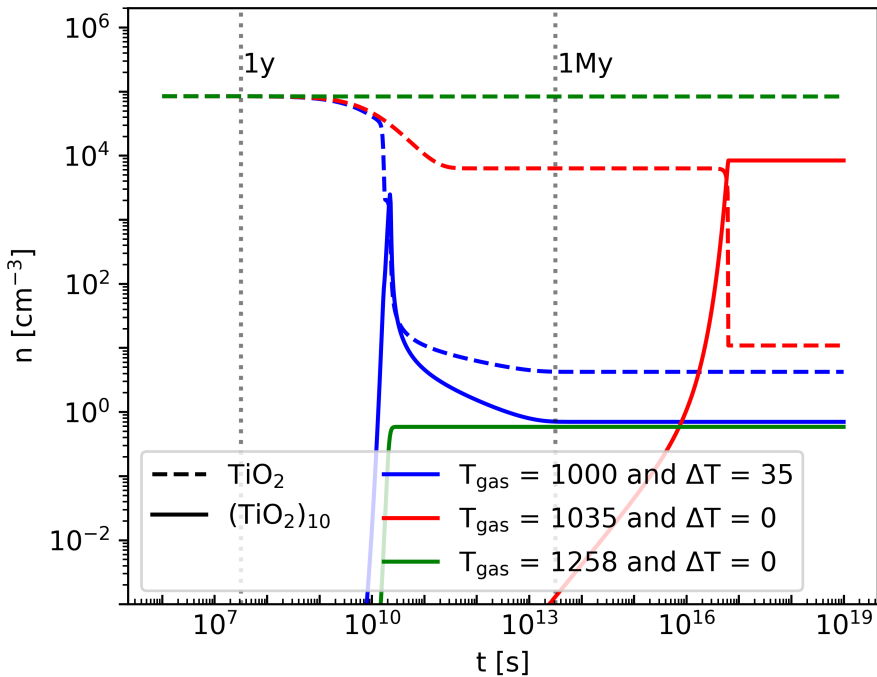


Figure 3.3: Comparison of TiO_2 and $(\text{TiO}_2)_{10}$ number densities under thermal equilibrium ($\Delta T = 0 \text{ K}$) and kinetic-to-gas thermal non-equilibrium ($\Delta T \neq 0 \text{ K}$) conditions.

3.5 Conclusion

We developed a kinetic nucleation model describing cluster formation and destruction in thermal non-equilibrium using non-identical temperatures for the clusters and the gas. This model does not rely on assumptions made by previous studies of thermal non-equilibrium nucleation frameworks. Our model includes realistic termolecular association and collisional dissociations for the smallest cluster sizes. To derive a dissociation rate in thermal non-equilibrium, we make use of the law of mass action, the principle of detailed balance, and the minimization of the Gibbs free energy in a general form accounting for non-equilibrium effects. All particles, which are not part of the nucleation process, are assumed to be in thermal equilibrium at the temperature T_{gas} . Clusters are described by a kinetic (transitional) temperature T_N^{kin} and an internal temperature T_N^{int} . All temperatures can differ from each other.

Thermal non-equilibrium can affect the synthesis of larger TiO₂ clusters. Lower cluster temperatures lead to an increased abundance of larger clusters. This relation was already predicted by previous studies and our simulations confirm and quantify the impact of thermal non-equilibrium on cluster formation. For TiO₂ at $n_{\text{TiO}_2} = 10^4 \text{ cm}^{-3}$ in a H₂ gas at $n_{\text{H}_2} = 10^{12} \text{ cm}^{-3}$ and $T_{\text{gas}} = 1000 \text{ K}$, we found that the number density of (TiO₂)₁₀ can decrease over an order of magnitude for kinetic-to-gas temperature offsets with $(T_{(\text{TiO}_2)_{10}}^{\text{kin}} - T_{\text{gas}}) \leq 21 \text{ K}$. For a higher gas temperature of $T_{\text{gas}} = 1250 \text{ K}$, we found over an order of magnitude increase in the (TiO₂)₁₀ number density for kinetic-to-gas temperature offsets of $(T_{(\text{TiO}_2)_{10}}^{\text{kin}} - T_{\text{gas}}) \leq -14 \text{ K}$.

In environments where thermal non-equilibrium is already observed or suspected, such as the outflows of AGB stars, it is crucial to consider the effect of thermal non-equilibrium on kinetic nucleation. Already small temperature offsets within clustering species can cause significant changes in the abundance of larger clusters. The model derived in this work can be used to add thermal non-equilibrium considerations to chemical (kinetic) networks.

Acknowledgments

The authors thank Julian Lang for his contribution and help to this work. S.K., L.D and C.H. acknowledges funding from the European Union H2020-MSCA-ITN-2019 under grant agreement no. 860470 (CHAMELEON). L.D and D.G. acknowledges support from the ERC consolidator grant 646758 AEROSOL. D.G. acknowledges support from the project grant “The Origin and Fate of Dust in the Universe” from the Knut and Alice Wallenberg foundation.

Chapter 4

Cloud Formation from a Non-Equilibrium Gas-Phase

This chapter is based on the publication:

Fully time-dependent cloud formation from a non-equilibrium gas-phase in exoplanetary atmospheres

Sven Kiefer, Helena Lecoq-Molinos, Christiane Helling, Nidhi Bangera, and Leen Decin

Astronomy & Astrophysics, Volume 682, February 2024, A150

Author contribution:

Sven Kiefer derived the equations, performed the simulations and analyses, and wrote the manuscript. Helena Lecoq-Molinos implemented the equilibrium chemistry calculations. Nidhi Bangera helped with the analysis of the SiO-SiO₂ cycle. Christiane Helling and Leen Decin contributed via discussions and advice.

Original abstract:

Recent observations suggest the presence of clouds in exoplanet atmospheres, but they have also shown that certain chemical species in the upper atmosphere might not be in chemical equilibrium. Present and future interpretation of data from, for example, CHEOPS, JWST, PLATO, and Ariel require a combined understanding of the gas-phase and the cloud chemistry. The goal of this work is to calculate the two main cloud formation processes, nucleation, and bulk growth consistently from a non-equilibrium gas phase. The aim is also to explore the interaction between a kinetic gas-phase and cloud microphysics. The cloud formation is modelled using the moment method and kinetic nucleation, which are coupled to a gas-phase kinetic rate network. Specifically, the formation of cloud condensation nuclei is derived from cluster rates that include the thermochemical data of $(\text{TiO}_2)_N$ from $N = 1$ to 15. The surface growth of nine bulk Al, Fe, Mg, O, Si, S, and Ti binding materials considers the respective gas-phase species through condensation and surface reactions as derived from kinetic disequilibrium. The effect of the completeness of rate networks and the time evolution of the cloud particle formation is studied for an example exoplanet, HD 209458 b. A consistent, fully time-dependent cloud formation model in chemical disequilibrium with respect to nucleation, bulk growth, and the gas-phase is presented and first test cases are studied. This model shows that cloud formation in exoplanet atmospheres is a fast process. This confirms previous findings that the formation of cloud particles is a local process. Tests on selected locations within the atmosphere of the gas-giant HD 209458 b show that the cloud particle number density and volume reach constant values within 1s. The complex kinetic polymer nucleation of TiO_2 confirms results from classical nucleation models. The surface reactions of $\text{SiO}[\text{s}]$ and $\text{SiO}_2[\text{s}]$ can create a catalytic cycle that dissociates H_2 to 2 H, resulting in a reduction of the CH_4 number densities.

4.1 Introduction

Clouds and dust are present in many astrophysical environments. In stellar environments, dust can be found in the outflows of asymptotic giant branch (AGB) stars (e.g. Gail et al. 1984; Fleischer et al. 1999; Ferrarotti & Gail 2006; Höfner 2009; Gobrecht et al. 2016; Khouri et al. 2016; Decin et al. 2017) and Wolf-Rayet (WR) stars (Williams et al. 1987; Crowther 2003; Lau et al. 2022). It can also be found in supernovae (Tinayanont et al. 2019; Niculescu-Duvaz et al. 2022; Zhang et al. 2022). Dust produced in these environments replenishes the interstellar medium (ISM) through radiation-driven mass loss. In cooler objects, clouds are predicted within brown dwarfs (Allard et al. 2001; Ackerman & Marley 2001; Helling et al. 2004), and indirect evidence of clouds in brown dwarfs has been found (Maire et al. 2020; Ward-Duong et al. 2020; Kammerer et al. 2021). Exoplanet atmospheres are also expected to have a strong cloud presence (Helling et al. 2023). Cloud particles typically have large opacities, which lead to characteristically flat spectra in the optical and near infrared. Furthermore, several exoplanet observations in these wavelength ranges show a flat spectrum (Bean et al. 2010; Kreidberg et al. 2014; Espinoza et al. 2019; Spyros et al. 2021; Libby-Roberts et al. 2022). To understand cloud formation, one also needs to understand gas-phase chemistry and the nucleation process. In AGB stars, many chemical species have been detected (e.g. AlF, MgNC, NaCN, CO, SiO, HCN, CS, PAHs; Highberger et al. 2001; Decin et al. 2008; Smolders et al. 2010). For exoplanets, recent medium- and high-resolution observations detected the presence of several atomic (e.g. Mg, Na, Ca, Cr, Fe, Ni, V, Ti, Mn, O; Hoeijmakers et al. 2018a, 2020; Prinot et al. 2022; Borsa et al. 2022) and molecular species (e.g. CO, H₂O, CH₄, NH₃, C₂H₂; Kok et al. 2013; Hoeijmakers et al. 2018b; Guilluy et al. 2022; Guillot et al. 2022), pointing to a chemically rich environment.

In collisionally dominated environments, the gas-phase can be modelled using chemical equilibrium models (Stock et al. 2018; Woitke & Helling 2021). This is a good assumption for the deep atmosphere of exoplanets and brown dwarfs (Venot et al. 2018) where the collisional timescales become small. In low-density environments, such as the outflow of AGB stars (Plane & Robertson 2022; Sande & Millar 2019) and the upper atmospheres of exoplanets (Rimmer & Helling 2013; Baxter et al. 2021; Tsai et al. 2023; Mendonça et al. 2018) and brown dwarfs (Helling & Rimmer 2019; Lee et al. 2020a), collisional timescales become large. In these environments, chemical disequilibrium processes such as radiation or quenching can drive the gas-phase abundances out of equilibrium.

The formation of clouds and dust starts with the formation of cloud condensation nuclei (CCNs). In gaseous exoplanets, CCNs cannot originate from the planet's surface as they do in terrestrial planets; they have to be formed directly

from the gas phase through nucleation, which marks the transition from gas-phase chemistry to solid-phase chemistry. Classical nucleation theory (CNT) or modified classical nucleation theory (MCNT) is an often-used approach to describe the rate at which CCNs are formed (nucleation rate). In order to describe the actual formation of clusters leading up to CCNs, a kinetic description can be used. (Patzer et al. 1998; Lee et al. 2015; Bromley et al. 2016; Boulanger et al. 2019b; Köhn et al. 2021; Gobrecht et al. 2022). To calculate kinetic nucleation, the thermodynamic properties of clusters of the nucleating species have to be known. There are active efforts to derive the structures and properties of species that are associated with nucleation processes (Chang et al. 2005, 2013; Patzer et al. 2014; Lee et al. 2015; Gobrecht et al. 2022; Sindel et al. 2022; Andersson et al. 2023). Even in the cases where data are available, this is often limited to the smallest cluster sizes because calculating the required properties becomes more computationally intensive for larger clusters (Sindel et al. 2022).

Supersaturated species can grow onto CCNs once they are present. There are two main ways these bulk growth processes can occur. First there is condensation, which describes the deposition of gas-phase species onto CCNs (e.g. $\text{SiO} \rightarrow \text{SiO[s]}$). Many models use condensation curves to determine where clouds can form (e.g. Demory et al. 2013; Webber et al. 2015; Crossfield 2015; Kempton et al. 2017; Roman & Rauscher 2017; Roman et al. 2021). Second, bulk growth can occur through kinetic surface reactions (Patzer et al. 1998; Helling & Woitke 2006; Helling & Fomins 2013). In contrast to condensation, surface reactions include multiple chemical species to form the bulk material (e.g. $\text{SiS} + \text{H}_2\text{O} \rightarrow \text{SiO[s]} + \text{H}_2\text{S}$). In addition to providing additional bulk growth paths for condensing species, surface reactions also allow the bulk growth of materials that may not be stable in the gas phase themselves. Both processes can be described kinetically (Patzer et al. 1998).

In this chapter, we present a fully time-dependent description of the processes that lead to the formation of clouds in exoplanets or dust in brown dwarfs, stars, and supernovae. We advanced the nucleation description by modelling potential chemical pathways based on thermodynamic cluster properties and expand the kinetic description of surface reactions to chemical disequilibrium. With this model, we studied the timescales of cloud formation in exoplanet atmospheres. The description of the chemical network, kinetic nucleation and bulk growth is given in Sect. 4.2. The kinetic chemistry and kinetic nucleation are investigated in Sect. 4.3. The fully kinetic cloud formation model is then applied to temperature-pressure ($T_{\text{gas}}-p_{\text{gas}}$) points within the atmosphere of HD 209458 b (Sect. 4.4). Lastly, the summary is given in Sect. 4.5.

4.2 Model

We present the models for the gas phase, kinetic nucleation, and bulk growth through condensation and surface reactions. In Sect. 4.2.1, we describe our chemical kinetics network of the gas phase. The kinetic nucleation, which describes the time-dependent nucleation within disequilibrium environments, is described in Sect. 4.2.2 (two-body reactions) and in Sect. 4.2.3 (three-body reactions). In Sect. 4.2.4, we describe the bulk growth through condensation and surface reactions. The derivation of the reaction supersaturation is given in Sect. 4.2.5. Finally, the connection between nucleation and bulk growth is described in Sect. 4.2.6.

4.2.1 Gas-phase chemistry

The evolution of the number density n_i [cm⁻³] of a given species i is determined by the following equation:

$$\frac{dn_i}{dt} = \sum_{r \in F_i} \left(\nu_{i,r} k_r \prod_{j \in E_r} n_j \right) - \sum_{r \in D_i} \left(\nu_{i,r} k_r \prod_{j \in E_r} n_j \right), \quad (4.1)$$

where F_i is the set of reactions where the i -th species is a product, D_i is the set of reactions where the i -th species is a reactant, E_r is the set of reactants of reaction r , n_j [cm⁻³] is the number densities of the reactants, $\nu_{i,r}$ is the stoichiometric coefficient of the i -th species within reaction r , k_r [cm^{3(J_r-1)}s⁻¹] is the reaction rate for the reaction r , and J_r is the number of reactants in E_r . The sum over all n_j is the total number density. The numerical solver is described in Appendix B.1.

Chemical kinetic networks for the atmospheres of exoplanets include several hundred species and several thousand reactions (e.g. Rimmer & Helling 2016; Tsai et al. 2017, 2021; Venot et al. 2012, 2020). For this chapter, we chose the NCHO thermo network of VULCAN¹ (Tsai et al. 2017, 2021). This network includes 69 species and 780 reactions. In this work, TiO₂ is considered as the nucleation species. Because NCHO thermo network of VULCAN does not include reactions for the formation of TiO₂, we added several reactions from Boulanger et al. (2019b) leading to the formation of TiO₂. The selected gas-phase reactions can be found in Table B.1. Furthermore, we added reactions including Si species for the bulk growth species SiO and SiO₂ (see Sect. 4.2.4 and Table B.1).

¹A comparison to the chemical kinetics networks of Decin et al. (2018) and Gobrecht et al. (2022) can be found in Appendix B.4.

All calculations start from chemical equilibrium abundances calculated using GGchem (Woitke & Helling 2021) for a solar-like composition (Asplund et al. 2009). A list of the considered species for the equilibrium calculation is given in Appendix B.2.

4.2.2 Nucleation

Nucleation reaction networks are ideally constructed by considering multiple reaction pathways. Unfortunately, few such studies exist (see e.g. Bromley et al. 2016; Gobrecht et al. 2022; Andersson et al. 2023). In the kinetic network approach, the change in cluster number densities can be described as

$$\frac{dn_N}{dt} = \sum_{r \in F_N} \left(\nu_{N,r} k_r^+ \prod_{j \in E_r} n_j \right) - \sum_{r \in D_N} \left(\nu_{N,r} k_r^- \prod_{j \in E_r} n_j \right), \quad (4.2)$$

where n_N [cm⁻³] is the number density of a given polymer of size N (also called N-mer), F_N is the set of forward reactions involving the N-mer, D_N is the set of backward reactions involving the N-mer, k_r^+ [cm^{3(J_r-1)}s⁻¹] is the forward reaction rate coefficient of reaction r , k_r^- [cm^{3(J_r-1)}s⁻¹] is the backward reaction rate coefficient of reaction r , and J_r is the number of reactants.

We describe the growth reactions of nucleating species as two-body reactions ($a + b \rightarrow c$). The forward reaction rate coefficient k_r^+ can then be described as follows (Peters 2017; Boulangier et al. 2019b):

$$k_r^+ = \int_0^\infty \alpha_r(v_r) \sigma_r(v_r) v_r f(v_r) dv_r, \quad (4.3)$$

where v_r [cm s⁻¹] is the relative velocity of the collision partners, $\alpha_r(v_r)$ is the sticking coefficient, $\sigma_r(v_r)$ [cm²] is the reaction cross-section, and $f(v_r)$ is the relative velocity distribution of the colliding particles. Similarly to other work, we set the sticking coefficient $\alpha_j(\nu_r)$ to 1 because detailed values for nucleation reactions are not yet available (e.g. Lazzati 2008; Bromley et al. 2016; Boulangier et al. 2019b). The cross-section is approximated by a collision of two hard spheres:

$$\sigma_j = \pi(r_1 + r_2)^2, \quad (4.4)$$

where r_1 and r_2 [cm] are the interaction radii of the reaction partners. For this work, we considered radii including electrostatic forces (Köhn et al. 2021; Gobrecht et al. 2022; Kiefer et al. 2023). The relative velocity distribution is

described by a Maxwell-Boltzmann distribution:

$$f(\nu_r) = \left(\frac{\mu}{2\pi k_B T_{\text{gas}}} \right)^{3/2} 4\pi\nu_r^2 \exp \left(-\frac{\mu\nu_r^2}{2k_B T} \right), \quad (4.5)$$

where T_{gas} [K] is the temperature, $k_B = 1.381 \times 10^{-23}$ erg K⁻¹ is the Boltzmann constant, and

$$\mu = \frac{m_1 m_2}{(m_1 + m_2)} \quad (4.6)$$

is the reduced mass [g] with m_1 ; m_2 [g] being the masses of the reaction partners. Solving the integral from Eq. 4.3 yields:

$$k_j^+ = \pi(r_1 + r_2)^2 \sqrt{\frac{8k_B T_{\text{gas}}}{\pi\mu}}. \quad (4.7)$$

The backwards reaction rate ($c \rightarrow a + b$) is derived by assuming detailed balance. For this, an equilibrium state needs to be defined, which we assume to be the chemical equilibrium state such that the law of mass action can be applied:

$$k_j^- = k_j^+ \frac{p^\ominus}{k_B T_{\text{gas}}} \exp \left(\frac{G_c^\ominus(T_{\text{gas}}) - G_a^\ominus(T_{\text{gas}}) - G_b^\ominus(T_{\text{gas}})}{k_B T_{\text{gas}}} \right), \quad (4.8)$$

where $p^\ominus = 10^5$ Pa is the standard pressure and $G_i^\ominus(T_{\text{gas}})$ [erg] is the Gibbs free energy of an i -mer at standard pressure.

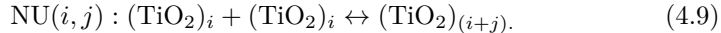
For this study, we considered TiO₂ as nucleating species. The chemical network is extended by including all forward (Eq. 4.3) and backward reactions (Eq. 4.8) from the monomer up to the 15-mer. The Gibbs free energy data is taken from Sindel et al. (2022).

4.2.3 Three-body reactions for cluster formation

Three-body reactions are important for the formation of small clusters. On the one hand, third bodies can remove the energy of formation from an association (forward) reaction, thus increasing cluster formation rates. On the other hand, collisions with third bodies can induce dissociation (backward) reactions. For this work, we considered three-body reactions for the cluster formation of TiO₂ up to (TiO₂)₄. The reaction rates are taken from Kiefer et al. (2023) (see reaction numbers RNr 19 to 26 in Table B.1).

To determine for which temperature and pressures three-body reactions dominate over two-body reactions, we compared the reaction rate coefficients.

To allow a direct comparison, we multiplied the reaction rate coefficients with the number density of third bodies (here assumed to be arbitrary gas-phase species). The comparison can be seen in Fig. 4.1. For reactions RNr 19 and 20, multiple pressures are shown. Since all three-body reactions have the same pressure dependence, the scaling is the same for all of them. For two-body reactions, we used the following shorthand notation:



For the association and dissociation of $(\text{TiO}_2)_2$ from and into two monomers, respectively (RNr 19/20 and NU(1, 1)), the three-body reaction becomes dominant below $T_{\text{gas}} = 400$ K and for pressures higher than $p_{\text{gas}} = 0.001$ bar. Above $T_{\text{gas}} = 1300$ K and for pressures lower than $p_{\text{gas}} = 10$ bar, the two-body reaction becomes dominant. In between, either type of reaction can be dominant. At higher pressures (e.g. $p_{\text{gas}} > 1000$ bar), the three-body reaction becomes dominant even at high temperatures (e.g. $T_{\text{gas}} > 2000$ K). For all other reactions compared in this section (RNr 21/22, 23/24, 25/26 and NU(2, 1), NU(2, 2), and NU(3, 1)), the two-body reaction typically dominates above $T_{\text{gas}} > 400$ K. Three-body reactions only start to become important at very high pressures (e.g. $p_{\text{gas}} > 1000$ bar).

4.2.4 Bulk growth

In order to describe the bulk growth by gas-surface reaction, we applied the moment method (Gail & Sedlmayr 1986, 1988; Dominik et al. 1993; Helling et al. 2001; Helling & Woitke 2006). The j -th moment L_j [$\text{cm}^J \text{ g}^{-1}$] is defined as

$$\rho L_j = \int_{V_l}^{\infty} f(V) V^{j/3} dV, \quad (4.10)$$

where $j \in \{0, 1, 2, 3\}$, V [cm^3] is the cloud particle volume, V_l [cm^3] is the minimum volume of a cloud particle to start bulk growth, ρ [cm^{-3}] is the gas density and $f(V)$ [cm^{-6}] is the cloud particle size distribution function. Using these moments the following cloud particle properties can be derived (Gail &

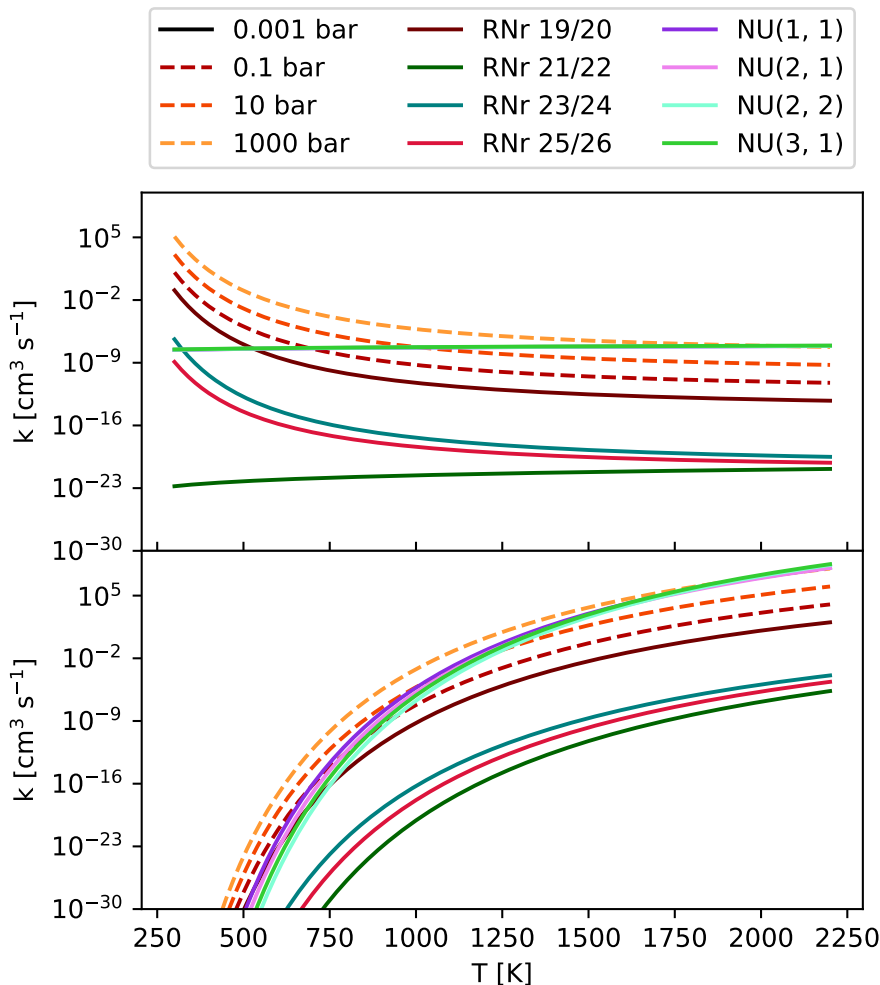


Figure 4.1: Reaction rate coefficients for formation of TiO₂ clusters up to (TiO₂)₄. All solid lines assume $p_{\text{gas}} = 0.002$ bar. **Top:** Association reactions. **Bottom:** Dissociation reactions.

Sedlmayr 1988; Helling et al. 2001):

$$n_d = \rho L_0, \quad (4.11)$$

$$\langle a \rangle = \sqrt[3]{\frac{3}{4\pi}} \frac{\rho L_1}{\rho L_0}, \quad (4.12)$$

$$\langle A \rangle = \sqrt[3]{36\pi} \frac{\rho L_2}{\rho L_0}, \quad (4.13)$$

$$\langle V \rangle = \frac{\rho L_3}{\rho L_0}, \quad (4.14)$$

where n_d [cm $^{-3}$] is the cloud particle number density, $\langle a \rangle$ [cm] the mean cloud particle radius, $\langle A \rangle$ [cm 2] the mean cloud particle surface area, and $\langle V \rangle$ [cm 3] the mean cloud particle volume. The change in the moments is determined by the nucleation and bulk growth and is described by the following set of equations² (Helling & Woitke 2006):

$$\frac{\partial}{\partial t} \rho L_0 = J_{\star}(V_l), \quad (4.15)$$

$$\frac{\partial}{\partial t} \rho L_j = V_l^{j/3} J_{\star}(V_l) + \frac{j}{3} \chi^{\text{net}} \rho L_{j-1}, \quad (4.16)$$

$$\chi^{\text{net}} = \sqrt[3]{36\pi} \sum_{r \in C_d} \Delta V_r n_r^{\text{key}} \langle v_r \rangle \frac{\alpha_r(v_r)}{\nu_r^{\text{key}}} \left(1 - \frac{1}{(S_r)^{1/\nu_r^{\text{key}}}} \frac{1}{b_r^{\text{surf}}} \right), \quad (4.17)$$

where $J_{\star}(V_l)$ [cm $^{-3}$] is the nucleation rate (see Sect. 4.2.6), C_d is the set of surface reactions, ΔV_r [cm 3] is the volume increase per surface reaction r , n_r^{key} [cm $^{-3}$] is the number density of the key gas-phase species, ν_r^{key} is the stoichiometric coefficient of the key gas-phase species for the surface reaction r , $\langle v_r \rangle$ [cm s $^{-1}$] is the average relative velocity between the cloud particle and the key gas-phase species, S_r is the reaction supersaturation (see Section 4.2.5), and b_r^{surf} is the surface area fraction of the given bulk growth material. χ^{net} [cm s $^{-1}$] is the net growth velocity. The key gas-phase species is the least abundant species involved in a given bulk growth reaction (Woitke & Helling 2003; Helling & Woitke 2006). The left term in the bracket of Eq. 4.17 represents the growth and the right term represents the evaporation. The cloud particle grows if the net sign of the bracket is positive and evaporates if it is negative. Similarly to Helling & Woitke (2006), we assume that the surface area fraction can be

²Gravitational settling and other transport processes may be added as source terms to the r.h.s. (Woitke & Helling 2003).

approximated by the following volume fraction:

$$b_r^{\text{surf}} = \frac{A_r}{A_{\text{tot}}} \approx \frac{V_r}{V_{\text{tot}}}, \quad (4.18)$$

where A_{tot} [cm²] is the total cloud particle surface area and V_{tot} [cm³] is the total cloud particle volume. The volume fraction of each cloud particle material is tracked separately.

The growth of cloud particles through bulk growth depletes the gas-phase. Therefore, we adjust the number densities n_i of the species i involved in the surface reaction r (Helling & Woitke 2006):

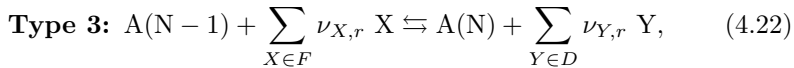
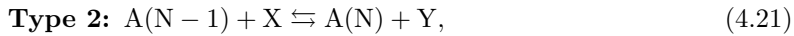
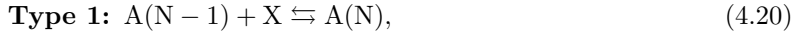
$$\frac{dn_i}{dt} = \delta(i) \nu_{i,r} \frac{\chi^{\text{net}}}{\Delta V_r} \rho L_2, \quad (4.19)$$

where $\delta(i)$ is equal to 1 for products and -1 for reactants.

For this study, we considered TiO₂[s], Al₂O₃[s], SiO[s], SiO₂[s], MgO[s], Mg₂SiO₄[s], FeO[s], FeS[s], Fe₂O₃[s], and Fe₂SiO₄[s] as bulk growth materials and include the surface reactions listed in Table B.4.

4.2.5 Reaction supersaturation

To calculate the net growth velocity as described in Eq. 4.17, the reaction supersaturation needs to be calculated. Surface growth and evaporation of a material s can occur via three types of reactions:



where X is a reactant, Y a product, A(N) a cloud particle containing N units of bulk growth material³ (e.g. Mg₂SiO₄ would be 1 unit for Mg₂SiO₄[s]), F the set of reactants, D the set of products, and $\nu_{i,r}$ the stoichiometric coefficients of the species i for the surface reaction r . Type 1 reactions describe condensation, Type 2 reactions are chemical growth reactions, and Type 3 reactions involve

³A(N) can be heterogeneous and contain multiple bulk growth materials. To simplify notation, we only note the number of bulk growth units N of the bulk growth material involved in a given reaction.

surface chemistry. Cloud particles are assumed to be large enough for the following approximation to hold:

$$G_{A(N)}^{\ominus} \approx G_{A(N-1)}^{\ominus} + G_A^{\ominus}, \quad (4.23)$$

where $G_{A(N)}^{\ominus}$ [erg] is the Gibbs free energy of formation at the standard pressure of the $A(N)$ cloud particle made from N units and G_A^{\ominus} [erg] is the Gibbs free energy of formation of a solid unit at standard pressure. The goal of this section is to find the reaction supersaturation S_r of these reactions defined as

$$S_r = \frac{R_f}{R_b}, \quad (4.24)$$

where R_f [s^{-1}] is the growth rate and R_b [s^{-1}] is the evaporation rate. It is important to note that the following derivations were done in chemical disequilibrium. At no point in this section do we assume chemical equilibrium.

S_r of Type 1 reactions (condensation)

Type 1 reactions are reactions where the reactant is also the bulk growth material. In this case the reaction supersaturation is equal to the supersaturation of the growth species:

$$S_r = S = \frac{p_X}{p_X^{\text{vap}}} = \frac{n_X}{k_B T} \frac{1}{p^{\ominus}} \exp\left(\frac{G_X^{\ominus} - G_A^{\ominus}}{k_B T_{\text{gas}}}\right), \quad (4.25)$$

where p_X^{vap} [dyn cm^{-2}] is the vapour pressure of species X, p_X [dyn cm^{-2}] is the partial pressure of species X, n_X [cm^{-3}] is the gas-phase number density of species X, T_{gas} [K] is the temperature, and G_X^{\ominus} [erg] is the Gibbs free energy of formation of the condensing species in the gas phase at standard pressure. Since the bulk growth material exists in the gas-phase, the supersaturation is well defined.

S_r of Type 2 reactions

Type 2 reactions were discussed in detail in previous studies (Gail & Sedlmayr 1988; Gauger et al. 1990; Dominik et al. 1993; Patzer et al. 1998). The reaction supersaturation is given by (adapted from Patzer et al. 1998):

$$S_r = \frac{n_X}{n_Y} \exp\left(\frac{G_X^{\ominus} - G_Y^{\ominus} - G_A^{\ominus}}{k_B T_{\text{gas}}}\right), \quad (4.26)$$

where G_X^\ominus [erg] and G_Y^\ominus [erg] are the Gibbs free energies of formation of the gas-phase reactant and product, respectively. n_X [cm^{-3}] is the number density of the reactant X and n_Y [cm^{-3}] is the number density of the product Y. Type 2 reactions are well defined even if the bulk growth material is not present in the gas-phase (see Patzer et al. (1998) for further details).

S_r of Type 3 reactions

Type 3 reactions involve surface chemistry. Considering these reactions is especially important if the bulk growth material is not present in the gas phase. For example, $\text{Mg}_2\text{SiO}_4[\text{s}]$ can condense via the surface reaction



To simplify the notation, we used the reaction of Eq. 4.27 as an example for this section and generalise the results at the end. For our example in this section, we assumed Mg to be the key gas-phase species. The bulk growth rate of this reaction can then be described by the following (adapted from Helling & Woitke 2006):

$$R_f = \left[A_{A(N-1)} v_{\text{key}} \frac{1}{\nu_r^{\text{key}}} \right] n_{\text{key}}, \quad (4.28)$$

where $A_{A(N-1)}$ [cm^2] is the surface area of the $A(N - 1)$ cloud particle, $n_{A(N-1)}$ [cm^{-3}] the number density of the $A(N - 1)$ cloud particle, ν_{key} [cm s^{-1}] the relative velocity of the cloud particle and the key gas-phase species (e.g. Mg), and n_{key} [cm^{-3}] the number density of the key gas-phase species (e.g. Mg). Phase equilibrium for a given bulk growth reaction (short PGR, noted with $^\circ$) is characterised⁴ by the evaporation rate equalling the growth rate ($R_f^\circ = R_b^\circ$). Therefore, according to Eq. 4.28, the evaporation rate is:

$$R_b = \left[A_{A(N-1)} v_{\text{key}} \frac{1}{\nu_r^{\text{key}}} \right] n_{\text{key}}^\circ, \quad (4.29)$$

where n_{key}° [cm^{-3}] is the number density of the key gas-phase species in PGR (e.g. Mg). Since all non-key-gas-phase species are typically much more abundant than the key-gas-phase species, their number densities in non-PGR only slightly differ from their number densities in PGR. Therefore, the following approximation holds:

$$\frac{n_{\text{SiO}}^\circ}{n_{\text{SiO}}} \approx \frac{n_{\text{H}_2\text{O}}^\circ}{n_{\text{H}_2\text{O}}} \approx \frac{n_{\text{H}_2}^\circ}{n_{\text{H}_2}} \approx 1. \quad (4.30)$$

⁴In this section, up to and including Eq. 4.41, PGR is towards the reaction from Eq. 4.27, but the same derivation holds for an arbitrary type 3 reaction.

This allows us to write the reaction supersaturation as

$$S_r^2 = \frac{(n_{\text{Mg}})^2}{(n_{\text{Mg}}^\circ)^2} = \frac{(n_{\text{Mg}})^2}{(n_{\text{Mg}}^\circ)^2} \frac{n_{\text{SiO}}^\circ (n_{\text{H}_2\text{O}}^\circ)^3 (n_{\text{H}_2})^3}{n_{\text{SiO}} (n_{\text{H}_2\text{O}})^3 (n_{\text{H}_2}^\circ)^3} \left[\frac{n_{\text{SiO}} (n_{\text{H}_2\text{O}})^3 (n_{\text{H}_2}^\circ)^3}{n_{\text{SiO}}^\circ (n_{\text{H}_2\text{O}}^\circ)^3 (n_{\text{H}_2})^3} \right], \quad (4.31)$$

$$\approx \frac{(n_{\text{Mg}})^2 n_{\text{SiO}} (n_{\text{H}_2\text{O}})^3}{(n_{\text{H}_2})^3} \frac{(n_{\text{H}_2}^\circ)^3}{(n_{\text{Mg}}^\circ)^2 n_{\text{SiO}}^\circ (n_{\text{H}_2\text{O}}^\circ)^3}, \quad (4.32)$$

leaving only the ratios of gas number densities in PGR to find.

We started the derivation with a thought experiment by imagining a box containing a given elemental abundance of Mg, SiO, H₂O, H₂, A(N - 1), and A(N). We assume that in this box, gas-phase species only react with each other via the specific surface reaction from Eq. 4.27. Over time, the box will evolve towards PGR for this specific chemical configuration. In PGR, the entropy of the box will be maximised, which is equivalent to minimising the Gibbs free energy for the reactants and products of the given reaction. This minimisation problem with its constraints can be expressed in the following Lagrangian function:

$$\begin{aligned} \mathcal{L} = & \left[\sum_{j \in E} N_j G_j^\ominus + N_j k_B T_{\text{gas}} \ln \left(\frac{N_j}{N} \right) \right] \\ & + \lambda_1 (C_1 + N_{\text{Mg}} - 2N_{\text{SiO}}) \\ & + \lambda_2 (C_2 + 3N_{\text{Mg}} - 2N_{\text{H}_2\text{O}}) \\ & + \lambda_3 (C_3 + N_{\text{Mg}} - 2N_{\text{A(N-1)}}) \\ & + \lambda_4 (C_4 - 3N_{\text{Mg}} - 2N_{\text{H}_2}) \\ & + \lambda_5 (C_5 - N_{\text{Mg}} - 2N_{\text{A(N)}}), \end{aligned} \quad (4.33)$$

where $E = \{\text{Mg, SiO, H}_2\text{O, H}_2, \text{A(N-1), A(N)}\}$ is the set of particles, N_j is the total number of particles j , N is the total number of gas particles, G_j^\ominus [erg] is the Gibbs free energy of formation of particle j at standard pressure, λ_i [erg] are the Lagrangian multipliers, and C_i are constants. The constraints from λ_1 , λ_2 , and λ_3 are keeping the ratio of Mg, SiO, H₂O, and A(N - 1) per reaction constant using Mg as reference. The constraints from λ_4 , and λ_5 ensure mass conservation. Minimising this Lagrangian for all molecules and cloud particles

results in the following set of equations:

$$\frac{d\mathcal{L}}{dN_{\text{Mg}}} = G_{\text{Mg}}^{\ominus} + k_B T_{\text{gas}} \ln \left(\frac{N_{\text{Mg}}}{N} \right) + \lambda_1 + 3\lambda_2 + \lambda_3 - 3\lambda_4 - \lambda_5, \quad (4.34)$$

$$\frac{d\mathcal{L}}{dN_{\text{SiO}}} = G_{\text{SiO}}^{\ominus} + k_B T_{\text{gas}} \ln \left(\frac{N_{\text{SiO}}}{N} \right) - 2\lambda_1, \quad (4.35)$$

$$\frac{d\mathcal{L}}{dN_{\text{H}_2\text{O}}} = G_{\text{H}_2\text{O}}^{\ominus} + k_B T_{\text{gas}} \ln \left(\frac{N_{\text{H}_2\text{O}}}{N} \right) - 2\lambda_2, \quad (4.36)$$

$$\frac{d\mathcal{L}}{dN_{\text{A(N-1)}}} = G_{\text{A(N-1)}}^{\ominus} + k_B T_{\text{gas}} \ln \left(\frac{N_{\text{A(N-1)}}}{N} \right) - 2\lambda_3, \quad (4.37)$$

$$\frac{d\mathcal{L}}{dN_{\text{H}_2}} = G_{\text{H}_2}^{\ominus} + k_B T_{\text{gas}} \ln \left(\frac{N_{\text{H}_2}}{N} \right) - 2\lambda_4, \quad (4.38)$$

$$\frac{d\mathcal{L}}{dN_{\text{A(N)}}} = G_{\text{A(N)}}^{\ominus} + k_B T_{\text{gas}} \ln \left(\frac{N_{\text{A(N)}}}{N} \right) - 2\lambda_5. \quad (4.39)$$

In PGR, the Lagrangian function is minimal and thus the derivatives are zero. Solving this set of equations, using the approximation of Eq. 4.23, and going from particle numbers N_j to particle number densities n_j leads to:

$$\begin{aligned} \frac{(n_{\text{Mg}}^{\circ})^2 n_{\text{SiO}}^{\circ} (n_{\text{H}_2\text{O}}^{\circ})^3}{(n_{\text{H}_2}^{\circ})^3} &\approx \left(\frac{p^{\ominus}}{k_B T_{\text{gas}}} \right)^3 \exp \left(\frac{-1}{k_B T_{\text{gas}}} \left[2G_{\text{Mg}}^{\ominus} + G_{\text{SiO}}^{\ominus} \right. \right. \\ &\quad \left. \left. + 3G_{\text{H}_2\text{O}}^{\ominus} - 3G_{\text{H}_2}^{\ominus} - G_{\text{Mg}_2\text{SiO}_4[\text{S}]}^{\ominus} \right] \right). \end{aligned} \quad (4.40)$$

This result gives us the relation between the number densities of the reactants and products of the bulk growth reaction. Hence, the reaction supersaturation for the reaction of Eq. 4.27 is given by:

$$\begin{aligned} S_r^2 &\approx \frac{(n_{\text{Mg}})^2 n_{\text{SiO}} (n_{\text{H}_2\text{O}})^3}{(n_{\text{H}_2})^3} \left(\frac{p^{\ominus}}{k_B T_{\text{gas}}} \right)^{-3} \\ &\quad \exp \left(\frac{1}{k_B T_{\text{gas}}} \left[2G_{\text{Mg}}^{\ominus} + G_{\text{SiO}}^{\ominus} + 3G_{\text{H}_2\text{O}}^{\ominus} - 3G_{\text{H}_2}^{\ominus} - G_{\text{Mg}_2\text{SiO}_4[\text{S}]}^{\ominus} \right] \right). \end{aligned} \quad (4.41)$$

For an arbitrary type 3 reaction that is limited by a key-gas-phase species, the reaction supersaturation is then given by

$$S_r^{\nu_{\text{key}}} = \frac{\prod_{X \in F} n_X^{\nu_X}}{\prod_{Y \in D} n_Y^{\nu_Y}} \left(\frac{p^\ominus}{k_B T_{\text{gas}}} \right)^{l_Y - l_X} \exp \left(\frac{1}{k_B T_{\text{gas}}} \left[G_A^\ominus - \sum_{X \in F} \nu_X G_X^\ominus + \sum_{Y \in D} \nu_Y G_Y^\ominus \right] \right), \quad (4.42)$$

where l_X is the number of reactants and l_Y is the number of products. If only one reactant is considered, this result matches the result for type 1 reactions. It also matches type 2 reactions if only one key reactant and one key product are considered. In the case of chemical equilibrium, our description of the supersaturation ratio for type 3 reactions is the same as the one found by Helling & Woitke (2006).

We define the right side of Eq. 4.40 as the reaction vapour coefficient c_r^{vap} [$\text{cm}^{-3(l_x - l_y)}$] and fit it with

$$\ln \left(\frac{c_r^{\text{vap}}}{[\text{cm}^{-3(l_x - l_y)}]} \right) = \sum_{i=0}^3 \frac{s_i}{T_{\text{gas}}^i}. \quad (4.43)$$

The fitting parameters for the surface reactions considered in this chapter are given in Table B.4. This allows us to write the reaction supersaturation as

$$S_r^{\nu_{\text{key}}} = \frac{\prod_{X \in F} n_X^{\nu_X}}{\prod_{Y \in D} n_Y^{\nu_Y}} \frac{1}{c_r^{\text{vap}}}. \quad (4.44)$$

4.2.6 Formation rate of CCNs

To describe nucleation kinetically, we require the properties of each considered cluster size up until the size N_* , where the clusters become preferably thermally stable. For this, the Gibbs free energies G_N (Eq. 4.8), the interaction radii r_N (Eq. 4.4 and 4.7), and the masses m_N (Eq. 4.6) of all considered cluster sizes need to be known. Unfortunately, only limited data are available (see e.g. the case of TiO_2 : Qu & Kroes 2006; Lundqvist et al. 2006; Zhai & Wang 2007; Chiodo et al. 2011; Lee et al. 2015; Sindel et al. 2022). We used the data of Sindel et al. (2022) and approximated the nucleation rate with the largest cluster for which all necessary data are available, which in this case is $N_{\max} = 15$. The quality of this assumption for N_{\max} is tested in Sect. 4.3.3.

We followed the approach of Patzer et al. (1998) and calculated the nucleation rate as

$$J_*(V_l) = \frac{dn_{N_{\max}}}{dt}, \quad (4.45)$$

which describes the rate at which CCNs are formed. The growth from clusters made from N_{\max} monomers to clusters with a volume of V_l depletes the gas phase of the clustering species. Because polymer nucleation is considered, all N-mers up to a given Q -mer are depleted:

$$\frac{dn_N}{dt} = -J_*(V_l) \frac{n_N}{\omega_m}, \quad (4.46)$$

$$\omega_m = \frac{V_l}{\Delta V_r} \sum_{N=1}^Q N n_N, \quad (4.47)$$

where n_N [cm^{-3}] are N-mer number densities and $1 \leq N \leq Q$. For TiO_2 , the change in the number density of clusters of size $N_{\max} = 15$ defines nucleation (see Eq. 4.45). We therefore excluded this size from the depletion description and selected $Q_{\text{TiO}_2} = 14$.

Starting from V_l , the particles can grow via surface growth. Similarly, they can shrink via evaporation down to size V_l . To numerically separate evaporation and nucleation, cloud particles should only evaporate down to size V_l . For the ODE solver, we needed a continuous transition and therefore adjusted the evaporating surface area by multiplying the evaporation term of Eq. 4.17 with

$$c_{\text{vol}} = \left(\frac{\rho L_3}{\rho L_0} - V_l \right) \frac{\rho L_0}{\rho L_3}. \quad (4.48)$$

Including Eq. 4.48 in Eq. 4.17 results in

$$\chi^{\text{net}} = \sqrt[3]{36\pi} \sum_{r \in C_d} \Delta V_r n_r^{\text{key}} \langle v_r \rangle \frac{\alpha_r(v_r)}{\nu_r^{\text{key}}} \left(1 - \frac{c_{\text{vol}}}{S_r^{1/\nu_r^{\text{key}}} b_r^{\text{surf}}} \right). \quad (4.49)$$

For the rest of this chapter, we use Eq. 4.49 for χ^{net} in Eqs. 4.16 and 4.19.

4.3 Exploring kinetic chemistry and nucleation

In Sect. 4.3.1, we create a chemical network for the kinetic cloud formation model. Using this network, we studied the impact on the gas phase when combining different chemical kinetics networks, nucleation, and bulk growth. Describing fully time-dependent bulk growth revealed a SiO-SiO_2 cycle within the surface reactions; this is discussed in Sect. 4.3.2. In Sect. 4.3.3, we evaluate the nucleation rate's dependence on different maximum cluster sizes N_{\max} .

Table 4.1: Offset values between number densities of given molecular species for the chemical networks VULCAN (V), VULCAN+ (V+), VULCAN+poly (V+p), and the full network according to Eq. 4.50.

	H ₂	H ₂ O	CO ₂	CH ₄
$P(A, \text{Equilibrium}, V)$	4.84e-05	7.35e-03	1.58e-02	6.35e-02
$P(A, V, V+)$	5.18e-11	1.34e-07	1.83e-05	1.18e-07
$P(A, V+, V+p)$	4.99e-08	1.32e-04	1.49e-04	1.32e-04
$P(A, V+p, \text{full})$	1.49e-03	0.41	0.41	1.74
	TiO ₂	SiO ₂	Mg	
$P(A, \text{Equilibrium}, V)$	-	-	-	
$P(A, V, V+)$	7.43e-04	5.25e-02	-	
$P(A, V+, V+p)$	1.89	1.32e-04	-	
$P(A, V+p, \text{full})$	5.21	2.35	12.8	

4.3.1 A chemical network for kinetic cloud formation

To find the impact of combining different chemical networks, nucleation, and bulk growth on the number densities of the gas-phase species, we compared the gas-phase abundances in five cases: These cases are (i) equilibrium, a time-independent calculation whereby chemical equilibrium number densities are calculated using `GGchem`; (ii) the NCHO thermo network reactions of VULCAN; (iii) VULCAN+, which combines the NCHO thermo network reactions of VULCAN and the Ti and Si reactions as listed in Table B.1; (iv) VULCAN+poly, which combines VULCAN+, the polymer nucleation reactions for TiO₂ as described in Sect. 4.2.2, and the formation of TiO₂ CCNs as described in Sect. 4.2.6; (v) Full, which combines VULCAN+poly and the bulk growth through condensation and surface reactions as described in Sect. 4.2.4.

All simulations start from equilibrium number densities calculated with `GGchem`. All time axes in this chapter measure the evaluation time t [s] of the disequilibrium chemistry starting from equilibrium conditions at $t = 0$ s. The results for the $T_{\text{gas}}\text{-}p_{\text{gas}}$ point⁵ $p_{\text{gas}} = 0.002$ bar at $T_{\text{gas}} = 1378$ K can be seen in Fig. 4.2. The chemical equilibrium number densities match the predicted number densities of VULCAN and are therefore not shown in the figure.

To compare the difference in the predicted number densities, we compared the maximum absolute difference between the logarithm of the number densities of

⁵This $T_{\text{gas}}\text{-}p_{\text{gas}}$ point corresponds to a location within the evening terminator of HD 209458 b.

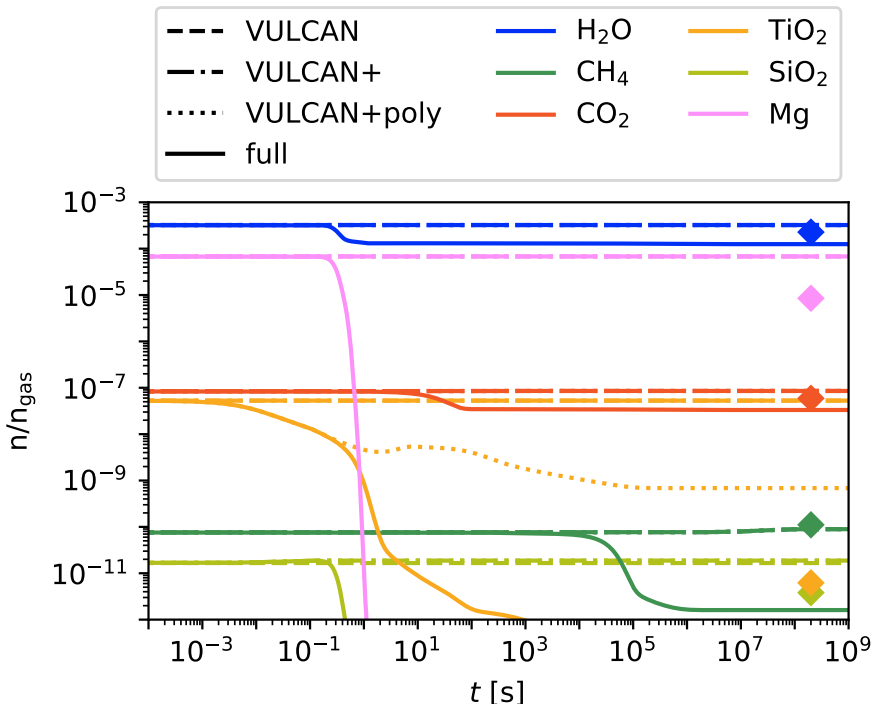


Figure 4.2: Concentrations of selected gas-phase species for $p_{\text{gas}} = 0.002$ bar at $T_{\text{gas}} = 1378$ K using different chemical kinetics networks. The diamond shaped marker shows GGchem results including equilibrium condensation.

species A between two chemical networks C_1 and C_2 :

$$P(A, C_1, C_2) = \max\{|\log_{10}(n_{C_1}^A(t)/n_{C_2}^A(t))|, \forall t \in [10^{-4}, 10^9]\}. \quad (4.50)$$

The P values for $p_{\text{gas}} = 0.002$ bar and $T_{\text{gas}} = 1378$ K, representing a low-pressure level in a relatively cool atmosphere, are shown in Table 4.1. For the comparison, we chose H_2 because it is the dominant gas-phase species, H_2O and CO_2 because they are commonly studied, methane (CH_4) because it has distinct spectral features, Mg and SiO_2 because they are condensing species, and TiO_2 because it is the nucleating species.

Comparing Equilibrium to VULCAN and VULCAN to VULCAN+ shows close to no difference ($P < 0.1$) in the predicted number densities of H_2 , H_2O , CO_2 , CH_4 , and SiO_2 in both cases. In VULCAN+poly TiO_2 nucleation reactions and the formation of TiO_2 CCNs are added. Therefore, it comes as no surprise that

the number density of TiO_2 decreases by close to two orders of magnitude. The impact for H_2 , H_2O , CO_2 , CH_4 , and SiO_2 on the other hand is still negligible. When bulk growth is added in the full network, the number densities of TiO_2 , SiO_2 and Mg decrease by several orders of magnitude due to their being depleted by the bulk growth processes. The impact of bulk growth can also be seen in the number densities of H_2O , CO_2 , and CH_4 . The change in CH_4 is discussed in Sect. 4.3.2. The number density of H_2 on the other hand is not significantly affected.

Also shown in Fig. 4.2 are the gas-phase concentrations calculated using **GGchem** including the equilibrium condensation of the bulk grow materials. Compared to our results, **GGchem** equilibrium condensation results predict higher gas-phase concentrations in the cloud-forming species TiO_2 , SiO_2 , and Mg , as well as the gas-phase-only species H_2O , CH_4 , and CO_2 . Because our work treats cloud formation kinetically, these differences can be caused by the nucleation or surface reactions, neither of which is considered within **GGchem**. In environments such as the ISM or Titan’s atmosphere, surface reactions are known to cause deviations from equilibrium gas-phase abundances (see Sect. 4.3.2).

Selecting a suitable gas-phase chemical kinetics network is important. We chose VULCAN because it includes commonly considered species such as H_2O , CO_2 , and CH_4 with a reasonably small number of reactions (780). Other chemical kinetics networks for exoplanet atmospheres include thousands of reactions (e.g. Venot et al. 2012; Venot & Agúndez 2015; Rimmer & Helling 2016; Hobbs et al. 2019; Venot et al. 2020). Because of the computational intensity of these networks, their evaluation is often limited to 1D models (e.g. Moses et al. 2005; Chadney et al. 2017; Hobbs et al. 2022; Barth et al. 2021). Adding kinetic nucleation and bulk growth to the chemical network can increase the computational time considerably. For the simulations in this section, the evaluation time doubled if nucleation and bulk growth were considered. If enough computational resources are available, our kinetic nucleation and bulk growth model can be combined with extensive chemical networks for a detailed study. Furthermore, models and observations have shown that the 3D structure of exoplanets can have an impact on the gas-phase chemistry (Baeyens et al. 2021; Prineth et al. 2022; Lee et al. 2023). To evaluate the chemistry and cloud formation within 3D models, the cloud formation description can be combined with small but accurate networks (Tsai et al. 2022).

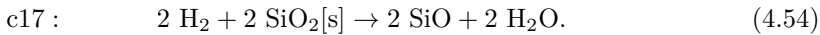
Most chemical kinetics networks for exoplanet atmospheres do not include many Mg-, Ti-, Si-, or Fe-bearing species. In our simulations, only the surface reactions c0, c1, c2, c4, c16, c71, c80, c85, c101, and c104 (see Table B.4) have all reactants and products within the chemical kinetics network. All other bulk growth reactions rely at least partially on gas-phase species that are only calculated in equilibrium. Ideally, all reactants and products of surface reactions

should be included in the chemical kinetics network but they are not always available in literature and would drastically increase the number of reactions.

4.3.2 SiO-SiO₂ cycle

In a fully kinetic description of cloud formation, minor species are affected as well. As shown in Fig. 4.2, adding bulk growth reactions significantly impacts the number density of CH₄, even though it is not directly involved in any bulk growth processes. This is important since CH₄ is discussed as a bio molecule in terrestrial atmospheres (Thompson et al. 2022; Huang et al. 2022) and is observable in hot Jupiter atmospheres (Swain et al. 2009; Barman et al. 2015; Guilluy et al. 2019).

The four bulk growth reactions causing the decrease in CH₄ are c17, c19, c42, and c44. A closer look at these surface reactions revealed the following cycle:



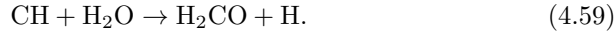
The net process of this cycle is



This additional pathway for the dissociation of H₂ to H decreases the number density of CH₄ through the following reactions:



Most of the carbon from CH₄ is transferred into H₂CO with the following reaction:



The change in carbon chemistry then also impacts other species like HCN, HCO, and C₂H₂.

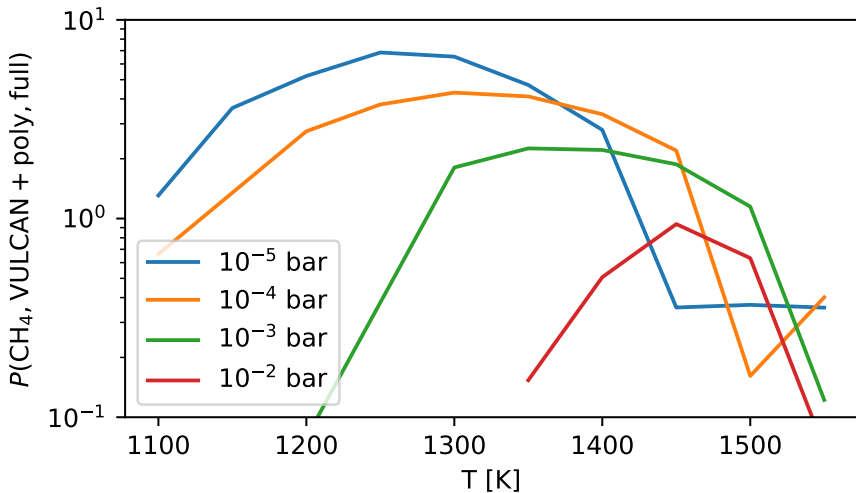


Figure 4.3: Differences in CH_4 abundance between chemical equilibrium and the VULCAN+poly network for various temperatures and pressures.

To investigate at which pressures and temperatures the SiO-SiO_2 cycle significantly impacts the CH_4 abundance, $P(\text{CH}_4, \text{Equilibrium}, \text{VULCAN} + \text{poly})$ values for a range of pressures and temperatures were calculated. The results are shown in Fig. 4.3. The difference in the CH_4 abundance is largest for pressures lower than $p_{\text{gas}} < 10^{-3}$ bar and for temperatures around 1300 K.

The surface reactions used in this work were derived using a stoichiometric argument (Helling & Woitke 2006; Helling et al. 2008b, 2017, 2019a). Unfortunately, more detailed studies of surface reactions of bulk growth materials are missing from the literature. To determine if all surface reactions of the SiO-SiO_2 cycle are likely to occur in exoplanet atmospheres, further investigations are needed. The fact that other processes, such as quenching or photo-chemistry, can have similar effects (Moses et al. 2011) makes it difficult to gain insights into surface reactions through observations.

Molaverdikhani et al. (2020) analysed the impact of clouds on the methane abundance. They found that clouds can increase the temperature in the photosphere, which in turn reduces the methane abundance. In contrast to our work, they used condensation curves rather than surface reactions, and therefore they did not observe a direct impact of cloud formation on the CH_4 abundance.

In the ISM, surface reactions are discussed as sources for molecular hydrogen in the gas phase (Hollenbach & Salpeter 1971; Williams 2005; Sabri et al. 2013; Dishoeck 2014; Herbst 2014, 2017). Similar to our study, in the ISM the surface of dust grains acts as a catalyst; however, in contrast to our work, they do not result in bulk material being deposited. The calculation of ISM surface reaction rates typically accounts for the vibrational frequency of the reactants and the energy barriers between different sites on the dust particle (Dishoeck 2014). Our surface reaction description could be improved by similar considerations. However, the large number of surface reactions considered and the heterogeneity of the cloud particle make such evaluations difficult.

Similarly to the ISM, the surfaces of aerosols in Titan’s atmosphere can enhance the recombination of H into H₂ (Courtin et al. 1991; Bakes et al. 2003; Sekine et al. 2008). In addition, gas-phase catalytic cycles using hydrocarbons for the hydrogen recombination are postulated (Yung et al. 1984; Toublanc et al. 1995; Lebonnois et al. 2003). Both effects change the atomic hydrogen abundance, which, similarly to our work, can affect the abundance of hydrocarbons in return. In contrast to our work, the catalytic cycles considered are gas-phase-only cycles and do not result in bulk material being deposited.

4.3.3 Kinetic nucleation of TiO₂

To accurately model the CCN formation in an exoplanet atmosphere, the nucleation rates of the dominant nucleating species need to be known. Previous studies determined TiO₂ (Goumans & Bromley 2013; Lee et al. 2015; Boulanger et al. 2019b; Köhn et al. 2021) as an important nucleating species. Other species that are discussed as nucleating species are Al₂O₃ (Gobrecht et al. 2022), SiO (Gail & Sedlmayr 1986; Lee et al. 2015) and VO (Lecoq-Molinos et al. 2024). In addition to TiO₂, we also analysed Al₂O₃ as a possible nucleating species for clusters up to size $N = 10$ (Gobrecht et al. 2022). The results were inconclusive (see Appendix B.3), and, therefore, for this study we decided to focus on TiO₂.

If the maximum cluster size is larger than the smallest thermally stable cluster ($N_{\max} > N_*$), the nucleation rate $J_*(V_i)$ is expected to be independent of the choice of the maximum cluster size. If the maximum cluster size is smaller than N_* , we expect to see different nucleation rates depending on the choice of N_{\max} . Therefore, we test different N_{\max} ($7 \leq N_{\max} \leq 15$) and their impact on the cloud particle number density and nucleation rate. For this section, we set $p_{\text{gas}} = 0.02$ bar and $T_{\text{gas}} = 1379$ K. We used the full network as described in Sect. 4.3.1. The cloud particle number densities and nucleation rates for different N_{\max} can be seen in Fig. 4.4. The predicted number densities for 7

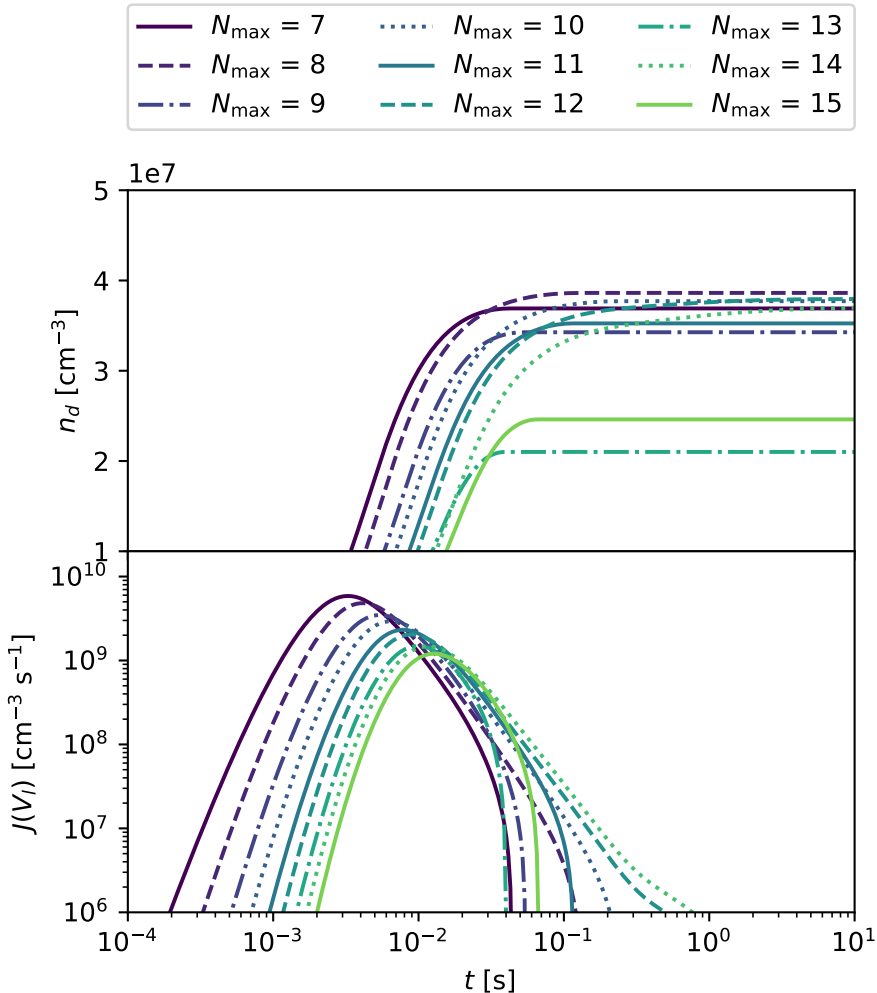


Figure 4.4: Cloud particle number densities (**Top**) and nucleation rates (**Bottom**) for TiO_2 nucleation with different N_{\max} at $p_{\text{gas}} = 0.02$ bar and $T_{\text{gas}} = 1379$ K.

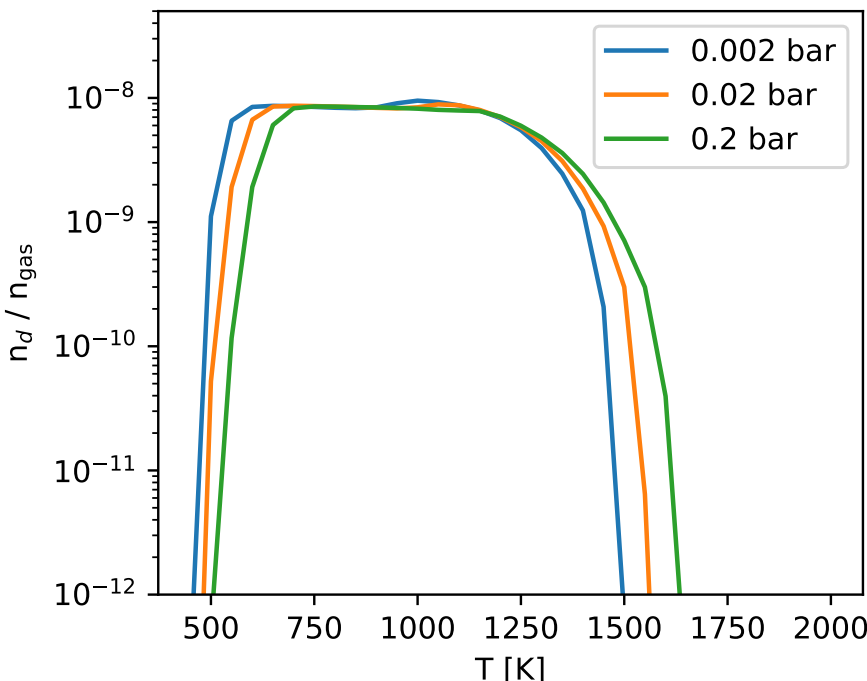


Figure 4.5: Cloud particle concentrations for TiO_2 nucleation for a range of temperatures and pressures.

$\leq N_{\max} \leq 15$ are all within a factor of 2. Furthermore, the peak in nucleation rate becomes smaller and appears later in time for larger clusters.

The biggest deviation in predicted cloud particle number density can be seen for $N_{\max} = 13$ and $N_{\max} = 15$, which predict lower cloud particle number densities than the rest. Looking at the Gibbs free energy per monomer unit ($G_{\text{TiO}_2(N)}^\ominus/N$) reveals that these sizes are the only N -mers that have a higher Gibbs free energy per monomer than their $(N-1)$ -mers:

$$\frac{G_{\text{TiO}_2(13)}^\ominus}{13} - \frac{G_{\text{TiO}_2(12)}^\ominus}{12} = 1.158, \quad (4.60)$$

$$\frac{G_{\text{TiO}_2(15)}^\ominus}{15} - \frac{G_{\text{TiO}_2(14)}^\ominus}{14} = 0.172. \quad (4.61)$$

Therefore, $N = 13$ and $N = 15$ are less thermally stable than their predecessors. Previous studies have shown the same preference for even N clusters (Lasserus

et al. 2019) that we find for the $(\text{TiO}_2)_N$ clusters but further studies of larger sizes clusters are needed to determine if it is a size-dependent trend that can affect the nucleation process. Because our nucleation rate is determined by the largest cluster size, having $N_{\max} = 13$ or $N_{\max} = 15$ naturally results in lower cloud particle number densities. Thermodynamic data for TiO_2 clusters larger than $N = 15$ are needed to further test this and to find the thermally stable cluster size N_* for TiO_2 .

Few studies have already evaluated nucleation using a non-classical approach. Lee et al. (2015) compared the nucleation rate predicted by CNT, MCNT, and non-classical nucleation for various temperatures without considering surface growth. We calculated the cloud particle number density over the same temperature range as they analysed (Fig. 4.5). In contrast to our work, they considered only $N_{\max} = 10$ and only monomer nucleation. Both their and our study predict significant nucleation of TiO_2 for temperatures up to roughly 1300 K. Above that, the nucleation of TiO_2 quickly decreases. For temperatures roughly between 600 K and 1200 K, our model predicts approximately constant cloud particle number densities, whereas the nucleation rate of Lee et al. (2015) decreases. This difference can be traced back to the polymer nucleation. Boulanger et al. (2019b) showed that for TiO_2 and other nucleation seeds monomer nucleation can underestimate the formation of larger clusters in cooler environments.

4.4 The time evolution of cloud formation in HD 209458b

We simulate the chemistry and cloud formation for various $T_{\text{gas}}\text{-}p_{\text{gas}}$ points within HD 209458 b (Henry et al. 2000), which is an often studied hot Jupiter (see e.g. Helling et al. 2016; Hobbs et al. 2021; Debrecht et al. 2022; Sainsbury-Martinez et al. 2023). The $T_{\text{gas}}\text{-}p_{\text{gas}}$ profiles used in this chapter were calculated using expert/MITgcm simulations of HD 209458 b conducted by Schneider et al. (2022c). The $T_{\text{gas}}\text{-}p_{\text{gas}}$ profiles for the sub-stellar point, anti-stellar point, evening terminator, and morning terminator can be seen in Fig. 4.6. The cloud particle concentrations and the mean cloud particle size as well as selected gas-phase concentrations and volume fractions⁶ for the sub-stellar point, evening terminator, anti-stellar point and morning terminator at $p_{\text{gas}} = 0.002$ bar can be seen in Fig. 4.7. This pressure layer was selected as it showed the largest spread in temperatures. The results for four logarithmically spaced pressure points ($p_{\text{gas}} \in \{0.002 \text{ bar}, 0.02 \text{ bar}, 0.2 \text{ bar}, 2 \text{ bar}\}$) along the evening terminator can be

⁶All volume fractions can be found in Fig. B.4.

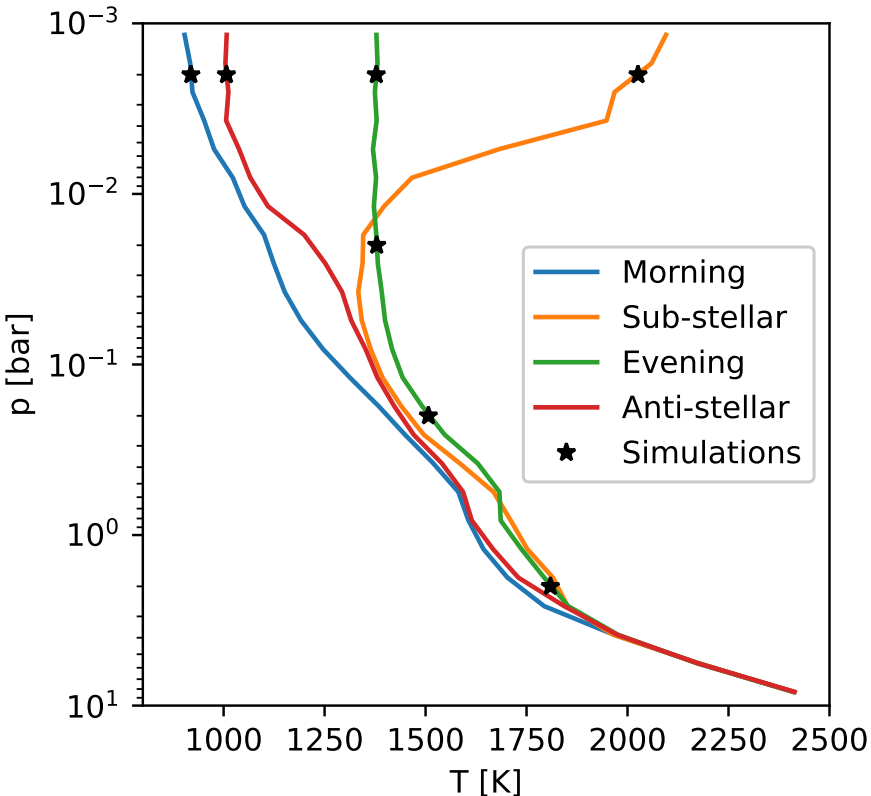


Figure 4.6: $T_{\text{gas}}-p_{\text{gas}}$ profiles of HD 209458 b taken from Schneider et al. (2022c). The $T_{\text{gas}}-p_{\text{gas}}$ points chosen for our simulations are marked with \star .

seen in Fig. 4.8. Only one $T_{\text{gas}}-p_{\text{gas}}$ profile was selected since the temperatures deeper in the atmosphere ($p_{\text{gas}} = 0.2$ bar and $p_{\text{gas}} = 2$ bar) are similar. The evening terminator was selected because of its intermediate temperature in the upper atmosphere at $p = 0.002$ bar. We used the full network as described in Sect. 4.3.1 for all simulations and start from chemical equilibrium calculated with **GGchem**.

To be able to compare gas-phase timescales to cloud formation timescales, we ran the VULCAN+ network (see Sect. 4.3.1) starting from solar-like atomic abundances for the $T_{\text{gas}}-p_{\text{gas}}$ points of the evening terminator. The resulting gas-phase concentrations of selected gas-phase species can be seen in Fig. 4.9. For all $T_{\text{gas}}-p_{\text{gas}}$ points, the concentrations of H_2O , TiO_2 , and SiO_2 quickly

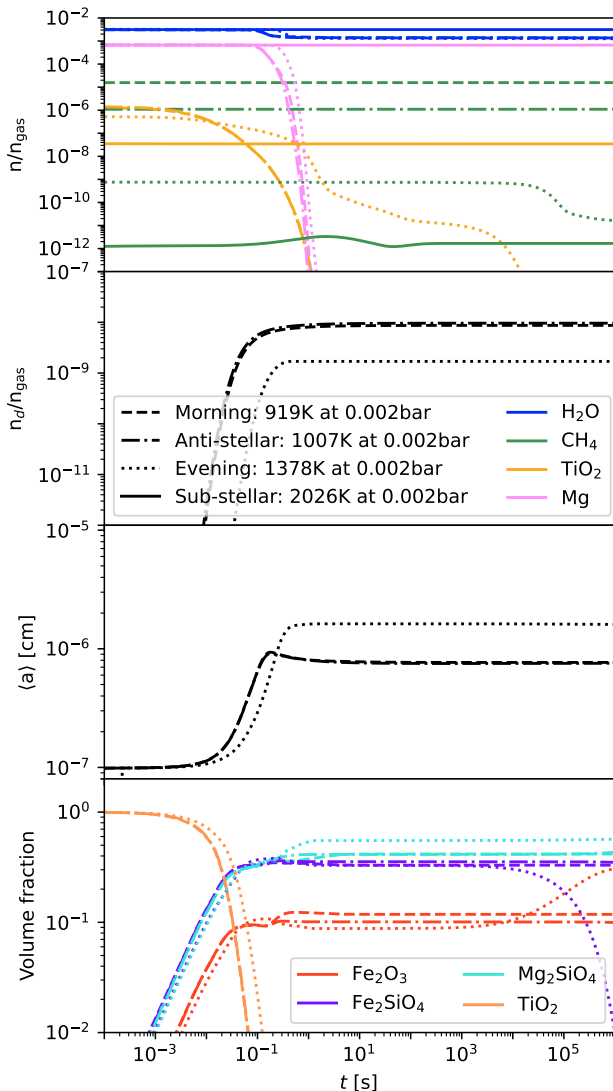


Figure 4.7: Concentrations of selected gas-phase species (**Top**), cloud particle number density (**Upper middle**), mean cloud particle size (**Lower middle**), and selected volume fractions (**Bottom**) at the sub-stellar point, evening terminator, anti-stellar point, and morning terminator at $p_{\text{gas}} = 0.002$ bar. The sub-stellar point does not form clouds.

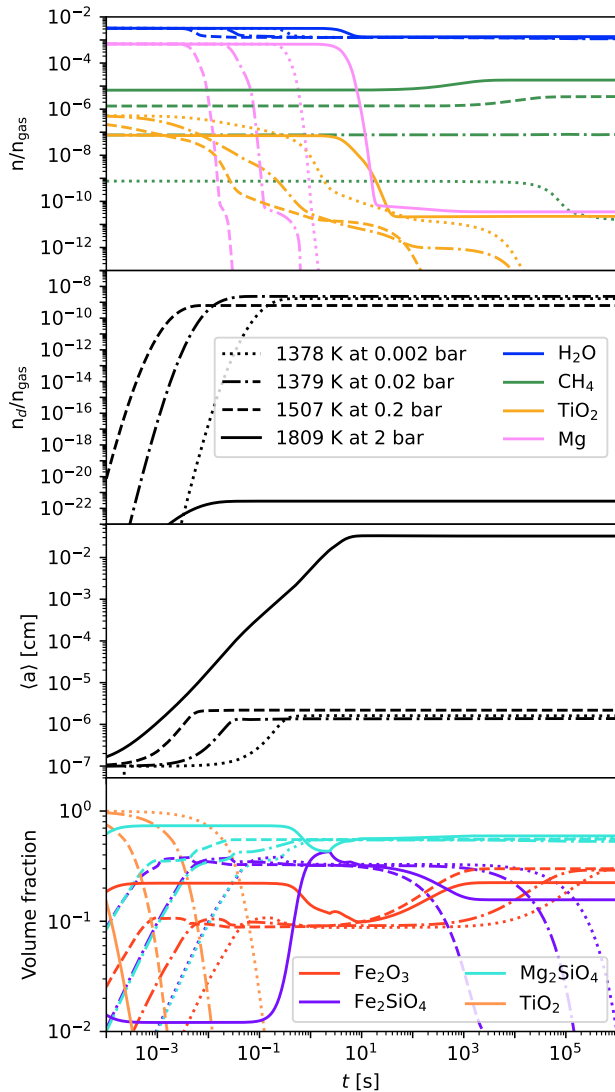


Figure 4.8: Concentrations of selected gas-phase species (**Top**), cloud particle number density (**Upper middle**), mean cloud particle size (**Lower middle**), and selected volume fractions (**Bottom**) for logarithmically spaced pressures along the evening terminator.

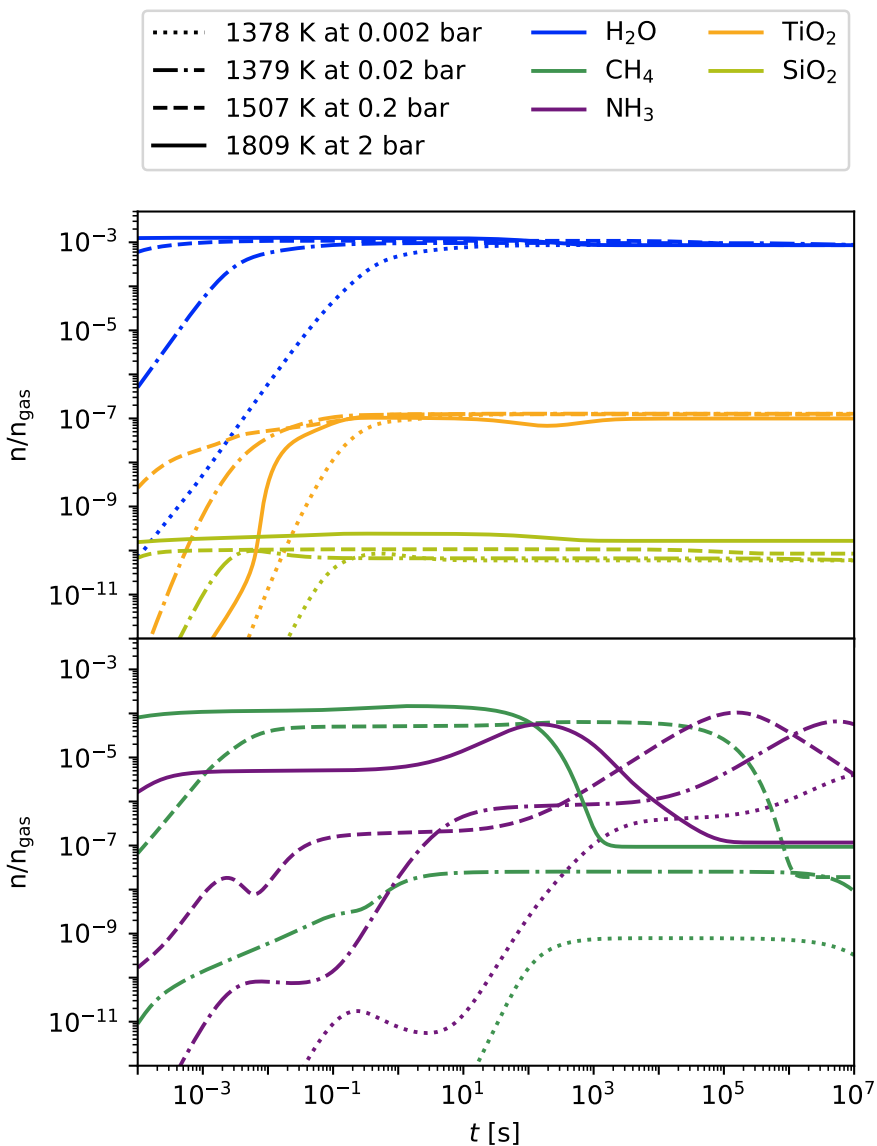


Figure 4.9: Concentrations of selected gas-phase species along evening terminator starting from solar-like atomic abundances.

approach their stationary values ($\tau_{\text{chem}} < 1$ s). Their chemical timescale is highly pressure dependent and decreases for higher pressures. CH₄ and NH₃ on the other hand, still show significant differences for $t > 10^5$ s for all but the highest pressure ($p_{\text{gas}} = 2$ bar).

4.4.1 Time evolution of cloud formation

Our results for the cloud formation within HD 208458 b start from a chemical equilibrium gas phase from which clouds are formed. These simulations can therefore give us an indication of the timescale of nucleation and bulk growth. The predicted cloud particle concentrations for most $T_{\text{gas}}\text{-}p_{\text{gas}}$ points of HD 209458 b quickly converge to stationary values ($\tau_{\text{nuc}} < 1$ s). The only exception is the sub-stellar point at $p_{\text{gas}} = 0.002$ bar where no cloud particles are predicted due to the high temperatures. Comparing the chemical timescales (see Fig. 4.9 or Tsai et al. 2018; Mendonça et al. 2018) to the nucleation timescale shows that nucleation happens on a similar timescale to the chemical species with a shorter chemical timescale (e.g. H₂O, TiO₂, SiO₂). The $T_{\text{gas}}\text{-}p_{\text{gas}}$ points at $p_{\text{gas}} = 0.002$ bar, other than the sub-stellar point, show only a small temperature dependence of the predicted cloud particle concentrations and nucleation timescale. This is not unexpected for temperatures ranging from 919 K to 1378 K. We have shown that TiO₂ nucleation is roughly constant for this temperature range (see Sect. 4.3.3). Similarly, along the evening terminator we see a decrease in cloud particle concentrations consistent with the findings of Sect. 4.3.3. At $p_{\text{gas}} = 2$ bar within the evening terminator, the cloud particle concentration reaches only $n_d/n_{\text{gas}} \approx 10^{-22}$. The lower number of cloud particles results in larger cloud particles because the bulk growth material condense onto fewer particles (Helling et al. 2023). Hence, the average cloud particle size reaches up to 0.033 cm.

The peak in bulk growth closely follows the peak in nucleation and also approaches stationary values on timescales shorter than 1 second ($\tau_{\text{bulk}} < 1$ s). The exception to this is the evening terminator at $p_{\text{gas}} = 2$ bar. The cloud particles still grow at roughly the same speed, but since much more material is available per cloud particle, it takes longer to reach stationary values for the average cloud particle size.

In all cases, the volume fractions start out TiO₂ dominated. After bulk growth starts the cloud particles become considerably heterogeneous. In all cases, Mg₂SiO₄ becomes the dominant bulk material and hence also the dominant Mg and Si bearing species. Around 0.1 to 1 second, a short increase in the average cloud particle size can be seen for the morning terminator and the anti-stellar point at $p_{\text{gas}} = 0.002$ bar. This size increase is caused by a temporary increase

in $\text{SiO}[\text{s}]$, $\text{SiO}_2[\text{s}]$, and $\text{Fe}_2\text{SiO}_4[\text{s}]$ (see also Fig. B.4). Without the $\text{SiO}-\text{SiO}_2$ cycle the temporary peak of Fe_2SiO_4 still occurs. This temporary increase is likely a result of feedback between cloud formation and disequilibrium chemistry. Because the cloud formation is directly coupled to the gas phase via the reaction supersaturation ratio, temporary changes in the gas-phase chemistry can be caused by cloud formation and vice versa.

For the dominant Fe bearing species we see a switch from Fe_2SiO_4 to Fe_2O_3 for $t > 10^3$ s. These are similar timescales of CH_4 and NH_3 (see Fig. 4.9 or Tsai et al. 2018; Mendonça et al. 2018). It is important to note that the change in the dominant Fe-bearing species is not related to the $\text{SiO}-\text{SiO}_2$ cycle. It still occurs even if $\text{SiO}[\text{s}]$ and $\text{SiO}_2[\text{s}]$ are not considered as bulk growth species. The timescale of the transition is highly pressure dependent and becomes shorter for higher pressures. Furthermore, the change in composition does not significantly affect the cloud particle size. Here, it is important to note that our cloud formation formalism does not include any solid-to-solid composition changes. All changes happen via the gas-phase through bulk growth reactions, as described in Sect. 4.2.5.

Helling & Woitke (2006) analysed the timescales of cloud formation with a similar cloud model to that used in this work. In contrast to our work, the gas phase is assumed to be in equilibrium (and depleted by cloud formation), MCNT is used to describe nucleation, and fewer surface reactions are used. The nucleation and bulk growth timescales they find are similar to ours ($\tau_{\text{nuc}} < 1$ s and $\tau_{\text{bulk}} < 1$ s). Coupling gas-phase chemistry and cloud formation does not seem to impact these timescales. However, secondary effects such as the change in the dominant Fe-bearing species and the $\text{SiO}-\text{SiO}_2$ cycle only appear once gas-phase chemistry and cloud formation are fully coupled.

Powell et al. (2018) also analysed the timescales of cloud formation using a diffusive approach. Their rates are limited by the time it takes for the key species to diffuse to the cloud particle. They calculated their timescales as the number density of cloud particles divided by the influx of new cloud particles once a stationary solution has been reached. Consequently, their growth and nucleation timescales for TiO_2 are larger than ours ($\tau_{\text{nuc}} > 10$ s and $\tau_{\text{bulk}} > 10$ s).

4.4.2 Comparison to dynamical processes

To find whether cloud formation happens in disequilibrium or is affected by disequilibrium chemistry, we compare our results to different dynamical processes.

Gravitational settling

Cloud particles in exoplanet atmospheres gravitationally settle over time. Whether gravitationally settling timescales are faster than cloud formation timescales depends on many factors, such as the bulk growth speed, bulk growth material replenishment, and the frictional force of cloud particles within the atmosphere (Woitke & Helling 2003). For smaller particles ($\langle a \rangle < 10^{-4}$ cm), growth is generally more efficient than gravitational settling (Woitke & Helling 2003; Powell et al. 2018). However, if the conditions favour larger particles and gravitational settling becomes more efficient, ‘cold traps’ can occur (Parmentier et al. 2013, 2016; Powell et al. 2018); this is where most cloud material is concentrated at the cloud base.

Comparing our cloud particle number densities and average radii to Powell et al. (2018) reveals differences that can be explained by gravitational settling and replenishment. In contrast to our work, they generally predict fewer and larger cloud particles. Settling removes cloud particles from the atmosphere thus leading to fewer particles. The replenished material then condenses onto already existing particles. Since fewer particles are present, they become larger. The exception to this is the evening terminator at $p_{\text{gas}} = 2$ bar. Here, nucleation is so inefficient that we predict very large cloud particles ($\langle a \rangle = 0.033$ cm). However, these particles would quickly settle, and they are unlikely to persist in a 1D model.

Vertical and horizontal transport

Quenching occurs when the chemical timescale τ_{chem} [s] becomes longer than the vertical mixing timescale τ_{dyn} [s] (Moses 2014). In low-density environments, chemical timescales typically become longer (Tsai et al. 2018) and dynamical timescales typically become smaller (Parmentier et al. 2013). Therefore, quenching becomes more relevant in the upper atmosphere of exoplanets (Baeyens et al. 2021). Typical vertical mixing timescales are between 10^3 s $< \tau_{\text{dyn}} < 10^7$ s (Agundez et al. 2014; Drummond et al. 2018; Baeyens et al. 2021). Our results show that nucleation happens on much shorter timescales than this ($\tau_{\text{nuc}} < 1$ s) and is therefore expected to be less affected by quenching. The cloud particle composition on the other hand changes on longer timescales, which are similar to the chemical timescales of CH₄ and NH₃. Both CH₄ and NH₃ are known to be gas-phase species affected by quenching (Moses et al. 2011). Therefore, the cloud particle composition might be susceptible to quenching as well.

Similarly to the vertical timescale, one can compare the nucleation and bulk

growth timescales to the horizontal mixing timescales, which consist of the latitudinal timescale and the longitudinal timescale. Mendonça et al. (2018) analysed⁷ WASP-43 b and found that latitudinal mixing happens on similar timescales to the vertical timescale. Longitudinal mixing, on the other hand, can be orders of magnitude shorter. This is mostly due to the strong equatorial wind jets. In their analysis, all (longitudinal, latitudinal, and vertical) mixing timescales are well above 10^3 s $> \tau_{\text{dyn}}$. Therefore, similar to quenching, nucleation and the peak in bulk growth might be less affected by horizontal mixing. The cloud particle composition on the other hand might be impacted.

Stellar flares

If periodic effects disturb the chemical abundances, the relaxation timescale τ_{relax} indicates how quickly the chemical abundances return back to pre-disruption values. An example for an effect that temporarily impacts chemistry are stellar flares. They periodically enhance the radiation received by a planet and cause chemical disequilibrium through photochemistry (Tilley et al. 2019; Louca et al. 2022). The chemical relaxation timescale after a stellar flare event can be of the order of hours ($\tau_{\text{relax}} > 10^3$ s; Konings et al. 2022). In the chemical relaxation scheme (Smith 1998; Cooper & Showman 2006; Kawashima & Min 2021), the relaxation timescale is given by the chemical timescale. This scheme typically also finds relaxation timescales of $\tau_{\text{relax}} > 10^3$ s for CH₄ and NH₃ (see Fig. 4.9 or Tsai et al. 2018; Mendonça et al. 2018). Nucleation and the peak in bulk growth occur on much shorter timescales than this and therefore can adjust to the temporary chemical disequilibrium. The cloud particle composition on the other hand takes longer to transition and might not adjust to the temporary chemical disequilibrium.

4.5 Summary

We established a fully kinetic cloud formation description combining disequilibrium chemistry, kinetic nucleation, and bulk growth through condensation and surface reactions. The kinetic gas-phase chemistry network for this study was based on the NCHO thermo-network of VULCAN. This network was expanded with Ti (and Si) reactions to connect the gas-phase chemistry with the kinetic nucleation of TiO₂. We considered TiO₂ polymer nucleation using cluster data up to cluster size N = 15. For the bulk material, we considered TiO₂[s],

⁷WASP-43 b ($T_{\text{eq}} = 1400$ K) is a hot Jupiter with a slightly cooler equilibrium temperature than HD 209458 b ($T_{\text{eq}} = 1500$ K) (Helling et al. 2021).

$\text{Al}_2\text{O}_3[\text{s}]$, $\text{SiO}[\text{s}]$, $\text{SiO}_2[\text{s}]$, $\text{Mg}_2\text{SiO}_4[\text{s}]$, $\text{FeO}[\text{s}]$, $\text{FeS}[\text{s}]$ $\text{Fe}_2\text{O}_3[\text{s}]$, and $\text{Fe}_2\text{SiO}_4[\text{s}]$. These materials can grow through 59 bulk growth reactions.

The kinetic polymer nucleation of TiO_2 indicates a similar temperature and pressure dependence to previous non-classical studies. We tested different maximum cluster sizes between $N_{\max} = 7$ and $N_{\max} = 15$ and found differences of the predicted cloud particle number density within a factor of two. For further investigations, thermodynamic data of larger TiO_2 clusters is required. Overall, our results suggest that kinetic nucleation is a viable alternative to classical nucleation theory if the cluster data of the nucleating species is available. The required cluster sizes depend on the nucleating species.

The fully kinetic description of surface reactions resulted in a $\text{SiO}-\text{SiO}_2$ catalytic cycle that dissociates H_2 into 2 H. The increase in atomic hydrogen can reduce the CH_4 abundance by over an order of magnitude. Whether this catalytic cycle occurs in exoplanet atmospheres remains to be seen.

We simulated the chemistry of various $T_{\text{gas}}-p_{\text{gas}}$ points within the atmosphere of HD 209458 b. For all $T_{\text{gas}}-p_{\text{gas}}$ points, except the sub-stellar point, nucleation and bulk growth occurred. In all cases where nucleation occurred, nucleation and bulk growth reached a stationary behaviour within 1 s. A comparison to the timescales of quenching and chemical relaxation showed that nucleation can happen on much shorter timescales. Hence, our work confirms that the assumption of localised nucleation is generally justified in exoplanet atmospheres. For the cloud particle composition on the other hand, we found changes on the timescale larger than 10^3 seconds. This indicates that the composition of cloud particles can be susceptible to quenching.

Acknowledgments

S.K, H.L.M., Ch.H., and L.D. acknowledge funding from the European Union H2020-MSCA-ITN-2019 under grant agreement no. 860470 (CHAMELEON). N.B acknowledges financial support from the Austrian Academy of Sciences.

Chapter 5

Optical Properties of Heterogeneous Cloud Particles

This chapter is submitted for publication as:

Why heterogeneous cloud particles matter: Iron-bearing species and cloud particle morphology affects exoplanet transmission spectra

Sven Kiefer, Dominic Samra, David Andrew Lewis, Aaron David Schneider, Michiel Min, Leen Carone, Ludmila Decin, Christiane Helling

Author contribution:

Sven Kiefer performed the simulations and analyses, and wrote the manuscript. Dominic Samra helped implementing the cloud particle opacity calculations. David Lewis conducted the cloud simulations of WASP-76b. Aaron Schneider helped with the implementation of the transmission spectra calculations. Michiel Min, Ludmila Carone, Leen Decin, and Christiane Helling contributed via discussions and advice.

Original abstract:

The possibility of observing spectral features in exoplanet atmospheres with space missions like JWST and ARIEL necessitates the accurate modelling of cloud particle opacities. In exoplanet atmospheres, cloud particles can be made from multiple materials and be considerably chemically heterogeneous. Therefore, assumptions on the morphology of cloud particles are required to calculate their opacities. The aim of this work is to analyse how different approaches to calculate the opacities of heterogeneous cloud particles affect cloud particle optical properties and how this may effect the interpretation of data observed by JWST and future missions. We calculate cloud particle optical properties using seven different mixing treatments: four effective medium theories (EMTs: Bruggeman, Landau-Lifshitz-Looyenga (LLL), Maxwell-Garnett, and Linear), core-shell, and two homogeneous cloud particle approximations. We conduct a parameter study using two-component materials to study the mixing behaviour of 21 commonly considered cloud particle materials for exoplanets. To analyse the impact on observations, we study the transmission spectra of HATS-6b, WASP-39b, WASP-76b, and WASP-107b. Materials with large refractive indices, like iron-bearing species or carbon, can change the optical properties of cloud particles when they comprise less than 1% of the total particle volume. The mixing treatment of heterogeneous cloud particles also has an observable effect on transmission spectroscopy. Assuming core-shell or homogeneous cloud particles results in less muting of molecular features and retains the cloud spectral features of the individual cloud particle materials. The predicted transit depth for core-shell and homogeneous cloud particle materials are similar for all planets used in this work. If EMTs are used, cloud spectral features are broader and cloud spectral features of the individual cloud particle materials are not retained. Using LLL leads to less molecular features in transmission spectra compared to Bruggeman.

5.1 Introduction

Cloud formation models for exoplanet atmospheres predict significant cloud coverage for all but the very hottest exoplanets (Roman et al. 2021; Helling et al. 2023). However, until recently, the only observable impact of clouds on observations were characteristically flat transmission spectra (Bean et al. 2010; Kreidberg et al. 2014; Espinoza et al. 2019; Spyros et al. 2021; Libby-Roberts et al. 2022). Only with observations from the James Webb Space Telescope (JWST) is it now possible to directly measure spectral features characteristic of, for example silicate clouds in exoplanet atmospheres (Grant et al. 2023; Dyrek et al. 2023).

Many different cloud models for exoplanet atmospheres exist in literature which use different assumptions in order to describe the ensemble of particles that make up the clouds. The formation of clouds in exoplanet atmospheres starts with the formation of cloud condensation nuclei (CCNs) onto which other cloud particle materials can grow. Species like TiO_2 (Sindel et al. 2022), SiO (Lee et al. 2015), VO (Lecoq-Molinos et al. 2024) and KCl (Gao & Benneke 2018) are predicted to nucleate and grow homogeneously. Other materials, for example MgSiO_3 or ZnS , form on the surface of the CCNs. This leads to heterogeneous cloud particles. In the cloud formation model of Arfaux & Lavvas (2024), hazes made from soot particles act as CCNs onto which MgSiO_3 and Na_2S can form. To calculate the cloud particle opacities, they assume that the soot particles are neglectable and cloud particles are considered to be homogeneous. The cloud formation model CARMA (Turco et al. 1979; Toon et al. 1988; Jacobson et al. 1994; Ackerman et al. 1995; Bardeen et al. 2008; Gao & Benneke 2018) starts with TiO_2 and KCl nucleation onto which other species can grow (e.g. Fe , Cr , Al_2O_3 , Mg_2SiO_4 , Cr , MnS , and Na_2S ; Komacek et al. 2022). Their cloud particles are therefore made from one core species (either TiO_2 or KCl) and one shell species. This cloud particle morphology is called core-shell or core-mantle. The cloud formation model of Helling & Woitke (2006) (see also Helling et al. 2001; Woitke & Helling 2003, 2004; Helling et al. 2004) starts with TiO_2 , SiO , KCl , NaCl , and C nucleation onto which multiple other species can grow. This model considers surface reactions for the growth of cloud particle materials that are not stable as gas-phase molecules. They assume that all cloud particle materials are well-mixed.

Radiative transfer calculation for exoplanet atmospheres require the calculation of cloud opacities. In computationally expensive retrieval frameworks, clouds are often considered as a grey cloud deck where the opacity is assumed wavelength independent (e.g. Alderson et al. 2023; Rustamkulov et al. 2023) or are wavelength-dependently parameterised (e.g. Chubb & Min 2022; Feinstein et al. 2023). However, cloud particles have spectral features in transmission

Table 5.1: List of assumptions made by exoplanet atmosphere studies. Studies that consider absorption features within transmission spectra are labelled "Transm.". Studies that consider absorption features within the thermal emission of the planet are labelled "Therm.". Studies that consider radiative feedback of clouds within global circulation models are labelled "GCM". All cloud species are in the solid phase ([s]). Abbreviations used in this table: Bruggeman (Brg.), core-shell (cs.), homogeneous cloud particles (hom.), grey cloud deck (grey), and parameterised cloud description (par.).

Paper	Planet	Code	Use case	Approach	Cloud Species
Dyrek et al. (2023)	WASP-107b	ARCIS	Transm.	Brg.	MgSiO ₃ , SiO ₂ , SIO
		pRT	Transm.	par.	-
Grant et al. (2023)	WASP-17b	ATMO	Transm.	hom.	MgSiO ₃ , SiO ₂ , KCl
		VIRGA	Transm.	grey	-
		POSEIDON	Transm.	hom.	SiO ₂ , Al ₂ O ₃
Alderson et al. (2023)	WASP-39b	pRT	Transm.	grey	-
		VIRGA	Transm.	hom.	SiO ₂
		ATMO	Transm.	hom.	MnS, Na ₂ S, MgSiO ₃
Rustankulov et al. (2023)	WASP-39b	PHOENIX	Transm.	grey	-
		PICASO 3.0	Transm.	grey	-
		SeCHIMERA	Transm.	grey	-
		ATMO	Transm.	grey	-
		PHOENIX	Transm.	grey	-

Table 5.2: Continuation of Table B.1

Paper	Planet	Code	Use case	Approach	Cloud Species
Ahrer et al. (2023)	WASP-39b	VIRGA	Transm.	hom.	MnS, Na ₂ S, MgSiO ₃
Feinstein et al. (2023)	WASP39b	ATMO	Transm.	par.	-
		PHOENIX	Transm.	par.	-
		VIRGA	Transm.	hom.	MnS, Na ₂ S, MgSiO ₃
Arfaux & Lavvas (2024)	WASP-39b	ScCHIMERA	Transm.	grey	-
Lustig-Yaeger et al. (2023)	LHS 457 b	ScCHIMERA	Transm.	hom.	MgSiO ₃
Min et al. (2020)	Multiple	"unnamed"	Transm.	hom.	Na ₂ S, MgSiO ₃
		CHIMERA	Transm.	grey	-
		ARCSIS	Transm.	grey	SiO ₂ , Fe, FeS, Al ₂ O ₃ ,
Wong et al. (2020)	HAT-P-12b	CARMA	Transm.	cs.	C, MgSiO ₃ , TiO ₂ ,
Powell et al. (2019)	Test case	CARMA	Transm.	hom.	SiC, TiO ₂ , VO,
Kempton et al. (2023)	GJ 1214b	HyDRO	Therm.	hom.	Al ₂ O ₃ , Mg ₂ SiO ₄ ,
Chubb & Min (2022)	WASP-43b	ARCSIS	Therm.	par.	MnS, Na ₂ S, KCl, ZnS
Gao & Powell (2021)	Grid	CARMA	Therm.	cs.	TiO ₂ , Fe,
					Mg ₂ SiO ₄ , Al ₂ O ₃ , KCl
					-
					TiO ₂ , Fe, Cr, KCl,
					Mg ₂ SiO ₄ , MnS,
					Al ₂ O ₃ , Na ₂ S

Table 5.3: Continuation of Table B.1

Paper	Planet	Code	Use case	Approach	Cloud Species
Webber et al. (2015)	Kepler-7b	"unnamed"	Therm.	hom.	MgSiO ₃ , Mg ₂ SiO ₄ , Fe
Demory et al. (2013)	Kepler-7b	"unnamed"	Therm.	hom.	Mg ₂ SiO ₄
Lee (2023)	HAT-P-1b	Mini-Cloud	GCM	LLL	TiO ₂ , Al ₂ O ₃ , Fe, Mg ₂ SiO ₄
Christie et al. (2022)	GJ 1214b	UM	GCM	hom.	KCl, ZnS
Konacek et al. (2022)	Grid	"unnamed"	GCM	cs.	TiO ₂ , Fe, Cr, KCl, Mg ₂ SiO ₄ , Cr, MnS, Al ₂ O ₃ , Na ₂ S
Roman et al. (2021)	Grid	"unnamed"	GCM	hom.	KCl, ZnS, Na ₂ S, MnS, SiO ₂ , Mg ₂ SiO ₄ , VO, Ca ₂ SiO ₄ , CaTiO ₂ , Al ₂ O ₃ , Fe, Cr ₂ O ₃ , Ni, MgSiO ₃
Tan & Showman (2021)	Test case	MITgem	GCM	hom.	TiO ₂ , SiO, SiO ₂ , MgSiO ₃ , Mg ₂ SiO ₄
Lines et al. (2018b)	HD20945b	UM	GCM	Brg./LLL	TiO ₂ , SiO, SiO ₂ , Mg ₂ SiO ₄ , MgSiO ₃
Lee et al. (2016)	HD18973b	"unnamed"	GCM	Brg./LLL	Mg ₂ SiO ₄ , MgSiO ₃

spectra, in particular for wavelengths above $8 \mu\text{m}$ (Wakeford & Sing 2015). While grey clouds account for the general muting of molecular features in transmission spectra, it has been shown that non-grey clouds are needed to accurately interpret observations (Powell et al. 2019; Feinstein et al. 2023). Many studies therefore consider separate populations of homogeneous cloud particles to account for cloud particle features (e.g. Demory et al. 2013; Powell et al. 2019; Roman et al. 2021; Tan & Showman 2021; Christie et al. 2022; Grant et al. 2023; Feinstein et al. 2023; Kempton et al. 2023; Arfaux & Lavvas 2024). Other models also consider the optical properties of heterogeneous cloud particles (Lee et al. 2016; Lines et al. 2018b; Komacek et al. 2022; Min et al. 2020; Komacek et al. 2022; Dyrek et al. 2023; Lee et al. 2024). A summary of currently used assumptions for cloud opacity calculations can be found in Table 5.1.

The optical properties of homogeneous materials has been widely studied (see e.g. Table C.2 or Kitzmann & Heng 2018). The optical properties of heterogeneous cloud particles, however, are more complicated to derive. If the cloud particle materials are well-mixed within the cloud particle, effective medium theories¹ (EMTs) can be used (see Sect. 5.2.3). The three most commonly used EMTs are Bruggeman (Bruggeman 1935), Landau-Lifshitz-Looyenga (LLL Landau & Lifshitz 1960; Looyenga 1965), and Maxwell-Garnett (Garnett & Larmor 1904). While comparison studies between EMTs exist, they were mostly done for materials common in solid state physics (see e.g. Kolokolova & Gustafson 2001; Du et al. 2004; Franta & Ohlídal 2005).

Modelling cloud particles as spherical is a common assumption for studies of exoplanet atmospheres (e.g. Kitzmann & Heng 2018; Mai & Line 2019; Sanghavi et al. 2021; Komacek et al. 2022; Arfaux & Lavvas 2024; Grant et al. 2023; Jaiswal & Robinson 2023; Lee 2023). Although efforts have been made to model the opacities of fractal, or otherwise irregularly shaped, cloud particles in exoplanet atmospheres (e.g. Ohno et al. 2020). However, calculating more accurate refractive indices at the highest level of theory, requires the full knowledge of the material distribution within the grain (see e.g. Lodge et al. 2023). For example with the Discrete Dipole approximation (Draine & Flatau 1994), or the T-Matrix Method (Mackowski & Mishchenko 1996). Other theories have sought to simplify the interactions of irregularly shaped particles, either by assuming a statistical distribution of simpler shapes such as ellipsoids (Bohren & Huffman 1983; Min et al. 2003), or ‘hollow spheres’ (Min et al. 2003, 2005). In addition to this, approximations to the electromagnetic field as it interacts with an irregularly shaped grain, to allow for self-interaction of the cloud particle, have also been tried (Tazaki et al. 2016; Tazaki & Tanaka 2018). Lastly, the shape of cloud particles, and their material distribution can have

¹Also called effective medium approximations.

important consequences for the polarisation of cloud-scattered light (Draine 2024; Chubb et al. 2024).

The opacities of heterogeneous particles is studied for aerosols in Earth's atmosphere (e.g. Mishchenko et al. 2016; Stegmann & Yang 2017). Chýlek et al. (1988) found that the predictions from Bruggeman and Maxwell-Garnett for water inclusions in acrylic produce similar, but not identical, results to experiments. However, this only holds for well-mixed particles. Liu et al. (2014) have shown that EMTs only give accurate results if the characteristic size of individual inclusions is less than 0.12 times the wavelength they interact with. Several studies have looked at core-shell particles (e.g. Katrib et al. 2004; Lee et al. 2020b). McGrory et al. (2022) performed experiments using silica aerosols within a mist of sulphuric acid particles. They showed that aerosols within their setup had a core-shell morphology with silica being the core and sulphuric acid building the shell. The existence of core-shell morphology within Earth's aerosols is also supported by observations from Unga et al. (2018). Using remote sensing, they found that 60% of urban and 20% of desert aerosols present residuals of a core-shell morphology.

In this chapter, we study the optical properties of heterogeneous cloud particles in exoplanet atmospheres. We consider four EMTs (Bruggeman, LLL, Maxwell-Garnett, and Linear), the core-shell morphology, and two homogeneous cloud particle approximations (Sect. 5.2). We conduct a parameter study using two-component materials (Sect. 5.4) to study the mixing behaviour of 21 commonly considered cloud particle materials for exoplanets (see e.g. Powell et al. 2018; Helling et al. 2019a; Gao et al. 2021): Fe[s], FeO[s], Fe₂O₃[s], Fe₂SiO₄[s], FeS[s], TiO₂[s], SiO[s], CaTiO₃[s], SiO₂[s], MgO[s], MgSiO₃[s], Mg₂SiO₄[s], Al₂O₃[s], NaCl[s], KCl[s], C[s], C_{amorphous}[s], ZnS[s], Na₂S[s], MnO[s], MnS[s]. To study how heterogeneous cloud particle affects potential observations, we analyse the pressure dependent cloud structure and the transmission spectra of HATS-6b, WASP-39b, WASP-76b, and WASP-107b (Sect. 5.5). The results are discussed in Sect. 5.6 and the conclusion is given in Sect. 5.7.

5.2 Theoretical Basis

Cloud particles are an important opacity source in exoplanet atmospheres with complex optical properties. Sect. 5.2.1 describes how cloud particle absorption and scattering coefficients can be calculated. In this work we assume spherical cloud particles which allows one to use Mie theory to calculate their absorption and scattering efficiency (Sect. 5.2.2). Cloud particles in exoplanet atmospheres can be made from a mixture of different cloud particle materials (see e.g. Helling

et al. 2019a; Gao & Powell 2021). The morphology of cloud particles in exoplanet atmospheres is currently unknown and depends on how the cloud particles are formed. A common assumption is that all materials are well-mixed (see e.g. Lee et al. 2016; Lines et al. 2018b; Min et al. 2020; Helling et al. 2021). This assumption allows one to use EMTs to calculate the effective refractive index of heterogeneous cloud particles (Sect. 5.2.3). Another assumption is the core-shell morphology which occurs when condensates form a shell around a CCN core (Gao et al. 2021; Komacek et al. 2022, see e.g.). The core-shell morphology and two additional non-mixed treatments are considered in this study (Sect. 5.2.4).

5.2.1 Cloud particle opacities

The amount of radiation that gets absorbed or scattered by cloud particles is determined by their absorption coefficient $\kappa_{\text{abs}}^{\text{cloud}}(\lambda)$ [$\text{cm}^2 \text{ kg}^{-1}$] and the scattering coefficient $\kappa_{\text{sca}}^{\text{cloud}}(\lambda)$ [$\text{cm}^2 \text{ kg}^{-1}$]. Assuming spherical particles with radii a [cm], these coefficients are given by:

$$\kappa_{\text{abs}}^{\text{cloud}}(\lambda) = \int_{a_{\min}}^{\infty} \frac{\pi a^2 f_d(a)}{\rho_{\text{gas}}} Q_{\text{abs}}(a, \lambda, \epsilon_{\text{eff}}) da \quad (5.1)$$

$$\kappa_{\text{sca}}^{\text{cloud}}(\lambda) = \int_{a_{\min}}^{\infty} \frac{\pi a^2 f_d(a)}{\rho_{\text{gas}}} Q_{\text{sca}}(a, \lambda, \epsilon_{\text{eff}}) (1 - g) da \quad (5.2)$$

where $f_d(a)$ [cm^{-4}] is the cloud particle size distribution, a_{\min} [cm] the smallest radius of a particle for it to be considered a cloud particle, ρ_{gas} [g cm^{-3}] is the gas density, and λ [cm] the wavelength of the radiation. The variable ϵ_{eff} is the effective refractive index which is further discussed in Sect. 5.2.3. The variables Q_{abs} , Q_{sca} , and g are the absorption efficiency, scattering efficiency, and anisotropy factor, respectively. These three variables are calculated using Mie Theory (Sect. 5.2.2).

5.2.2 Mie Theory

Mie theory (Mie 1908) describes the solution to the Maxwell equations for the interaction of radiation with a sphere. The solution depends on the wavelength of the radiation λ , the radius of the sphere a , the dielectric constant ϵ_s of the sphere, and the dielectric constant of the surrounding medium ϵ_m . For cloud particles, the surrounding medium is vacuum which has $\epsilon_m = 1$. Mie theory calculations only depend on the relative size of the cloud particle and

the wavelength of the radiation. Thus Mie calculations use the size parameter:

$$x = 2\pi \frac{a}{\lambda} \quad (5.3)$$

A detailed description on how the absorption and scattering coefficients are calculated for cloud particles can be found in Gail & Sedlmayr (2013).

5.2.3 Effective medium theory

To calculate the interaction of cloud particles and radiation, the refractive index $n + ik$ of the cloud particles must be known. The refractive index is directly related to the dielectric constant ϵ of a material:

$$\epsilon = (n + ik)^2 \quad (5.4)$$

The real part of the refractive index n describes the ratio of the speed of light and the phase velocity of light in the medium. The imaginary part k describes the attenuation of the electromagnetic wave travelling through the medium.

Many studies of the optical properties of homogeneous cloud particle materials in exoplanet atmospheres exist (e.g. Wakeford & Sing 2015; Kitzmann & Heng 2018; Potapov & Bouwman 2022). The data used in this work can be found in Table C.2. Mixed materials on the other hand have complicated dielectric properties which depend on their composition and material distribution. Hence, simplifying assumptions have to be made to investigate these properties for clouds in exoplanet atmospheres. If one assumes a heterogeneous material to be well-mixed, its optical properties can be approximated by the effective dielectric constant

$$\epsilon_{\text{eff}} = (n_{\text{eff}} + ik_{\text{eff}})^2 \quad (5.5)$$

EMTs solve the electric fields for a mixture of materials to derive ϵ_{eff} . While ϵ is a precise description of the properties of a homogeneous material, ϵ_{eff} is an approximation under the assumption that a well-mixed material can be described equivalently to a homogeneous material.

The Maxwell-Garnett approximation (Garnett & Larmor 1904; Markel 2016) was derived to explain colours in metal glasses and in metallic films. It assumes one dominant material with small inclusions. This simplifies the calculation of the effective refractive index by neglecting interactions between inclusions. The effective dielectric constant is then given by the following formula:

$$\frac{\epsilon_{\text{eff}} - \epsilon_d}{\epsilon_{\text{eff}} + 2\epsilon_d} = \sum_i f_i \frac{\epsilon_i - \epsilon_d}{\epsilon_i + 2\epsilon_d} \quad (5.6)$$

where ϵ_d is the dielectric constant of the dominant material, ϵ_i are the dielectric constants of inclusions, and $f_i = V_i/V_{\text{tot}}$ is the volume fractions of the inclusions of material i , V_i [cm³] the volume of material i within a cloud particle, and V_{tot} [cm³] is the total volume of the cloud particle. For this work, we assume the cloud particle material with the largest volume fraction to be the dominant material and all others to be inclusions. Because this theory was derived for small inclusions, the accuracy of Maxwell-Garnett becomes questionable for volume fractions of inclusions above 10⁻⁶ (Belyaev & Tyurnev 2018). In exoplanet atmospheres, the volume fraction of the second most dominant cloud particle material is often predicted to be over 1% (Helling et al. 2023). Therefore, Maxwell-Garnett might not always be applicable.

The LLL approximation (Landau & Lifshitz 1960; Looyenga 1965) was derived for dispersive, powder-like mixtures. The derivation of the effective dielectric constant assumes small variations of the dielectric constant within small spherical inclusions of a larger sphere. The effective dielectric constant is then given by:

$$\epsilon_{\text{eff}} = \left(\sum_i f_i \sqrt[3]{\epsilon_i} \right)^3. \quad (5.7)$$

This equation presents an analytical solution for the effective dielectric constant ϵ_{eff} . Due to the short computational time, this technique is of special interest for larger frameworks which include heterogeneous cloud particles, like global circulation models (GCMs; see e.g., Lee 2023).

The Bruggeman approximation (Bruggeman 1935) assumes small, homogeneous inclusions. The derivation of the effective dielectric constant is done by replacing a small spherical inclusion within a sphere with a different material. The effective dielectric constant is then derived using the following equation:

$$\sum_i f_i \frac{\epsilon_i - \epsilon_{\text{eff}}}{\epsilon_i + 2\epsilon_{\text{eff}}} = 0. \quad (5.8)$$

The calculation of ϵ_{eff} using Bruggeman requires a minimisation scheme making it computationally intensive. This is in particular impractical for the implementation of cloud particles in larger frameworks. To combat this problem, Lee et al. (2016) used a Newton-Raphson minimisation, but fall back to LLL if no solution can be found within a given number of iteration steps.

The most simplistic approximation of the effective dielectric constants is derived by linearly summing dielectric constants for each material, weighted by their volume fraction (Mackwell et al. 2014; Kahnert 2015):

$$\epsilon_{\text{eff}} = \sum_i f_i \epsilon_i. \quad (5.9)$$

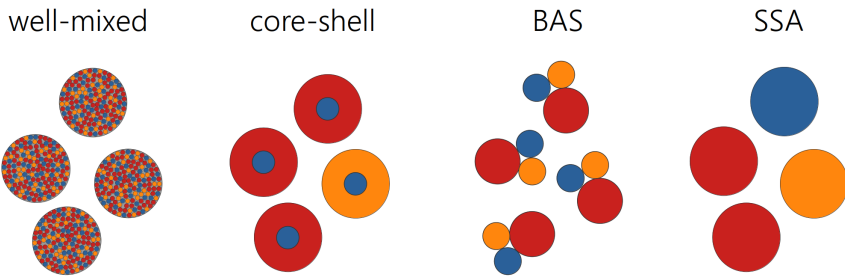


Figure 5.1: Representation of the cloud particle morphology assumptions behind well-mixed, core-shell, batch approximation of spheres (BAS), and system of spheres approximation (SSA) cloud particles.

This approximation is called Linear from here on. It is important to note that the Linear approximation is not derived from the electrical properties of the mixed material like the other EMTs. Thus, it is unlikely to accurately represent the optical properties of a mixed material. However, this technique can be used to, for example, finding a suitable starting condition for the minimisation of Bruggeman.

5.2.4 Non-mixed treatments of cloud particles

In the most general case, cloud particle opacities will depend on their exact composition, shape, and material distribution. EMTs simplify this complexity by assuming well-mixed grains. However, certain materials within a cloud particle might form larger homogeneous inclusions making EMTs no longer applicable. In this case, non-mixed treatments are required. A visualisation of the different theories used in this work is shown in Fig. 5.1.

The core-shell morphology describes a particle consisting of a homogeneous core surrounded by a homogeneous shell. This morphology is consistent with cloud particle materials forming a shell around a CCN core and is assumed by, for example, CARMA. Typically, both core and shell are assumed spherical. The absorption and scattering efficiency for a core-shell morphology can be calculated similar to Mie theory (Toon & Ackerman 1981). In the case where multiple species can condense simultaneously, each shell material is assumed to form their own population of cloud particles. Therefore, each cloud particle consists at most of two cloud particle materials.

The Batch Approximation of Spheres (BAS) assumes that each cloud particle material forms a single sphere within the cloud particle. The volume of this sphere is equal to the volume fraction of the cloud particle material. Each cloud particle therefore consists of multiple spheres, each made from a single material. To simplify the calculation of the cloud particle opacities, interactions between the spheres and their overlaps are neglected. The absorption and scattering coefficients (see Eq. 5.1 and 5.2) are then adjusted accordingly:

$$\kappa_{\text{abs}}^{\text{cloud}}(\lambda) = \int_{a_{\min}}^{\infty} \frac{\pi f_d(a)}{\rho_{\text{gas}}} \sum_{i \in \mathcal{M}} \left(f_i^{1/3} a \right)^2 Q_{\text{abs}}(f_i^{1/3} a, \lambda, \epsilon_i) da \quad (5.10)$$

$$\kappa_{\text{sca}}^{\text{cloud}}(\lambda) = \int_{a_{\min}}^{\infty} \frac{\pi f_d(a)}{\rho_{\text{gas}}} \sum_{i \in \mathcal{M}} \left(f_i^{1/3} a \right)^2 Q_{\text{sca}}(f_i^{1/3} a, \lambda, \epsilon_i)(1 - g) da \quad (5.11)$$

where \mathcal{M} is the set of all cloud particle materials. Since overlapping is neglected, this represents an upper limit of the cloud particle opacity. Furthermore, the interaction between cloud particle materials could lead to spectral features which cannot be reproduced with BAS.

The System of Spheres Approximation (SSA) assumes that all cloud particle materials are separated into homogeneous, spherical cloud particles with a radius of $\langle a \rangle$. This assumption is equivalent to other studies which assume multiple homogeneous species with the same cloud particle radius but different number densities (e.g. Roman et al. 2021; Dyrek et al. 2023). For SSA, the cloud particle number density of each cloud particle material is proportional to the volume fraction f_i . The absorption and scattering coefficients (see Eq. 5.1 and 5.2) are than adjusted accordingly:

$$\kappa_{\text{abs}}^{\text{cloud}}(\lambda) = \int_{a_{\min}}^{\infty} \frac{\pi a^2}{\rho_{\text{gas}}} \sum_{i \in \mathcal{M}} f_i f_d(a) Q_{\text{abs}}(a, \lambda, \epsilon_i) da \quad (5.12)$$

$$\kappa_{\text{sca}}^{\text{cloud}}(\lambda) = \int_{a_{\min}}^{\infty} \frac{\pi a^2}{\rho_{\text{gas}}} \sum_{i \in \mathcal{M}} f_i f_d(a) Q_{\text{sca}}(a, \lambda, \epsilon_i)(1 - g) da \quad (5.13)$$

While SSA does not require any additional assumption on the optical properties of the cloud particles, it is inconsistent with cloud formation models which predict that materials like $\text{Mg}_2\text{SiO}_4[\text{s}]$ form heterogeneously (see e.g. Helling & Woitke 2006; Gao et al. 2020). It is therefore not expected that cloud particles in exoplanet atmospheres will all be homogeneous.

5.3 Approach

After examining the theoretical basis, we continue to detail our approach. The calculation of the cloud particle opacities are explained in Sect. 5.3.1 with the transmission spectra calculations following in Sect. 5.3.3. All methods laid out here are available within the software package **Claus**.

5.3.1 Cloud opacity calculation

For all calculations in this study, we assume spherical cloud particles and calculate the absorption and scattering efficiencies using Mie theory. However, the solution of Mie theory includes an infinite sum and thus has to be solved numerically. A comparison between different Mie-solvers can be found in Appendix C.1. Overall, we found little differences between the implementations and thus decided to use **PyMieScatt** for this study (Sumlin et al. 2018). Within **Claus**, **miepython** (Wiscombe 1979; Prahl 2023), and **Miex** (Wolf & Voshchinnikov 2004) are also available.

The cloud particle opacities are calculated by approximating the optical properties of all cloud particle sizes with cloud particles of an average radius $\langle a \rangle$ [cm]. While size distributions do affect the optical properties of cloud layers, a detailed investigation of their impact on transmission spectra goes beyond the scope of this thesis. To calculate the cloud particle number density, we use the cloud particle mass fraction ρ_v/ρ_{gas} :

$$n_d = \frac{\rho_v}{\rho_{\text{gas}}} \frac{1}{\frac{3}{4}\pi\langle a \rangle^3\rho_c} \quad (5.14)$$

where ρ_v [g cm⁻³] is the cloud particle mass per atmospheric volume, ρ_{gas} [g cm⁻³] is the gas density, and ρ_c [g cm⁻³] is the cloud particle material density. The cloud particle absorption coefficient from Eq. 5.1 is thus given by:

$$\kappa_{\text{abs}}^{\text{cloud}}(\lambda) = \frac{\pi\langle a \rangle^2}{\frac{3}{4}\pi\langle a \rangle^3\rho_c} \frac{\rho_v}{\rho_{\text{gas}}} Q_{\text{abs}}(\langle a \rangle, \lambda, \epsilon_{\text{eff}}) \quad (5.15)$$

The opacity calculations from Eq. 5.2, 5.10, 5.11, 5.12, and 5.13 are adjusted accordingly. The cloud particle opacities therefore depend on the following cloud particle properties:

- The average cloud particle radius $\langle a \rangle$ [cm]
- The cloud particle material density ρ_c [g cm⁻³]

- The cloud mass fraction ρ_v/ρ_{gas}
- The refractive index of the cloud particle ϵ_{eff} or ϵ_i

To study the opacities of heterogeneous cloud particles, we first analyse two-component materials (Sect. 5.4). A two-component material {A, B} is a composite material made from the mixture of the materials A and B. They find a broad use in solid state physics and hence multiple effective medium studies exist (see e.g. Du et al. 2004; Ghanbarian & Daigle 2016). In this study, we use materials commonly considered in exoplanet atmospheres and vary the relative abundance of A and B. First, the two-component material {Fe[s], Mg₂SiO₄[s]} is used to compare the effective refractive index from different EMTs (Sect. 5.4.1). Afterwards, we consider the mixture of Mg₂SiO₄[s] with 16 other commonly considered cloud particle materials² in hot Jupiters (Sect. 5.4.2) and ZnS[s] with 5 commonly considered cloud particle materials³ of temperate atmospheres (Sect. 5.4.3). To compare the absorption and scattering coefficients of EMTs and non-mixed approaches, we use again the two-component material {Fe[s], Mg₂SiO₄[s]} (Sect. 5.4.4).

In hot Jupiter atmospheres, cloud particles can consist of more than two materials. To study the optical properties of considerably heterogeneous cloud particles, we use the results from a detailed micro-physical cloud model (Helling & Woitke 2006). First, we investigate the optical properties of clouds at various heights within the atmosphere of WASP-39b (Sect. 5.5.1). Afterwards, we analyse the impact of cloud particle mixing treatments on the transmission spectrum of WASP-39b and HATS-6b (Sect. 5.5.2). The best target for studying the composition and morphology of cloud particles is an exoplanet where cloud materials have been detected in the gas phase and whose atmosphere is predicted to contain clouds. One such planet is WASP-76b, which we are analysing in more detail (Sect. 5.5.3). Since the optical properties of cloud particles do not only affect the predictions of forward models but also retrievals, we take a closer look at WASP-107b using the results from the ARCiS retrieval of Dyrek et al. (2023) (Sect. 5.5.4).

5.3.2 Cloud modelling

In Sect. 5.5, the cloud structure of 4 planets is studied: HATS-6b, WASP-39b, WASP-76b, and WASP-107b. The cloud modelling approaches for these planets

²For hot Jupiters we consider Fe[s], FeO[s], Fe₂O₃[s], Fe₂SiO₄[s], FeS[s], TiO₂[s], SiO[s], CaTiO₃[s], SiO₂[s], MgO[s], MgSiO₃[s], Mg₂SiO₄[s], Al₂O₃[s], NaCl[s], KCl[s], C[s], and C_{Amorphous}[s].

³For temperate atmospheres, we consider NaCl[s], KCl[s], ZnS[s], Na₂S[s], MnO[s], and MnS[s].

is described in this section.

The cloud structures of HATS-6b , WASP-39b, and WASP-76b are done using a hierarchical forward modelling approach. The temperature and wind structure are modelled using expeRT/MITgcm (Carone et al. 2020; Schneider et al. 2022c) which is cloud-free. The GCM simulations were done by Carone et al. (2023) for WASP-39b, Kiefer et al. subm. for HATS-6b, and Schneider et al. (2022b) for WASP-76b. The output of the GCM is then used to calculate the cloud structure. For this, one dimensional temperature, pressure, and vertical velocity profiles were extracted from the GCM and used as input for the kinetic cloud model developed by Helling & Woitke (2006) (see also Woitke & Helling 2003, 2004; Helling et al. 2004, 2008b, 2019a). This model includes micro-physical nucleation, bulk growth, and evaporation which are combined with gravitational settling, element consumption, and replenishment. A list of all nucleating species and cloud particle materials considered can be found in Table C.1. The cloud structures were derived by Carone et al. (2023) for WASP-39b and Kiefer et al. subm. for HATS-6b. For WASP-76b, the cloud structures are produced here for the first time. All 1D profiles used in this work are shown in Fig. C.12 (HATS-6b), Fig. C.13 (WASP-39b), and Fig. C.14 (WASP-76b).

To calculate the transmission spectra of all three planets, 1D profiles from multiple latitudes within the morning and evening terminator were considered. The opacities of the cloud particles were calculated based on these profiles and the different mixing treatments as described in Sect. 5.2. For the calculation of core-shell opacities, the dominant nucleation species was selected as the core species. For WASP-39b and HATS-6b, this is SiO[s]. For WASP-76b this is TiO₂[s].

The cloud structure of WASP-107b is taken from the ARCiS (Min et al. 2020) retrieval results of Dyrek et al. (2023). In contrast to the other planets, the temperature-pressure profile, gas-phase abundances, and cloud particle properties (V_s/V_{tot} , $\langle a \rangle$, n_d) are derived from a free retrieval based on JWST MIRI observations. This means that the model does not include a micro-physical cloud formation description. The opacities of the cloud particles were calculated based on the retrieved cloud particle properties and the different mixing treatments as described in Sect. 5.2. For the calculation of core-shell opacities, SiO[s] was selected as the core species.

5.3.3 Transmission spectrum

To calculate the transmission spectrum of cloudy exoplanet atmospheres, the cloud particle opacities are added as an additional opacity source to petitRADTRANS (Mollière et al. 2019, 2020; Alei et al. 2022). The number

densities of gas-phase species are calculated within the cloud model, thereby assuming chemical equilibrium and including the depletion of gas-phase species due to cloud formation⁴.

The following species were considered as gas-phase opacity species within the radiative transfer (Chubb et al. 2020): H₂O (Polyansky et al. 2018), CO₂ (Yurchenko et al. 2020), CO (Li et al. 2015), TiO (McKemmish et al. 2019), Na (Piskunov et al. 1995), and K (Piskunov et al. 1995). Rayleigh scattering is included by considering H₂ (Dalgarno & Williams 1962) and He (Chan & Dalgarno 1965). Collision-induced absorption (CIA) is considered from H₂–H₂ and H₂–He (Borysow et al. 1988, 1989; Borysow & Frommhold 1989; Borysow et al. 2001; Richard et al. 2012; Borysow 2002).

The references for the optical properties of homogeneous materials are listed in Table C.2. Because no opacity data are available for CaSiO₃[s], its refractive index is set to vacuum for all calculations⁵. Heterogeneous particles are calculated using EMT (see Sect. 5.2.3). Planetary parameters used for the transmission spectrum calculation can be found in Table C.1. Generally, it is expected that clouds mute molecular features in the optical and near infrared, resulting in a flat transmission spectrum (Bean et al. 2010; Kreidberg et al. 2014; Powell et al. 2019). Signatures of metal-oxide bonds of cloud particle materials can impact the spectra typically around and above 10 μm (Wakeford & Sing 2015; Grant et al. 2023; Dyrek et al. 2023).

5.4 Mixing behaviour of cloud particle materials

We present the effective refractive index of mixed cloud particles. Here, we focus on two-component materials in order to understand the differences between the mixing treatments and different cloud particle materials. In Sect 5.4.1, we compare the predicted effective refractive index and absorption efficiency from LLL, Bruggeman, Maxwell-Garnett, and Linear. In Sect. 5.4.2, we analyse materials commonly predicted to form clouds in hot Jupiter atmospheres and in Sect. 5.4.3, materials commonly predicted for temperate exoplanets. Non-mixed treatments do not assume an effective refractive index but employ different types of Mie theory calculation. In Sect. 5.4.4, we compare the absorption and scattering efficiencies from LLL, core-shell, BAS, and SSA.

⁴The only exception to this is the transmission spectrum of WASP-107b which uses the retrieval results instead.

⁵Another approach is to approximate the opacity of CaSiO₃[s] with MgSiO₃[s]. A comparison between the two approaches can be found in Appendix C.2.

5.4.1 Effective refractive index from EMTs

The effective refractive index is calculated using Bruggeman (Eq. 5.8), LLL (Eq. 5.7), Maxwell-Garnett (Eq. 5.6), and Linear (Eq. 5.9). These calculation depend only on the refractive index and the volume mixing ratio of the cloud particle material. Here, we use the example two-component material {Fe[s], Mg₂SiO₄[s]}. Since forsterite (Mg₂SiO₄[s]) is often discussed as a dominant cloud particle material (Powell et al. 2018; Gao et al. 2020; Helling et al. 2021, 2023), we chose it to be the first component of all two-component materials in this section. Iron-bearing species are of great interest for this study because of their large imaginary part k of the refractive index compared to other cloud particle materials. We therefore choose Fe[s] as the second material. The effective refractive index of {Fe[s], Mg₂SiO₄[s]} for a wavelength range of 0.08 μm to 39 μm and for Fe[s] volume fractions between 0 and 1 can be seen in Fig. 5.2. The absolute relative differences between the EMTs can be seen in Appendix Fig. C.2.

In Fig.. 5.2, LLL and Linear predict similar effective refractive indices for most wavelengths. In contrast to the other EMTs, both LLL and Linear show a strong increase in k_{eff} with increasing Fe[s] volume fraction. From 10 μm to 30 μm , features in the n_{eff} and k_{eff} values can be seen which are caused by peaks in the values of the refractive index of Mg₂SiO₄[s]. These features diminish with increasing Fe[s] volume fraction. The biggest difference between LLL and Linear is around 10 μm where LLL predicts up to 50% smaller n_{eff} and k_{eff} values. This wavelength corresponds to a vibrational resonance of Si-O bonds (see e.g. Gunde 2000; Sogawa et al. 2006). Therefore, this difference can be explained by the third root of the dielectric constant within LLL (see Eq. 5.7) which reduces the impact of resonances on the effective dielectric constant.

Maxwell-Garnett shows an abrupt change in k_{eff} and n_{eff} values at 0.5 volume fraction. This corresponds to the change in the dominant cloud particle material. When Mg₂SiO₄[s] is the dominant cloud particle material the values for k_{eff} and n_{eff} are lower for wavelengths above 8 μm . Maxwell-Garnett showing differences to other EMTs for larger volume fractions of iron is not unexpected since the validity of Maxwell-Garnett is only guaranteed for volume fractions below 10⁻⁶ (Belyaev & Tyurnev 2018). However, our results show that for Mg₂SiO₄[s] volume fractions of less than 0.1, Maxwell-Garnett and Bruggeman differ by less than 10% for this particular two-component material.

Bruggeman and LLL predict different effective refractive indices for all wavelengths above 0.2 μm . This finding is in agreement with other studies which also found significant differences between Bruggeman and LLL (Du et al. 2004). Especially for Fe[s] volume fraction below 0.3 and for wavelengths above 1 μm ,

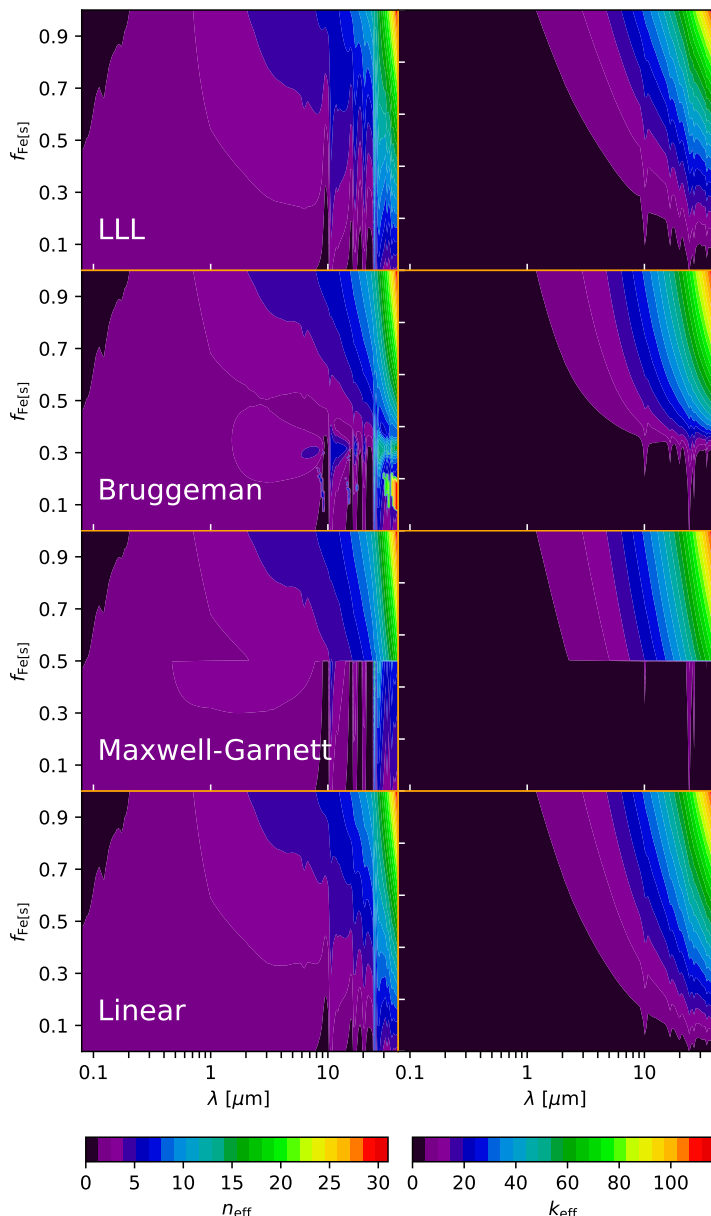


Figure 5.2: Effective refractive index of the two-component material $\{\text{Fe[s]}, \text{Mg}_2\text{SiO}_4[\text{s}]\}$ calculated using different EMTs. **Left:** real part n_{eff} . **Right:** imaginary part k_{eff} .

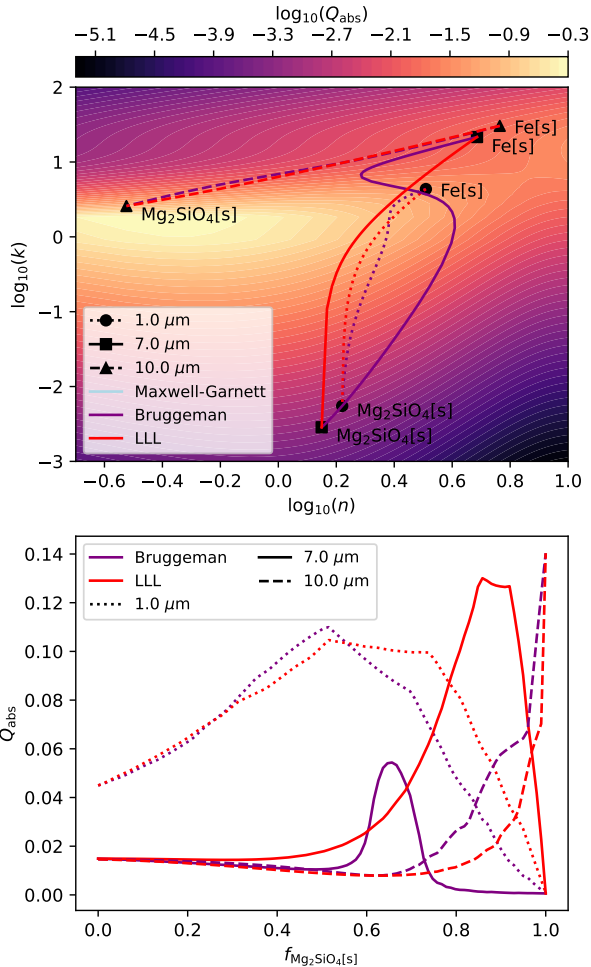


Figure 5.3: **Top:** Absorption efficiency Q_{abs} for a range of n and k values at $x = 0.1$. Also shown are the k_{eff} and n_{eff} values for the two-component material $\{\text{Fe}[\text{s}], \text{Mg}_2\text{SiO}_4[\text{s}]\}$ at wavelengths 1 μm , 7 μm , and 10 μm . The end points denote homogeneous materials. The lines between the end points represent different volume fractions of the two materials. **Bottom:** Absorption efficiency Q_{abs} for different volume fractions of the two-component material $\{\text{Fe}[\text{s}], \text{Mg}_2\text{SiO}_4[\text{s}]\}$ at wavelengths 1 μm , 7 μm , and 10 μm .

Bruggeman predicts significantly lower k_{eff} . The computational cost of LLL, Maxwell-Garnett and Linear is roughly the same. Linear is $\sim 10\%$ faster than LLL, and LLL is $\sim 5\%$ faster than Maxwell-Garnett. Bruggeman, however, takes roughly 1000 times longer than LLL. This is mainly due to the minimisation required to solve Bruggeman whereas LLL, Maxwell-Garnett and Linear have analytical solutions.

The effective refractive index calculation for the two component material $\{\text{Fe[s]}, \text{Mg}_2\text{SiO}_4[\text{s}]\}$ clearly highlights the limitations of Maxwell-Garnett and Linear for applications to heterogeneous cloud particles in exoplanet atmospheres. From here on, we will therefore focus on the EMTs Bruggeman and LLL.

The effective refractive index directly impacts the absorption efficiency Q_{abs} and scattering efficiency Q_{sca} . To investigate how Mie theory and EMTs interact, we calculate Q_{abs} for the Bruggeman, Maxwell-Garnett, and LLL EMTs. We use the two-component material $\{\text{Fe[s]}, \text{Mg}_2\text{SiO}_4[\text{s}]\}$ and assume a size parameter of $x = 0.1$ for the Mie calculation. The top panel of Fig. 5.3 shows the values of Q_{abs} for different k_{eff} and n_{eff} values. Within this figure, the change of the effective refractive indices with volume fraction is shown for the wavelengths $1 \mu\text{m}$, $7 \mu\text{m}$, and $10 \mu\text{m}$. The end points of each line denote homogeneous materials. The bottom panel of Fig. 5.3 shows the Q_{abs} along the volume fraction lines shown in the top panel. The same evaluation for a size parameter of $x = 1$ (Fig. C.3), the extinction efficiency (Fig. C.4), the scattering efficiency (Fig. C.5), and the two component material $\{\text{TiO}_2[\text{s}], \text{Mg}_2\text{SiO}_4[\text{s}]\}$ (Fig. C.6) can be found in the Appendix C.

For $1 \mu\text{m}$, both LLL and Bruggeman predict a higher Q_{abs} for volume fractions around 0.5 than a homogeneous particle made from either Fe[s] or $\text{Mg}_2\text{SiO}_4[\text{s}]$ alone. This can be explained by a maxima of Q_{abs} for k around ~ 1.4 as predicted by Mie-theory. Min et al. (2005) showed that this maximum is a consequence of the spherical particles assumption. Because k_{eff} and n_{eff} values for a volume fraction around 0.5 are closer to the maxima, these particles have a larger Q_{abs} value. At $7 \mu\text{m}$ a similar behaviour as for $1 \mu\text{m}$ can be seen. However, LLL approaches the maxima much closer than Bruggeman, resulting in a peak in Q_{abs} values around 0.9 $\text{Mg}_2\text{SiO}_4[\text{s}]$ volume fraction. Bruggeman, on the other hand, avoids the maxima and only peaks around 0.65 $\text{Mg}_2\text{SiO}_4[\text{s}]$ volume fraction. At $10 \mu\text{m}$, the refractive index of homogeneous $\text{Mg}_2\text{SiO}_4[\text{s}]$ particles is very close to the maxima, resulting in large Q_{abs} values. The higher the volume fraction of Fe[s] , the weaker this peak in opacity becomes. Here, all EMTs predict a similar behaviour with volume fraction.

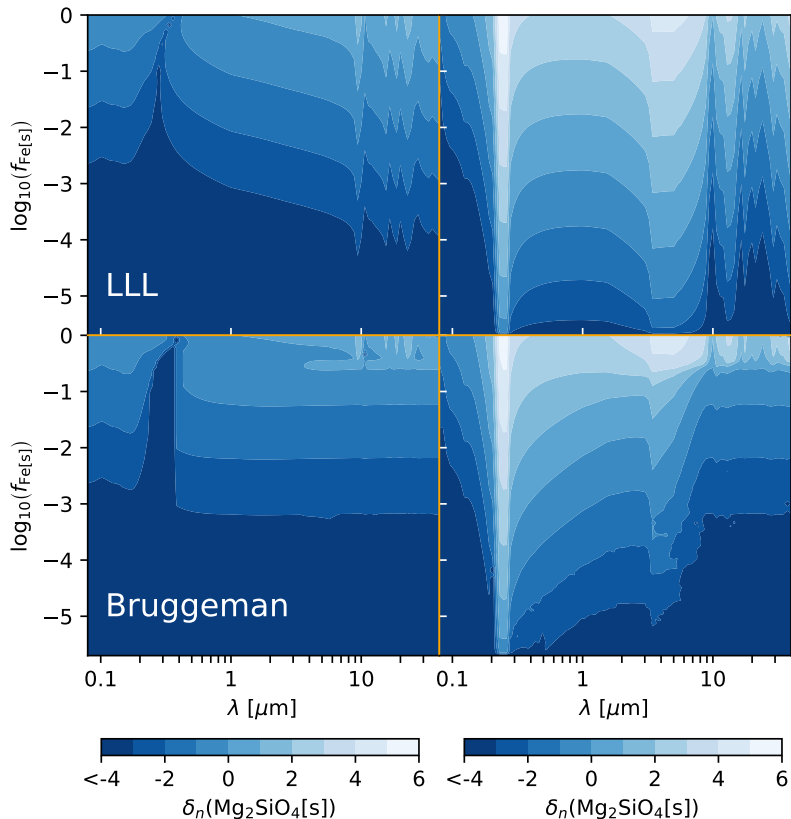


Figure 5.4: Differences of the real and imaginary part of the refractive index (Eq. 5.16) of the two-component material $\{\text{Mg}_2\text{SiO}_4[\text{s}], \text{Fe}[\text{s}]\}$ compared to the refractive index of $\text{Mg}_2\text{SiO}_4[\text{s}]$.

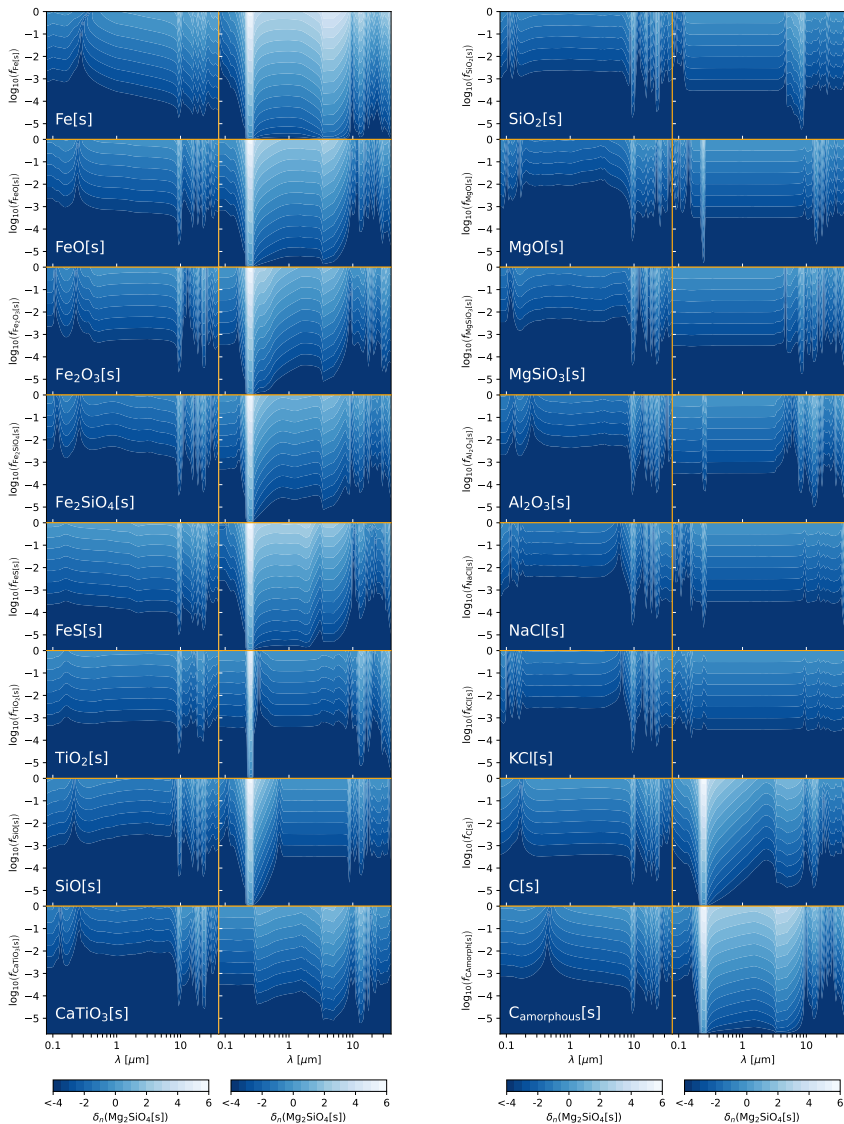


Figure 5.5: Differences of the real and imaginary part of the refractive index (Eq. 5.16) for two-component materials compared to the refractive index of $Mg_2SiO_4[s]$. The first component is $Mg_2SiO_4[s]$ and the second component is specified in each plot.

5.4.2 Effective refractive index for clouds in hot Jupiter

Clouds in atmospheres of hot Jupiters can be significantly heterogeneous. The most common materials are thought to be iron-, silicon-, or magnesium-bearing species (Helling & Woitke 2006; Powell et al. 2018; Helling et al. 2023). In this section, we use two-component materials to analyse the mixing behaviour of different cloud particle materials. While this does not reflect the complexity of cloud particles in a real exoplanet atmosphere, it allows for an analytical study of the wavelength and volume fraction dependence of the effective refractive index. Similar to Sect. 5.4.1, we choose the two-component material $\{\text{Mg}_2\text{SiO}_4[\text{s}], \text{Fe}[\text{s}]\}$. The goal is to determine at which volume fraction $\text{Fe}[\text{s}]$ inclusions significantly impact the effective refractive index.

We calculate the logarithm of the absolute relative difference δ_n of n_{eff} compared to $n_{\text{Mg}_2\text{SiO}_4[\text{s}]}$ as:

$$\delta_n(\text{Mg}_2\text{SiO}_4[\text{s}]) = \log_{10} \left(\frac{|n_{\text{eff}} - n_{\text{Mg}_2\text{SiO}_4[\text{s}]}|}{n_{\text{Mg}_2\text{SiO}_4[\text{s}]}} \right) \quad (5.16)$$

and equivalently the absolute relative difference $\delta_k(\text{Mg}_2\text{SiO}_4[\text{s}])$ of k_{eff} compared to $k_{\text{Mg}_2\text{SiO}_4[\text{s}]}$. The results for a wavelength range of $0.08 \mu\text{m}$ to $39 \mu\text{m}$ are shown in Fig. 5.4. Iron volume fractions of less than 1% can already increase k_{eff} more than 10 times for the wavelength range from $\sim 0.2 \mu\text{m}$ to $\sim 10 \mu\text{m}$. The peak difference around $\sim 0.2 \mu\text{m}$ is caused by a sudden drop in $k_{\text{Mg}_2\text{SiO}_4[\text{s}]}$ values for these wavelengths. This increase can be seen for both LLL and Bruggeman. LLL also shows a large increase for volume fractions below 0.1% around $4 \mu\text{m}$ which is less pronounced for Bruggeman. Overall, these results show that the effective refractive index of cloud particles are strongly affected by the EMT used to calculate it.

To analyse further two-component materials of cloud forming species in hot Jupiter, we focus on LLL. We consider a bulk material of forsterite with inclusions of various other likely cloud materials. Forsterite ($\text{Mg}_2\text{SiO}_4[\text{s}]$) is chosen as the bulk material, because it is frequently the dominant cloud particle material in the observable part of the atmosphere (Gao et al. 2020; Helling et al. 2023). Fig. 5.5 shows the absolute relative differences compared to the refractive index of $\text{Mg}_2\text{SiO}_4[\text{s}]$. The same evaluation using Bruggeman instead of LLL can be found in Appendix Fig. C.7. The results show that all iron-bearing species ($\text{Fe}[\text{s}]$, $\text{FeO}[\text{s}]$, $\text{Fe}_2\text{O}_3[\text{s}]$, $\text{Fe}_2\text{SiO}_4[\text{s}]$, and $\text{FeS}[\text{s}]$) and carbon ($\text{C}[\text{s}]$ and $\text{C}_{\text{amorphous}}[\text{s}]$) strongly impact k_{eff} in the wavelength range from approximately $\sim 0.2 \mu\text{m}$ to $\sim 10 \mu\text{m}$. $\text{TiO}_2[\text{s}]$ and $\text{SiO}[\text{s}]$ can also significantly impact k_{eff} , but mostly around $0.2 \mu\text{m}$ which is caused by a sudden drop in $k_{\text{Mg}_2\text{SiO}_4[\text{s}]}$ values. The other materials ($\text{CaTiO}_3[\text{s}]$, $\text{SiO}_2[\text{s}]$, $\text{MgO}[\text{s}]$, $\text{MgSiO}_3[\text{s}]$, $\text{Al}_2\text{O}_3[\text{s}]$, $\text{NaCl}[\text{s}]$, and $\text{KCl}[\text{s}]$) have a lesser impact on the effective refractive index. While they

still can change k_{eff} by more than 10 times, they do so only for volume fractions above 10%. The real part of the effective refractive index n_{eff} is mostly affected around 10 μm . This wavelength corresponds to optical features of Mg_2SiO_4 .

5.4.3 Effective refractive index for clouds in temperate atmospheres

In temperate exoplanet atmospheres refractive cloud particle materials, like $\text{Mg}_2\text{SiO}_4[\text{s}]$, might form cloud layers only below the photosphere of the planet (Morley et al. 2012). In these environments, cloud particle materials like $\text{KCl}[\text{s}]$, $\text{ZnS}[\text{s}]$, and $\text{MnS}[\text{s}]$ are often discussed as the dominant cloud particle opacity species (Mbarek & Kempton 2016; Gao & Benneke 2018; Christie et al. 2022). We analyse two component materials with $\text{ZnS}[\text{s}]$ as bulk species and $\text{KCl}[\text{s}]$, $\text{MnS}[\text{s}]$, $\text{Na}_2\text{S}[\text{s}]$, $\text{MnO}[\text{s}]$, and $\text{NaCl}[\text{s}]$ as inclusions. All results are obtained using LLL and expressed in $\delta_n(\text{ZnS}[\text{s}])$ and $\delta_n(\text{ZnS}[\text{s}])$. Inclusions of $\text{KCl}[\text{s}]$ and $\text{NaCl}[\text{s}]$ do not affect the effective refractive index up to volume fractions of 10%. Sulphur-bearing and $\text{MnO}[\text{s}]$ inclusions on the other hand can become important at volume fractions of less than 1%. Overall, our results show that sulphur-bearing species do not have common properties like iron-bearing species. Their impact on heterogeneous cloud optical properties depend on the specific sulphur-bearing cloud particle species.

5.4.4 Non-mixed versus EMT

In contrast to EMTs, non-mixed treatments assume that cloud particles consist of multiple, homogeneous parts. In this section, we compare the absorption and scattering efficiency for a 1 μm cloud particle made of $\text{TiO}_2[\text{s}]$ and $\text{Fe}[\text{s}]$. $\text{TiO}_2[\text{s}]$ is often considered as a CCN in hot Jupiters (Lee et al. 2015; Powell et al. 2018; Sindel et al. 2022; Kiefer et al. 2023, 2024). Therefore for the core-shell morphology, we assume that $\text{TiO}_2[\text{s}]$ forms the core and $\text{Fe}[\text{s}]$ forms the shell. The results for a wavelength range of 0.08 μm to 39 μm and $\text{TiO}_2[\text{s}]$ volume fractions between 0 and 1 are shown in Fig. 5.7.

The absorption and scattering efficiencies are different for each mixing treatment. At 7 μm to 8 μm , the absorption efficiency from LLL, Bruggeman, and core-shell have higher values than either $\text{Fe}[\text{s}]$ or $\text{TiO}_2[\text{s}]$ in their homogeneous form. This matches the findings from Sect. 5.4.1, where we have shown that mixed cloud particle can have higher absorption efficiencies than homogeneous particles. BAS and SSA on the other hand have their maximum value for homogeneous $\text{Fe}[\text{s}]$ or $\text{TiO}_2[\text{s}]$. Furthermore, their absorption efficiency shows a $\text{TiO}_2[\text{s}]$ feature above 10 μm even at volume fractions below 30%. The same feature for LLL,

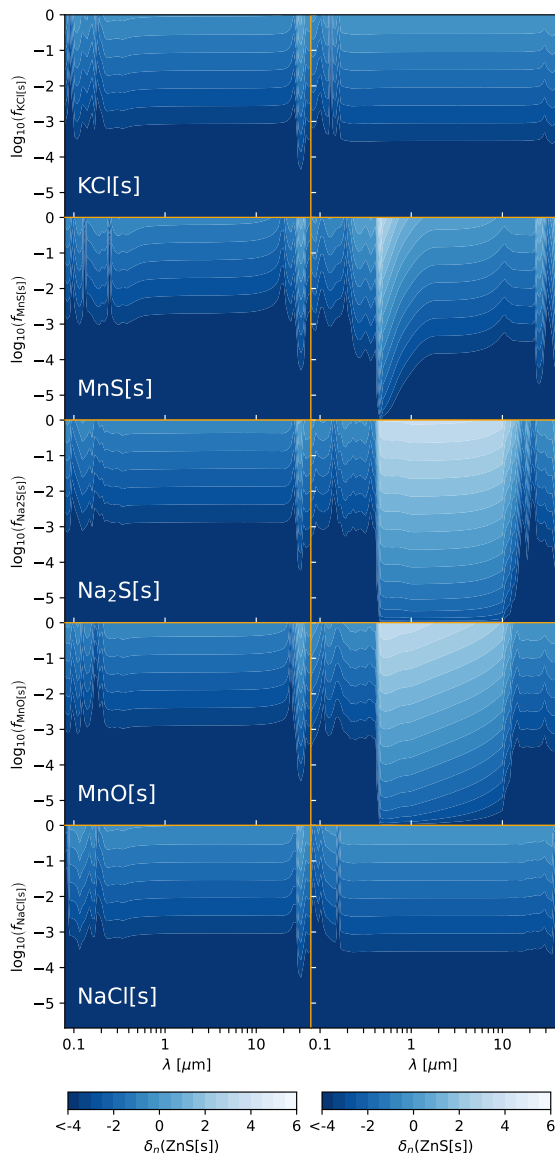


Figure 5.6: Differences of the real and imaginary part of the refractive index (Eq. 5.16) for two-component materials compared to the refractive index of ZnS[s]. The first component is ZnS[s] and the second component is specified in each plot.

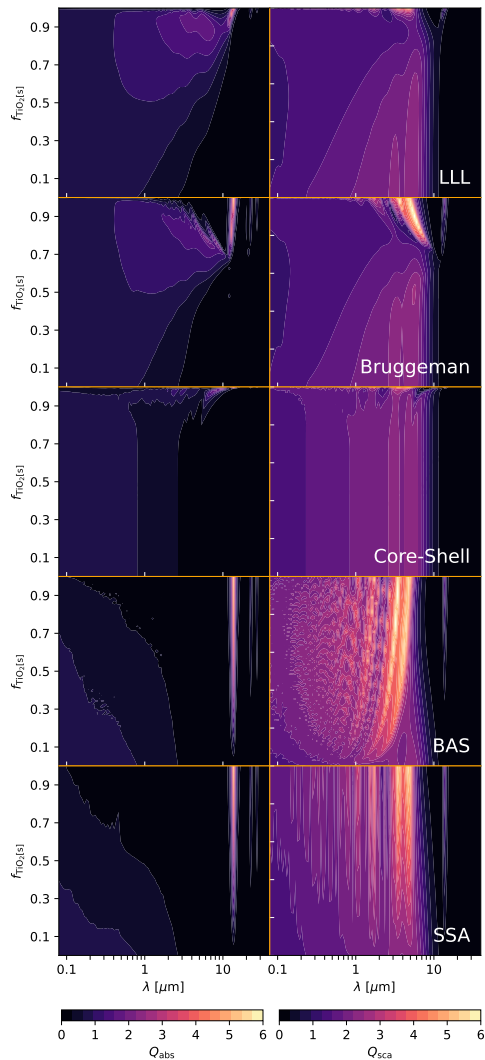


Figure 5.7: Absorption efficiency Q_{abs} (**Left**) and scattering efficiency Q_{sca} (**Right**) for the two-component material $\{\text{TiO}_2[\text{s}], \text{Mg}_2\text{SiO}_4[\text{s}]\}$.

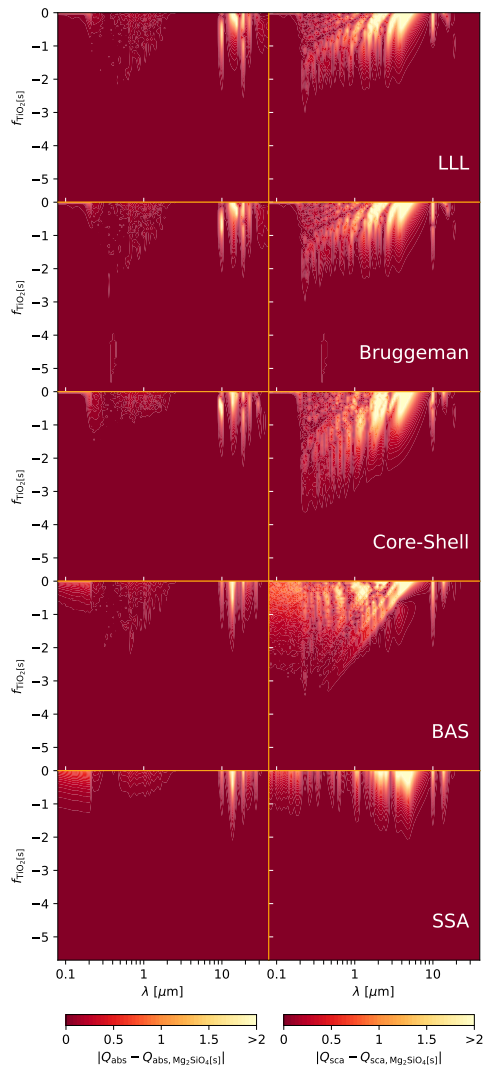


Figure 5.8: Absolute difference of the absorption efficiency (**Left**) and scattering efficiency (**Right**) of the two-component material $\{\text{TiO}_2[\text{s}], \text{Mg}_2\text{SiO}_4[\text{s}]\}$ compared to the absorption efficiency $Q_{\text{abs}, \text{Mg}_2\text{SiO}_4[\text{s}]}$ and scattering efficiency $Q_{\text{sca}, \text{Mg}_2\text{SiO}_4[\text{s}]}$ of homogeneous $\text{Mg}_2\text{SiO}_4[\text{s}]$.

Bruggeman, and core-shell vanishes for volume fractions below 70%. Since heterogeneous particles have inclusions, their effective optical properties are not equivalent to the optical properties of a homogeneous sphere. Therefore, spectral features originating from a spherical geometry might no longer appear in mixed cloud particles. All cloud particles within SSA and BAS on the other hand are perfect homogeneous spheres and therefore can retain the spectral features from the spherical geometry even at low volume fractions.

For core-shell, the absorption and scattering efficiencies start to be dominated by the Fe[s] even at TiO₂[s] volume fractions over 80%. For all other mixing treatments, TiO₂[s] still impacts the absorption and scattering efficiencies even at TiO₂[s] volume fractions below 10%. To analyse if the core can contribute more significantly for other materials, we consider the two component material {TiO₂[s], Mg₂SiO₄[s]}. The absolute differences between Q_{abs} and Q_{sca} compared to the absorption efficiency $Q_{\text{abs}, \text{Mg}_2\text{SiO}_4[\text{s}]}$ and scattering efficiency $Q_{\text{sca}, \text{Mg}_2\text{SiO}_4[\text{s}]}$ of homogeneous Mg₂SiO₄[s] are shown in Fig. 5.8. For Bruggeman, Core-Shell, and BAS, a TiO₂[s] core volume fraction of less than 1% can already impact the absorption and scattering efficiency by more than 0.5. For SSA on the other hand, the TiO₂[s] volume fraction needs to be above 1% for a change in the the absorption and scattering efficiency of more than 0.5. Similar to Sect. 5.4, this means that even spurious materials with a contribution of 1% or less may have an affect on the opacity of the cloud particles.

5.5 Heterogeneous clouds on exoplanets

To explore how choices of EMTs description or particle morphology can effect the interpretation of exoplanet atmosphere observations, the cloud structure of four planets are analysed: HATS-6b (Hartman et al. 2015), WASP-39b (Faedi et al. 2011), WASP-76b (West et al. 2016), and WASP-107b (Anderson et al. 2017).

The 1D cloud profiles of WASP-39b, HATS-6b, and WASP-76b at the equator of the morning and evening terminator can be seen in Fig. 5.9. For WASP-76b, only the morning terminator has clouds and thus the evening terminator is not shown. All cloud profiles are shown in Fig. C.12 (HATS-6b), Fig. C.13 (WASP-39b), and Fig. C.14 (WASP-76b). The cloud structure of WASP-107b can be seen in Fig. 5.9 as well. This cloud structure was derived through a one dimensional ARCiS retrieval rather than forward modelling and thus considers fewer cloud particle materials and assumes constant volume fractions with pressure.

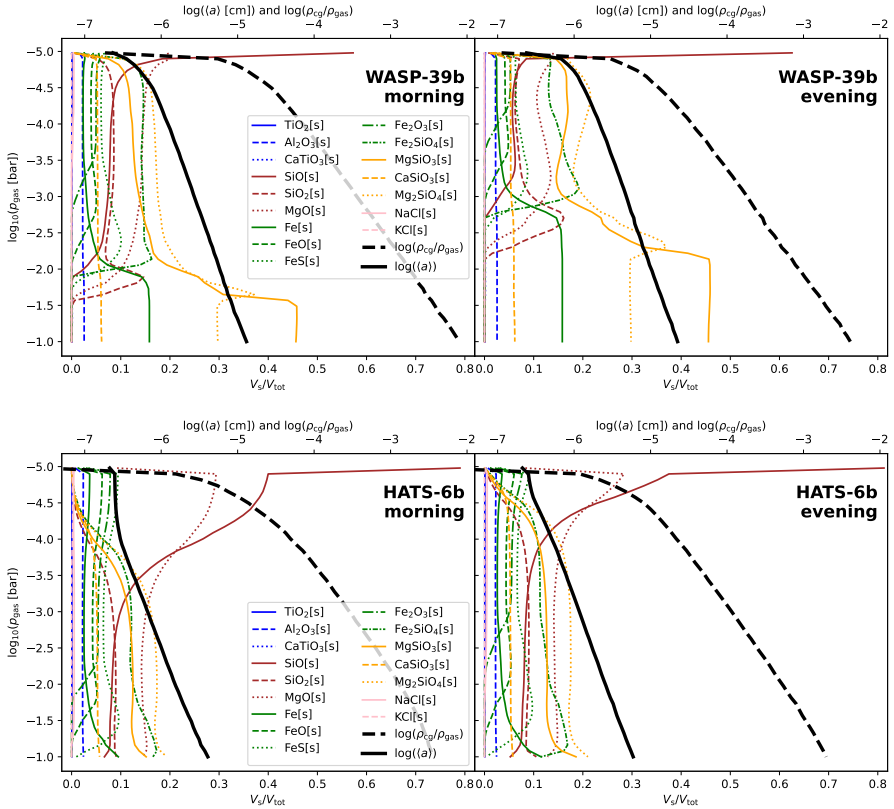


Figure 5.9: Volume fractions V_s/V_{tot} of each cloud particle species considered (coloured lines), average cloud particle radius $\langle a \rangle$ of all cloud particles, and the total cloud mass fraction $\rho_{\text{cloud}}/\rho_{\text{gas}}$ at the equator of the morning and evening terminators. Data taken from Carone et al. (2023) (WASP-39b), Kiefer et al. subm. (HATS-6b), and Dyrek et al. (2023) (WASP-107b).

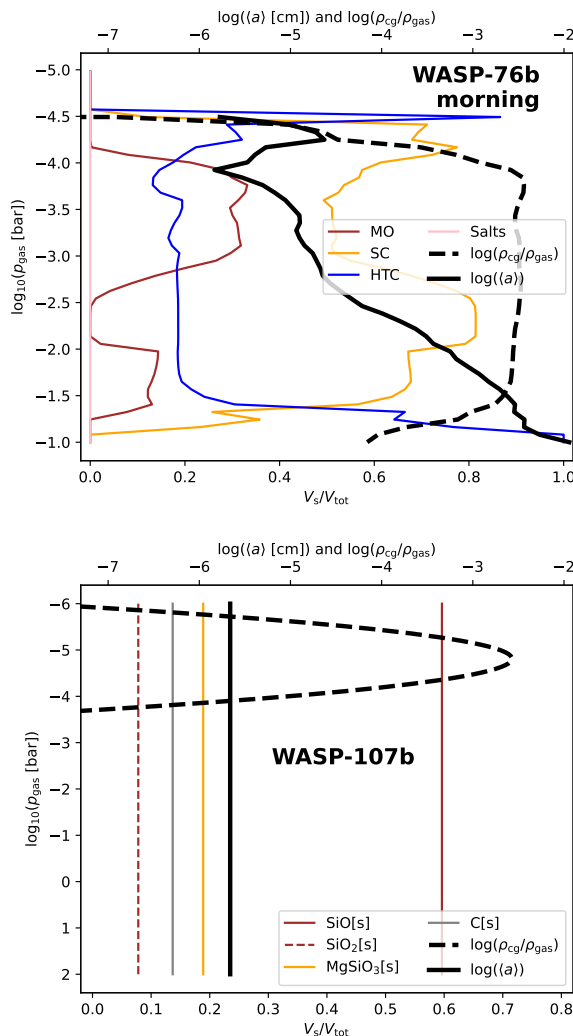


Figure 5.10: Continuation of Fig. 5.9

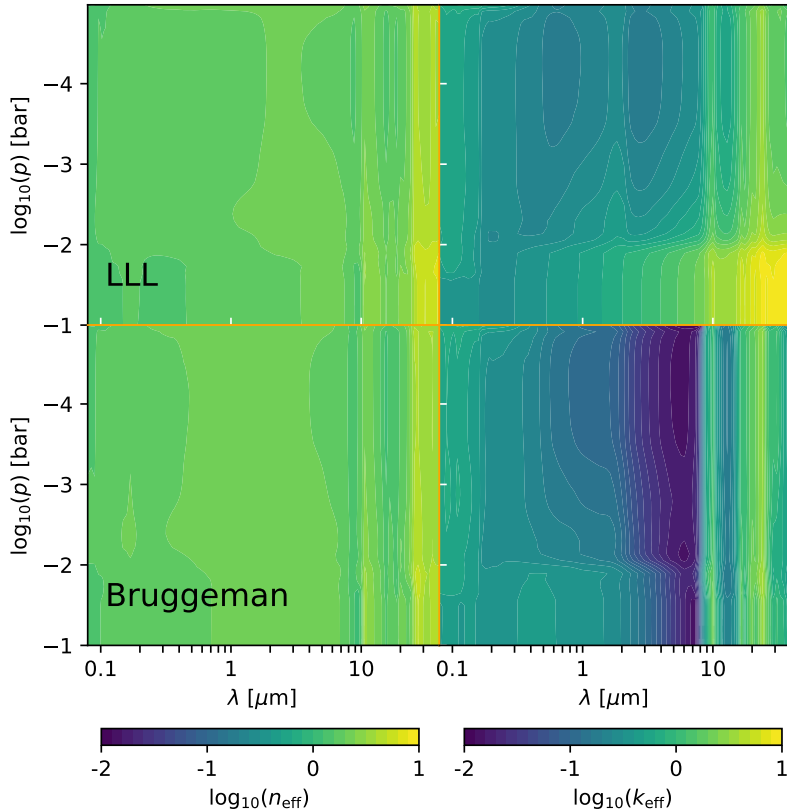


Figure 5.11: Effective refractive index at the equator of the morning terminator of WASP-39b.

5.5.1 Pressure dependent cloud optical properties of WASP-39b

To investigate the pressure dependent refractive index, absorption efficiency and scattering efficiency, the cloud structure of WASP-39b at the equator of the morning terminator was selected⁶.

At the top of the atmosphere around 10^{-5} bar, the cloud particle composition is dominated by SiO from nucleation. Going deeper into the atmosphere, the volume fraction of other species rapidly increases due to the increasing

⁶The figures of HATS-6b, and WASP-76b can be seen in Fig. C.8, C.9, C.10, and C.11.

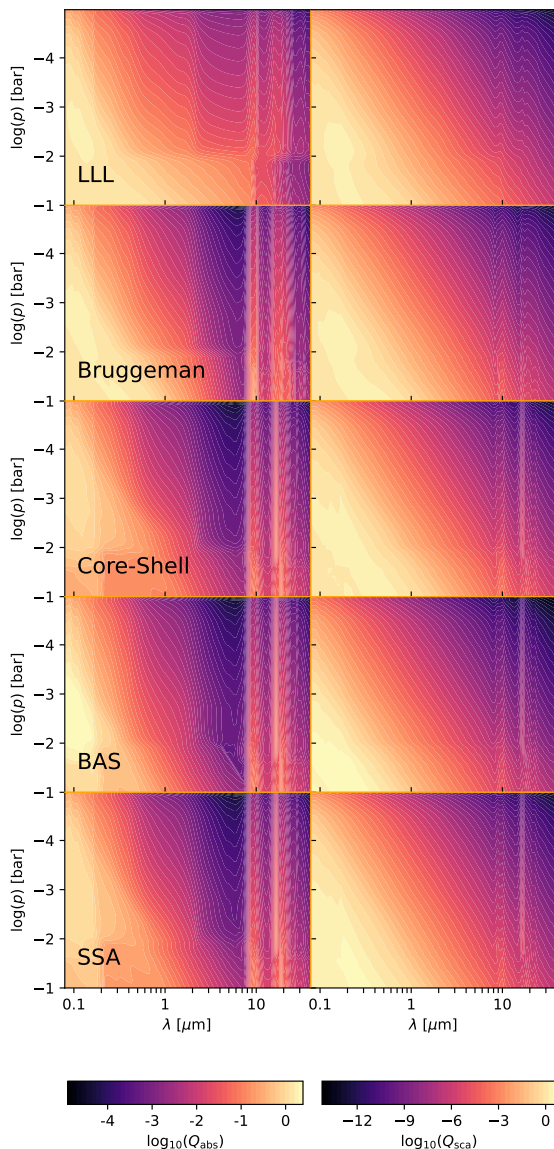


Figure 5.12: Absorption (Left) and scattering efficiency (Right) of WASP-39b at the equator of the morning terminator.

density. Cloud particles remain highly mixed throughout the atmosphere with $\text{Mg}_2\text{SiO}_4[\text{s}]$, $\text{MgSiO}_3[\text{s}]$, $\text{MgO}[\text{s}]$ and Fe_2SiO_4 being the dominant materials. Other materials are present at lower volume fractions. There is a rapid change in material composition around 10^{-2} bar where the magnesium-silicates enstatite (MgSiO_3) and forsterite (Mg_2SiO_4) become more dominant. This change happens at the same pressure where $\text{Fe}_2\text{SiO}_4[\text{s}]$ evaporates and $\text{Fe}[\text{s}]$ becomes the dominant iron-bearing cloud particle material. Presumably the liberation of oxygen from Fe_2SiO_4 leads to the Mg:O 1:3 stoichiometry (enstatite) to become favoured over the Mg:O 1:2 stoichiometry (forsterite). This effect is further amplified by the evaporation of SiO_2 around the same pressure layer which liberates additional oxygen. Throughout the atmosphere, the average particle size and cloud particle mass load increases steadily with increasing pressure due to bulk growth. The same is broadly true for the evening terminator, with the major difference that the evaporation of $\text{Fe}_2\text{SiO}_4[\text{s}]$ happens at a lower pressure (higher altitude), closer to 10^{-3} bar. This is due to higher temperatures of the evening terminator in general. The effective refractive index from different EMTs throughout the morning terminator is shown in Fig. 5.11.

All EMTs show the highest n_{eff} and k_{eff} values for pressures higher than 10^{-2} bar. This coincides with the change from $\text{Fe}_2\text{SiO}_3[\text{s}]$ to $\text{Fe}[\text{s}]$ being the dominant iron-bearing species. As we have seen in Sect. 5.4.2, $\text{Fe}[\text{s}]$ has a stronger effect on the effective refractive index than $\text{Fe}_2\text{SiO}_3[\text{s}]$. This increase is much stronger for LLL than for Bruggeman. For pressures lower than 10^{-2} bar (higher altitudes) a slight increase in refractive index values can be seen which is due to $\text{SiO}[\text{s}]$ being the dominant material. While this is a consequence of the upper boundary condition of the model, the changes in refractive index are small and unlikely to be significant in transmission spectra calculations.

Between 10^{-4} bar to 10^{-2} bar, the refractive index values are generally lower. Compared to LLL, Bruggeman predicts lower values for k_{eff} , especially between $3 \mu\text{m}$ to $8 \mu\text{m}$. As is shown in Sect. 5.5.2, this results in a "window" where cloud particles are less opaque. This is a direct consequence of the reduced impact of inclusions made from iron-bearing species within Bruggeman compared to LLL and shows the impact of the choice of EMT.

To further analyse the impact of mixing treatments on cloud optical properties, the absorption and scattering efficiencies for Bruggeman and LLL as well as the non-mixed treatments core-shell, BAS, and SSA are shown in Fig. 5.12. The absorption efficiencies of Bruggeman, core-shell particles, BAS and SSA are similar for all pressures and wavelengths up to $8 \mu\text{m}$. Only LLL shows clear deviations around $1 \mu\text{m}$ to $8 \mu\text{m}$ where Q_{abs} is larger compared to the others. The non-mixed treatments show silicate features around and above $10 \mu\text{m}$. The same features can be seen in LLL and Bruggeman but are weaker in comparison. This indicates that non-mixed treatments might retain more spectral features

from the individual cloud particle materials than EMTs.

5.5.2 Transmission spectrum

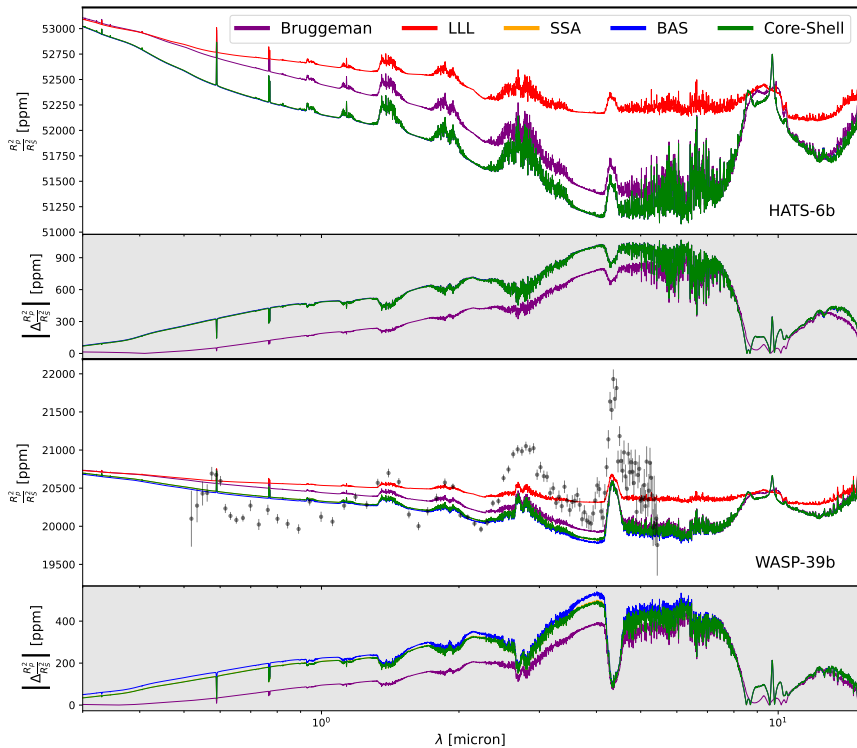


Figure 5.13: Transmission spectra of different planets using EMTs and non-mixed treatments. The absolute difference to LLL are shown underneath each plot. In both figures, Core-Shell, BAS, and SSA are overlapping. For WASP-39b, JWST NIRspec Prism data from Rustamkulov et al. (2023) is shown.

To investigate the impacts of EMTs and non-mixed treatments on transmission spectra, we choose a wavelength range of $0.3 \mu\text{m}$ to $15 \mu\text{m}$ which covers the JWST instruments NIRspec Prism and MIRI LRS. In this section, we show the transmission spectrum of HATS-6b and WASP-39b calculated using different mixing treatments (Fig. 5.13). The results of WASP-39b are compared to the observations of Rustamkulov et al. (2023). An offset of -867 ppm was applied to all synthetic spectra of WASP-39b to achieve the best fit of LLL with the

data. The planets WASP-76b and WASP-107b are analysed in more detail in Sect. 5.5.3 and 5.5.4, respectively. To analyse the differences between EMTs, the absolute differences of the transit depth compared to LLL are calculated:

$$\left| \Delta \frac{R_p^2(\lambda)}{R_s^2(\lambda)} \right| = \left| \frac{R_p^2(\lambda) - R_{p,LLL}^2(\lambda)}{R_s^2(\lambda)} \right| \quad (5.17)$$

Both HATS-6b and WASP-39b have cloud particle radii of less than $0.1 \mu\text{m}$ between 10^{-5} bar to 10^{-2} bar. Their cloud mass fraction steadily increases with pressure and reaches more than 10^{-4} at pressures higher than 10^{-4} bar. Hence, the transmission spectra of both planets is affected by the cloud particle opacities. For WASP-39b, the differences are up to 500 ppm. HATS-6b has an M-dwarf host star and thus already a larger transit depth, resulting in up to 1000 ppm differences.

The three non-mixed treatments Core-Shell, BAS and SSA produce nearly identical spectra for both planets. The main difference in the opacity calculation between SSA and BAS is that SSA divides the cloud particle materials into larger, but fewer particles and BAS into smaller, but more particles. This is in particular interesting since changes in size can impact the spectral features of cloud particles (Wakeford & Sing 2015). The number density of cloud particles, however, only impacts the overall amount of light that gets absorbed but not the shape of spectral features. While these differences could impact the transmission spectrum, we see little differences between BAS and SSA in both exoplanets. Core-Shell differs from BAS and SSA by considering interactions between the core and the shell. As we showed in Sect. 5.4.4, this produces features in the absorption and scattering efficiency which could result in spectral features in the transmission spectrum. However, no such features are seen in both planets because the cloud particle composition is dominated by the growth material which forms the shell, not the nucleation that forms the core. This matches the results from Powell et al. (2019) who found contributions of $\text{TiO}_2[\text{s}]$ cores within $\text{Fe}[\text{s}]$, $\text{Mg}_2\text{SiO}_4[\text{s}]$, and $\text{Al}_2\text{O}_3[\text{s}]$ shells negligible.

For both planets, non-mixed cloud particles exhibit stronger spectral features around $8 \mu\text{m}$ to $10 \mu\text{m}$ than well-mixed cloud particles. In particular a large feature from $\text{Mg}_2\text{SiO}_4[\text{s}]$ can be seen in core-shell, BAS, and SSA but not in Bruggeman, or LLL. This matches the findings from Sect. 5.5.1 where non-mixed approximations showed larger silicate features in the absorption and scattering efficiencies.

In both exoplanets, Bruggeman, Core-Shell, SSA, and BAS predict a lower transmission depth than LLL. This can be explained by the high refractive index of iron-bearing species which strongly impacts LLL (see Sect. 5.4.2). Even when silicate species are the dominant cloud material, the large values for

the imaginary part of the refractive index k of iron-bearing species dominates the effective refractive index calculation. Within SSA and BAS, iron-bearing species are assumed to form their own homogeneous cloud particles. As we have shown in Sect. 5.4.1, homogeneous iron-bearing species can have lower absorption efficiency than mixed particles. Similarly within Core-Shell, the iron bearing species form a homogeneous shell and thus do not increase the absorption efficiency as much.

All 5 methods produce a featureless spectrum at wavelengths below $1\text{ }\mu\text{m}$ in HATS-6b and WASP-39b. This effect is most clearly shown in the narrow sodium and potassium lines. For WASP-39b, we can compare our results to the observations of Rustamkulov et al. (2023). We find that all our spectra show less molecular features than the observations. This indicates that WASP-39b might have fewer clouds than predicted by the model. LLL shows larger differences to the observations than the other mixing treatments. However, WASP-39b shows that it is difficult to disentangle the effect of cloud particle mixing treatments and the amount of cloud coverage. Observations of cloud spectral features might help to gain further insights. In our results, the non-mixed treatments Core-Shell, BAS, and SSA produce sharper cloud particle features than LLL and Bruggeman. Cloud particle features are most relevant around $10\text{ }\mu\text{m}$. This is in agreement with previous theoretical studies Wakeford & Sing (2015) and with the detections of silicate features by Grant et al. (2023) and Dyrek et al. (2023).

5.5.3 Iron-bearing cloud particle materials in WASP-76b

WASP-76b is an ultra hot Jupiter (West et al. 2016) which is a type of exoplanet that is typically predicted to have cloud free day-sides and cloudy night-sides (Helling et al. 2023; Demangeon et al. 2024). Several high resolution observations have confirmed the presence of gas-phase iron, vanadium, magnesium, and sodium species (Ehrenreich et al. 2020; Pelletier et al. 2023; Gandhi et al. 2023; Maguire et al. 2024). The observations of Ehrenreich et al. (2020) found neutral iron in the morning limb but not in the evening limb. This detection was followed up by Savel et al. (2022) using post processed GCMs. They found that the differences between the limbs can be explained by the impact of clouds on the observations. WASP-76b is thus an interesting target to study cloud particle morphologies since it has iron in the atmosphere and is expected to have a cloudy morning terminator. This is in agreement with our modelling results. We find no clouds at the equator of the evening terminator and only few cloud particles at higher latitudes. The morning terminator has cloud coverage for all latitudes and their composition includes iron-bearing species. To derive the cloud structure, Savel et al. (2022) used an equilibrium thermal

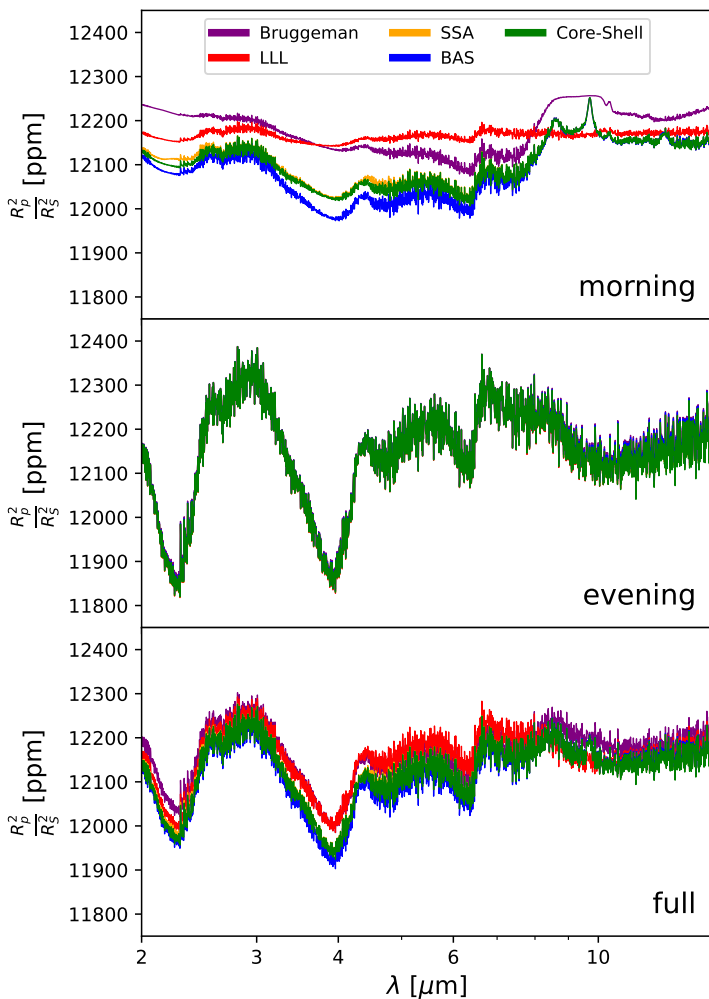


Figure 5.14: Transmission spectra of WASP-76b by considering the contributions of all terminator profiles (full), only the morning terminator profiles (morning), and only the evening terminator profiles (evening). Because the evening and morning terminator only cover half of the terminator region each, there transit depths were multiplied by 2 to be comparable to the full transit spectrum.

stability criteria. As a result, they do not predict iron clouds in the uppermost atmosphere because iron is already thermally stable in deeper layers. In contrast, our cloud model is kinetic which allows to consider the micro-physics of cloud formation and therefore it is possible for cloud particle materials to grow in regions outside where an equilibrium model would predict.

The full transmission spectrum of WASP-76b is produced by considering the contribution of all latitudes along both terminators. For the morning and evening terminator spectrum, only the contributions of $\text{lat} = -90^\circ$ and $\text{lat} = 90^\circ$ are considered, respectively. Since each limb only covers half the planet, the transit depth values of morning and evening only spectra were doubled to be comparable to the full transit spectrum. The transit depth of the morning limb, evening limb, and full transmission spectrum can be seen in Fig. 5.14. The evening terminator spectrum shows no cloud features and no significant muting of the molecular lines. Both EMTs and non-mixed treatments predict nearly an identical transmission spectra despite the presence of some high latitude clouds. The morning terminator spectrum shows clear signs of clouds. In agreement with Sect. 5.5.2, LLL leads to the flattest spectra. BAS leads to the least flat spectrum. The difference in transit depth between LLL and BAS is maximum ~ 200 ppm. Bruggeman, core-shell, and SSA are between the other methods. Similar to Sect. 5.5.2, SSA and core-shell have a nearly identical transmission spectrum. All techniques other than SSA and core-shell are separated by at least ~ 50 ppm to each other. Around $10 \mu\text{m}$, the non-mixed treatments show clear $\text{Mg}_2\text{SiO}_4[\text{s}]$ spectral features. Bruggeman shows a broad feature and LLL predicts only a flat spectrum. The full transit spectrum still exhibits differences between well-mixed and non-mixed cloud particles. However, the differences in the flatness of the spectrum is much less pronounced than in the morning limb alone. The spectral features of $\text{Mg}_2\text{SiO}_4[\text{s}]$ can no longer be seen for any method for the full transit spectrum.

Our results show that the EMTs and three non-mixed treatments show clear differences in the flatness of the spectrum and the cloud particle spectral features around $10 \mu\text{m}$. Detailed limb asymmetry observations of WASP-76b thus might allow the investigation of cloud particle morphologies at the morning terminator, removing the dilution of the effect by a mostly cloudless evening terminator.

5.5.4 Cloud detections in WASP-107b

Dyrek et al. (2023) detected silicon-bearing clouds in the atmosphere of WASP-107b. Within their ARCiS retrieval (Min et al. 2020), they assumed heterogeneous cloud particles made from $\text{SiO}[\text{s}]$, $\text{SiO}_2[\text{s}]$, $\text{MgSiO}_3[\text{s}]$, and $\text{C}_{\text{amorphous}}[\text{s}]$. They assumed well-mixed particles and calculated the effective

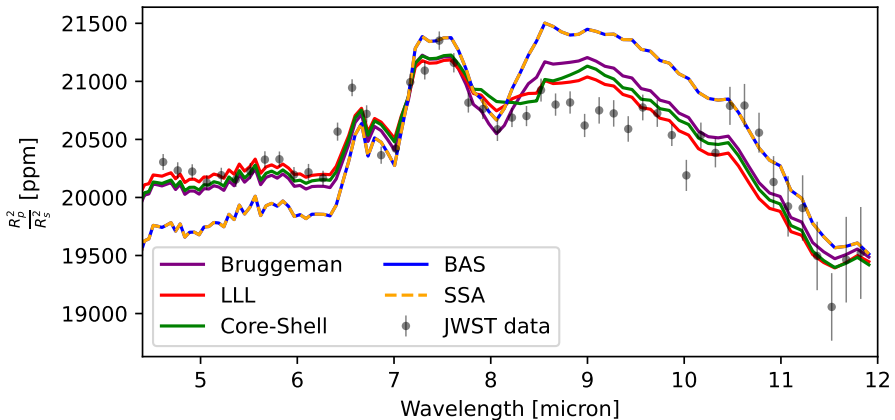


Figure 5.15: Transmission spectra of WASP-107b reproduced from the cloud structure retrieved by ARCiS. Cloud structure and JWST MIRI data taken from Dyrek et al. (2023).

refractive index using Bruggeman. Furthermore, they considered a distribution of hollow-spheres (DHS; Min et al. 2005). It is important to note that the cloud modelling used for WASP-107b is therefore different than the modelling used for HATS-6b, WASP-39b, and WASP-76b.

In this section, we reproduce the results of the ARCiS retrieval using the best fit parameters from Dyrek et al. (2023). This fit includes the temperature-pressure profile, gas-phase abundances, and cloud particle properties. The cloud structure is shown in Fig. 5.9. For the gas-phase, we consider the following opacity species: H₂O, CO, CO₂, CH₄ (Yurchenko et al. 2017), SO₂ (Underwood et al. 2016), H₂S (Azzam et al. 2016), NH₃ (Coles et al. 2019), SiO (Barton et al. 2013), PH₃ (Sousa-Silva et al. 2015), HCN (Barber et al. 2014), and C₂H₂ (Chubb et al. 2020). We compare the differences in the transit spectrum caused by EMTs (Bruggeman and LLL) and non-mixed treatments (core-shell, BAS, and SSA). For core-shell, SiO[s] was assumed as the core material. In contrast to Dyrek et al. (2023), we do not consider a DHS. The results are shown in Fig. 5.15. Because the cloud particle properties were retrieved using Bruggeman, the reference pressure and pressure range of the transmission spectrum calculation were chosen to minimise the differences to the observational data when using Bruggeman. However, our solution still slightly differs to the ARCiS fit from Dyrek et al. (2023). This can be explained by the fact that ARCiS is a retrieval model that searches for the best fit parameters for its set-up. Differences in our set-up for transmission spectrum calculations compared to theirs therefore

result in slightly different transmission spectra. For all other mixing treatments, the same reference pressure and pressure range as for Bruggeman was used. Afterwards, an offset was applied to the transmission spectra from each mixing treatment except Bruggeman to achieve the best fit to the data.

Between the different mixing treatment there are transit depth differences of up to 500 ppm around 9 μm . The differences are mainly caused by $C_{\text{amorphous}}[\text{s}]$. As we have shown in Sect. 5.4.2, $C_{\text{amorphous}}[\text{s}]$ has a similarly effect on cloud particle optical properties than iron-bearing species. Similar to Sect. 5.5.2 and 5.5.3, LLL leads to the overall flattest transmission spectrum. SSA and BAS have the largest differences compared to the other mixing treatments while for all other planets both were close to core-shell. This difference can be explained by a large volume fraction of the core species ($f_{\text{SiO}} = 0.906$). For the other planets, such high SiO[s] concentrations were only present at the top of the atmosphere where they impact the transmission spectrum less.

Overall, our results show that the differences in the optical properties between the mixing treatments have an observable effect. Depending on which treatment is used, different solutions to the atmospheric structure might be reached (See Sect 5.6.2).

5.6 Discussion

Our results show that the choice of EMT or non-mixed theory can have an observable impact on transmission spectra of cloudy atmospheres with heterogeneous cloud particles. The differences between mixing treatments is discussed in Sect. 5.6.1. The impact of mixing treatments on transmission spectra is analysed in Sect. 5.6.2. Lastly, in Sect. 5.6.3, the importance of carbon and iron-bearing species as cloud particle material are discussed.

5.6.1 Comparing mixing treatments

For non-mixed particles, our results show little difference between core-shell, BAS and SSA in most transmission spectra produced for this study. Only at high volume fractions of the core species (e.g. for WASP-107b) does SSA and BAS produce different transit spectra than core-shell. The similar results in the other cases can be explained with how the cloud particle materials are separated depending on the mixing treatment. Dominant species, like $\text{Mg}_2\text{SiO}_4[\text{s}]$, have large enough volume fractions that neither the size change of BAS, the number density change of SSA, nor a small core made from a

different material significantly impacts their contribution to the optical property of the cloud layer. Non-dominant species on the other hand, like MgO, have low number densities in SSA, small sizes in BAS, and small contributions to the core-shell calculations. This makes their contributions to the cloud particle optical properties negligible.

If cloud particles are assumed to be well-mixed, EMTs have to be used to describe their optical properties. The most common EMTs used to study mixed materials in exoplanets are Bruggeman and LLL (see Table 5.1). However, our analysis of two-component materials (see Sect. 5.4.1) and transit spectra (see Sect. 5.5) show that the optical properties of cloud particles can differ significantly between Bruggeman and LLL. This difference is mainly caused by species with a high imaginary part of the refractive index, like iron-bearing species or carbon. Laboratory experiments of mixed materials have shown that either Bruggeman or LLL can be more accurate, depending on the material and wavelength (see e.g. Kolokolova & Gustafson 2001; Voshchinnikov et al. 2007; Thomas & Gautier 2009). For clouds in exoplanet atmospheres, it is unknown if Bruggeman or LLL is more accurate. A big advantage of LLL over Bruggeman is the computation time. Bruggeman requires a computationally intensive minimisation algorithm whereas LLL presents an analytical solution which is quick to execute. Many larger frameworks, like GCM, thus either use LLL (Lee 2023), or a combination of LLL and Bruggeman (Lee et al. 2016; Lines et al. 2018a). Smaller frameworks, like transmission spectrum calculations, can afford the slower computational times and can use Bruggeman (Min et al. 2020; Dyrek et al. 2023). While the choice between LLL or Bruggeman, motivated by computational time makes sense, it also has implications on the optical properties of the clouds and thus on the derived temperature structure from observations, the calculation of opacities in forward models, and on transmission spectra of the exoplanet.

5.6.2 How do assumptions about heterogeneous cloud particles affect predicted observables?

The optical properties of heterogeneous cloud particles depends on their shape, composition, and material distribution. However, in exoplanet atmospheres, only few cloud particle properties can currently be precisely determined from observations (e.g. Grant et al. 2023; Dyrek et al. 2023). Therefore multiple assumptions have to be made to calculate cloud particle optical properties. The validity of these assumptions is hard to prove and most often depends on the underlying physics of cloud formation.

Many observations of flat transmission spectra in the optical wavelength range

have been explained by clouds (e.g. Bean et al. 2010; Kreidberg et al. 2014; Espinoza et al. 2019; Spyros et al. 2021; Libby-Roberts et al. 2022). Our results for HATS-6b and WASP-39b show that all mixing treatments predict strongly muted spectra in the optical. Therefore, observations in optical wavelengths on their own are not suited to study cloud particle morphologies. Observing the spectral features of cloud particle materials in the infrared allows more detailed insights. Grant et al. (2023) found in their observations of WASP-17b a peak between $8 \mu\text{m}$ to $9 \mu\text{m}$ which was linked to $\text{SiO}_2[\text{s}]$ clouds. Furthermore, they argue that this spectral feature is better explained with crystalline $\text{SiO}_2[\text{s}]$ than with amorphous $\text{SiO}_2[\text{s}]$. Dyrek et al. (2023) found a more broad cloud feature in the same wavelength range. Their retrieval model considers well-mixed cloud particles made from $\text{SiO}[\text{s}]$, $\text{SiO}_2[\text{s}]$, $\text{MgSiO}_3[\text{s}]$, and $\text{C}_{\text{amorphous}}[\text{s}]$. They predict considerably heterogeneous cloud particles. Both these findings agree well with our results. Within the transit spectrum of HATS-6b, WASP-39b, and the morning terminator of WASP-76b, all three non-mixed treatments show a clear peak in transit depth around $10 \mu\text{m}$ which is caused by homogeneous $\text{Mg}_2\text{SiO}_4[\text{s}]$. Well-mixed particles on the other hand only show a generally muted spectrum or a single broad feature. However, seeing a broad feature in the transit depth does not automatically prove that cloud particles are well-mixed. For WASP-107b (Sect. 5.5.4), also non-mixed treatments show a broad cloud feature. Here, it is important to note that the shape of cloud particles also impacts the spectral features of cloud particles. One of the advantages of BAS and SSA is that they can more easily account for non-spherical particles. Only the Mie theory calculations need to be adjusted which can be done using DHS, for example. Accounting for non-spherical particles is more difficult for well-mixed particles, since LLL and Bruggeman already assume that inclusions are spherical.

In this study, we used a forward modelling approach which shows clear differences in the transit depth between the mixing treatments. Extracting information from observations, however, is more difficult. Cloud free evening terminators, like in the case of WASP-76b, can reduce the signal from clouds if limbs are not observed separately. For WASP-39b, the muting of molecular features by the cloud structure predicted by Carone et al. (2023) is larger than the muting found in the observations of Rustamkulov et al. (2023). While some mixing treatments do result in less muting than others, this alone cannot explain the differences between the forward modelling and the observations. Higher cloud mass fractions or the atmospheric extent of the clouds also impact the muting of molecular features, but it is difficult to disentangle their effects. This degeneracy can also affect retrieval models. In our analysis of WASP-107b (Sect. 5.5.4), some mixing treatments over-predict the cloud contributions more than others. A retrieval run using our transmission spectra calculation could result in different cloud mass fractions, cloud particle radii, or vertical extent of the clouds depending on the mixing treatment selected. For a detailed analysis

of how mixing treatments affect retrievals, a more detailed study is required which is beyond the scope of this work.

5.6.3 Iron-bearing species and carbon require precise modelling

In Sect. 5.4, we show that iron-bearing species (Fe[s] , FeO[s] , $\text{Fe}_2\text{O}_3[\text{s}]$, $\text{Fe}_2\text{SiO}_4[\text{s}]$, and FeS[s]) and carbon (C[s] , $\text{C}_{\text{amorphous}}[\text{s}]$) can significantly change the optical properties of cloud particles even at volume fractions of less than 1%. The strong impact is caused by the large imaginary part of the refractive index k of these species and the assumption of spherical particles (see Sect. 5.4.1). Small amounts of iron-bearing species can lead to an effective refractive index closer to the resonance values of a spherical particle. This can lead to an increased absorption efficiency of mixed spherical particles compared to homogeneous spherical particles.

Min et al. (2006) investigated how the shape of particles impact their optical properties. For irregularly shaped particles, they showed that species with high n and k values have a much larger absorption efficiency than spherical particles of the same material. Assuming spherical and homogeneous cloud particles therefore can underestimate the absorption efficiency of clouds. A detailed study on how EMTs and non-mixed treatments affect non-spherical particles is, while important, beyond the scope of this study.

Our results show that precisely modelling the carbon and iron-bearing cloud particle materials is crucial to accurately predict the optical properties of clouds. This holds true for EMTs as well as non-mixed treatments and for spherical as well as non-spherical cloud particles. Observing exoplanets where it can be reasonably expected that iron-bearing species occur as cloud particle materials, like WASP-76b, might allow further insights into cloud particle properties in exoplanet atmospheres. In particular, the morning terminator of WASP-76b is expected to have iron-bearing clouds. Detailed observations of the muting of molecular features around $5 \mu\text{m}$ and the cloud features around $10 \mu\text{m}$ might help to differentiate cloud particle morphologies.

5.7 Conclusion

Cloud particles in exoplanet atmospheres might be considerably heterogeneous. We analyzed how 21 common cloud particle materials and different assumptions on the mixing treatment of cloud particle materials impact cloud particle optical properties. In total 4 EMTs (Bruggeman, LLL, Maxwell-Garnett, Linear) and

3 non-mixed treatments (core-shell, BAS, SSA) were studied. The mixing treatments were used to calculate the transmission spectrum of the planets HATS-6b, WASP-39b, WASP-76b, and WASP-107b.

Species with large refractive indices, like iron-bearing species ($\text{Fe}[\text{s}]$, $\text{FeO}[\text{s}]$, $\text{Fe}_2\text{O}_3[\text{s}]$, $\text{Fe}_2\text{SiO}_4[\text{s}]$, $\text{FeS}[\text{s}]$) or carbon ($\text{C}[\text{s}]$, $\text{C}_{\text{amorphous}}[\text{s}]$), can change the optical properties of cloud particles at volume fractions below 1%. Therefore, it is crucial to accurately model such species. Other cloud materials like high temperature condensates ($\text{TiO}_2[\text{s}]$, $\text{Al}_2\text{O}_3[\text{s}]$, $\text{CaTiO}_3[\text{s}]$), magnesium-silicates ($\text{MgSiO}_3[\text{s}]$, $\text{Mg}_2\text{SiO}_4[\text{s}]$) metal oxides ($\text{SiO}[\text{s}]$, $\text{SiO}_2[\text{s}]$, $\text{MgO}[\text{s}]$, $\text{MnO}[\text{s}]$), and salts ($\text{KCl}[\text{s}]$, $\text{NaCl}[\text{s}]$) also impact the transmission spectrum, but do so typically at volume fractions above 10%. For sulphur-bearing species ($\text{ZnS}[\text{s}]$, $\text{Na}_2\text{S}[\text{s}]$, $\text{MnS}[\text{s}]$), the impact on the optical properties of heterogeneous cloud particles is different depending on the species.

The mixing treatment of heterogeneous cloud particles impacts cloud spectral features as well as the muting of molecular features. All mixing treatments lead to a muting of molecular features, with LLL typically leading to the strongest muting. non-mixed treatments can retain the spectral features of individual cloud particle materials, whereas well-mixed theories typically exhibit broader features. For non-mixed particles, assuming a core-shell morphology, equally-sized homogeneous cloud particles (SSA), or equally-numbered homogeneous cloud particles (BAS) resulted in similar transit spectra. In particular SSA and core-shell were for most parts indistinguishable. For well-mixed particles, the differences in transit depth between Bruggeman and LLL can reach up to 500 ppm for WASP-39b and 1000 ppm for HATS-6b. Maxwell-Garnett and Linear are not suitable for cloud particles in exoplanet atmospheres.

While we have shown the impact of cloud particle morphologies and composition on the transmission spectra of exoplanets, it is difficult to disentangle them observationally from cloud particle properties like the dust to gas-ratio. Here, observations of cloud spectral features around $10 \mu\text{m}$ in addition to the muting of molecular features at lower wavelengths might help to break these degeneracies. In particular, observations of planets were iron-bearing species can be expected to from clouds, like WASP-76b, could help to investigate the morphologies of heterogeneous cloud particles.

Acknowledgments

S.K., A.D.S, L.C., M.M., Ch.H, and L.D. acknowledge funding from the European Union H2020-MSCA-ITN-2019 under grant agreement no. 860470 (CHAMELEON). D.S. and D.A.L. acknowledge financial support from the Austrian Academy of Sciences.

Chapter 6

The Cloudy Climate of HATS-6b

This chapter is submitted for publication as:

Under the magnifying glass: A combined 3D model applied to cloudy warm Saturn type exoplanets around M-dwarfs

Sven Kiefer, Nanna Bach-Møller , Dominic Samra, David Andrew Lewis, Aaron David Schneider, Flavia Amadio, Helena Lecoq-Molinos, Ludmila Carone, Leen Decin, Uffe Gråe Jørgensen, Christiane Helling

Author contribution:

S. Kiefer performed the cloudy GCM simulations, produced the transmission spectra, preformed analyses, and wrote the manuscript. N. Bach-Møller ran the ARGO simulations and preformed the analyses of the disequilibrium chemistry. D. Samra and D. Lewis ran the cloud simulations and contributed to the analyses of the cloud structure. A. D. Schneider performed the cloudless GCM simulations. N Bach-Møller, D. Samra, D. Lewis, L. Carone, and Ch. Helling actively contributed to the manuscript. F. Amadio, H. Lecoq-Molinos, L. Decin and U. Jørgensen contributed via discussions and advice.

Original abstract:

Warm Saturn type exoplanets orbiting M-dwarfs are particularly suitable for in-depth cloud characterisation through transmission spectroscopy due to their favourable stellar to planetary radius contrast. The global temperatures of warm Satellites suggest efficient cloud formation in their atmospheres which in return affects the temperature, velocity, and chemical structure. However, modelling the formation processes of cloud particles consistently within the 3D atmosphere remains computationally challenging. The aim is to explore the combined atmospheric and micro-physical cloud structure, and the kinetic gas-phase chemistry of warm Saturn-like exoplanets in the irradiation field of an M-dwarf. The combined modelling approach will support the interpretation of observational data from present (e.g. JWST, CHEOPS) and future missions (PLATO, Ariel, HWO). A combined 3D cloudy atmosphere model for HATS-6b is constructed by iteratively executing the 3D General Circulation Model (GCM) `expeRT/MITgcm` and a detailed, kinetic cloud formation model, each in its full complexity. Resulting cloud particle number densities, particles sizes, and material compositions are used to derive the local cloud opacity which is then utilised in the next GCM iteration. The disequilibrium H/C/O/N gas-phase chemistry is calculated for each iteration to assess the resulting transmission spectrum in post-processing. The first model atmosphere that iteratively combines cloud formation and 3D GCM simulation is presented and applied to the warm Saturn HATS-6b. The cloud opacity feedback causes a temperature inversion at the sub-stellar point and at the evening terminator at gas pressures higher than 10^{-2} bar. Furthermore, clouds cool the atmosphere between 10^{-2} bar and 10 bar, and narrow the equatorial wind jet. The transmission spectrum shows muted gas-phase absorption and a cloud particle silicate feature at $\sim 10\mu\text{m}$. The combined atmosphere-cloud model retains the full physical complexity of each component and therefore enables a detailed physical interpretation with JWST NIRSpec and MIRI LRS observational accuracy. The model shows that warm Saturn type exoplanets around M-dwarfs are ideal candidates to search for limb asymmetries in clouds and chemistry, identify cloud particle composition by observing their spectral features, and identify the cloud-induced strong thermal inversion that arises on these planets specifically.

6.1 Introduction

Warm Saturns are a class of Saturn-sized gas-giants with equilibrium temperatures T_{eq} between 500 K and 1200 K (Fig. 6.1). The atmospheres of warm Saturns have so far been difficult to characterise because observations with the Hubble Space Telescope (HST) showed either absent or muted spectral features. Such observations can be interpreted either with a cloud-free high metallicity composition or a global extended cloud coverage with lower metallicity (Komacek et al. 2020; Carone et al. 2021; Wong et al. 2022). JWST observations together with better models can resolve the ambiguous results for warm Saturns (or warm Neptunes like WASP 107b).

The majority of warm Saturns have been observed around metal rich F, G, or K stars (Buchhave et al. 2018). A selected few have now been detected around M-dwarfs (Cañas et al. 2022; Lin et al. 2023; Hartman et al. 2015). Atmosphere characterisation of warm Saturns in the era of JWST provides an excellent opportunity for in-detail cloud and chemistry characterisation across very different host stars. M-dwarfs are too faint for planetary atmosphere characterisation in the optical and around 1 μm with HST. Their luminosities peak at longer wavelengths, making warm Saturns around M-dwarfs together with their favourable stellar to planetary radius ratio ideal targets for infrared transmission spectroscopy with JWST.

First studies with cloudless GCMs predict more uniform temperatures of warm Saturns (Christie et al. 2022; Helling et al. 2023) compared to (ultra) hot Jupiters. Moreover, due to their relatively low planetary global temperature, a very efficient horizontal heat circulation has been inferred (e.g. Kataria et al. 2016; Komacek & Showman 2016). Thus, a global and highly mixed composition cloud coverage can be expected for warm Saturn type exoplanets (Christie et al. 2022; Helling et al. 2023). Clouds scatter light at the top of the planet (Rowe et al. 2008) leading to less absorbed incoming stellar light, which tends to cool a planetary atmosphere. At the same time, clouds absorb and re-emit outgoing thermal radiation of the planet and thus impose an additional greenhouse effect that can warm the underlying atmosphere. Understanding which effects determine the thermodynamic environment of the planet requires 3D modelling of the cloud properties and their horizontal and vertical distribution, as has been demonstrated for hot Jupiters (Lines et al. 2018b; Powell et al. 2019; Parmentier et al. 2021; Lee et al. 2023) and rocky exoplanets (Yang et al. 2014; Turbet et al. 2021). Recent JWST observations, as well as recent theoretical work, showcase that the properties of cloud particles within a planetary atmosphere are not necessarily uniform, even on planets where global cloud cover is expected. In the case of the hot Jupiter WASP-39b, cloud asymmetries between the morning and evening terminator have been predicted (Carone et al. 2023; Arfaux &

Lavvas 2024) and confirmed (Espinoza et al. 2024).

For the in-detail characterisation of cloud properties, gas-phase chemistry, and feedback with the 3D wind flow in exoplanet atmospheres, complex 3D cloud models are needed. Clouds and their formation in gas-giant exoplanets have been described with multiple levels of theory. Simplified descriptions assume phase equilibrium to determine where clouds can potentially be present (e.g. Demory et al. 2013; Webber et al. 2015; Crossfield 2015; Kempton et al. 2017; Roman & Rauscher 2017; Roman et al. 2021). To be able to make predictions of the material composition, cloud particle sizes, location of formation, and effect on the gas-phase abundances by depletion, fully self-consistent, micro-physical theories are needed (e.g. Woitke & Helling 2003; Helling & Woitke 2006; Helling & Fomins 2013; Powell et al. 2018; Woitke et al. 2020; Gao et al. 2020). Atmosphere models combining radiative transfer and micro-physical cloud formation are often solved for one dimension (Helling et al. 2008a; Witte et al. 2011; Juncker et al. 2017; Gao et al. 2020). However, atmospheric processes such as equatorial wind jets (e.g. Showman & Guillot 2002), day-night cold traps (e.g. Parmentier et al. 2013; Pelletier et al. 2023), day-night asymmetry (e.g. Perez-Becker & Showman 2013; Komacek et al. 2017; Helling et al. 2019a) and patchy clouds (e.g. Line & Parmentier 2016; Tan & Showman 2021) cannot be captured by 1D models.

3D General Circulation Models (GCMs) are successfully used to understand the cloud-free wind flow and basic thermodynamic structures of extrasolar planets. These models predict the hot spot offset within hot Jupiters due to equatorial superrotation (Showman & Guillot 2002; Showman & Polvani 2011; Carone et al. 2020) which has been observed since Knutson et al. (2007). To model the interaction of clouds and climate, cloud models and 3D GCMs need to be combined, which is computationally intensive. There are currently several approaches to tackle this problem. In a hierarchical approach, the output of GCMs can be used to post-process cloud structures (Helling et al. 2016; Kataria et al. 2016; Parmentier et al. 2016; Helling et al. 2019b, 2021; Robbins-Blanch et al. 2022; Savel et al. 2022; Helling et al. 2023). While these models can account for detailed micro-physical cloud formation, they are missing the feedback of clouds on the GCM. So far, only a few models couple micro-physical cloud models with GCMs (Lee et al. 2016, 2017; Lines et al. 2018b,a). To reduce the computational cost, some models use simplifications for the atmosphere models (Ormel & Min 2019; Min et al. 2020) or the cloud modelling (Christie et al. 2021; Lee et al. 2023). Others use radiatively passive (Parmentier et al. 2013; Charnay et al. 2015b; Komacek et al. 2019) or active (Charnay et al. 2015a) cloud particle tracers. Others parametrise the advection of clouds and use condensation curves to prescribe the location of clouds in the 3D GCM (Parmentier et al. 2016, 2018; Tan & Showman 2017, 2021; Roman & Rauscher

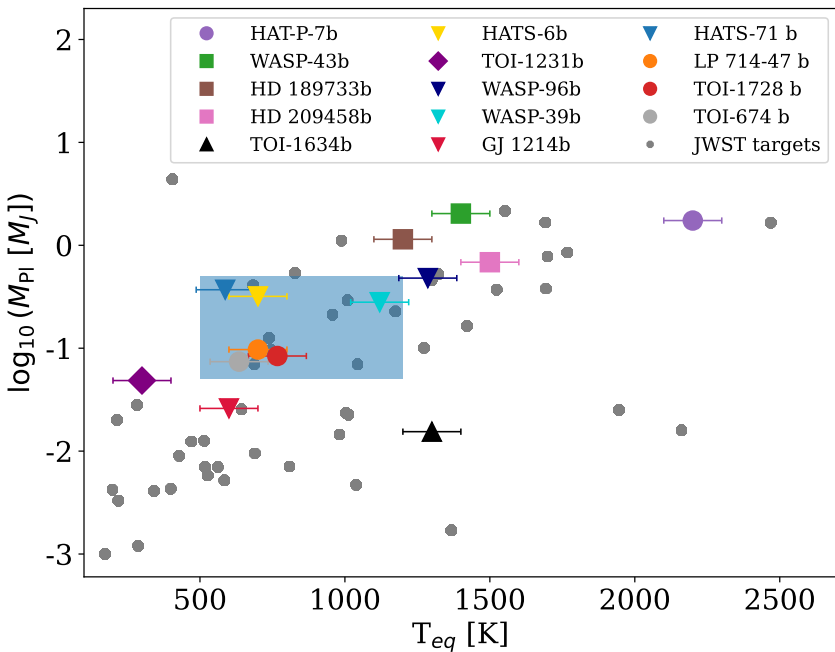


Figure 6.1: Known gas-giants and JWST targets. The blue shaded area represents the approximate parameter space of warm Saturns. Several often studied exoplanets are shown.

2017, 2019; Harada et al. 2021; Christie et al. 2021, 2022). In all cases, there is a trade off between computational cost and the detail by which the models describe the interaction of clouds and climate.

Warm Saturns around M-dwarf stars are interesting targets to study cloud formation and chemistry. The existence of such planets question formation models that predict that only more massive host stars produce a protoplanetary disk with enough material to form a gas-giant (e.g. Pascucci et al. 2016). M-dwarfs have a higher stellar activity than solar-type stars (Mignon et al. 2023). Specifically, the higher magnetic activity of M-dwarfs is expected to expose planets around these stars to higher amounts of stellar energetic particles (SEPs, e.g. Fraschetti et al. 2019; Rodgers-Lee et al. 2023), which can affect the chemistry on these planets (Venot et al. 2016; Barth et al. 2021; Konings et al. 2022).

HATS-6b is a rare case of a transiting warm Saturn that orbits an M-dwarf

host star. HATS-6b was discovered by the HATSouth survey in 2015 and has well-constrained planetary and stellar parameters. The planet has a mass of $0.319 \pm 0.070 M_J$, a radius of $0.998 \pm 0.019 R_J$ and an orbital period of 3.3253 d, where M_J is the mass of Jupiter and R_J the radius of Jupiter. The zero-albedo equilibrium temperature is ≈ 700 K (Hartman et al. 2015). The host star, HATS-6, is an early M-dwarf (M1V) with a mass of $0.57 M_\odot$, a radius of $0.57 R_\odot$, a metallicity of $[Fe/H] = 0.2 \pm 0.09$, and an effective temperature of $T_{eff} = 3724$ K, where M_\odot is the mass of the Sun and R_\odot is the radius of the Sun. Consequently, HATS-6b has one of the deepest transit depths known with $(R_P/R_\star)^2 = 0.0323 \pm 0.0003$ around 600 nm, where R_P is the observed planetary radius and R_\star the host star's radius. In addition, the host star has a J band magnitude of 12.05, making HATS-6b very well suited for atmospheric characterisation in the infrared. HATS-6b, together with eight other warm Saturns, have been selected as targets for two general observer programs for the James Webb Space Telescope (JWST) Cycle 2 (GO 3171 and 3731).

This chapter has two aims. Firstly, we aim to explore the atmospheric, microphysical cloud and gas-phase structure of the warm Saturn HATS-6b orbiting an M-dwarf. We use a combined model in the form of step-wise iterations between a detailed cloud formation description and `expeRT/MITgcm`, a 3D GCM with full radiative transfer and deep atmosphere extension. The second goal is to demonstrate how the combined modelling approach can help to support the interpretation of the data from space missions (e.g. JWST) for warm Saturn type planets. The step-wise iterative approach between the GCM (Sect. 6.2.1) and cloud structure (Sect. 6.2.2) is described in Sect. 6.2. The evaluation of the combined model for the warm Saturn HATS-6b is presented in Sect. 6.3. The resulting atmospheric solution and transmission spectra of HATS-6b are shown in Sect. 6.4. The discussion is in Sect. 6.5 and the conclusion in Sect. 6.6.

6.2 Approach

The step-wise iterative process applied in this study is initiated by 3D GCM simulations of the temperature, gas, densities, and wind velocities (Sect. 6.2.1). 1D profiles are extracted from this 3D atmosphere solution and used as input for a kinetic cloud formation model and the local cloud opacities are calculated (Sect. 6.2.2). The cloud opacity structure is then used as input for the 3D GCM and a new atmosphere structure is calculated. Each of the models is executed in their full complexity. Such an iteration is possible because the cloud formation time scales are considerably shorter than the hydrodynamic timescales (Helling et al. 2001; Helling & Woitke 2006; Powell et al. 2018; Kiefer et al. 2024). The stopping criterion for the iteration is described in Sect. 6.2.3. In order to explore

how the iterative processes may affect the spectral information, transmission spectra are created for each iteration. This is done by first modelling the non-equilibrium gas-phase chemistry of H/C/N/O species based on the final output from each GCM run (Sect. 6.2.4). The resulting number densities of the gas species are then used to calculate the transmission spectra for each iteration and the JWST’s observability of the differences is assessed (Sect. 6.2.5)

6.2.1 3D atmosphere

The 3D temperature and horizontal (zonal and meridional) wind velocities in the atmosphere of HATS-6b are simulated with the non-gray 3D GCM `expeRT/MITgcm` (Schneider et al. 2022c; Carone et al. 2020). This model solves the hydrostatic primitive equations (HPE) in vertical pressure coordinates on a rotating sphere (see, e.g. Showman et al. 2009). Hydrostatic equilibrium and the ideal gas law as equation of state are assumed. The model uses the dynamical core of `MITgcm` (Adcroft et al. 2004a) which solves the HPE on an Arakawa C type cubed-sphere grid. Here, we employ the nominal horizontal resolution C32¹ and a vertical grid with 41 logarithmically spaced grid cells between 1×10^{-5} bar and 100 bar and six linearly spaced grid cells between 100 bar and 700 bar. `expeRT/MITgcm` couples the dynamical core of the `MITgcm` (Adcroft et al. 2004a) to the radiative transfer solver of `petitRADTRANS` (Mollière et al. 2019). The model includes Rayleigh friction at the top (at 10^{-5} bar) and the bottom (at 700 bar) of the computational domain in order to stabilize the atmosphere against unphysical gravity waves and to mimic Ohmic dissipation (Carone et al. 2020).

We use a stellar effective temperature and stellar radius of HATS-6 of 3724 K and $0.57 R_{\odot}$, respectively, and assume HATS-6b to be tidally locked on a circular orbit with an orbital separation and period of 0.03623 AU and 3.3252725 days, respectively. The surface gravity is assumed to be 7.94 ms^{-2} and the internal temperature is set to $T_{\text{int}} = 50 \text{ K}$ following (Thorngren et al. 2019).

The thermal forcing part of `expeRT/MITgcm` solves the radiative transfer equation including isotropic scattering using the Feautrier method (Feautrier 1964) with approximate lambda iteration (Olson et al. 1986). `expeRT/MITgcm` uses 11 correlated-k wavelength bins for the radiative transfer calculations (S1 resolution; Schneider et al. 2022c). We chose to use a radiative time-step of 100 s, which is four times the dynamical time-step². `GGchem` (Woitke et al. 2018) is used to pre-calculate a grid of chemical equilibrium abundances that are then

¹C32 corresponds to a resolution of 128x64 in longitude and latitude

²This is a typical choice for hot Jupiters (see, e.g. Showman et al. 2009; Lee et al. 2021; Schneider et al. 2022c,b)

used to generate a premixed opacity grid for `expeRT/MITgcm`. The elemental abundances are assumed solar (Asplund et al. 2009) with a solar C/O ratio and scaled for the metalicity of HATS-6b of $[Fe/H] = 0.2 \pm 0.09$ (Hartman et al. 2015). A gas temperature T_{gas} and gas pressure p_{gas} grid for 100 K - 10000 K, 10^{-5} bar - 650 bar is calculated. Taking the temperature and pressure averages from this premixed grid, the specific gas constant $R = 3925 \text{ J kg}^{-1}\text{K}^{-1}$ and specific heat capacity at constant pressure of $c_p = 14966 \text{ J K}^{-1}$ are obtained.

Most absorption cross sections are obtained from `exomol`³. H_2O (Polyansky et al. 2018), CO_2 (Yurchenko et al. 2020), CH_4 (Yurchenko et al. 2017), NH_3 (Coles et al. 2019), CO (Li et al. 2015), H_2S (Azzam et al. 2016), HCN (Barber et al. 2014), PH_3 (Sousa-Silva et al. 2015), TiO (McKemmish et al. 2019), VO (McKemmish et al. 2016), FeH (Wende et al. 2010), Na (Piskunov et al. 1995), and K (Piskunov et al. 1995) opacities are used for the gas absorbers. Furthermore, we include Rayleigh scattering with H_2 (Dalgarno & Williams 1962) and He (Chan & Dalgarno 1965) and collision-induced absorption (CIA) with $\text{H}_2\text{-H}_2$ and $\text{H}_2\text{-He}$ (Borysow et al. 1988, 1989; Borysow & Frommhold 1989; Borysow et al. 2001; Richard et al. 2012; Borysow 2002) and H^- (Gray 2008).

6.2.2 Cloud Structure

The results from `expeRT/MITgcm` are used as input to a kinetic cloud formation model. 1D ($T_{\text{gas}}(z)$, $p_{\text{gas}}(z)$, $v_z(z)$)-profiles are extracted for each point in a longitude-latitude grid, with spacing of 45° in longitude ($\phi = \{-135^\circ, -90^\circ, -45^\circ, 0^\circ, 45^\circ, 90^\circ, 135^\circ, 180^\circ\}$) and $\sim 22.5^\circ$ in latitude ($\theta = \{0^\circ, 23^\circ, 45^\circ, 68^\circ, 86^\circ\}$), similar to previous works (Helling et al. 2016, 2019b,a, 2020, 2021; Samra et al. 2022; Carone et al. 2023; Helling et al. 2023). $T_{\text{gas}}(z)$ [K] is the local gas temperature, $p_{\text{gas}}(z)$ [bar] is the local gas pressure, and $v_z(z)$ [cm s^{-1}] is the local vertical velocity component of the 1D profile extracted from the 3D GCM. Each 1D model was run top-down in the atmosphere until it reached at least 0.1 bar. For the southern hemisphere ($\theta < 0^\circ$), all grid points are mirrored across the equator ($\theta = 0^\circ$). GGChem is used to determine the local gas-phase composition in chemical equilibrium for which solar elemental abundances from Asplund et al. (2009) are initially assumed which are scaled for the metalicity of HATS-6b. The vertical velocity component is used to compute the mixing timescales as described in Appendix B in Helling et al. (2023).

³<https://www.exomol.com/>

Cloud formation

Our kinetic cloud formation model treats the micro-physical processes of nucleation, bulk growth, and evaporation in combination with gravitational settling, element consumption, and replenishment using the moment method for the moments $L_j(V)$ in volume space V (Gail & Sedlmayr 1986, 1988; Dominik et al. 1993; Woitke & Helling 2003, 2004; Helling et al. 2004; Helling & Woitke 2006; Helling et al. 2008b). Cloud condensation nuclei (CCNs) are considered to form from four nucleating species: TiO_2 , SiO , KCl , and NaCl . This choice was based on the ones included in previous studies (Lee et al. 2015; Bromley et al. 2016; Lee et al. 2018; Gao & Benneke 2018; Köhn et al. 2021; Sindel et al. 2022; Kiefer et al. 2023). However, we note that there are current efforts to expand the list of nucleating species (e.g. Gobrecht et al. 2022, 2023; Lecoq-Molinos et al. 2024). The growth of the mixed material cloud particles is modelled through the surface growth of 16 bulk materials: $\text{TiO}_2[\text{s}]$, $\text{Mg}_2\text{SiO}_4[\text{s}]$, $\text{MgSiO}_3[\text{s}]$, $\text{MgO}[\text{s}]$, $\text{SiO}[\text{s}]$, $\text{SiO}_2[\text{s}]$, $\text{Fe}[\text{s}]$, $\text{FeO}[\text{s}]$, $\text{FeS}[\text{s}]$, $\text{Fe}_2\text{O}_3[\text{s}]$, $\text{Fe}_2\text{SiO}_4[\text{s}]$, $\text{Al}_2\text{O}_3[\text{s}]$, $\text{CaTiO}_3[\text{s}]$, $\text{CaSiO}_3[\text{s}]$, $\text{KCl}[\text{s}]$, $\text{NaCl}[\text{s}]$. These materials grow and evaporate through 132 surface reactions (Helling et al. 2019a) onto the surface of the CCN. The formation and evaporation of cloud particles depletes and replenishes the 11 participating elements Mg, Si, Ti, O, Fe, Al, Ca, S, Na, K and Cl, which affects the gas-phase equilibrium abundances. The kinetic cloud model assumes a cloud free element reservoir deep in the planet. Through mixing, the upper layers are replenished with cloud forming elements. The exact strength of mixing within exoplanet atmospheres is difficult to determine (Parmentier et al. 2013; Steinrueck et al. 2019; Samra et al. 2022). For this study, we used a quasi-diffusive approach utilising the standard deviation of neighbouring cells to compute a relaxation timescale (see Appendix B in Helling et al. (2023)). Previous work (e.g. Gao et al. 2020) considered sulfur, manganese and zinc-bearing species which typically condense below 1000 K for pressure ranges between 10^{-4} bar to 10^2 bar. However, these elements are much less abundant and therefore do not contribute significantly to the cloud particle material composition.

The resulting cloud particle material volume fractions V_s/V_{tot} , where V_s is the cloud particle volume of a given species s and V_{tot} the total cloud particle volume, average particle size $\langle a \rangle$ [cm], and cloud particle number density n_d [cm^{-3}] are provided as input for the opacity calculation in the 3D GCM. All cloud particles are assumed to be spherical.

Numerical Aspects of Cloud-GCM Interface

The 3D GCM employs a sponge layer to stabilize the upper boundary and basal Rayleigh drag to stabilize the lower boundary. While both layers ensure numerical stability, they are also physically justified.

The cloud model that interfaces with the GCM, similarly, requires numerical stabilisation measures that are justified by physical mechanisms that limit the condensate cloud model. At the upper boundary of the modelling domain, the growth of the cloud particles is limited by decreasing collisional rates in the upper atmosphere. At the lower boundary, cloud growth is limited by evaporation of cloud materials in the dense and hot deeper atmosphere. To ensure numerical stability, the cloud particle opacities were decreased linearly at the upper and lower pressure limit of the `expeRT/MITgcm` pressure grid until they reach 0. This decrease prevents a sudden drop in opacities that would otherwise trigger instabilities in the radiative transfer. At the top of the atmosphere, the cloud structure is only interpolated in the upper most grid cell at $p = 10^{-5}$ bar. At the high pressure limit of the cloud structures, the interpolation starts from the the lowest pressure of the cloud structure which is at pressures higher than 10^{-1} bar.

The `expeRT/MITgcm` uses a cubed-sphere C32 grid (Adcroft et al. 2004a). The cells of this grid are more uniformly distributed than a longitude-latitude grid which prevents overcrowding at the poles. The resolution of each cell in the C32 grid is approximately 2.8 by 2.8 degrees. The interpolation from the low resolution longitude-latitude cloud model grids to the `expeRT/MITgcm` cubed-sphere grid was done using two interpolation steps to reduce interpolation artifacts while keeping the structure of the low resolution grid. First, a bilinear interpolation to a longitude-latitude grid with cell size $\Delta\text{lon} = \Delta\text{lat} = 3$ degrees was performed. Afterwards, a bilinear interpolation to a cubed-sphere grid is used. During runtime, clouds are added incrementally to prevent sharp changes in the opacity structure. Out of the 2000 total simulation days, the first 100 simulation days are run without clouds. Then, cloud opacities are linearly increased over the next 100 simulation days until they are fully added at simulation day 200.

The step-wise iterative process applied here is a hands-on version of the iteration processes executed in every complex model implemented as, for example, an operator splitting method in Helling et al. (2001). Such methods make use of the time-scale difference that may occur, for example, between condensation and hydrodynamical processes. In the case of cloud formation, the formation processes modelled here (nucleation, grow and evaporation) act on very short time scales since they predominantly occur in collisionally dominated gases in

exoplanet atmospheres. This may, however, change in the upper atmosphere regions between $10^{-4} - 10^{-5}$ bar where the densities are so low that e.g. photochemistry affects the gas-phase. In this work, photochemistry is taken into account in post-processing. The majority of the cloud formation occurs at deeper levels and, generally, cloud haze models that extend higher up (Steinrueck et al. 2021) still find that the hydrodynamic assumption for these layers is adequate. Further, we aim to resolve here the atmosphere regions accessible in the infrared by JWST which are typically at pressures higher than 10^{-4} bar.

Possible long-term changes of the thermodynamic atmosphere structure may be linked to the deep atmosphere which can take more than 80000 simulation days to converge (Wang & Wordsworth 2020; Schneider et al. 2022b). Similarly, 1D time dependent cloud models have shown that convergence times can reach up to 8000 simulation days (Woitke et al. 2020). Fully coupled cloudy GCMs are computationally intensive and therefore often limited to evaluation times below 5000 simulation days (e.g. Lee et al. 2016, 2017; Roman & Rauscher 2017, 2019; Lines et al. 2018a,b; Roman et al. 2021; Komacek et al. 2022). However, recent run-time improvements of GCMs (Schneider et al. 2022c) might allow for longer simulation times in the future. It should be noted, however, that this work showed only a minor change in the upper atmosphere structure ($p < 1$ bar) after 2000 days simulation time (see Appendix D.2).

Cloud opacities

To calculate the interaction between the photons and the cloud particle, we use Mie-theory (Mie 1908). This theory is an analytical solution to the Maxwell equations under the assumption of spherical particle with an effective refractive index ϵ_{eff} .

To find the effective refractive index ϵ_{eff} of a given mixture of bulk material, we follow the approach of Lee et al. (2016) and start by using the Bruggeman mixing rule (Bruggeman 1935). In case of non-convergence, we fall back to the Landau-Lifshitz-Looyenga method (Looyenga 1965). The homogeneous opacity values for all species s used in this chapter can be found in the Table C.2. Using the effective refractive index, Mie-theory is used to calculate the absorption efficiency Q_{abs} , the scattering efficiency Q_{sca} and the anisotropy factor g . From these, the wavelength dependent absorption coefficient $\kappa_{\text{abs}}^{\text{cloud}}(\lambda)$ [$\text{cm}^2 \text{ kg}^{-1}$] and

the scattering coefficient $\kappa_{\text{sca}}^{\text{cloud}}(\lambda)$ [$\text{cm}^2 \text{ kg}^{-1}$] are calculated:

$$\kappa_{\text{abs}}^{\text{cloud}}(\lambda) = \pi \langle a \rangle^2 \frac{n_{\text{d}}}{\rho_{\text{gas}}} Q_{\text{abs}}(\langle a \rangle, \lambda, \epsilon_{\text{eff}}) \quad (6.1)$$

$$\kappa_{\text{sca}}^{\text{cloud}}(\lambda) = \pi \langle a \rangle^2 \frac{n_{\text{d}}}{\rho_{\text{gas}}} Q_{\text{sca}}(\langle a \rangle, \lambda, \epsilon_{\text{eff}}) (1 - g) \quad (6.2)$$

where n_{d} [cm^{-3}] is the number density of cloud particles, $\langle a \rangle$ [cm] the mean cloud particle radius, ρ_{gas} [g cm^{-3}] the gas density, and λ [cm] the wavelength of the photon. Our cloud model uses the moment method which allows to efficiently model heterogeneous cloud particles without an explicit cloud particle size distribution. Reconstructing the complex size distribution of cloud particles (Helling et al. 2008b) would introduce additional assumptions. We therefore assume monodisperse cloud particles with a local mean particle size derived from the kinetic cloud model as used in Helling et al. (2020). A study on the effect of the assumptions of monodisperse cloud particles can be found in Samra et al. (2020). The absorption and scattering coefficients are then added to the gas-phase opacities of the radiative transfer of `expeRT/MITgcm`:

$$\kappa_{\text{abs}}^{\text{tot}}(\lambda) = \kappa_{\text{abs}}^{\text{gas}}(\lambda) + \kappa_{\text{abs}}^{\text{cloud}}(\lambda) \quad (6.3)$$

$$\kappa_{\text{sca}}^{\text{tot}}(\lambda) = \kappa_{\text{sca}}^{\text{gas}}(\lambda) + \kappa_{\text{sca}}^{\text{cloud}}(\lambda) \quad (6.4)$$

where $\kappa_{\text{abs}}^{\text{gas}}$ [$\text{m}^2 \text{ kg}^{-1}$] and $\kappa_{\text{sca}}^{\text{gas}}$ [$\text{m}^2 \text{ kg}^{-1}$] are the absorption and scattering coefficients for the gas, respectively. $\kappa_{\text{abs}}^{\text{tot}}$ [$\text{m}^2 \text{ kg}^{-1}$] and $\kappa_{\text{sca}}^{\text{tot}}$ [$\text{m}^2 \text{ kg}^{-1}$] are the total absorption and scattering coefficients, respectively.

6.2.3 Stopping the step-wise iteration

One of the aims of this work is to demonstrate that a 3D atmosphere solution including detailed cloud formation is computationally feasible for warm Saturn type exoplanets. We do this through a step-wise iteration between the two modelling complexes. This enables the full complexity of both the 3D GCM and the cloud model, to achieve a conceivable accuracy for a global exoplanet atmosphere structure.

Here, the conceivable accuracy is determined from the observational accuracy, hence, the stopping criterion depends on the observational facilities used. For this project, the spectral precision of transmission spectra from the JWST instruments NIRspec Prism and MIRI LRS after two and after ten transit measurements are used as the primary stopping criterion. After each iteration, a transmission spectrum is calculated (Sect. 6.2.5) and compared to the previous iteration step. If the observational differences between iterations fall below the

spectral precision (dotted line in Fig. 6.9), the step-wise iteration is stopped. Since our model iterates between the cloud model and the GCM, the main goal is to have no observable impact of the cloud structure on the transmission spectra. The abundances in chemical disequilibrium are calculated in post-processing and the impact on the transmission spectra is used as a secondary stopping criteria.

Additional secondary stopping criteria may be derived from the $(T_{\text{gas}}, p_{\text{gas}})$ -structures and the cloud opacity. As will be demonstrated later, once changes in transmission spectra fall below the observable accuracy, the cloud properties between the two successive iterations remain similar. This suggests that the still existing changes between the $(T_{\text{gas}}, p_{\text{gas}})$ -structures, which may be substantial but locally confined, do not affect the gas-phase and cloud opacity structure sufficiently enough to change the spectrum beyond spectral precision. Hence, these changes will not affect the interpretation of the data.

6.2.4 Disequilibrium gas-phase chemistry

The disequilibrium chemistry for the H/C/N/O complex of HATS-6b is modelled to assess how each iteration affects the atmospheric chemistry, and as a result the transmission spectra. This is done using an updated version of the chemical network STAND2020 (Rimmer & Helling 2016, 2019; Rimmer & Rugheimer 2019) in combination with the 1D photochemistry and diffusion code **ARGO** (Rimmer & Helling 2016). **ARGO** models chemical transport, wavelength-dependent photochemistry, and cosmic ray transport by following a parcel of gas as eddy diffusion leads it up and down through the atmosphere (further description in e.g. Rimmer & Helling (2016) and Barth et al. (2021)). STAND2020 is a chemical H/C/N/O network containing the reaction rates for more than 6600 reactions in the temperature range of 100 K to 30000 K. STAND2020 involves all reactions for species containing up to six H, two C, two N, and three O atoms and also contains reactions with He, Na, Mg, Si, Cl, Ar, K, Ti, and Fe bearing species. The network has been tested for the atmospheres of Earth and Jupiter (Rimmer & Helling 2016) in addition to a number of hot-Jupiter models (Barth et al. 2021; Hobbs et al. 2021; Tsai et al. 2023). The chemical network is run through the 1D photochemistry and diffusion code, **ARGO**, which models chemical transport and the effect of photochemistry and cosmic rays.

The inputs for **ARGO** and STAND2020 have been chosen as follows:

1. $(T_{\text{gas}}, p_{\text{gas}})$ profiles and vertical eddy diffusion profile: Eight different 1D profiles are extracted from the output of the **expeRT/MITgcm** by averaging over areas of the 3D grid. The eight profiles are six terminator regions

with the longitudes ($\phi = \{90^\circ, 270^\circ\}$) and latitudes ($\theta = \{0^\circ, 23^\circ, 68^\circ\}$), and the sub-stellar and anti-stellar points.

2. Atmospheric element abundances: Solar abundances which are adapted for metallicity ($[\text{Fe}/\text{H}] = 0.2$) in accordance with the the initial abundances used for the GCM.
3. Stellar XUV spectrum driving photochemistry: Spectrum obtained from the MUSCLES survey where the M1.5V star, GJ667C, is chosen as a proxy to HATS6. The spectrum covers the XUV range and is composed of a combination of modelled and observed spectra (France et al. 2016; Youngblood et al. 2016, 2017; Loyd et al. 2016, 2018). The XUV spectrum used in this study can be seen in Appendix D.5.
4. Cosmic rays: Implemented based on the ionization rate of low energy cosmic rays (LECR) as explained by Rimmer & Helling (2013) and Barth et al. (2021).
5. Stellar energetic particles: To account for the higher activity of M-dwarf host stars, SEPs have been included in the model. The SEPs are introduced by scaling the spectrum of a solar SEP event to fit the host star based on the X-ray flare intensity (method further described in Barth et al. (2021)). A number of X-ray flare intensities has been reported for M-dwarf stars (Hünsch et al. 2003; Namekata et al. 2020) ranging from ~ 0.001 to 0.2 W m^{-2} at 1 AU. For this study we chose to implement SEPs corresponding to X-ray flare intensities of 0.1 W m^{-2} at 1AU. The effect of the SEPs will be included continuously throughout the run, and not as a finite event.

Different locations on the planet will experience a different influx of stellar radiation and SEPs, and the model inputs are therefore varied accordingly. For the sub-stellar point, both the stellar spectrum and SEPs are included. For the anti-stellar point, neither the stellar spectrum nor SEPs are included. For the terminator coordinates, only SEPs are included. The reason for including SEPs but not the stellar spectrum for the terminator region is that the shallow angle of incidence for radiation from the host star causes the radiation to pass through so many atmospheric layers before it reach the bulk of the 1D simulated atmosphere profile above the terminator that its influence is negligible. Since XUV radiation is easily scattered by the atmosphere, the stellar spectrum is not included for the terminator regions, whereas SEPs have been shown to penetrate deeper into the atmosphere (Barth et al. 2021) and are therefore included. The SEPs are not scaled based on the incident angle. The output of the STAND2020-ARGO run is the relative number density of more than 511 gas-phase species. Based on these number densities as well as the cloud opacities mentioned previously, the transmission spectra can be produced.

6.2.5 Transmission radiative transfer

The transmission spectrum of HATS-6b is produced by adding the cloud opacities to *petitRADTRANS* (Mollière et al. 2019, 2020; Alei et al. 2022), where the cloud opacities from the micro-physical cloud model are included as opacity source (Sect. 6.2.2). Each transmission spectrum uses the input cloud structure for the GCM, the temperature structure of the GCM, and the post-processed gas-phase number densities from ARGO. The transmission spectrum of the cloudless GCM run (iteration 0) is calculated cloud free.

To calculate the transmission spectrum, the terminator region is divided into ten equally spaced, and equally sized grid cells. Each cell covers a latitudinal range of $\Delta\text{lat} = 22.5^\circ$. Choosing a constant longitudinal range would lead to the neglect of data points within the terminator region, especially close to the poles. Therefore, a latitude dependent longitudinal range was chosen to ensure equally sized grid cells. At the equator the longitudinal range is $\pm\Delta\text{lon} = 10^\circ$ (Lacy & Burrows 2020). The total transmission spectrum is then calculated as the average of the transmission spectra from all regions:

$$R_{\text{tot}}(\lambda) = \sqrt{\frac{1}{N} \sum_{i=1}^N R_i^2(\lambda)} \quad (6.5)$$

Similar to previous studies (Lee et al. 2019; Baeyens et al. 2021; Nixon & Madhusudhan 2022), the following gas-phase species were considered as line opacity species⁴: H₂O, CO, CH₄, CO₂, C₂H₂, OH, NH₃, and HCN. Furthermore, H₂ and He were considered as Rayleigh scattering opacities, and collision-induced absorption (CIA) from H₂–H₂ and H₂–He.

6.3 Evaluation of the combined model

To study the atmosphere of the warm-Saturn HATS-6b, 6 iterations using *expeRT/MITgcm* and the kinetic cloud model have been conducted. After each iteration of the GCM, the thermodynamic structure is used to produce a cloud-structure which is included in the next iteration of the GCM. The cloud-free simulations are shown in Sect. 6.3.1. The effect of clouds are presented in Sect. 6.3.2. After each GCM run, the disequilibrium chemistry (Sect. 6.3.3) is post-processed and the differences in the transmission spectrum are determined (Sect. 6.3.4).

⁴References can be found in Sect. 6.2.1.

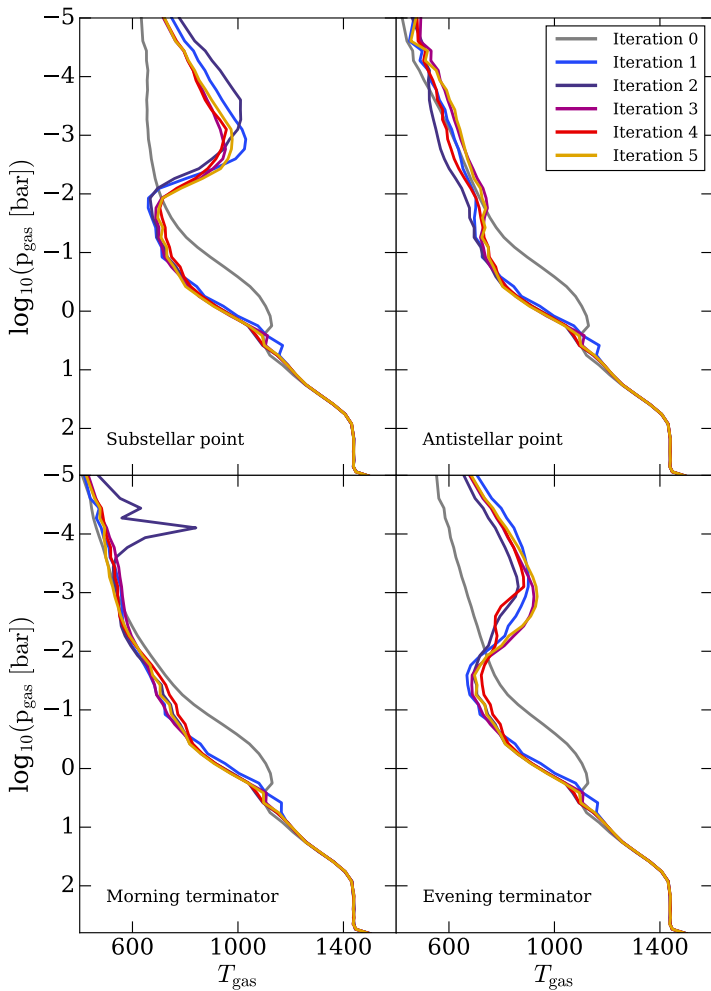


Figure 6.2: $(T_{\text{gas}}, p_{\text{gas}})$ -profiles of the sub-stellar point, anti-stellar point, evening terminator, and morning terminator.

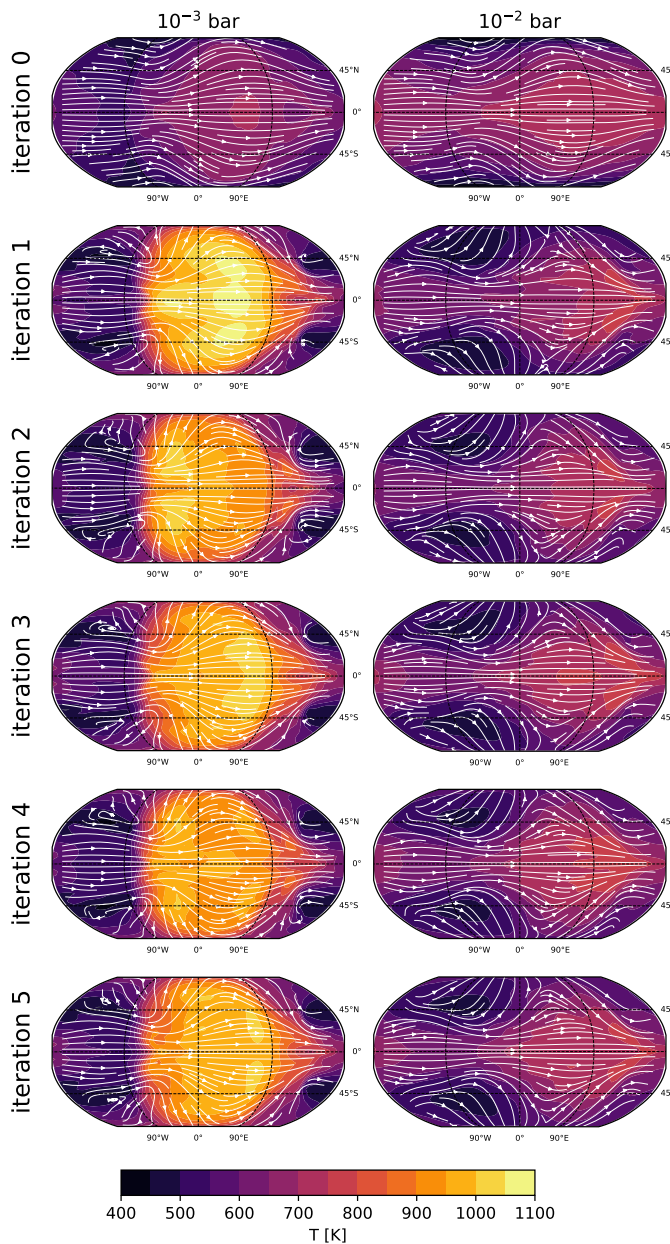


Figure 6.3: Isobaric slices of the expeRT/MITgcm runs at $t = 2000$ simulation days. The white lines indicate the horizontal wind velocity fields.

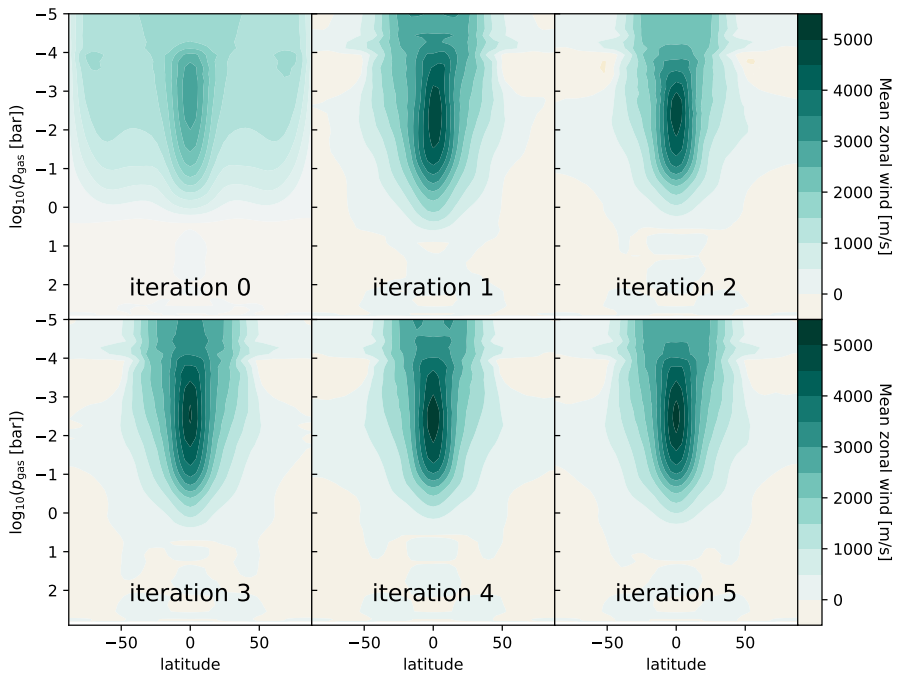


Figure 6.4: Zonally averaged zonal wind velocities at $t = 2000$ simulation days.

6.3.1 Cloud-free GCM and post-processed clouds

The first run, i.e. iteration 0, of the GCM was conducted without clouds. A total of 2000 days were simulated using `expeRT/MITgcm`. After 2000 days, there was little change in the global average of the $(T_{\text{gas}}, p_{\text{gas}})$ -profiles for pressure layers lower than 1 bar (see Appendix D.2). For pressures higher than 1 bar, the temperature did not change by more than 20 K from the initial conditions for the GCM. It is well known, that the convergence deeper in the atmosphere is computationally intensive and difficult to achieve (Wang & Wordsworth 2020; Skinner & Cho 2022; Schneider et al. 2022c,b). In the cloudy iterations (see Sect. 6.3.2), the clouds become opaque for pressures higher than 10^{-2} bar. Therefore, the atmospheric layers of interest for this study can be assumed to be reasonably converged.

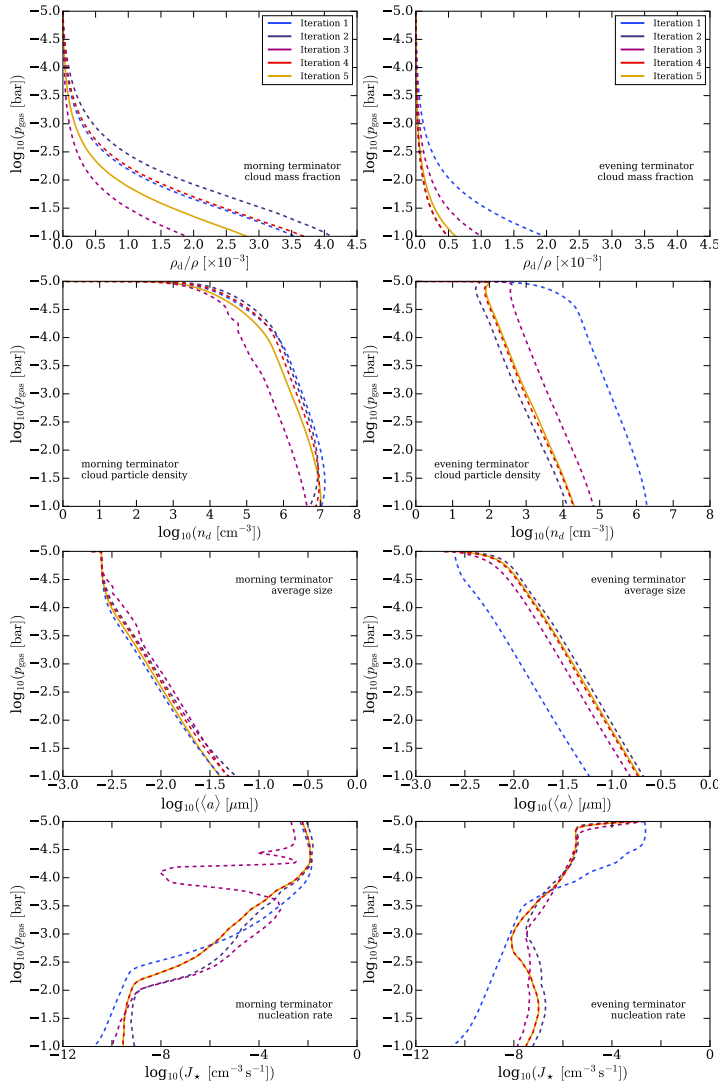


Figure 6.5: Cloud particle properties of the step-wise iterated cloud structure for the warm Saturn example HATS-6b. Iteration 5 is shown as a solid line to highlight the final result. **Left:** morning terminator. **Right:** evening terminator. **Top:** cloud mass fraction ρ_d/ρ . **Upper middle:** cloud particle number density n_d . **Lower middle:** average cloud particle size $\langle a \rangle$. **Bottom:** Nucleation rate J_* . The sub- and anti-stellar point can be found in Fig D.1.

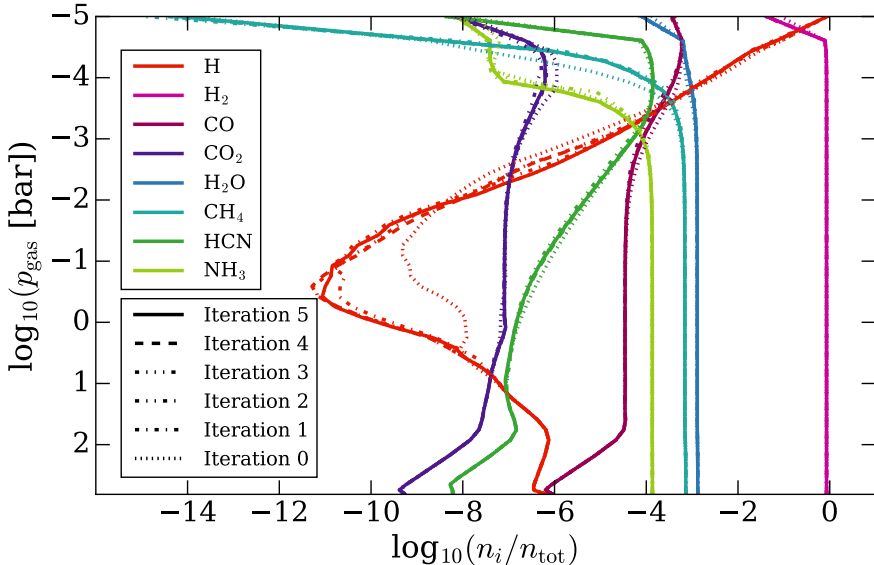


Figure 6.6: Concentrations of non-equilibrium gas species for the warm Saturn example HATS-6b at the terminator region (both morning and evening) averaged over all six coordinates for all iterations.

The $(T_{\text{gas}}, p_{\text{gas}})$ profiles for the sub-stellar point, anti-stellar point, morning terminator, and evening terminator are shown in Fig. 6.2. The iteration 0 profiles only show minor differences in temperature for pressures greater than 10^{-1} bar. Higher up in the atmosphere, the day-side is roughly 200 K hotter than the night side. The isobaric temperature maps for $p = 1.2 \times 10^{-3}$ bar and $p = 1.2 \times 10^{-2}$ bar can be seen in the left panels of Fig. 6.3. The zonal mean wind velocities are shown in the left panel of Fig. 6.4 which describe the longitudinal average of winds parallel to the equator and are known to redistribute heat longitudinally (Vuitton 2021). Overall, the global temperature and wind velocity structure of HATS-6b show the characteristics of a highly irradiated gas-giant including a super-rotating equatorial jet stream. This jet stream transports heat from the dayside to the nightside and causes a hot spot offset (e.g. Showman & Polvani 2011; Cowan et al. 2012; Dang et al. 2018). In addition to the equatorial jet stream, two weak polar jet streams can be observed.

Using the output from the cloudless GCM (iteration 0) the cloud structure was post-processed. This cloud structure is labelled iteration 1 because it will be

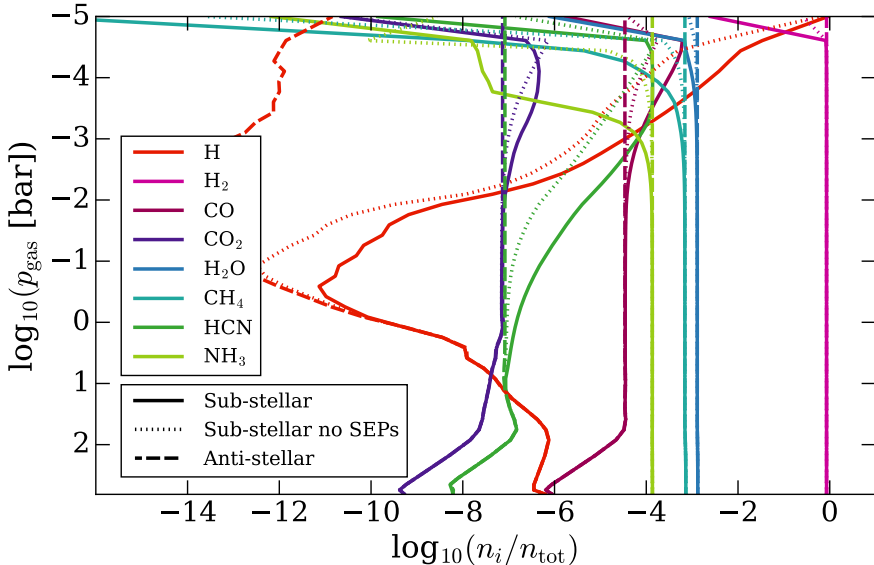


Figure 6.7: Concentrations of non-equilibrium gas species for the warm Saturn example HATS-6b at the sub- and anti-stellar point for the final iteration (Iteration 5).

later used as input for the first cloudy iteration of the GCM (iteration 1). The iteration 1 cloud profile of HATS-6b shows global cloud coverage. In Fig. 6.5, the nucleation rate J_* , cloud particle number density n_d , average cloud particle size $\langle a \rangle$, and cloud mass fraction⁵ ρ_d/ρ are shown for the morning and evening terminator. The sub-stellar and anti-stellar point can be found in Fig. D.1. The cloud particle properties of these profiles are largely the same, although there is an increase in the nucleation rate for the upper atmosphere ($p < 10^{-3}$ bar) for the cooler profiles (morning terminator and anti-stellar point) with a corresponding increases in cloud particle number density and cloud mass fraction for these points. The formation of cloud condensation nuclei (CCNs) happens predominantly in the upper atmosphere ($p < 10^{-2}$). Though it should be noted that condensation still occurs in these upper regions - hence the increase in average particle size. Going to deeper layers, the cloud particle sizes steadily increase while cloud particle number densities steadily decrease. This inverse correlation between cloud particle number density and cloud particle size is well known (see Helling et al. 2021). If more cloud particles are present, the same

⁵Also sometimes called dust-to-gas ratio.

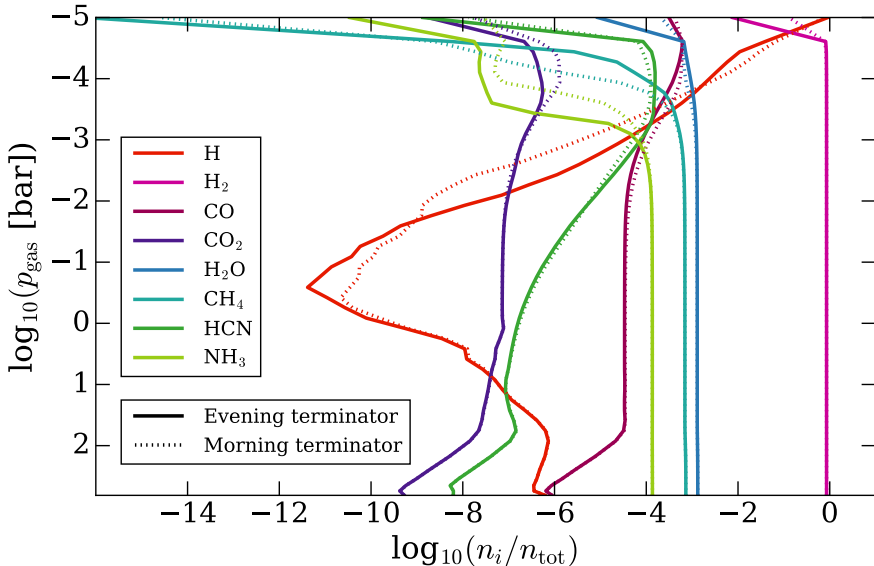


Figure 6.8: Concentrations of non-equilibrium gas species for the warm Saturn example HATS-6bat the morning and evening terminators for the final iteration (Iteration 5).

mass of condensation material is spread out over more particles hence reducing the average size of the particles.

6.3.2 Impact of clouds on the atmospheric structure

Iteration 1, 2, 3, 4, and 5 of the GCM are created by including the post-processed cloud opacities from the previous iteration into `expeRT/MITgcm` as described in Sect. 6.2.2. The GCM was again run for 2000 simulation days. Similar to iteration 0, there was little change in the global average temperature above 1 bar after 2000 simulation days (see Appendix D.2).

Going from iteration 0 to iteration 1 highlights the impact of clouds on the temperature and wind structure due to the increased local opacities. The most striking difference is a strong temperature inversion for pressures lower than 10^{-2} bar (higher altitudes) on the sub-stellar point and the evening terminator (Fig. 6.2). This increased temperature is also visible in the isobaric plots (Fig. 6.3). At pressures between 10^{-2} bar and 10 bar, the $(T_{\text{gas}}, p_{\text{gas}})$ profiles of

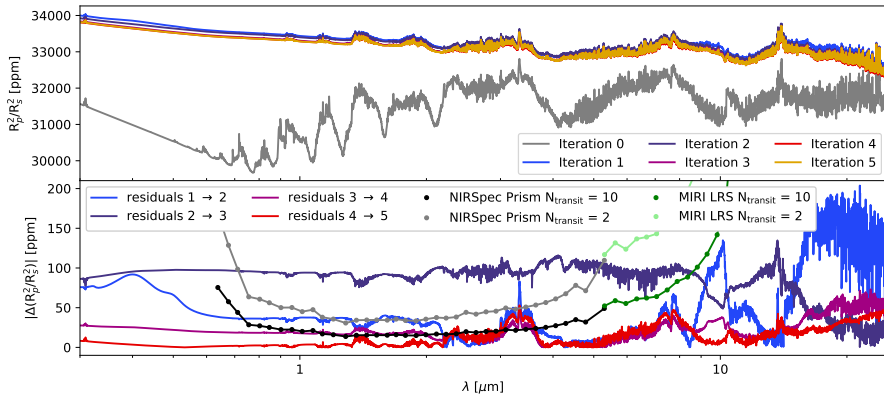


Figure 6.9: Comparison of the transmission spectra for the warm Saturn example HATS-6b for $\lambda = 0.3 \mu\text{m}$ to $25 \mu\text{m}$. **Top:** Transmission spectrum for each iteration. **Bottom:** Absolute residuals between subsequent iterations and the spectral precision for JWST observations with NIRspec Prism and MIRI LRS for 2 and 10 transits.

iteration 1 show a considerably colder temperature. This drop can be explained with an anti-greenhouse effect (see Sect. 6.5.1). For pressures higher than 10 bar, no significant differences in the $(T_{\text{gas}}, p_{\text{gas}})$ profiles were found. Furthermore, iteration 1 has a stronger and narrower equatorial wind jet than iteration 0 (see left panel of Fig. 6.4). This matches the results of Baeyens et al. (2021), who showed that for the temperature range of warm Satellites (500 K to 1200 K) an increase in equilibrium temperature results in a faster and narrower jet. The cloud-induced temperature inversion seems to have a similar effect. Furthermore, the weak polar jets of the iteration 0 are not observed in iteration 1.

Going from iteration 1 to iteration 2 shows less differences in the thermal and wind structure of HATS-6b than from iteration 0 to 1. However, the temperature profile still changes by up to 90 K. The exception to this is the morning terminator around 10^{-4} bar where a temperature increase of up to 350 K can be seen. This increase in temperature also reduces the nucleation rate which in turn leads to fewer but larger particles (Fig. 6.5). The sudden change in the morning terminator is caused by a dynamical instability caused by the iteration 2 cloud structure which leads to hot air being advected from the day-side into the morning terminator. The general thermal instabilities of the morning terminator are discussed in more detail in Sect. 6.5.2. While an

instability is present in all cloudy iterations, it is more pronounced in iteration 2. The persistence of this instability is a result of the cloud structures being static. Since no other iteration shows a similar behaviour, the temperature increase in the morning terminator of iteration 2 is considered an artefact of the specific configurations of the static clouds.

Iteration 3, 4, and 5 all show the same general characteristics as iteration 1 and 2: a temperature inversion around 10^{-3} bar, a cooling around 0.1 bar to 1 bar, a narrow equatorial wind jet, and global cloud coverage. However, the temperature between iterations after iteration 2 still vary by up to ~ 130 K. Similarly, differences in the temperature structure around 10^{-3} bar can be seen in the isobaric plots (Fig. 6.3) and in the zonal mean winds (Fig. 6.4). The cloud particle properties on the other hand vary little between iterations 3, 4, and 5. In particular the nucleation rate between iteration 4 and 5 is close to identical. Nevertheless, there are still changes in the cloud particle number density and average size between iteration 4 and 5. As mentioned previously, the goal of this work is to find a solution within the observational accuracy of JWST and therefore only observable changes within the atmospheric structure matter. Whether the changes described here have an observable effect is analysed in Sect. 6.3.4.

6.3.3 Disequilibrium chemistry

To assess the impact of the kinetic gas-phase chemistry and photo-chemistry on the observable atmosphere, and more specifically on transmission spectra of HATS-6b, the disequilibrium chemistry was modelled for each iteration at six coordinates along the terminator region (longitudes ($\phi = \{90^\circ, 270^\circ\}$) and latitudes ($\theta = \{0^\circ, 23^\circ, 68^\circ\}$)). The resulting gas concentration profiles were averaged over the six coordinates. The relative number densities n_i/n_{gas} of H, H₂, CO, CO₂, H₂O, CH₄, HCN, and NH₃ can be seen in Fig. 6.6. These eight molecules have been chosen due to their high concentrations in the atmospheres or because they are some of the more interesting atmospheric species when looking at the effects of external radiation (e.g. Barth et al. (2021); Baeyens et al. (2022)). The concentration profiles show very little variation among the five iterations with clouds, whereas the difference between the cloudless (iteration 0) and cloudy iterations (1 - 5) is somewhat larger. The largest differences between the cloudless and cloudy iterations occurs between $p_{\text{gas}} \sim 10^{-2} - 10^0$ bar (Fig. 6.6). This pressure range corresponds to a cloud-induced cooling which is present in iterations 1 - 5. Some species (e.g. NH₃, CO₂, and CH₄) also show a difference between cloudy and cloudless at lower pressures (Fig. 6.6) corresponding to a cloud-induced heating in iterations 1 - 5. The cloud-induced

heating in the upper atmosphere in combination with a cooling of the lower atmosphere comprises the temperature inversion (see Fig. 6.2).

The chemical variations along the equator are illustrated in the middle (sub-stellar and anti-stellar point) and bottom panel (morning and evening terminator). Comparing the top and middle panel we notice that the relative number densities of all species show significantly larger differences between the day- and night-side (the solid and the dashed lines in the middle panel) than the differences between the different iterations (all lines in the top panel). We will further describe the chemistry observed for HATS-6b in Sect. 6.4.1.

6.3.4 Observable differences between iterations

The goal of the step-wise iteration approach is to reach observational accuracy here chosen to be the JWST NIRspec and MIRI LRS. For HATS-6b, this was reached after six iterations, i.e. after iteration 5.

All transmission spectra were produced using the temperature structure of the GCM and the chemistry of ARGO. The spectrum of the cloudy iterations included the cloud structures as well. All 6 spectra are shown in the top panel of Fig. 6.9. The residuals between iterations 1, 2, 3, 4, and 5 are shown in the bottom panel of the same figure. Additionally, the spectral precision for the JWST instruments NIRSpec Prism (Birkmann et al. 2022; Ferruit et al. 2022) and MIRI LRS (Kendrew et al. 2015, 2016) are shown. The spectral precision was calculated using PandExoh (Batalha et al. 2017) assuming a spectral resolution⁶ of $R = 10$ for two and ten observed transits. If the residuals are significantly larger than the spectral precision, the differences between the iterations are observable. If the residuals are of the same order or lower, observing the differences between iterations will be challenging.

The transmission spectra of iteration 0 and 1 show clear differences due to the presence of clouds in iteration 1. Compared to iteration 0, the molecular features of iteration 1 are muted for wavelengths below $2 \mu\text{m}$. Around $10 \mu\text{m}$, an additional increase of the relative transit depth can be seen which is caused by silicate species within the cloud particles. Both these effects are known and expected if clouds are present in exoplanet atmospheres (Wakeford & Sing 2015; Powell et al. 2019; Grant et al. 2023).

The residuals in transit depth between iterations 1, and 2 are around 50 ppm for wavelengths between $0.7 \mu\text{m}$ to $10 \mu\text{m}$. This can be related to a shift in the cloud top, which is defined as the pressure level at which clouds become

⁶This resolution was chosen to maximise the spectral precision while keeping enough data points to detect gas-phase features.

optically thick (see e.g. Estrela et al. 2022). A clear CH₄ feature can be seen at 3 μm to 4 μm with a residual depth of around 100 ppm. This indicates that the differences between the (T_{gas} , p_{gas}) profiles are still strong enough to significantly impact the disequilibrium chemistry of the planet, and that CH₄ might be particularly susceptible to these differences.

Iteration 2 and 3 differ by roughly 100 ppm for wavelengths between 0.7 μm to 10 μm . This difference can again be related to shifts in the cloud top. Since the spectral precision for NIRSpec Prism between $\lambda = 1 \mu\text{m}$ and 4 μm is below 50 ppm, such differences might still be observable. The same holds for MIRI LRS which has a spectral precision of less than 100 ppm for wavelengths below 10 μm if ten transits are observed.

From iteration 3 to 4 and 4 to 5, the cloud top again changes but by less than 25 ppm. The residuals between iteration 4 to 5 are now consistently below the spectral precision of NIRSpec Prism, as illustrated by the black data points. The only exception to this is the CH₄ feature around 3 μm to 4 μm , that still has a residual depth of around 50 ppm. However, this difference in the transit depth is on the same order as the spectral precision NIRSpec Prism after two transit observations, which will make detections difficult. Since the differences between the transmission spectra of iteration 3, 4, and 5 are close to or below the spectral precision of JWST NIRSpec Prism, we stop our iterative procedure after iteration 5.

Furthermore, comparing the residuals to the differences between the morning and evening terminator (see Fig. 6.11) shows that the differences between the limbs are generally larger than the residuals between iterations 4 and 5. This holds for the cloud continuum (limb \approx 500 ppm versus residuals < 10 ppm), the methane features (limbs \approx 750 ppm versus residuals < 50 ppm), and the water features (limb \approx 500 ppm versus residuals ≈ 20 ppm).

6.4 The combined 3D model for the warm Saturn HATS-6b that orbits an M-dwarf

The final combined 3D model for the warm Saturn HATS-6b that orbits an M-dwarf has been demonstrated in Sect 6.3. The two isobar maps at pressure ranges that are accessible to transmission spectroscopy are shown in the bottom right panel of Fig. 6.3 (iteration 5). HATS-6b is affected by a strong equatorial jet that reaches down to depth of $p_{\text{gas}} \approx 1\text{bar}$. Horizontally converging flows⁷ further contribute to the global mixing of the atmosphere in the pole regions

⁷Convergence is here defined as $\nabla \cdot \mathbf{v} < 0$, where \mathbf{v} is the horizontal velocity vector.

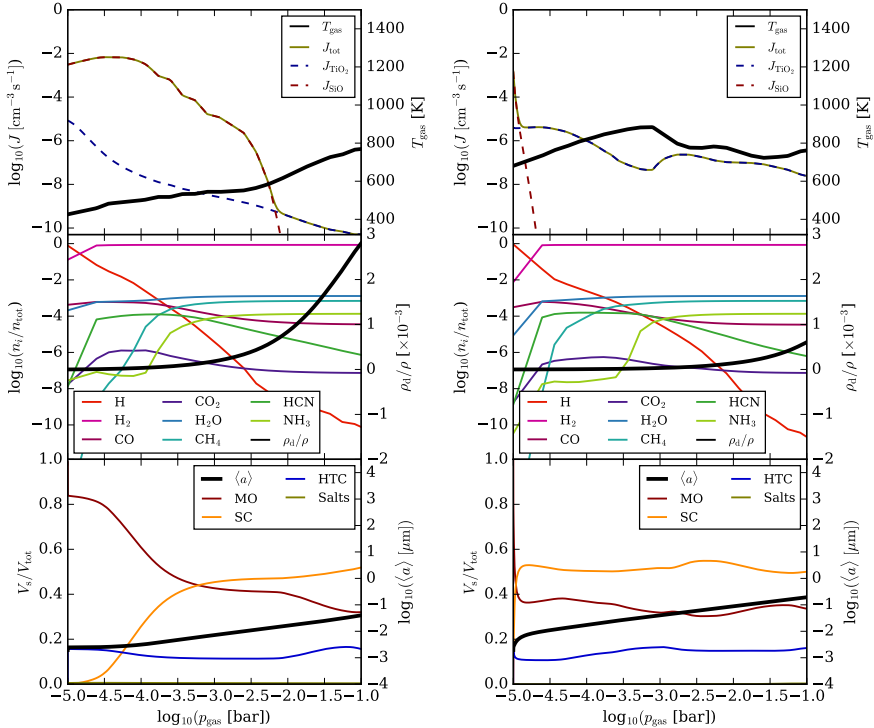


Figure 6.10: Atmospheric cloud structure of the morning (**left**) and evening (**right**) terminator of HATS-6b. **Top:** gas temperature T_{gas} and total J_{\star} and J_{TiO_2} , and J_{SiO} . **Middle:** gas-phase concentrations n_i/n_{tot} and cloud mass fraction ρ_{d}/ρ . **Bottom:** cloud particle volume fractions $V_{\text{s}}/V_{\text{tot}}$ and mean cloud particle size $\langle a \rangle$ (MO = Metal oxides, SC = Silicates, HTC = High temperature condensates). Salts are a minor component and have a volume fraction close to 0.

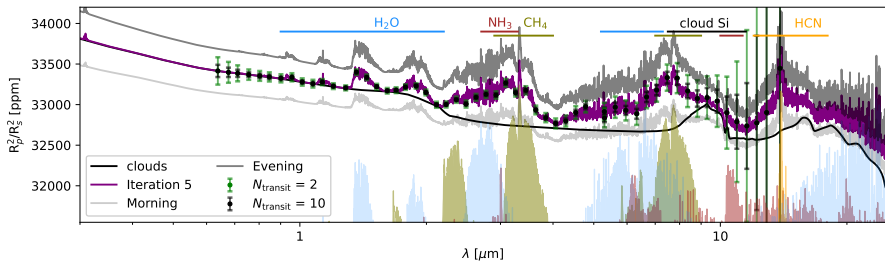


Figure 6.11: Transmission spectra for the warm Saturn HATS-6b for $\lambda = 0.3 \mu\text{m}$ to $25 \mu\text{m}$ including the total spectrum of the final iteration (iteration 5) as well as the morning and evening terminator separately. Also shown are the contributions of selected gas-phase species, the contribution of the Si-bearing cloud particle materials, and the spectral accuracy of the JWST instruments NIRSpec Prism and MIRI LRS for 2 and 10 transits.

(e.g. Baeyens et al. 2021). The temperature inversion is well represented in the upper atmosphere with a temperature difference of $\approx 400\text{K}$ as compared to lower regions where $p_{\text{gas}} \approx 10^{-2} \text{ bar}$. Sect. 6.4.1 presents the final results from the combined model and Sect. 6.4.2 shows the transmission spectrum as observable with JWST NIRspec Prism and MIRI LRS.

6.4.1 The atmospheric structure of HATS-6b

HATS-6b is a warm Saturn with a hydrogen dominated atmosphere that is assumed to be oxygen rich in this study. Figure 6.10 presents the solution of the combined 3D model. The morning (left) and the evening (right) 1D terminator profiles were selected to demonstrate the cloud and kinetic chemistry results in enough detail to gain insights into the physical reasons for the differences between the respective transmission spectra that are shown in Sect. 6.4.2.

Figure 6.10 (top) shows that the local gas temperatures differ between the morning and the evening terminator which has direct consequences for the cloud formation efficiency. By comparing the nucleation rates ($J_* [\text{cm}^{-3}\text{s}^{-1}]$), we notice that the cooler morning terminator (left) forms more cloud particles than the hotter evening terminator. Consequently, the mean particles size, $\langle a \rangle [\mu\text{m}]$, is smaller in the respective low gas pressure region of the morning terminator. The lower panels in Fig. 6.10 show which material groups dominate the cloud particle composition, and hence, their opacities. Fig. D.2 contains the detailed breakdown of all 16 modelled bulk materials. Materials that are determined by

low-abundance elements like Cl, Mn etc. can be thermally stable but appear with $\sim 1\%$ volume contribution (Helling et al. 2017; Woitke et al. 2018).

Figure 6.10 demonstrates that it is reasonable to expect the cloud particles that form in the atmosphere of a warm Saturn like HATS-6b to be made of a mix of materials and that their mean particles sizes changes throughout the atmosphere. It further demonstrates that the bulk cloud mass (ρ_d/ρ , black line, middle panel) is not necessarily equally distributed through the atmospheres and differs between the two terminators, hence, emphasising the terminator asymmetry. Comparing to the material volume fractions, V_s/V_{tot} , in the lower panels demonstrates that the bulk mass comes from silicates ($\text{MgSiO}_3[\text{s}]$, $\text{Mg}_2\text{SiO}_4[\text{s}]$, $\text{CaSiO}_3[\text{s}]$, $\text{Fe}_2\text{SiO}_4[\text{s}]$) and metal oxides ($\text{SiO}[\text{s}]$, $\text{SiO}_2[\text{s}]$, $\text{MgO}[\text{s}]$, $\text{FeO}[\text{s}]$, $\text{Fe}_2\text{O}_3[\text{s}]$) because Mg/Si/Fe/O are the most abundant elements amongst those considered here. It is, hence, the result of mass conservation. Far less important for the cloud material composition are the high temperature condensates ($\text{TiO}_2[\text{s}]$, $\text{Al}_2\text{O}_3[\text{s}]$) and salts ($\text{KCl}[\text{s}]$, $\text{NaCl}[\text{s}]$) for the same reason. Since most dominant condensation species are oxygen bearing species and oxygen is far more abundant than Ti, Mg, Si, and Fe, these condensation species do not significantly impact the gas-phase chemistry of non Ti, Mg, Si, and Fe bearing species.

As introduced in Sect. 6.3.3, the disequilibrium chemistry of HATS-6b is shown in Fig. 6.7 and Fig. 6.8. The middle and bottom panels show the relative number densities for a selection of molecular gas species for the last iteration at four coordinates along the equator of the planet: sub-stellar point, anti-stellar point, and the two terminators. The variations along the equator are caused both by differences in the $(T_{\text{gas}}, p_{\text{gas}})$ profiles for the four coordinates, and by differences in the stellar XUV radiation and the SEPs. The sub-stellar point is irradiated both by XUV radiation and SEPs, the terminators are irradiated only by SEPs, and the anti-stellar point is irradiated by neither. Comparing the four cases it can be seen that the sub-stellar point and the two terminators are relatively similar, whereas the anti-stellar point differs significantly from the rest. By comparing the sub- and anti-stellar point, we notice a steep decrease in the concentration of many of the gas species at the sub-stellar point (incl. H_2 , CH_4 , and NH_3) in the upper atmosphere, indicating a break down of these molecules through photolysis by the XUV radiation or ionisation by the SEPs. Other species (such as H, HCN, and partly CO and CO_2) show an increase in concentration for the sub-stellar point compared to the anti-stellar point as we move further up into the atmosphere, indicating that these are positively influenced by photochemical reactions. Comparing model runs for the sub-stellar point with and without SEPs (middle panel), we notice a significant contribution by the SEPs on the gas-phase concentrations and that this effect reaches far down into the atmosphere. The middle and bottom

panels show that the sub-stellar point with SEPs bear a strong resemblance to the terminator regions, which could indicate that SEPs can have a larger effect than the XUV radiation on the concentrations of the gas species, including observationally interesting species such as CH₄ and HCN. The bottom panel shows that the differences between the terminator regions are generally higher at lower pressures, with the exception of H that also show differences deeper into the atmosphere.

As mentioned in Sect. 6.1, M-dwarf stars such as HATS-6 are known to have higher magnetic activities compared to more massive stars like the Sun. This increased activity leads to increased amounts of SEPs. As explained in Sect. 6.2.4, the amount of SEPs has been found to scale with the X-ray flare intensity of the star, which for M-dwarf stars has been reported to range from 0.001 to 0.2 Wm⁻² at 1AU. In this study we scale our SEP spectrum based on a X-ray flare intensity of 0.1 Wm⁻² at 1AU, indicating that the amount of SEPs could be significantly higher than what we show, leading to a greater impact on the disequilibrium gas-phase chemistry.

6.4.2 Transmission spectra

Transmission spectra are used to study the chemical composition and atmospheric asymmetries of gaseous planets. To determine the number densities of known non-equilibrium species (e.g. CH₄ and HCN), the H/C/N/O complex of the gas-phase is determined using ARGO (Sect. 6.3.3). As the methods used in this study may help to efficiently interpret the data of JWST and future space missions, the focus was set on spectral features relevant for the JWST instruments NIRspec and MIRI. In the following, the near-IR transmission spectra that also include non-equilibrium species like CH₄ and HCN for a wavelength range of $\lambda = 0.3 \mu\text{m}$ to $12 \mu\text{m}$ are presented.

To create the transmission spectrum of HATS-6b, we used the (T_{gas} , p_{gas}) profiles from the GCM, the cloud opacities from the kinetic cloud model and the disequilibrium chemistry from ARGO. The transmission spectrum for the morning and evening limb is shown in the top panel of Fig. 6.11. The bottom panel shows the full transmission spectra. Additionally, the clouds and the gas-phase contributions are shown. The transmission spectrum shows a roughly flat spectra for wavelengths below $2 \mu\text{m}$, owing to scattering which is typical for cloudy exoplanets (Bean et al. 2010; Crossfield et al. 2013; Kreidberg et al. 2014; Knutson et al. 2014; Sing et al. 2015, 2016; Benneke et al. 2019). Observing HATS-6b at these wavelengths would allow us to determine the height of the cloud deck (Mukherjee et al. 2021). Above $3 \mu\text{m}$ the gas-phase species start to contribute significantly to the spectrum. Especially CH₄ (around $3 \mu\text{m}$ and

8 μm), H₂O (around 6 μm), and HCN (around 10.5 μm) can be seen. However, the clouds still heavily mute the spectral features, making them harder to detect.

Around 10 μm , the cloud opacities show a broad silicate feature from the Si-bearing cloud particle materials. This feature originates from Si-O vibrations (Wakeford & Sing 2015). It causes an increase of the transit depth of more than 1000 ppm compared to a cloud free planet. Detecting this feature could confirm the presence of silicon-bearing cloud particle materials in HATS-6b as has been done previously for WASP-17b (Grant et al. 2023) and WASP-107b (Dyrek et al. 2023).

HATS-6b itself may reveal differences in cloud coverage and chemistry between the morning and evening terminator similar to WASP 39b (Carone et al. 2023; Espinoza et al. 2024). The cloud deck is slightly higher at the evening terminator compared to the morning terminator leading to a \approx 500 ppm offset at the short wavelengths ($0.3 \mu\text{m} < \lambda < 2 \mu\text{m}$). The observable difference in the gas-phase is mainly caused by CH₄ which has \approx 750 ppm higher signal at the evening terminator than at the morning terminator. H₂O has \approx 500 ppm higher signal in the evening terminator than the morning terminator. At the morning terminator, the contribution of chemical species to the transmission spectrum can vary strongly with latitude (see Fig. D.3). Especially at $\pm 68^\circ$ of the morning terminator, stronger transmission features of CH₄ and HCN arise as a consequence of the Rossby gyres that represent particularly cold regions in the atmosphere (see Fig. 6.3). Warm Saturns and Jupiters in the temperature range between 800 K and 1200 K typically exhibit extended Rossby wave gyres at the morning terminator (e.g. Baeyens et al. 2021, Fig. 2). Thus, a study of morning terminator chemistry in warm Saturns needs to take into account special locations like the dynamically cool Rossby gyres to correctly infer global atmosphere properties.

6.5 Discussion

In this work, a 3D climate model in combination with a microphysical cloud model was implemented to capture the feedback between the heating, the 3D climate, and cloud formation in its full complexity. The model was applied to the particular example of a warm Saturn around an M-dwarf, HATS-6b. Many exoplanet theories predict temperature inversions in exoplanet atmospheres due to various reasons. In Sect. 6.5.1, the strong cloud-induced temperature inversion of HATS-6b is discussed. Furthermore, we discuss the dynamics of the terminators in Sect. 6.5.2. While several studies have modelled the climate and cloud structure of warm Saturns, there have been no detailed studies of warm

Saturns around M-dwarf stars like HATS-6b so far. Therefore in Sect. 6.5.3, the results for HATS-6b are compared to grid studies including warm Saturns and detailed models of other Saturn-mass planets similar to HATS-6b.

6.5.1 Anti-greenhouse effect

The clouds in HATS-6b have considerable cloud particle sizes and number densities for pressures lower than 10^{-3} bar. The high cloud deck leads to scattering and absorption of the incoming short wavelength radiation on cloud particles. This reduces the radiative heating of the lower atmospheric layers while simultaneously heating up the upper layers. Both effects lead to a temperature inversion in the layers where clouds are located and a cooling of the layers below. This effect is called the anti-greenhouse effect and was first observed in Titan (McKay et al. 1991). It has also been theoretically predicted for exoplanet atmospheres with either an extended cloud deck or photochemical hazes (Heng et al. 2012; Morley et al. 2012; Steinrueck et al. 2023).

In hotter exoplanets, temperature inversions are not caused by scattering from high-altitude clouds but by gas-phase species like TiO and VO (Hubeny et al. 2003; Fortney et al. 2008) or AlO, CaO, NaH, and MgH (Gandhi & Madhusudhan 2019). These species heat up the upper atmosphere due to very efficient absorption of stellar radiation in the optical wavelength range. These absorption-driven temperature inversions have been observed in (ultra) hot Jupiters (Haynes et al. 2015; Yan et al. 2020, 2022). HATS-6b orbits an M-dwarf that emits less flux in the optical wavelength range than a hotter star (Lothringer & Barman 2019). Furthermore, Hu & Ding (2011) predicted that an exoplanet with a CO₂ dominated atmosphere orbiting an M-dwarf stars would also have an anti-greenhouse effect mainly due to highly efficient Rayleigh scattering of CO₂ at the top of the atmosphere. In this study, however, CO₂ is a minor species and Rayleigh scattering is dominated by hydrogen and helium. In our simulation of HATS-6b, no temperature inversion is present in the GCM runs without clouds. Therefore, we are confident in our conclusion that the temperature inversion is indeed caused mainly by scattering of stellar irradiation at the top of the extended cloud deck similar to the anti-greenhouse effect observed in Titan due to scattering at the top of the atmosphere due to hazes.

To observe a temperature inversion directly, emission from the lower atmosphere needs to be observable (Gandhi & Madhusudhan 2019). The strong cloud coverage will likely block all emissions from the lower atmosphere and make direct detections of the temperature inversion unlikely. However, HATS-6b lies in a temperature regime where quenching is expected to affect the chemistry

(e.g. Baeyens et al. 2021). Fig. 6.9 and 6.11 shows a CH₄ feature that is visible despite the cloud layer, which indicates that the CH₄ extends into the upper layers of the atmosphere where it is exposed to photolysis and high degrees of SEPs. Since CH₄ is very susceptible to photo-chemical reactions (Moses et al. 2011; Line et al. 2011; Baeyens et al. 2021, 2022; Konings et al. 2022), it will most likely break down in the upper atmosphere, and in order to maintain a visible CH₄ feature, a constant up-welling from the lower protected part of the atmosphere would be necessary. A visible CH₄ feature could therefore indicate that vertical mixing has connected the observable gas-phase chemistry above the clouds to deeper atmosphere layers, thereby forming a probe through the temperature inversion and into the layers cooled by the anti-greenhouse effect (Agundez et al. 2014; Fortney et al. 2020). In addition, this work confirmed the influence of stellar energetic particles (SEP) on the day side chemistry of a planet around a relatively active planet as was already pointed out by Barth et al. (2021) for HD 189733b.

6.5.2 Dynamics of the terminator regions

In Sect. 6.3, we seen that the morning terminator of iteration 2 develops a temperature spike in the upper atmosphere (see Fig. 6.2). Since no other iteration shows such a spike, we can conclude that it is caused by the impact of the specific configuration of the static cloud opacities of iteration 2 on the temperature and wind structure of HATS-6b. A closer inspection of the potential temperature profiles across the morning and evening terminators of all iterations (Fig. 6.12) reveals a potential temperature anomaly at the equator for the morning terminator in iteration 2. The potential temperature is linked to atmospheric stability. If the potential temperature increases monotonically with height, the atmosphere is dynamically stable (e.g. Holton & Hakim 2013).

The equatorial morning terminator is a region, where the super-rotating wind jet advects colder air from the night side to the day-side that is heated by the cloud feedback (see Fig. 6.3). The advection of cold air results in a minimum in potential temperature between -40 degree and +40 degree latitude. In contrast to that, the potential temperature across the evening terminator is more barotropic. Here, the wind jet broadens and encompasses almost the whole evening terminator region (Fig. 6.3), resulting in a more uniform advection of warm air towards the night side.

The aim of this work is to identify a stable climate solution for a cloudy warm Saturn orbiting an M-dwarf star. However, it may be worthwhile investigating if the strong temperature gradients of the morning terminator at the boundary of the super-rotating jet give rise to instabilities and thus variations at the morning

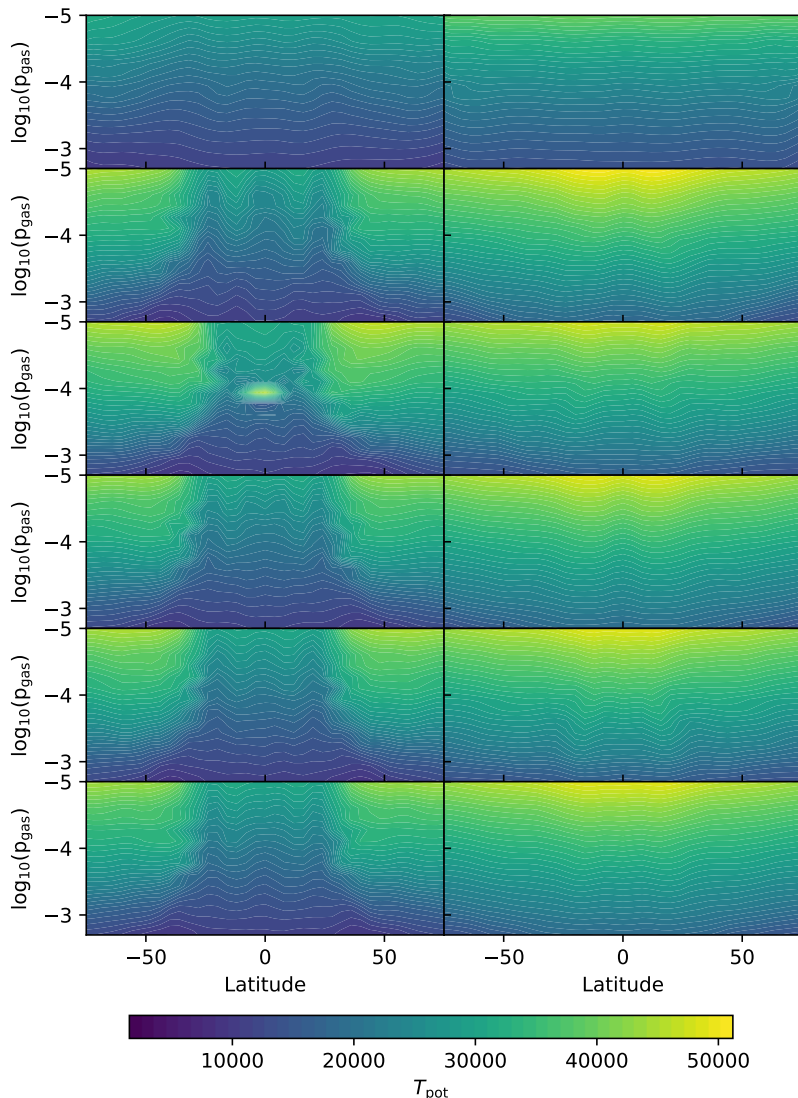


Figure 6.12: Potential temperature cross section across the morning (left panels) and evening terminators (right panels) for iterations 0 to 5 (from top to bottom).

terminators as is evident in iteration 2. Observations that aim to disentangle the atmospheric properties of the morning and evening terminator of gas-giants with JWST could confirm the stronger dynamical variability of the morning terminator compared to the evening terminator. However for HATS-6b, we do not see observable differences due to variations across the terminators.

6.5.3 Comparison to other models

The cloud structure and climate of HATS-6b was simulated as a first example of a warm Saturn around an M-dwarf host star. To extend our findings from HATS-6b to general warm Satellites, the results are compared to other studies focusing on including the 3D cloud and climate of warm Saturn type exoplanets.

Helling et al. (2023) conducted a grid study of post-processed cloud structures for temperatures between 400 K and 2600 K for F, G, K and M-dwarf stars. For exoplanets with an equilibrium temperature of 700 K around M-dwarf stars, they predict a strong uniform cloud coverage. The equilibrium temperature and cloud structure of HATS-6b falls with their "class (i)" planets which are characterised by global and mostly homogenous cloud coverage. Our results suggest that at least for exoplanets around M-dwarf stars like HATS-6b an anti-greenhouse effect is expected for these class (i) planets caused by the clouds.

Christie et al. (2022) studied the impact of clouds on the climate of the warm Neptune GJ 1214b. They considered phase equilibrium clouds within the EddySed model (Ackerman & Marley 2001). Their cloud model parameterises the settling of cloud particles with the parameter f_{sed} , where a lower f_{sed} results in vertically extended clouds. In contrast to our work, and matching other studies of cloud composition of GJ 1214b (Gao & Benneke 2018; Ormel & Min 2019), they consider only KCl and ZnS as cloud particle material. Christie et al. (2022) found that clouds can cause cooling in the lower atmosphere (10^{-2} bar $< p < 1$ bar) which matches our findings. This temperature decrease is most pronounced for higher metallicities and lower f_{sed} . However, they did not find a significant temperature increase in the upper atmosphere, as we find in our work.

Another planet similar to HATS-6b, is the Saturn-mass exoplanet WASP-39b that is part of the JWST Early Release Science program (Feinstein et al. 2023; Ahrer et al. 2023; Rustamkulov et al. 2023; Alderson et al. 2023; JWST Transiting Exoplanet Community Early Release Science-Team et al. 2023). WASP-39b is at the upper limit of the class(i) cloud temperature regime identified by Helling et al. (2023) with $T_{\text{eq}} \sim 1100$ K. Cloudless GCMs of WASP-39b show relatively small day-night temperature differences of $\Delta T \sim 500$ K (Carone et al. 2023; Lee et al. 2023), similar to the cloudless simulations of

HATS-6b. Post-processed cloud modelling by Carone et al. (2023) predicts global cloud coverage of WASP-39b. Pre-JWST observations pointed towards a relatively cloud free atmosphere, with estimates of atmospheric metallicities ranging from $0.1 \times - 100 \times$ solar (Sing et al. 2016; Nikolov et al. 2016; Fischer et al. 2016; Wakeford et al. 2018). Observations with JWST revised these earlier observational results and indicate the presence of clouds and a $\gtrsim 10 \times$ solar metallicity, with some models favouring inhomogeneous cloud coverage (Feinstein et al. 2023). Thus, JWST observations of WASP-39b demonstrated that it is possible to break the high metallicity and cloudiness degeneracy that also plagued warm Saturns pre-JWST (Carone et al. 2021). JWST observations of WASP-39b could reveal cloud asymmetries between the morning and evening terminator as predicted by Carone et al. (2023). Also in this work, we find a tendency for cloud asymmetries between both terminators (see Sect. 6.4.2.)

6.6 Conclusion

In this chapter, we explored the atmospheric, micro-physical cloud and gas-phase structure of the warm Saturn HATS-6b, orbiting an M-dwarf using a combined model in the form of step-wise iterations between a detailed cloud formation description and `expeRT/MITgcm`, a 3D GCM with full radiative transfer and deep atmosphere extension. We demonstrated how the combined modelling approach can help to support the interpretation of the data from space missions (e.g. JWST) for warm Saturn type planets.

We find a significant cloud coverage on both the day and night side of HATS-6b, which is to be expected for the generally low temperatures ($500 \text{ K} < T < 1200 \text{ K}$) of warm Saturn type exoplanets. On the day-side and evening terminator, we find that clouds cause a significant temperature inversion in the upper atmosphere ($p < 10^{-2} \text{ bar}$). This also results in a globally reduced temperature of the deeper atmospheric layers ($10^{-2} \text{ bar} < p < 1 \text{ bar}$) which is consistent with an anti-greenhouse effect. Including clouds in the GCM also leads to a stronger and narrower equatorial jet stream. The transmission spectra of HATS-6b shows a characteristically flat spectrum in the optical. In the infrared, however, major molecular absorption features like CO₂, CH₄ and H₂O are visible despite the global cloud coverage. Around $10 \mu\text{m}$, a silicate cloud feature is predicted. The small radii of M-dwarf stars compared to more massive stars leads to a 'magnifying effect' of spectral features within transmission spectra. This makes planets like HATS-6b prime targets for deciphering gas chemistry and cloud compositions for warm Saturn type exoplanets. For wavelengths up to $8 \mu\text{m}$, it may even be possible to identify morning and evening terminator differences with the CH₄ feature around $3 \mu\text{m}$.

When iterating between the GCM and the cloud model, the differences in the atmospheric structure of HATS-6b quickly drop below the observational accuracy of the JWST NIRSpec Prism and MIRI LRS. For HATS-6b this was reached after 5 iterations. Even after 1 iteration (GCM → Clouds → GCM) the GCM predicts an atmospheric structure that differs by less than 200ppm to iteration 5. Furthermore, differences in the transmission spectra between the iteration steps are smaller than the differences between the morning and evening terminator. Therefore a combined model that enables the full complexity of all modelling components (here 3D GCM and cloud formation) proves useful for the scientific interpretation of observational data for larger sets of exoplanets to be studied with CHEOPS, JWST, and also ELT, PLATO, and Ariel in the future.

Warm Saturn type exoplanets around M-dwarfs are ideal candidates to identify cloud particle composition by observing their spectral features and identify the cloud-induced thermal inversion that arises on these planets. In particular limb asymmetry studies will allow us to study differences in the chemistry and cloud top which are caused by the feedback of clouds on the atmospheric structure. Using the combined model allows us to account for the full physical complexity of each model in a computationally feasible manner and enables a detailed interpretation of observational data within the accuracy of JWST NIRSpec and MIRI LRS.

Acknowledgments

S.K. N.B.M., A.D.S, F.A, H.L.M., L.C., Ch.H., L.D., and U.G.J. acknowledge funding from the European Union H2020-MSCA-ITN-2019 under grant agreement no. 860470 (CHAMELEON). D.A.L. and D.S. acknowledge financial support from the Austrian Academy of Sciences. We acknowledged the computation support at the IWF Graz and CPH. LD acknowledges support from the KU Leuven IDN grant IDN/19/028 grant Escher. U.G.J. further acknowledges funding from the Novo Nordisk Foundation Interdisciplinary Synergy Programme grant no. NNF19OC0057374. To achieve the scientific results presented in this article we made use of the Python, especially the NumPy (Harris et al. 2020) and Matplotlib (Hunter 2007). The post-processing of GCM data was performed with gcm-toolkit (Schneider et al. 2022a).

Chapter 7

Conclusions and Outlook

In this thesis, we have analyzed the interplay of cloud formation, atmospheric chemistry, and the climate of exoplanet atmospheres. We started with a detailed study of the micro-physics of cloud formation by examining the effect of thermal disequilibrium on nucleation and the interaction of clouds with a non-equilibrium gas phase. We then investigated the opacity of heterogeneous cloud particles by comparing mixing treatments and analyzing the optical properties of cloud particle materials. Finally, we studied the influence of clouds on the atmospheric structure using HATS-6b as an example. Based on these results, the research questions from Chapter 1.3.1 are addressed (Sect. 7.1) and an outlook on future work is given (Sect. 7.2).

7.1 Conclusion

The work presented in this thesis has shown that clouds are an integral part of exoplanet atmospheres. The following three science questions have been addressed to provide a detailed understanding of how clouds affect and are affected by the thermal and chemical structure of an exoplanet.

How do thermal and chemical non-equilibria interact with cloud formation?

To answer this research question, we have derived and evaluated a description of kinetic polymer nucleation that accounts for thermal non-equilibrium of the clustering species (Chapter 3). We have modeled the nucleation of TiO_2 using two toy models that describe temperature differences between clusters.

In Chapter 4, we have investigated the interplay of clouds and the gas-phase. To account for all possible interactions, we have fully coupled the gas-phase chemistry, nucleation, condensation, and cloud particle surface reactions. All processes are described kinetically and time-dependent. To achieve this, we have derived the reaction supersaturation for a gas-phase in chemical non-equilibrium, accounted for three-body reactions of small clusters, and considered the full polymeric nucleation network of TiO_2 up to a cluster size of $(\text{TiO}_2)_{15}$. By fully coupling the gas-phase chemistry and bulk growth surface reactions, we have discovered a catalytic SiO-SiO_2 cycle. The full model was then applied to the atmosphere of HD 209458 b.

Our results show that clouds are fundamentally linked to the gas-phase from which they form. Based on our research on the effect of thermal and chemical non-equilibria, we find that:

- Thermal non-equilibrium can increase or decrease the formation of larger clusters if they are cooler or hotter than the gas-phase, respectively.
- Cloud formation depletes the local gas-phase of cloud forming elements (e.g. Mg, Si, Fe) and oxygen. The lower oxygen abundance leads to a decrease in the concentration of oxygen bearing gas-phase species.
- Surface reactions of cloud particles can lead to catalytic cycles which can impact the abundances of gas-phase species not directly linked to cloud formation, for example CH_4 .
- Low pressure environments are affected more by non-equilibrium effects. In collision-dominated environments, thermal and chemical equilibria are suitable assumptions.

The atmospheres of exoplanets are known to be affected by disequilibrium processes like quenching and photo-chemistry. Our work has shown that clouds are not only affected by but can also cause a disequilibrium gas-phase. Studies of disequilibrium chemistry in non-collision-dominated environments should therefore take the detailed micro-physical interaction of gas-phase and cloud formation into account.

What are the optical properties of heterogeneous cloud particles?

The morphology of cloud particles in exoplanets is unknown and therefore multiple assumptions have to be made. In Chapter 5, we studied the optical properties of considerably heterogeneous cloud particles under the assumption that they are either well-mixed or non-mixed. The effective refractive index of

well-mixed particles was calculated using LLL or Bruggeman. The opacity of non-mixed cloud particles was calculated assuming either a core-shell morphology or homogeneous particles. To determine which cloud particle materials affect the overall optical properties the most, we have studied 21 commonly considered cloud particle materials. To analyze the impact of cloud particle morphologies on observations, we have produced the transmission spectra of WASP-39b, HATS-6b, WASP-76b, and WASP-107b.

The optical properties of heterogeneous cloud particles depend strongly on their morphology and composition. From our investigation of five mixing treatments and 21 commonly considered cloud particle materials, we find that:

- Non-mixed particles (core-shell, SSA, and BAS) can retain the spectral properties of the individual cloud particle materials.
- The opacity of well-mixed cloud particles (LLL and Bruggeman) is complex and typically results in broad spectral features.
- The effective refractive index of well-mixed particles differs if calculated with either LLL or Bruggeman. LLL typically results in more muted transmission spectra.
- Iron-bearing cloud particle species and carbon (amorphous or crystalline) can dominate the optical properties of cloud particles even when their inclusions make up less than 1%.

Considering the heterogeneity of cloud particles is important for the interpretation of observations. Depending on the mixing treatment used, the transit spectrum will exhibit different cloud spectral features and different strengths in the muting of molecular lines. It is therefore potentially possible to observe cloud particle morphologies in exoplanet atmospheres. This also implies that predictions from forward models and cloud particle properties determined by retrieval models are affected by cloud particle morphologies. Some studies have preferred homogeneous cloud particles due to their simplicity or LLL due to the faster computation time. However, we have shown that such choices have an observable impact on the predicted transit spectra and the assumptions should be based on the micro-physical cloud properties.

How do clouds affect the climate of warm Saturns?

To research the interplay of clouds and climate, we studied the atmosphere of the warm Saturn HATS-6b (Chapter 6). By iteratively combining a detailed micro-physical cloud formation model and expeRT/MITgcm, we have shown that the

observable differences in the atmospheric structure after iteration 5 fall below the observational accuracy of the JWST instruments NIRSpec Prism and MIRI LRS. The atmospheric structure of HATS-6b exhibits the typical hallmarks of a tidally locked gas-giant: strong temperature differences between day- and night-side, a hot spot offset, and an equatorial wind jet. Furthermore, HATS-6b has a global but not a uniform cloud structure which affects the temperature and wind structure. The chemical structure has been post-processed using ARGO. The results show that photo-chemistry as well as SEPs reduce the CH₄ abundance in the upper atmosphere. Nevertheless, our results predict that CH₄ as well as cloud silicate features are potentially observable through transmission spectroscopy. Furthermore, we found differences between the morning and evening terminator in the CH₄ features as well as the height of the cloud layers.

Warm Saturns can be expected to have a global cloud coverage which impacts their climate as well as observations. Through our study of HATS-6b using the iterative cloud-climate model, we find that:

- Iterating between a micro-physical cloud model and a GCM enables computationally feasible modeling of temperate exoplanets while keeping the full complexity of both models.
- The presence of clouds can cause a temperature inversion in the upper atmosphere ($p_{\text{gas}} \approx 10^{-3}$ bar) which is propagated to the evening terminator through the equatorial wind jet, and an anti-greenhouse effect deeper in the atmosphere ($p_{\text{gas}} \approx 1$ bar).
- The change in the temperature structure caused by the clouds results in a narrower and faster equatorial wind jet.
- HATS-6b has a favourable transit depth due to its large radius compared to that of its M-dwarf host star, enabling the potential detection of CH₄ and silicate clouds.

The methods developed here for HATS-6b can be used to support the physical interpretation of observations with, for example, JWST, CHEOPS, PLATO or Ariel. While we used five iterations to confirm that there are no observable differences within the simulations for HATS-6b, conducting one iteration already captured all the hallmarks of the cloudy climate. If computational resources are limited, it is therefore advisable to include cloud particle opacities at least once within the GCM.

7.2 Outlook

In this work, we have confirmed that the interplay of atmospheric processes is complex. It is therefore important to conduct detailed studies of the interactions between clouds, gas-phase chemistry, and climate. Here we elaborate on how future studies can build on the findings presented in this thesis.

A comprehensive understanding of processes that affect the atmospheric chemistry of exoplanets is key for the interpretation of observations. This is best illustrated in the discussion about biomarkers where a detailed understanding of abiotic processes is required to prevent false positives (see e.g. Schwierman et al. 2018; Barth et al. 2024). In Chapter 4, we have shown that surface reactions of cloud particles are also a potential driver for disequilibrium chemistry. While the SiO-SiO₂ cycle showcases how cloud particles can act as catalysts, more detailed investigations into the surface reactions are needed. Currently only 59 reactions and 10 cloud particle materials are included in our model. As a next step, the number of cloud particle species and surface reactions included should be increased to investigate whether more catalytic cycles are possible. Furthermore, to study for which exoplanet atmospheres these catalytic cycles are most relevant, the fully kinetic cloud formation model should be extended to one, two, or three dimensions. Because the gas-phase chemistry and cloud formation are described fully kinetically, our model can be combined with other multidimensional chemical disequilibrium models like, for example, VULCAN (Tsai et al. 2017, 2024). Adding time-dependent cloud formation to these models would also allow to study the effect of quenching and photochemistry on cloud formation.

Cloud particles are an important opacity source in exoplanet atmospheres. With the capabilities of JWST, the spectral features of cloud particles can be observed (Grant et al. 2023; Dyrek et al. 2023). In this thesis, we have demonstrated that assumptions about cloud particle morphologies of heterogeneous cloud particles have an observable impact on transmission spectra (see Chapter 5). It therefore becomes crucial to understand what the morphology of cloud particles in exoplanet atmospheres is. A suitable target to constrain the morphology observationally is WASP-76b, where high-resolution spectroscopy has revealed the presence of iron in the atmosphere (Ehrenreich et al. 2020; Pelletier et al. 2023; Gandhi et al. 2023). As we have seen in Chapter 5, if cloud particles contain iron bearing species, well-mixed and non-mixed particles exhibit different spectral features. Compared to non-mixed cloud particles, well-mixed particles absorb more between 3 μm to 6 μm and have broader silicate features around 10 μm . Observations with the JWST instrument MIRI could therefore capture these spectral features and potentially constrain the morphologies of clouds in WASP-76b. However, while there are observable

differences in the transmission spectra of forward models, characterizing cloud properties through observations is more challenging. The optical properties of cloud particles are likely degenerate depending on their size distribution, number density, composition, shape, material distribution, or morphology. To determine which of these properties can reliably be retrieved from observations, a detailed sensitivity study is required. Luckily, thousands of exoplanets are known which cover a large variety of atmospheric conditions. By studying the cloud structures of multiple planets, we are hopefully able to lift some of the observational degeneracies and learn more about the micro-physical properties of cloud particles in exoplanet atmospheres.

The atmospheric modeling of HATS-6b in Chapter 6 demonstrates the importance of considering the impact of clouds on the climate of exoplanets. Similar studies can now be conducted for other planets. A particularly suitable next step is the application of the iterative model to the GCM grid by Baeyens et al. (2021) which was already followed up with micro-physical cloud modeling by Helling et al. (2023). Applying the iterative model to this grid will allow to determine the impact of clouds on the climate of exoplanets over a large range of stellar and planetary parameters. For such a large-scale effort, it is important to consider the computational feasibility. For HATS-6b, the climate structure after one iteration already has similar characteristics to the final solution. The same can be expected for other temperate exoplanets that have a global cloud coverage. For hotter gas-giants, the iterative model has to be applied more carefully. As we have seen for HATS-6b, cloud particles can lead to a temperature inversion. If the temperature increases above the thermal stability of the cloud particle materials, the next iteration might have significantly less opaque clouds or might be cloud-free. Iterations would then alternate between clouds and no clouds, potentially never reaching a stationary solution. To prevent this, cloud opacities have to be added gradually, which requires more iterations. A similar approach is also useful for GCMs with a fully coupled cloud model. While considering detailed micro-physical cloud formation in GCMs remains computationally prohibitive, our iterative approach has shown that cloud structures might not necessarily need to be recalculated in every hydrodynamic time step. A study analyzing different time intervals for the cloud structure calculation would allow to greatly improve the runtime of GCMs with a fully coupled cloud model.

Appendix A

Cluster data

Cluster radius

The radius of small TiO_2 clusters cannot be calculated in a straightforward manner, owing to the diverse and non-identical cluster shapes (i.e. geometries). However, a cluster volume can be derived by using either the coordinates of the atomic cores (i.e. purely geometrical), or by including Van der Waals volumes accounting for the presence of electrons. Assuming sphericity, a cluster radius can be deduced. Both sets of values are shown in Table A.1. The difference between these two on the resulting cross section can be seen in Fig. A.1. For the calculations in Section 3.3 and 3.4, we used the radius calculated using Van der Waals forces. Readers can also refer to Köhn et al. (2021) for an additional discussion on cluster radii.

Table A.1: Cluster data for $(\text{TiO}_2)_N$ clusters, including: geometrical (Geo) radius, Van-der-Waals (VdW) radius, and mass.

cluster properties	N=1	N=2	N=3	N=4	N=5
radius (Geo) [Å]	0	0.90	1.40	1.77	2.04
radius (VdW) [Å]	2.32	2.81	3.14	3.41	3.66
mass [u]	79.9	159.7	239.6	319.4	399.3
cluster properties	N=6	N=7	N=8	N=9	N=10
radius (Geo) [Å]	2.27	2.54	2.77	2.95	3.18
radius (VdW) [Å]	3.87	4.06	4.27	4.39	4.57
mass [u]	79.9	159.7	239.6	319.4	399.3

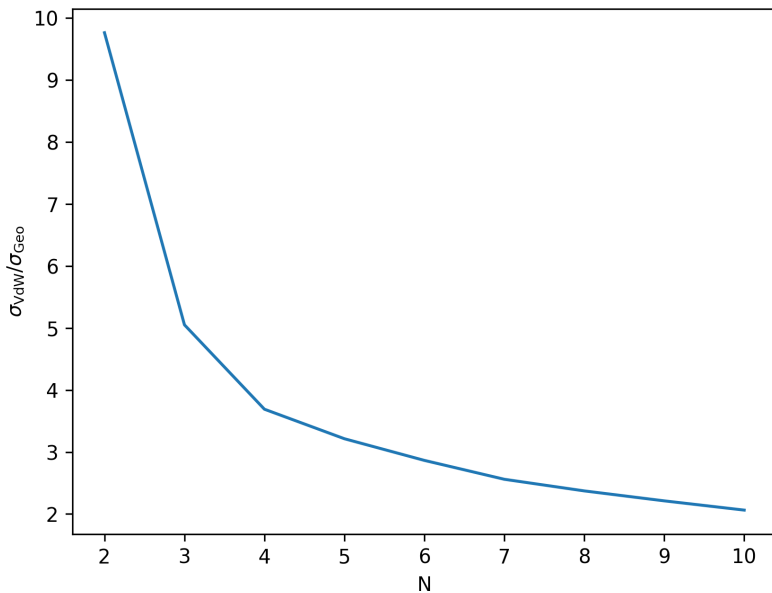


Figure A.1: Ratio of the Van der Waals (VdW) and the geometrical (Geo) cross section for different cluster sizes.

Gibbs free energy

The Gibbs free energies of formation of the TiO₂ clusters were taken from Sindel et al. (2022).

Reaction energy

The reaction energy E_{reac} of the TiO₂ dimerisation (i.e. TiO₂+TiO₂ → (TiO₂)₂) was calculated with density functional theory using the software package Gaussian16 (Frisch et al. 2016). The calculations were performed at the B3LYP/cc-pVTZ level of theory (Becke 1993) including the vibrational zero-point correction:

$$\begin{aligned}
 E_{\text{reac}} &= E((\text{TiO}_2)_2) - 2 \times E(\text{TiO}_2) \\
 &\simeq 7.8610^{-19} J.
 \end{aligned} \tag{A.1}$$

Dissociation reactions

All collisional dissociation reactions for TiO₂ considered in Section 3.4.2 are listed in Table A.2. The termolecular association rates are calculated using the dissociation rate and detailed balance as described in Section 3.2.4. The thermal non-equilibrium correction factor q_i is defined as follows:

$$q_i = \sqrt{\frac{m_{\text{gas}} T_i^{\text{kin}} + m_i T_{\text{gas}}}{(m_{\text{gas}} + m_i) T_{\text{gas}}}}. \quad (\text{A.2})$$

Example values for the reaction rate coefficients of three-body association reactions of TiO₂ are shown in Table A.3.

Table A.2: Collisional dissociation reactions of TiO_2 for cluster sizes $N \leq 4$ including thermal non-equilibrium effects.

Reaction	Reaction rate coefficient [$\text{cm}^3 \text{s}^{-1}$]	References
$(\text{TiO}_2)_2 + \text{M} \rightarrow \text{TiO}_2 + \text{TiO}_2 + \text{M}$	$1.4 \times 10^{-4} \exp(-48870/T_{(\text{TiO}_2)_2}^{\text{int}}) q_{(\text{TiO}_2)_2}$	Plane (2013)
$(\text{TiO}_2)_3 + \text{M} \rightarrow (\text{TiO}_2)_2 + \text{TiO}_2 + \text{M}$	$1.4 \times 10^{-9} \exp(-62411/T_{(\text{TiO}_2)_3}^{\text{int}}) q_{(\text{TiO}_2)_2}$	Estimate from CCSD(T)
$(\text{TiO}_2)_4 + \text{M} \rightarrow (\text{TiO}_2)_3 + \text{TiO}_2 + \text{M}$	$1.4 \times 10^{-9} \exp(-53569/T_{(\text{TiO}_2)_4}^{\text{int}}) q_{(\text{TiO}_2)_2}$	Estimate from CCSD(T)
$(\text{TiO}_2)_4 + \text{M} \rightarrow (\text{TiO}_2)_2 + (\text{TiO}_2)_2 + \text{M}$	$1.4 \times 10^{-9} \exp(-57194/T_{(\text{TiO}_2)_4}^{\text{int}}) q_{(\text{TiO}_2)_2}$	Estimate from CCSD(T)

Table A.3: Recombination rate coefficients for the three-body association reactions of TiO_2 clusters up to size $N \leq 4$ including thermal non-equilibrium effects. All rates are calculated in kinetic-to-internal thermal equilibrium using exponential temperature offsets (See Eq. 3.69).

Reaction	Reaction rate coefficient [$\text{cm}^6 \text{s}^{-1}$] for $T_{\text{gas}} = 1000 \text{ K}$ and $\Delta T = 35 \text{ K}$	Reaction rate coefficient [$\text{cm}^6 \text{s}^{-1}$] for $T_{\text{gas}} = 1250 \text{ K}$ and $\Delta T = -35 \text{ K}$
$\text{TiO}_2 + \text{TiO}_2 + \text{M} \rightarrow (\text{TiO}_2)_2 + \text{M}$	5.580×10^{-28}	1.219×10^{-28}
$(\text{TiO}_2)_2 + \text{TiO}_2 + \text{M} \rightarrow (\text{TiO}_2)_3 + \text{M}$	1.107×10^{-37}	1.788×10^{-37}
$(\text{TiO}_2)_3 + \text{TiO}_2 + \text{M} \rightarrow (\text{TiO}_2)_4 + \text{M}$	1.074×10^{-38}	1.741×10^{-38}
$(\text{TiO}_2)_2 + (\text{TiO}_2)_2 + \text{M} \rightarrow (\text{TiO}_2)_4 + \text{M}$	4.318×10^{-39}	7.117×10^{-39}

Appendix B

Chemical network

B.1 Numerical solver

The chemical kinetic network can be described as an ordinary differential equation (ODE). Therefore, a fast and accurate ODE solver is required. Similar to other works (e.g. Agundez et al. 2014; Rimmer & Helling 2016; Molaverdikhani et al. 2019; Baeyens et al. 2021), we chose DLSODES from ODEPACK (Hindmarsh 1983; Radhakrishnan & Hindmarsh 1993).

Combining chemistry, nucleation, and bulk growth through condensation and surface reactions results in a stiff ODE system, especially during the onset of nucleation and the onset of bulk growth. To prevent the solver from getting stuck, we introduce dynamic tolerances. During the iteration, the solver tries to compute a given time step Δt with a given relative tolerance ζ_{rel} and a given absolute tolerance ζ_{abs} . If the solver only reaches a percentage $\chi < 1$ of the time step, ζ_{rel} and ζ_{abs} are increased by a factor of δ_{rel}^+ and δ_{abs}^+ , respectively. If the solver reaches the full time step, $\chi = 1$, the relative and absolute tolerances are decreased by a factor of δ_{rel}^- and δ_{abs}^- , respectively. To ensure sufficient precision of the ODE, the tolerances have an upper limit, $\zeta_{\text{rel}}^{\max}$ and $\zeta_{\text{abs}}^{\max}$, and a lower limit, $\zeta_{\text{rel}}^{\min}$ and $\zeta_{\text{abs}}^{\min}$, respectively. The schematics of the algorithm are shown

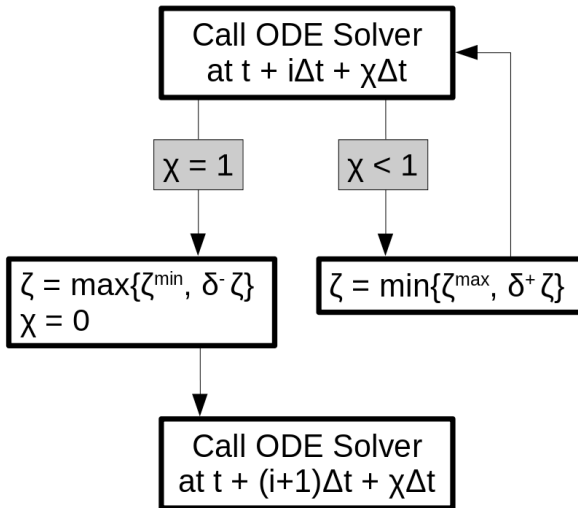


Figure B.1: Dynamic tolerances scheme for the ODE solver.

in Fig. B.1. In this thesis, the following values are used:

$$\zeta_{\text{rel}}^{\max} = 10^{-3}, \quad (\text{B.1})$$

$$\zeta_{\text{abs}}^{\max} = 10^{-40}, \quad (\text{B.2})$$

$$\zeta_{\text{rel}}^{\min} = 10^{-9}, \quad (\text{B.3})$$

$$\zeta_{\text{abs}}^{\min} = 10^{-60}, \quad (\text{B.4})$$

$$\delta_{\text{rel}}^- = \delta_{\text{abs}}^- = 0.1, \quad (\text{B.5})$$

$$\delta_{\text{rel}}^+ = \delta_{\text{abs}}^+ = 1.1. \quad (\text{B.6})$$

The starting tolerance is always equal to the minimum tolerance and was selected depending on the simulation.

B.2 GGchem

We considered the following species in our chemical equilibrium calculations done with **GGchem**: OH, H₂, H₂O, H, O, CH, C, CH₂, CH₃, CH₄, C₂, C₂H₂,

C₂H, C₂H₃, C₂H₄, C₂H₅, C₂H₆, CO, CO₂, CH₂OH, H₂CO, HCO, CH₃O, CH₃OH, CH₃CO, O₂, H₂CCO, HCCO, N, NH, CN, HCN, NO, NH₂, N₂, NH₃, N₂H₂, N₂H, N₂H₃, N₂H₄, HNO, H₂CN, HNCO, NO₂, N₂O, C₄H₂, CH₂NH₂, CH₂NH, CH₃NH₂, CH₃CHO, HNO₂, NCO, HO₂, H₂O₂, HC₃N, CH₃CN, CH₂CN, C₂H₃CN, C₃H₃, C₃H₂, C₃H₄, C₄H₃, C₄H₅, C₆H₆, C₆H₅, (O)₁, (CH₂)₁, (N₂)_D, He, Ti, TiO, SO₂, SO, TiO₂, SiO⁺, Si⁺, SiH⁺, H⁻, Si, HF, SiF⁺, He⁺, SiO₂, Na, Na⁺, SiO, HCO⁺, P⁺, P, S⁺, S, e⁻, Fe, Fe⁺, F, (TiO₂)₂, (TiO₂)₃, (TiO₂)₄, (TiO₂)₅, (TiO₂)₆, (TiO₂)₇, (TiO₂)₈, (TiO₂)₉, (TiO₂)₁₀, (TiO₂)₁₁, (TiO₂)₁₂, (TiO₂)₁₃, (TiO₂)₁₄, (TiO₂)₁₅, Mg, Al, Ca, Cl, FeO₂, Al₂O₃, AlH₂, AlH₃, Al(OH)₂, Al(OH)₃, H₂S₂, F₂, Mg₂, Al₂, Si₂, S₂, Cl₂, MgH, AlH, SiH, HS, HCl, CaH, TiH, FeH, CF, SiC, CS, CCl, FN, AlN, SiN, SN, NCl, TiN, FO, MgO, AlO, ClO, CaO, FeO, MgF, AlF, SiF, SF, CaF, MgS, AlS, SiS, CaS, TiS, MgCl, AlCl, SiCl, CaCl, FeCl, AlClF, AlClF₂, AlOCl, AlCl₂, AlCl₂F, AlCl₃, AlOF, AlF₂, AlF₂O, AlF₃, AlOH, HALO, AlO₂H, AlO₂, Al₂Cl₆, (AlF₃)₂, Al₂O, Al₂O₂, AlC, CFCIO, CClF₃, CCIN, CClO, CCl₂, CCl₂F₂, COCl₂, CCl₃, CCl₃F, CCl₄, CFN, CFO, CF₂, CF₂O, CF₃, CF₄, CF₄O, CF₈S, CHCl, CHCl₃, CHF, CHFO, CHF₃, CHNO, CH₂Cl₂, CH₂ClF, CH₂F₂, CH₃Cl, CH₃F, CNO, CNN, NCN, COS, CS₂, Si₂C, C₂Cl₂, C₂Cl₄, C₂Cl₆, C₂F₂, C₂F₃N, C₂F₄, C₂F₆, C₂HCl, C₂HF, C₂H₄O, C₂N, C₂N₂, SiC₂, C₂O, C₃, C₃O₂, C₄, C₄N₂, C₅, Fe(CO)₅, CaCl₂, CaF₂, CaOH, Ca(OH)₂, Ca₂, ClF, MgClF, ClFO₂S, ClFO₃, ClF₃, ClF₃Si, ClF₅, ClF₅S, CHClF₂, CHCl₂F, OHCl, SiH₃Cl, NOCl, NO₂Cl, TiOCl, ClO₂, ClO₃, SCl, ClS₂, TiCl, FeCl₂, SiH₂Cl₂, MgCl₂, ClOCl, ClCIO, TiOCl₂, ClO₂Cl, ClOCIO, SO₂Cl₂, SCl₂, SiCl₂, TiCl₂, SiFCl₃, FeCl₃, SiHCl₃, SiCl₃, TiCl₃, Fe₂Cl₄, Mg₂Cl₄, SiCl₄, TiCl₄, (FeCl₃)₂, FeF, FHO, FHO₃S, SiH₃F, FNO, FNO₂, FNO₃, TiOF, OFO, FOO, TiF, FeF₂, H₂F₂, SiH₂F₂, MgF₂, F₂N, F₂N₂(cis), F₂N₂(trans), F₂O, F₂OS, SiOF₂, TiOF₂, F₂O₂, F₂O₂S, SF₂, FSSF, F₂S₂, SiF₂, TiF₂, FeF₃, SiHF₃, F₃H₃, NF₃, NOF₃, SF₃, SiF₃, TiF₃, F₄H₄, Mg₂F₄, N₂F₄, SF₄, SiF₄, TiF₄, F₅H₅, SF₅, F₆H₆, SF₆, F₇H₇, F₁₀S₂, Fe(OH)₂, FeS, MgOH, HONO, HNO₃, Mg(OH)₂, H₂SO₄, H₂S, SiH₄, MgN, NO₃, Si₂N, N₂O₃, N₂O₄, N₂O₅, N₃, S₂O, O₃, SO₃, S₃, S₄, S₅, S₆, S₇, S₈, Si₃, TiC, Si(CH₃)₄, SiCH₃Cl₃, SiH₂, SiH₃, TiC₂, C₃H, Si₂C₂, and TiC₄.

B.3 Al₂O₃ nucleation

To calculate the nucleation rate of potential nucleation species, thermodynamic data of their clusters need to be available. With TiO₂, we are in the fortunate position of having data available up to N = 15 (Sindel et al. 2022). For Al₂O₃, we only have data up to N = 10 from Gobrecht et al. (2022). They also derived a detailed chemical kinetics network up to (Al₂O₃)₄, including a small C-H-O network for the gas phase.

As in Sect. 4.3.3, we calculated the predicted cloud particle number densities and nucleation rate of Al_2O_3 using $5 \leq N_{\max} \leq 10$, but the results were inconclusive and no stable nucleation behaviour was found. Neither the cloud particle number density nor the nucleation rate showed any clear trends with N_{\max} . A possible explanation for this non-convergence could be that the thermally stable cluster is (much) larger than $N_{\max} = 10$ or that Al_2O_3 does not follow homogeneous nucleation. More studies on the formation of Al_2O_3 clusters are required to model the kinetic nucleation of Al_2O_3 .

B.4 Comparing chemical networks

The cloud formation model described in this thesis can be combined with any chemical kinetics network. Typically, the more extensive the network, the longer individual model runs take. In the development of this model, we first relied on a small C-H-O network taken from Gobrecht et al. (2022) (**Gobrecht**). Later, we used the chemical network of Tsai et al. (2017) (**Vulcan**). Here, we compare the two networks.

Throughout this section, we reference multiple reactions from the chemical network of **Gobrecht** and use the following shorthand:

- (G02): $\text{H}_2 + \text{H}_2 \rightarrow \text{H} + \text{H} + \text{H}_2$
- (G04): $\text{H}_2 + \text{H} \rightarrow \text{H} + \text{H} + \text{H}$
- (G06): $\text{H}_2 + \text{He} \rightarrow \text{H} + \text{H} + \text{He}$
- (G11): $\text{OH} + \text{H} + \text{H}_2\text{O} \rightarrow \text{H}_2\text{O} + \text{H}_2\text{O}$
- (G12): $\text{H}_2\text{O} + \text{H}_2\text{O} \rightarrow \text{OH} + \text{H} + \text{H}_2\text{O}$
- (G24): $\text{OH} + \text{H} + \text{M} \rightarrow \text{H}_2\text{O} + \text{M}$
- (G25): $\text{H}_2\text{O} + \text{M} \rightarrow \text{OH} + \text{H} + \text{M}$.

B.4.1 Gobrecht versus Vulcan

With three exceptions, all reactions of **Gobrecht** can be found within **Vulcan**. The first exceptions are reaction G11 and G12, which do not appear in **Vulcan**. Reaction G12 in particular has a significant impact on the concentration of all species. The reaction rate for G12 and its corresponding forward reaction G11 were derived in supersonic combustion chemistry experiments at

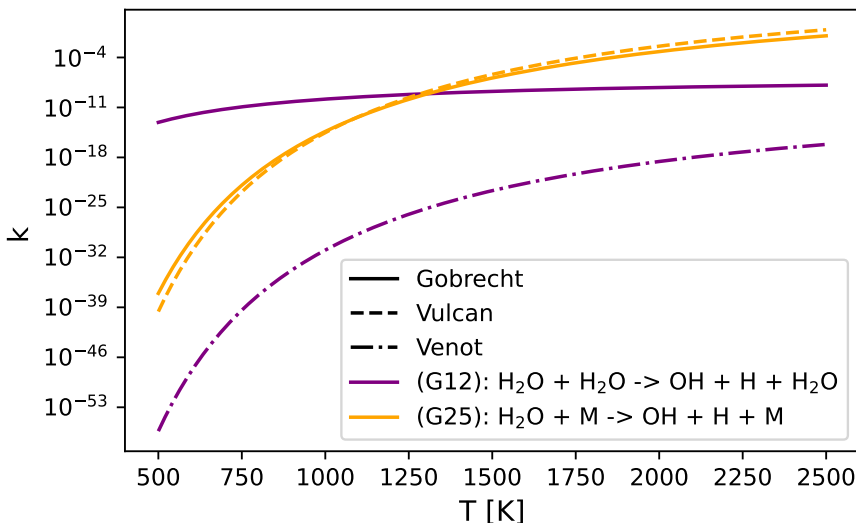


Figure B.2: Comparison of reaction rate coefficients at $p_{\text{gas}} = 0.01$ bar. The unit of k is $\text{cm}^3 \text{s}^{-1}$ for G12 and s^{-1} for G25.

$2790 \text{ K} < T < 3200 \text{ K}$ and $p = 250 \text{ kPa}$ (Javoy et al. 2003). A comparison with other chemical networks for exoplanet atmospheres revealed inconsistencies. Instead of G11 and G12, **Vulcan** only considers the reactions G24 and G25. These are similar reactions, but they have an arbitrary third body instead of H_2O . Venot et al. (2012) included reactions G11 and G12, but did not include G24 and G25. Rimmer & Helling (2016) did not consider any of the reactions G11, G12, G24, and G25. A comparison between the reaction rate coefficients of G12 and G25 can be seen in Fig. B.2.

The second difference between **Gobrecht** and **Vulcan** is the reaction G17. This reaction describes the radiative association of CO. Since we did not include any photochemical reactions in **Vulcan**, we also excluded this reaction for **Gobrecht**. Hereafter we call the collection of reactions corresponding to the network of **Gobrecht** without reactions G11, G12, and G17 the 'base' network.

The third difference is the description of H+H reactions. In **Gobrecht**, they are described as three-body reactions with specific collision partners H, H_2 , and He (G02, G04, and G06). In **Vulcan**, these reactions are described with a generic third body M. We used each network's description of H+H reactions and did not adjust them.

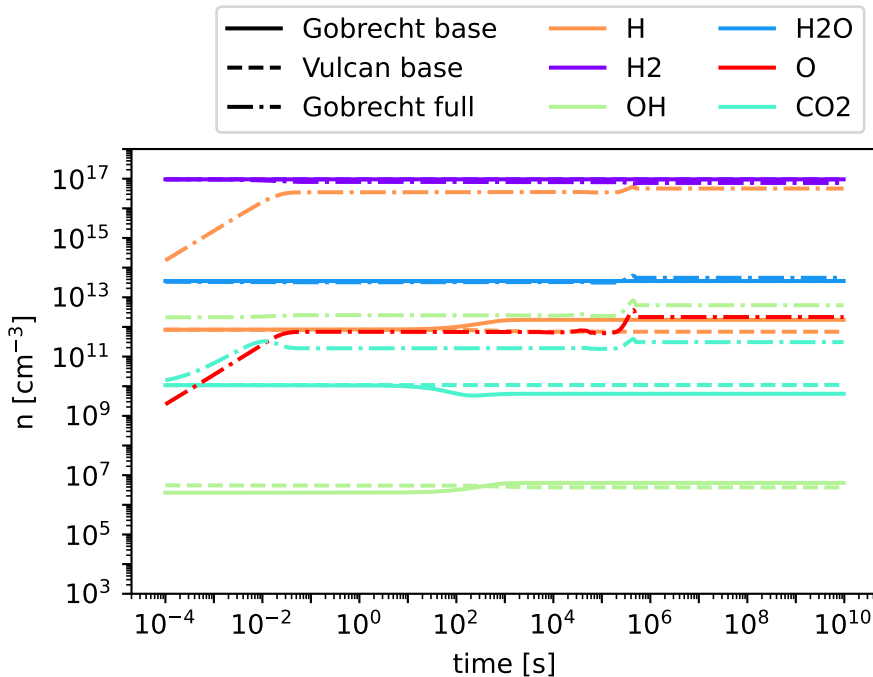


Figure B.3: Comparison of chemical network of **Gobrecht** and **Vulcan**.

Evaluating the base network for $T = 1300$ K and $p = 2000$ (Fig. B.3) once with reaction rates from **Gobrecht** and once with reaction rates from **Vulcan** only showed minor differences in CO_2 , OH , and H abundance. The differences are within expected offsets due to slightly different reaction rates and different Gibbs free-energy values. The full network of **Gobrecht** still produced significantly different abundances.

B.4.2 Vulcan

We separated Vulcan's 780 reactions into three categories:

- **base:** The base **Vulcan** network as described in Appendix B.4.1.
- **won:** The reactions of the "NCHO thermo network" of **Vulcan** without Nitrogen species as reactant or product.

- **full:** The full "NCHO thermo network" of **Vulcan**.

Comparing the base and won network for $p_{\text{gas}} = 0.002$ bar and $T \in \{500 \text{ K}, 1300 \text{ K}, 2000 \text{ K}\}$ shows little to no differences in H, O, OH, H₂, H₂O, CO, and CO₂ number densities. Using the evaluation from Eq. 4.50 we find $P(A, \text{base, won}) < 10^{-3}$ for all of these species. Furthermore, the deviations from chemical equilibrium as calculated with **GGchem** are minimal. Comparing the won and full network for $p_{\text{gas}} = 0.002$ bar and $T \in \{500 \text{ K}, 1300 \text{ K}, 2000 \text{ K}\}$ showed little to no differences in H, O, OH, H₂, H₂O, CO, and CO₂ abundance. Using the evaluation from Eq. 4.50 we find $P(A, \text{won, full}) < 10^{-4}$ for all of these species.

Our results suggest that the VULCAN network could be used in the base or won configuration as well if a smaller network is desired. The won network in particular might prove useful since it includes the major species H₂O, CO, CO₂, and CH₄ while having only 416 of the 780 reactions of the NCHO thermo network of **Vulcan**.

B.5 Data and additional plots

The Ti and Si reactions selected from Boulangier et al. (2019b) and Kiefer et al. (2023) are listed in Table B.1. Some backward reactions are derived using detailed balance with the following coefficients:

$$\text{EQS}_{18} = \exp \left(\frac{G_{\text{TiO}_2}^\ominus + G_{\text{H}}^\ominus - G_{\text{TiO}}^\ominus - G_{\text{OH}}^\ominus}{k_B T_{\text{gas}}} \right), \quad (\text{B.7})$$

$$\text{EQS}_{20} = \left(\frac{k_B T}{p^\ominus} \right) \exp \left(\frac{G_{\text{TiO}_2}^\ominus + G_{\text{TiO}_2}^\ominus - G_{(\text{TiO}_2)_2}^\ominus}{k_B T_{\text{gas}}} \right), \quad (\text{B.8})$$

$$\text{EQS}_{22} = \left(\frac{k_B T}{p^\ominus} \right) \exp \left(\frac{G_{(\text{TiO}_2)_2}^\ominus + G_{\text{TiO}_2}^\ominus - G_{(\text{TiO}_2)_3}^\ominus}{k_B T_{\text{gas}}} \right), \quad (\text{B.9})$$

$$\text{EQS}_{24} = \left(\frac{k_B T}{p^\ominus} \right) \exp \left(\frac{G_{(\text{TiO}_2)_3}^\ominus + G_{\text{TiO}_2}^\ominus - G_{(\text{TiO}_2)_4}^\ominus}{k_B T_{\text{gas}}} \right), \quad (\text{B.10})$$

$$\text{EQS}_{26} = \left(\frac{k_B T}{p^\ominus} \right) \exp \left(\frac{G_{(\text{TiO}_2)_2}^\ominus + G_{(\text{TiO}_2)_2}^\ominus - G_{(\text{TiO}_2)_4}^\ominus}{k_B T_{\text{gas}}} \right). \quad (\text{B.11})$$

The condensation reactions taken from Helling et al. (2019a) and the fitting values for the reaction vapour coefficient (Eq. 4.43) are listed in Table B.4. In Fig. B.4, the volume fraction of all species from the simulations of Sect. 4.4 are shown.

B.6 Additional plots

Table B.1: Chemical reactions from Boulangier et al. (2019b) and Kiefer et al. (2023) added to the NCHO thermo network of VJILCAN. The first block describes the Ti chemistry; the second block describes the Si chemistry. For the definition of EQR_i , see Boulangier et al. (2019b), where i is the reaction number as defined in their work. References: (0) this work, (1) Campbell & McClean (1993), (2) McElroy et al. (2013), (3) Plane (2013), (4) Ritter & Weisshaar (2002), (5) Higuchi et al. (2008), and (6) Kiefer et al. (2023).

Index (RNr)	Reaction	Reaction rate coefficient k	Origin
1	Ti + CO ₂ → TiO + CO	$7 \times 10^{-11} \exp(-14.9/(RT))$	(1)
2	TiO + CO → Ti + CO ₂	$7 \times 10^{-11} \exp(-14.9/(RT))$	EQR ₅₆₄ (1)
3	Ti + N ₂ O → TiO + N ₂	$1.74 \times 10^{-10} \exp(-14.3/(RT))$	(1)
4	TiO + N ₂ → Ti + N ₂ O	$1.74 \times 10^{-10} \exp(-14.3/(RT))$	EQR ₅₆₆ (1)
5	Ti + NO → TiO + N	$3.28 \times 10^{-11} \exp(-3.62/(RT))$	(1)
6	TiO + N → Ti + NO	$3.28 \times 10^{-11} \exp(-3.62/(RT))$	EQR ₅₆₅ (1)
7	Ti + NO ₂ → TiO + NO	9×10^{-11}	(1)
8	TiO + NO → Ti + NO ₂	9×10^{-11}	EQR ₅₆₇ (1)
9	Ti + O ₂ → TiO + O	$1.69 \times 10^{-10} \exp(-11.6/(RT))$	(1)
10	TiO + O → Ti + O ₂	$1.69 \times 10^{-10} \exp(-11.6/(RT))$	EQR ₅₆₉ (1)
11	Ti + SO ₂ → TiO + SO	$1.7 \times 10^{-10} \exp(-2.66/(RT))$	(1)
12	TiO + SO → Ti + SO ₂	$1.7 \times 10^{-10} \exp(-2.66/(RT))$	EQR ₅₇₂ (1)
13	TiO + NO → TiO ₂ + N	2.2×10^{-12}	(4)
14	TiO ₂ + N → TiO + NO	2.2×10^{-12}	EQR ₅₇₄ (4)
15	TiO + O ₂ → TiO ₂ + O	7.07×10^{-12}	(5)
16	TiO ₂ + O → TiO + O ₂	7.07×10^{-12}	EQR ₅₇₀ (5)
17	TiO + OH → TiO ₂ + H	$2.07 \times 10^{-10} T^{0.39}$	(3)
18	TiO ₂ + H → TiO + OH	$2.07 \times 10^{-10} T^{0.39}$	EQS ₁₈ (0)
19	(TiO ₂) ₂ + M → TiO ₂ + TiO ₂ + M	$1.4 \times 10^{-4} \exp(-48870/T)$	(3)
20	TiO ₂ + TiO ₂ + M → (TiO ₂) ₂ + M	$1.4 \times 10^{-4} \exp(-48870/T)$	EQS ₂₀ (6)

Table B.2: Continuation of Table B.1

Index (RNr)	Reaction	Reaction rate coefficient k	Origin
21	$(\text{TiO}_2)_3 + \text{M} \rightarrow (\text{TiO}_2)_2 + \text{TiO}_2 + \text{M}$	$1.4 \times 10^{-9} \exp(-62411/T)$	(6)
22	$(\text{TiO}_2)_2 + \text{TiO}_2 + \text{M} \rightarrow (\text{TiO}_2)_3 + \text{M}$	$1.4 \times 10^{-9} \exp(-62411/T)$ EQS ₂₂	(6)
23	$(\text{TiO}_2)_4 + \text{M} \rightarrow (\text{TiO}_2)_3 + \text{TiO}_2 + \text{M}$	$1.4 \times 10^{-9} \exp(-53569/T)$	(6)
24	$(\text{TiO}_2)_3 + \text{TiO}_2 + \text{M} \rightarrow (\text{TiO}_2)_4 + \text{M}$	$1.4 \times 10^{-9} \exp(-53569/T)$ EQS ₂₄	(6)
25	$(\text{TiO}_2)_4 + \text{M} \rightarrow (\text{TiO}_2)_2 + (\text{TiO}_2)_2 + \text{M}$	$1.4 \times 10^{-9} \exp(-57194/T)$	(6)
26	$(\text{TiO}_2)_2 + (\text{TiO}_2)_2 + \text{M} \rightarrow (\text{TiO}_2)_4 + \text{M}$	$1.4 \times 10^{-9} \exp(-57914/T)$ EQS ₂₆	(6)
27	$\text{Si} + \text{OH} \rightarrow \text{SiO} + \text{H}$	10^{-10}	(2)
28	$\text{Si} + \text{CO} \rightarrow \text{SiO} + \text{C}$	$1.3 \times 10^{-9} \exp(-34513/T)$	(2)
29	$\text{Si} + \text{CO}_2 \rightarrow \text{SiO} + \text{CO}$	$2.72 \times 10^{-11} \exp(-282/T)$	(2)
30	$\text{Si} + \text{NO} \rightarrow \text{SiO} + \text{N}$	$9 \times 10^{-11} (T/300)^{-0.96} \exp(-28/T)$	(2)
31	$\text{Si} + \text{O}_2 \rightarrow \text{SiO} + \text{O}$	$1.72 \times 10^{-10} (T/300)^{-0.53} \exp(-17/T)$	(2)
32	$\text{Si} + \text{O} \rightarrow \text{SiO}$	$5.52 \times 10^{-18} (T/300)^{0.31}$	(2)
33	$\text{Si} + \text{OH} \rightarrow \text{SiO} + \text{H}$	1×10^{-10}	(2)
34	$\text{SiO} + \text{OH} \rightarrow \text{SiO}_2 + \text{H}$	2×10^{-12}	(2)
35	$\text{SiO}_2 + \text{H} \rightarrow \text{SiO} + \text{OH}$	2×10^{-12} EQR ₅₁₆	(2)
36	$\text{Si} + \text{HCO}^+ \rightarrow \text{SiH}^+ + \text{CO}$	1.6×10^{-9}	(2)
37	$\text{Si} + \text{P}^+ \rightarrow \text{Si}^+ + \text{P}$	1×10^{-9}	(2)
38	$\text{Si} + \text{He}^+ \rightarrow \text{Si}^+ + \text{He}$	3.3×10^{-9}	(2)
39	$\text{Si} + \text{S}^+ \rightarrow \text{Si}^+ + \text{S}$	1.6×10^{-9}	(2)
40	$\text{Si}^+ + \text{OH} \rightarrow \text{SiO}^+ + \text{H}$	$6.3 \times 10^{-10} (T/300)^{-0.5}$	(2)

Table B.3: Continuation of Table B.1

Index (RNr)	Reaction	Reaction rate coefficient k	Origin
41	$\text{Si}^+ + \text{H} \rightarrow \text{Si} + \text{H}$	$1.17 \times 10^{-17} (\text{T}/300)^{-0.14}$	(2)
42	$\text{Si}^+ + \text{H}^- \rightarrow \text{Si} + \text{H}$	$7.51 \times 10^{-8} (\text{T}/300)^{-0.5}$	(2)
43	$\text{Si}^+ + \text{HF} \rightarrow \text{SiF}^+ + \text{H}$	$5.7 \times 10^{-9} (\text{T}/300)^{-0.5}$	(2)
44	$\text{Si}^+ + \text{Na} \rightarrow \text{Si} + \text{Na}^+$	2.7×10^{-9}	(2)
45	$\text{Si}^+ + \text{Fe} \rightarrow \text{Si} + \text{Fe}^+$	1.9×10^{-9}	(2)
46	$\text{SiO}^+ + \text{N} \rightarrow \text{Si}^+ + \text{NO}$	2.1×10^{-10}	(2)
47	$\text{SiO}^+ + \text{Fe} \rightarrow \text{SiO} + \text{Fe}^+$	1×10^{-9}	(2)
48	$\text{SiO}^+ + \text{C} \rightarrow \text{Si}^+ + \text{CO}$	1×10^{-9}	(2)
49	$\text{SiO}^+ + \text{O} \rightarrow \text{Si}^+ + \text{O}_2$	2×10^{-10}	(2)
50	$\text{SiO}_2 + \text{He}^+ \rightarrow \text{O}_2 + \text{Si}^+ + \text{He}$	2×10^{-9}	(2)
51	$\text{SiH}^+ + \text{H} \rightarrow \text{Si}^+ + \text{H}_2$	1.9×10^{-9}	(2)
52	$\text{Si}^+ + \text{e}^- \rightarrow \text{Si} + \gamma$	$4.26 \times 10^{-12} (\text{T}/300)^{-0.61}$	(2)
53	$\text{SiO}^+ + \text{e}^- \rightarrow \text{Si} + \text{O}$	$2 \times 10^{-7} (\text{T}/300)^{-0.5}$	(2)
54	$\text{SiH}^+ + \text{e}^- \rightarrow \text{Si} + \text{H}$	$2 \times 10^{-7} (\text{T}/300)^{-0.5}$	(2)
55	$\text{SiF}^+ + \text{e}^- \rightarrow \text{Si} + \text{F}$	$2 \times 10^{-7} (\text{T}/300)^{-0.5}$	(2)

Table B.4: Bulk growth reactions considered for this study. The list of reactions was taken from Helling et al. (2019a). s_0 , s_1 , s_2 , and s_3 are the fitting parameters of the vapour number density (Eq. 4.43). ΔV is the volume increase per bulk growth reaction.

nr	reaction	s_0	s_1 [K]	s_2 [K ²]	s_3 [K ³]	ΔV [cm ⁻³]
c1	Ti+2 H ₂ O → TiO ₂ [s]+2 H ₂	7.902e+01	-1.622e+05	-4.690e+06	9.013e+08	3.136e-23
c2	TiO ₂ → TiO ₂ [s]	6.194e+01	-6.731e+04	-5.024e+06	9.890e+08	3.136e-23
c3	TiO+H ₂ O → TiO ₂ [s]+H ₂	6.431e+01	-7.986e+04	-5.635e+06	1.084e+09	3.136e-23
c4	TiS+2 H ₂ O → TiO ₂ [s]+H ₂ S+H ₂	5.244e+01	-2.031e+05	-4.500e+05	1.000e+00	3.136e-23
c5	2 Mg+SiO+3 H ₂ O → Mg ₂ SiO ₄ [s]+3 H ₂	1.695e+02	-2.951e+05	-1.166e+07	2.383e+09	7.278e-23
c6	2 MgOH+SiO+H ₂ O → Mg ₂ SiO ₄ [s]+2 H ₂	1.429e+02	-1.986e+05	-1.275e+07	2.560e+09	7.278e-23
c7	2 Mg(OH) ₂ +SiO → Mg ₂ SiO ₄ [s]+H ₂ O+H ₂	8.983e+01	-3.337e+05	-4.754e+06	1.094e+09	7.278e-23
c8	2 MgH+SiO+3 H ₂ O → Mg ₂ SiO ₄ [s]+4 H ₂	1.591e+02	-2.695e+05	-1.247e+07	2.518e+09	7.278e-23
c9	2 Mg+SiS+4 H ₂ O → Mg ₂ SiO ₄ [s]+H ₂ S+3 H ₂	1.590e+02	-4.198e+05	-1.889e+06	1.000e+00	7.278e-23
c10	2 MgOH+SiS+2 H ₂ O → Mg ₂ SiO ₄ [s]+H ₂ S+2 H ₂	1.304e+02	-3.169e+05	-9.041e+06	1.909e+09	7.278e-23
c11	2 Mg(OH) ₂ +SiS → Mg ₂ SiO ₄ [s]+H ₂ +H ₂ S	8.892e+01	-3.312e+05	-5.254e+06	1.201e+09	7.278e-23
c12	2 MgH+SiS+4 H ₂ O → Mg ₂ SiO ₄ [s]+H ₂ S+4 H ₂	1.489e+02	-3.948e+05	-2.229e+06	1.000e+00	7.278e-23
c13	4 Mg+2 SiH+8 H ₂ O → 2 Mg ₂ SiO ₄ [s]+9 H ₂	1.731e+02	-3.558e+05	-1.181e+07	2.406e+09	7.278e-23
c14	4 MgOH+2 SiH+4 H ₂ O → 2 Mg ₂ SiO ₄ [s]+7 H ₂	1.466e+02	-2.594e+05	-1.290e+07	2.583e+09	7.278e-23

Table B.5: Continuation of Table B.4

nr	reaction	s_0	s_1 [K]	s_2 [K ²]	s_3 [K ³]	ΔV [cm ⁻³]
c15	4 Mg(OH) ₂ +2 SiH → 2 Mg ₂ SiO ₄ [s]+5 H ₂	1.051e+02	-2.737e+05	-9.116e+06	1.875e+09	7.278e-23
c16	4 MgH+2 SiH+8 H ₂ O → 2 Mg ₂ SiO ₄ [s]+11 H ₂	1.628e+02	-3.303e+05	-1.262e+07	2.541e+09	7.278e-23
c17	SiO+H ₂ O → SiO ₂ [s]+H ₂	6.335e+01	-5.758e+04	-5.536e+06	1.075e+09	3.768e-23
c18	SiS+2 H ₂ O → SiO ₂ [s]+H ₂ +H ₂ S	5.085e+01	-1.759e+05	-1.823e+06	4.249e+08	3.768e-23
c19	SiH+2 H ₂ O → SiO ₂ [s]+2 H ₂ +H	2.547e+01	-1.214e+05	-4.299e+06	8.301e+08	3.768e-23
c20	2 AlOH+H ₂ O → Al ₂ O ₃ [s]+2 H ₂	8.592e+01	-1.837e+05	-2.900e+06	1.000e+00	4.265e-23
c21	2 AlH+3 H ₂ O → Al ₂ O ₃ [s]+4 H ₂	1.015e+02	-2.605e+05	-9.682e+06	2.040e+09	4.265e-23
c22	Al ₂ O+2 H ₂ O → Al ₂ O ₃ [s]+2 H ₂	8.493e+01	-1.698e+05	-9.002e+06	1.914e+09	4.265e-23
c23	2 AlO2H → Al ₂ O ₃ [s]+H ₂ O	7.369e+01	-2.994e+05	-7.691e+05	1.000e+00	4.265e-23
c24	FeO → FeO[s]	5.784e+01	-5.214e+04	-5.698e+06	1.137e+09	1.992e-23
c25	Fe+H ₂ O → FeO[s]+H ₂	5.687e+01	-4.231e+04	-5.829e+06	1.140e+09	1.992e-23
c26	FeS+H ₂ O → FeO[s]+H ₂ S	5.660e+01	-3.904e+04	-6.238e+06	1.248e+09	1.992e-23
c27	Fe(OH) ₂ → FeO[s]+H ₂ O	2.854e+00	-2.023e+04	-1.184e+06	2.648e+08	1.992e-23
c28	2 FeH+2 H ₂ O → 2 FeO[s] + 3 H ₂	4.592e+01	-2.430e+04	-5.662e+06	1.071e+09	1.992e-23
c29	FeS → FeS[s]	5.647e+01	-4.348e+04	-6.716e+06	1.289e+09	3.022e-23
c30	Fe+H ₂ S → FeS[s]+H ₂	5.673e+01	-4.675e+04	-6.307e+06	1.181e+09	3.022e-23
c31	FeO+H ₂ S → FeS[s]+H ₂ O	5.771e+01	-5.659e+04	-6.176e+06	1.177e+09	3.022e-23
c32	2 FeH+2 H ₂ S → FeS[s]+3 H ₂	4.579e+01	-2.874e+04	-6.140e+06	1.111e+09	3.022e-23
c33	2 Fe+3 H ₂ O → FeO ₃ [s]+3 H ₂	1.097e+02	-2.119e+05	-9.578e+06	1.885e+09	5.032e-23
c34	2 FeO+H ₂ O → Fe ₂ O ₃ [s]+H ₂	9.543e+01	-1.597e+05	-1.067e+07	2.079e+09	5.032e-23
c35	2 Fe(OH) ₂ → Fe ₂ O ₃ [s]+H ₂ O+H ₂	2.885e+01	-2.487e+05	-1.944e+06	4.502e+08	5.032e-23
c36	2 FeS+3 H ₂ O → Fe ₂ O ₃ [s]+2 H ₂ S+H ₂	8.260e+01	-2.675e+05	-6.998e+06	1.433e+09	5.032e-23
c37	2 FeH+3 H ₂ O → Fe ₂ O ₃ [s]+4 H ₂	9.879e+01	-1.939e+05	-9.411e+06	1.816e+09	5.032e-23

Table B.6: Continuation of Table B.4

nr	reaction	s_0	s_1 [K]	s_2 [K ²]	s_3 [K ³]	ΔV [cm ⁻³]
c38	Mg+H ₂ O → MgO[s]+H ₂	5.870e+01	-5.209e+04	-4.378e+06	8.392e+08	1.869e-23
c39	2 MgOH → 2 MgO[s]+H ₂	2.061e+01	-7.653e+04	-1.259e+06	2.587e+08	1.869e-23
c40	Mg(OH) ₂ → MgO[s]+H ₂ O	5.951e+00	-3.197e+04	-4.611e+05	1.100e+08	1.869e-23
c41	2 MgH+2 H ₂ O → 2 MgO[s]+3 H ₂	4.839e+01	-2.657e+04	-5.190e+06	9.741e+08	1.869e-23
c42	SiO → SiO[s]	6.025e+01	-4.653e+04	-1.387e+06	2.685e+08	3.358e-23
c43	SiS+H ₂ O → SiO[s]+H ₂ S	5.935e+01	-4.397e+04	-1.887e+06	3.753e+08	3.358e-23
c44	2 SiH+2 H ₂ O → 2 SiO[s]+3 H ₂	4.865e+01	-4.527e+04	-2.760e+06	4.893e+08	3.358e-23

Table B.7: Continuation of Table B.4

nr	reaction	s_0	s_1 [K]	s_2 [K ²]	s_3 [K ³]	ΔV [cm ⁻³]
c45	2 Fe+SiO+3 H ₂ O → Fe ₂ SiO ₄ [s]+3 H ₂	1.679e+02	-2.708e+05	-1.494e+07	3.135e+09	7.708e-23
c46	2 Fe+SiS+4 H ₂ O → Fe ₂ SiO ₄ [s]+H ₂ S+3 H ₂	1.584e+02	-3.983e+05	-2.538e+06	1.000e+00	7.708e-23
c47	4 Fe+2 SiH+8 H ₂ O → 2 Fe ₂ SiO ₄ [s]+9 H ₂	1.716e+02	-3.316e+05	-1.509e+07	3.158e+09	7.708e-23
c48	2 FeO+SiO+H ₂ O → Fe ₂ SiO ₄ [s]+H ₂	1.536e+02	-2.186e+05	-1.603e+07	3.329e+09	7.708e-23
c49	2 FeO+SiS+2 H ₂ O → Fe ₂ SiO ₄ [s]+H ₂ S+H ₂	1.411e+02	-3.369e+05	-1.232e+07	2.678e+09	7.708e-23
c50	4 FeO+2 SiH+4 H ₂ O → 2 Fe ₂ SiO ₄ [s]+5 H ₂	1.573e+02	-2.794e+05	-1.618e+07	3.352e+09	7.708e-23
c51	2 FeS+SiO+3 H ₂ O → Fe ₂ SiO ₄ [s]+3 H ₂ S	1.440e+02	-3.363e+05	-2.978e+06	1.000e+00	7.708e-23
c52	2 FeS+SiS+4 H ₂ O → Fe ₂ SiO ₄ [s]+3 H ₂ S+H ₂	1.416e+02	-3.480e+05	-1.231e+07	2.678e+09	7.708e-23
c53	4 FeS+2 SiH+8 H ₂ O → 2 Fe ₂ SiO ₄ [s]+4 H ₂ S+5 H ₂	1.477e+02	-3.972e+05	-3.045e+06	1.000e+00	7.708e-23
c54	2 Fe(OH) ₂ +SiO → Fe ₂ SiO ₄ [s]+H ₂ O+H ₂	8.704e+01	-3.075e+05	-7.303e+06	1.700e+09	7.708e-23
c55	2 Fe(OH) ₂ +SiS → Fe ₂ SiO ₄ [s]+H ₂ S+H ₂	8.614e+01	-3.049e+05	-7.803e+06	1.806e+09	7.708e-23
c56	4 Fe(OH) ₂ +2 SiH → 2 Fe ₂ SiO ₄ [s]+5 H ₂	1.023e+02	-2.474e+05	-1.167e+07	2.480e+09	7.708e-23
c57	2 FeH+SiO+3 H ₂ O → Fe ₂ SiO ₄ [s]+4 H ₂	1.570e+02	-2.528e+05	-1.477e+07	3.065e+09	7.708e-23
c58	2 FeH+SiS+4 H ₂ O → Fe ₂ SiO ₄ [s]+H ₂ S+4 H ₂	1.474e+02	-3.801e+05	-2.614e+06	1.000e+00	7.708e-23
c59	4 FeH+2 SiH+8 H ₂ O → 2 Fe ₂ SiO ₄ [s]+11 H ₂	1.607e+02	-3.136e+05	-1.492e+07	3.089e+09	7.708e-23

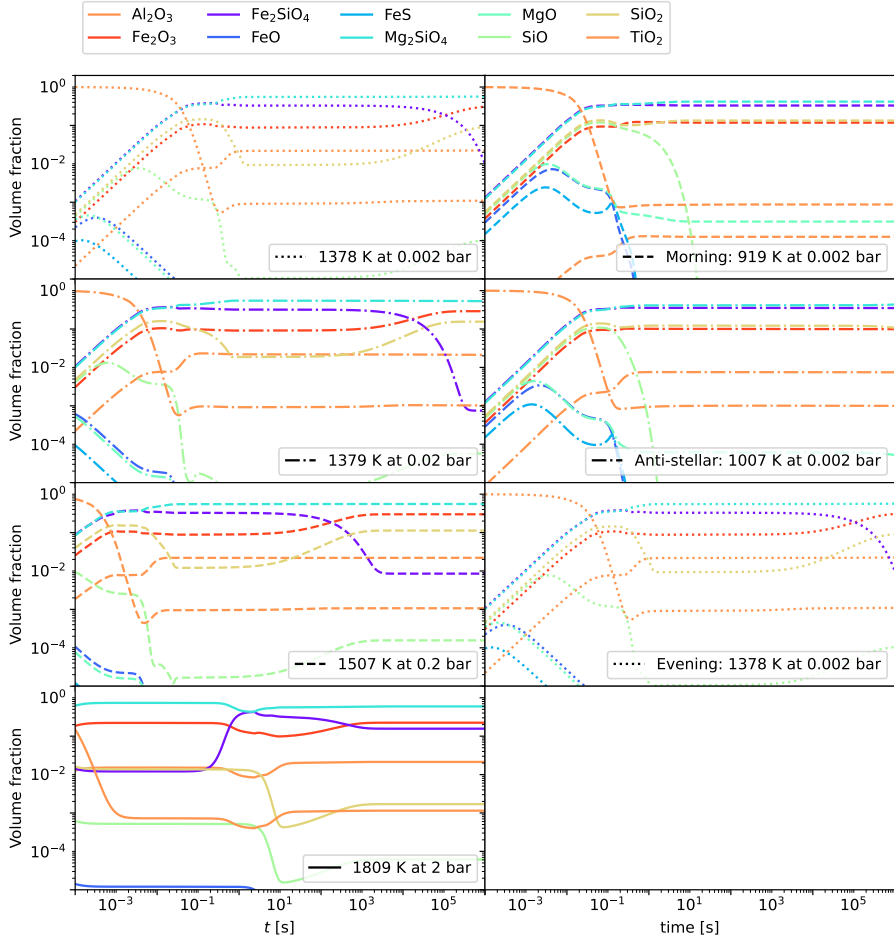


Figure B.4: Volume fractions for $T_{\text{gas}}-p_{\text{gas}}$ points of HD 209458 b. The sub-stellar point ($p_{\text{gas}} = 0.002$ bar, $T_{\text{gas}} = 2026$ K) is not shown since no cloud formation occurs.

Appendix C

Cloud particle optical properties

C.1 Mie Theory

Mie theory (Mie 1908) describes the solution to the Maxwell equations for a sphere with an effective refractive index of ϵ_{eff} in a medium with refractive index ϵ_m . For cloud particles the medium is vacuum and thus we have $\epsilon_m = 1$. While Mie theory has a well defined solution, numerical implementations differ. Here we test three different implementations of calculate Mie-Theory:

- PyMieScatt (Sumlin et al. 2018)
- miepython (Wiscombe 1979; Prahl 2023)
- Miex (Wolf & Voshchinnikov 2004)

The solution of Mie theory includes an infinite sum over Riccati-Bessel functions. For a numerical solution a suitable maximum number of summation terms N_{max} has to be selected. According to Wiscombe (1979) the following N_{max} is a suitable choice:

$$N_{\text{max}} = x + 4.05 \sqrt[3]{x} + 2, \quad (\text{C.1})$$

where x is the size parameter. This N_{max} was used by both miepython and PyMieScatt. Miex calculates N_{max} based on Loskutov (1971) which is given by:

$$N_{\text{max}} > |\epsilon_{\text{eff}}|^2 * x + 28 \quad (\text{C.2})$$

However, it is worth mentioning that Wiscombe (1979) notes in their work that the scaling of the Mie scattering error with N_{\max} dependants only slightly on the refractive index and mostly on the size parameter x . All three technique use the logarithmic derivative the Riccati-Bessel function D_n . The solution is derived following Bohren & Huffman (2008) and using (mostly) downward recursion starting from N_{\max} . PyMieScatt and Miex initialise the recursion with $D_{\max} = 0$. Miepython uses the Lentz method (Lentz 1973) to derive a more precise initial condition.

We calculate the relative differences in extinction efficiency Q_{ext} and scattering efficiency Q_{sca} relative to Miex to test the difference in the three routines. The following materials are tested: $\text{Al}_2\text{O}_3[\text{s}]$, $\text{Fe}_2\text{SiO}_4[\text{s}]$, $\text{FeO}[\text{s}]$, $\text{FeS}[\text{s}]$, $\text{Mg}_2\text{SiO}_4[\text{s}]$, $\text{MgO}[\text{s}]$, $\text{SiO}_2[\text{s}]$, $\text{SiO}[\text{s}]$, and $\text{TiO}_2[\text{s}]$. We tested multiple particle sizes in the range of $0.001 \mu\text{m}$ up to $1 \mu\text{m}$ and found that $a = 0.1 \mu\text{m}$ generally produced the largest differences. The relative difference between Miex and miepython is always below 10^{-6} for the extinction efficiency and 10^{-8} for the scattering efficiency. Between PyMieScatt and Miex, the relative difference reaches up to 31% for the extinction efficiency and 1.3% for the scattering efficiency. To investigate the impact of these differences on observations, we produced the transmission spectrum of HATS-6b (Hartman et al. 2015, ; Kiefer et al. subm.) using all 3 routines. For this spectrum, we also considered the equilibrium chemistry from the kinetic cloud formation model. The relative differences in the transit depth between Miex, PyMieScatt and miepython are all below 10^{-33} . Since observational limits are in the order of 10^{-5} , there is no observable difference between all three routines.

Overall, we found no significant differences between Miex and miepython. The differences between Miex and PyMieScatt do not impact the transmission spectrum. However, it cannot be ruled out that these differences can impact the thermal structure of an exoplanet atmospheres.

C.2 CaSiO_3 opacity treatment

Because no opacity data is available for $\text{CaSiO}_3[\text{s}]$, the refractive index has to be approximated. One possibility is to use vacuum values. However, this will lead to an under-prediction of the cloud particle opacities. Another approach is to approximate the refractive index of $\text{CaSiO}_3[\text{s}]$ with $\text{MgSiO}_3[\text{s}]$. While this approximation is likely closer to the real refractive index of $\text{CaSiO}_3[\text{s}]$, it also introduces additional $\text{MgSiO}_3[\text{s}]$ spectral features that might not be representative for $\text{CaSiO}_3[\text{s}]$.

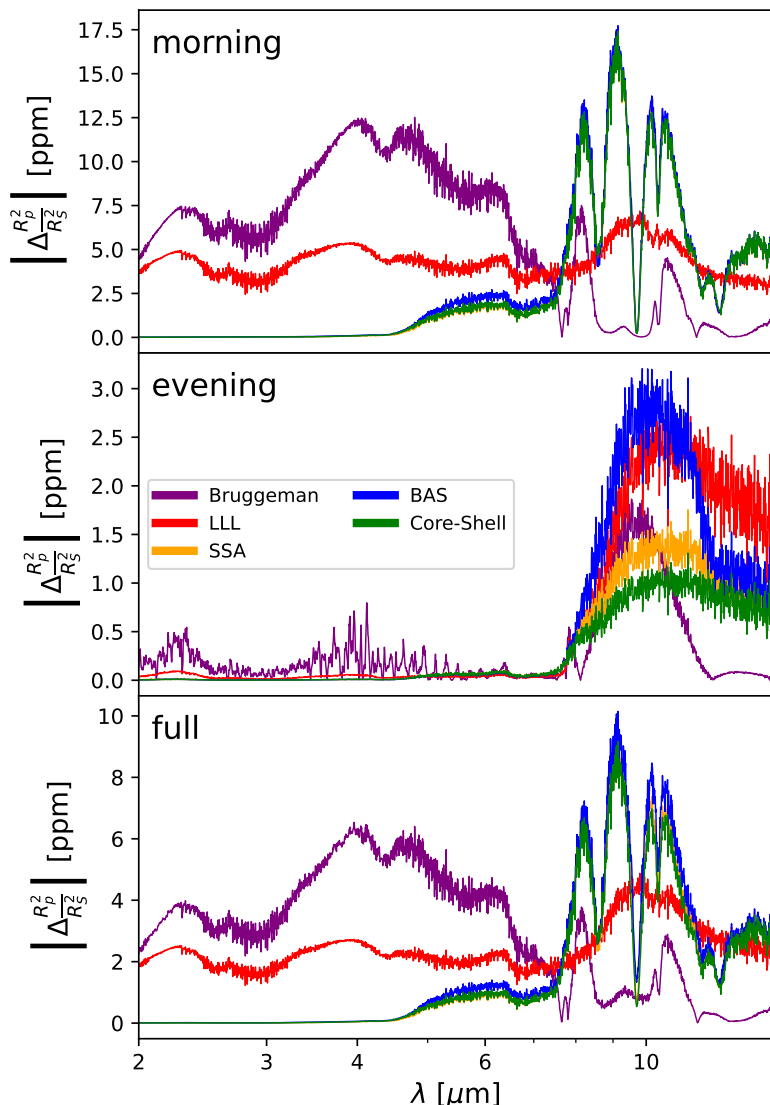


Figure C.1: Absolute relative differences in the transmission spectra of WASP-76b between the approximation of CaSiO₃[s] refractive index with vacuum and MgSiO₃[s] values.

From the four planets studied in Sect. 5.5, WASP-76b has the highest $\text{CaSiO}_3[\text{s}]$ volume fractions. We therefore calculate the transmission spectra of WASP-76b once using vacuum values and once using the refractive index values of $\text{MgSiO}_3[\text{s}]$ for the refractive index of $\text{CaSiO}_3[\text{s}]$. The absolute relative difference between the transit depths can be seen in Fig. C.1. The two approximations lead to differences in transit depth of up to 17 ppm between $8 \mu\text{m}$ to $11 \mu\text{m}$. This wavelength range corresponds to an increase in the imaginary part of the refractive index $k_{\text{MgSiO}_3[\text{s}]}$ which is specific to $\text{MgSiO}_3[\text{s}]$. Between $2 \mu\text{m}$ to $4 \mu\text{m}$ $k_{\text{MgSiO}_3[\text{s}]}$ is close to zero. In this wavelength range only the well-mixed particles show a difference in the transmission spectra. Overall, the differences in transit depth due to the two approximations for the $\text{CaSiO}_3[\text{s}]$ opacity is much smaller than the general variations in transit depth.

C.3 Data

The parameters used for the calculation of the transmission spectra in Sect. 5.5 are shown in Table C.1. The cloud particle opacities are listed in Table C.2.

C.4 Additional figures

Table C.1: Planetary parameters and model details for the exoplanets used in this study including the planetary Radius R_{pl} [R_{jup}], gravitational acceleration g [$\text{cm}^2 \text{ s}^{-1}$], stellar Radius R_{star} [R_{sun}], nucleating species considered (Nuc. spec.), and cloud particle materials considered (Cl. mat.).

	HATS-6b	WASP-39b	WASP-76b	WASP-107b
R_{pl} [R_{jup}]	1.27	1.279	1.83	0.94
g [$\text{cm}^2 \text{ s}^{-1}$]	430	426	681	260
R_{star} [R_{sun}]	0.57	0.932	1.73	0.66
Nuc. spec.				
TiO ₂	✓	✓	✓	-
SiO	✓	✓	✓	-
NaCl	✓	✓	✓	-
KCl	✓	✓	✓	-
Cl. mat.				
TiO ₂ [s]	✓	✓	✓	-
Al ₂ O ₃ [s]	✓	✓	✓	-
CaTiO ₃ [s]	✓	✓	✓	-
SiO[s]	✓	✓	✓	✓
SiO ₂ [s]	✓	✓	✓	✓
MgO[s]	✓	✓	✓	-
Fe[s]	✓	✓	✓	-
FeO[s]	✓	✓	✓	-
FeS[s]	✓	✓	✓	-
Fe ₂ O ₃ [s]	✓	✓	✓	-
Fe ₂ SiO ₃ [s]	✓	✓	✓	-
MgSiO ₃ [s]	✓	✓	✓	✓
CaSiO ₃ [s]	✓	✓	✓	-
Mg ₂ SiO ₄ [s]	✓	✓	✓	-
NaCl[s]	✓	✓	✓	-
KCl[s]	✓	✓	✓	-
C _{amorphous} [s]	-	-	-	✓

Table C.2: References for the refractive indices of the cloud particle materials. Data for KCl[s], ZnS[s], MnS[s], Na₂S[s], and NaCl[s] is taken from Kitzmann & Heng (2018).

Material species	Wavelength range (μm)	Reference
Al ₂ O ₃ [s] (grass)	0.10 - 200	Begemann et al. (1997)
C[s] (graphite)	0.2 - 794	Palik (1985)
C _{amorphous} [s]	0.05 - 10000	Zubko et al. (1996)
CaTiO ₃ [s] (amorphous)	2 - 5843	Posch et al. (2003)
Fe[s] (metallic)	0.00012 - 285	Palik (1985)
FeO[s] (amorphous)	0.20 - 500	Henning et al. (1995)
Fe ₂ O ₃ [s] (amorphous)	0.10 - 1000	Amaury H.M.J. Triaud (unpublished)
Fe ₂ SiO ₄ [s] (amorphous)	0.20 - 500	Dorschner et al. (1995)
FeS[s] (amorphous)	0.10 - 100000	Henning (unpublished)
KCl [s] (cubic)	0.01 - 166	Palik (1985); Quarry (1998)
MgSiO ₃ [s] (grass)	0.20 - 500	Dorschner et al. (1995)
Mg ₂ SiO ₄ [s] (crystalline)	0.10 - 1000	Suto et al. (2006)
MgO[s] (Cubic)	0.017 - 625	Palik (1985)
MnS[s]	0.01 - 190	(Huffman & Wild 1967; Montaner et al. 1979)
MnO[s]	0.1 - 11	(Kumar et al. 2021)
NaCl [s] (cubic)	0.05 - 166	Palik (1985); Quarry (1998)
Na ₂ S[s]	0.05 - 200	(Montaner et al. 1979; Khachai et al. 2009)
SiO ₂ [s] (alpha-Quartz)	0.00012 - 10000	Palik (1985), Zeidler et al. (2013)
SiO[s] (polycrystalline)	0.0015 - 14	Philipp in Palik (1985)
TiO ₂ [s] (Rutile)	0.47 - 36	Zeidler et al. (2011)
ZnS[s]	0.02 - 280	(Palik 1985)

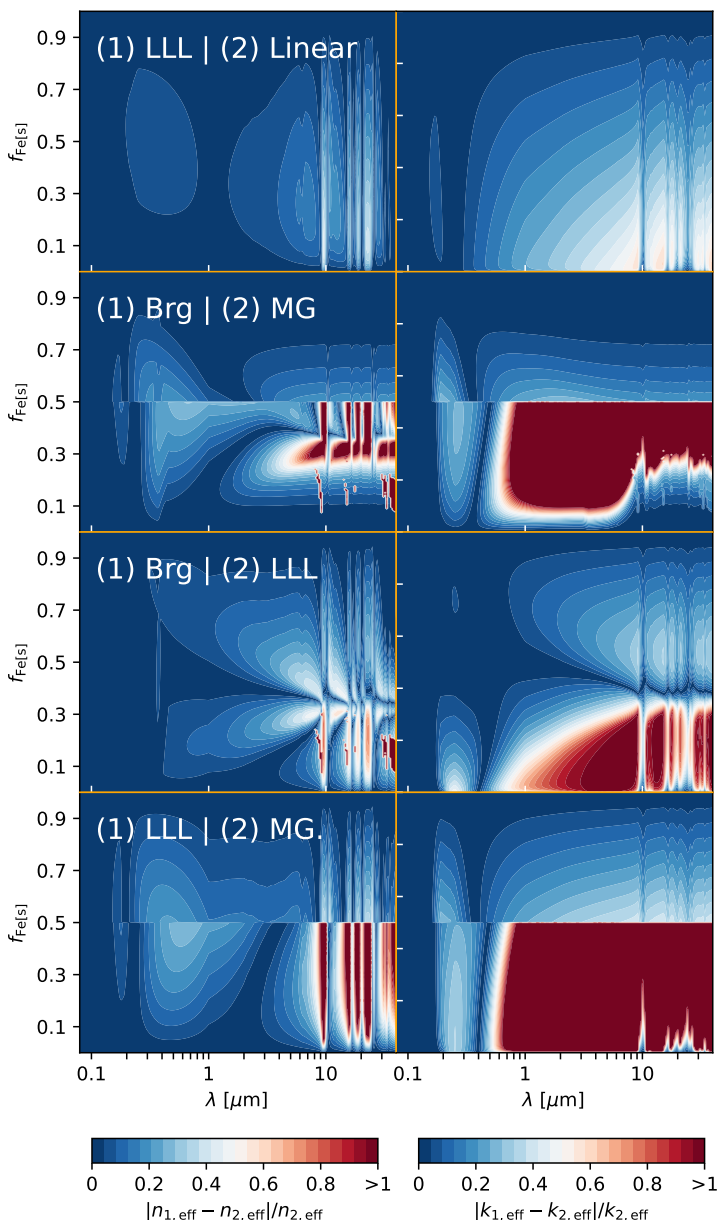


Figure C.2: Relative differences in the effective refractive index for the two-component material $\{\text{Fe[s]}, \text{Mg}_2\text{SiO}_4[\text{s}]\}$. Compared are LLL, Bruggeman (Brg), Maxwell-Garnett (MG), and Linear.

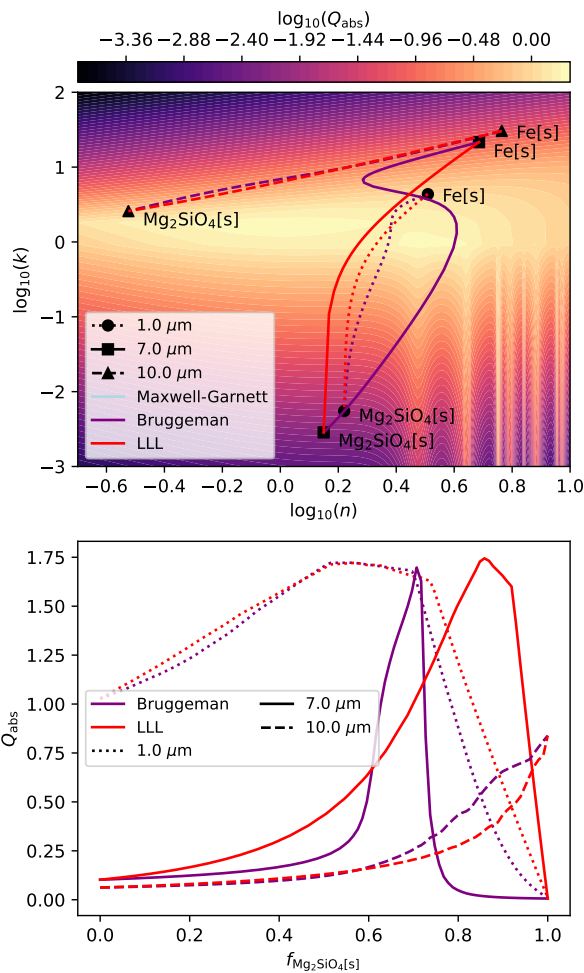


Figure C.3: Analysis of cloud particle optical property of two component materials using the same set-up as in Sect. 5.4.1 except for the size parameter which is here $x = 1$.

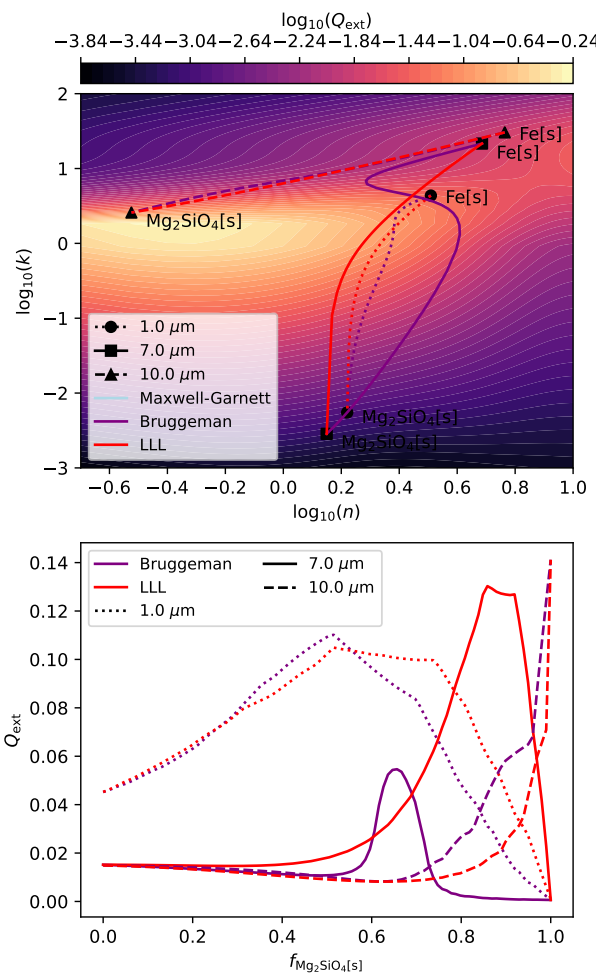


Figure C.4: Analysis of cloud particle optical property of two component materials using the same set-up as in Sect. 5.4.1 except that here the extinction efficiency instead of absorption efficiency is shown.

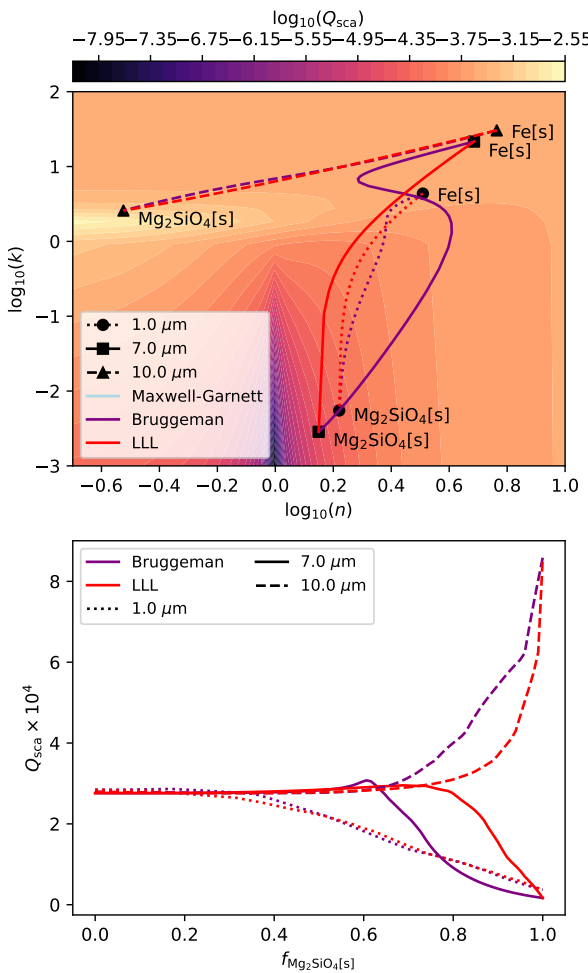


Figure C.5: Analysis of cloud particle optical property of two component materials using the same set-up as in Sect. 5.4.1 except that here the scattering efficiency instead of absorption efficiency is shown.

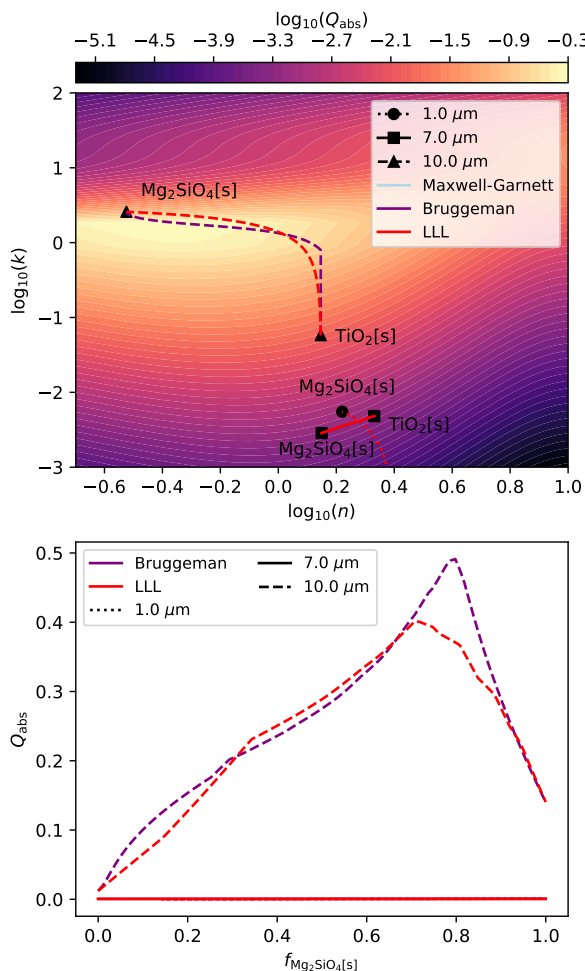


Figure C.6: Analysis of cloud particle optical property of two component materials using the same set-up as in Sect. 5.4.1 except that here the two component material $\{\text{TiO}_2[\text{s}], \text{Mg}_2\text{SiO}_4[\text{s}]\}$ is used.

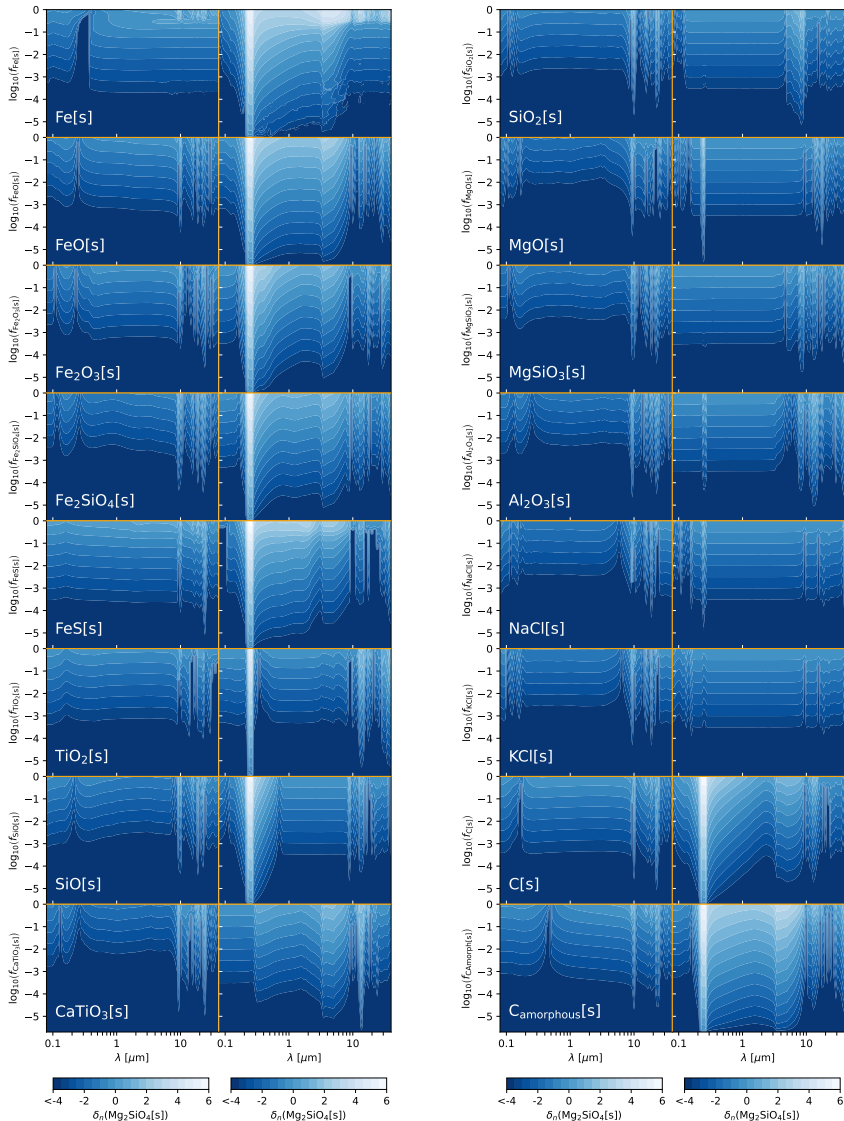


Figure C.7: Differences of the real and imaginary part of the refractive index (Eq. 5.16) for two-component materials compared to the refractive index of $\text{Mg}_2\text{SiO}_4[\text{s}]$ using Bruggeman. The first component is $\text{Mg}_2\text{SiO}_4[\text{s}]$ and the second component is specified in each plot. **Left:** real part n_{eff} . **Right:** imaginary part k_{eff} .

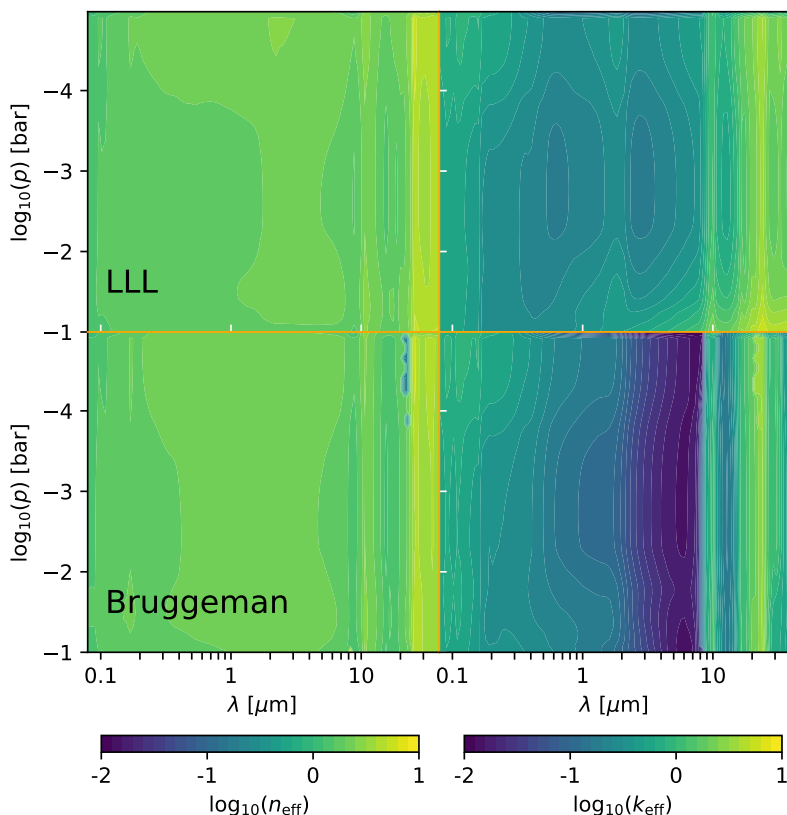


Figure C.8: Pressure dependent effective refractive index at the equator of the morning terminator of HATS-6b.

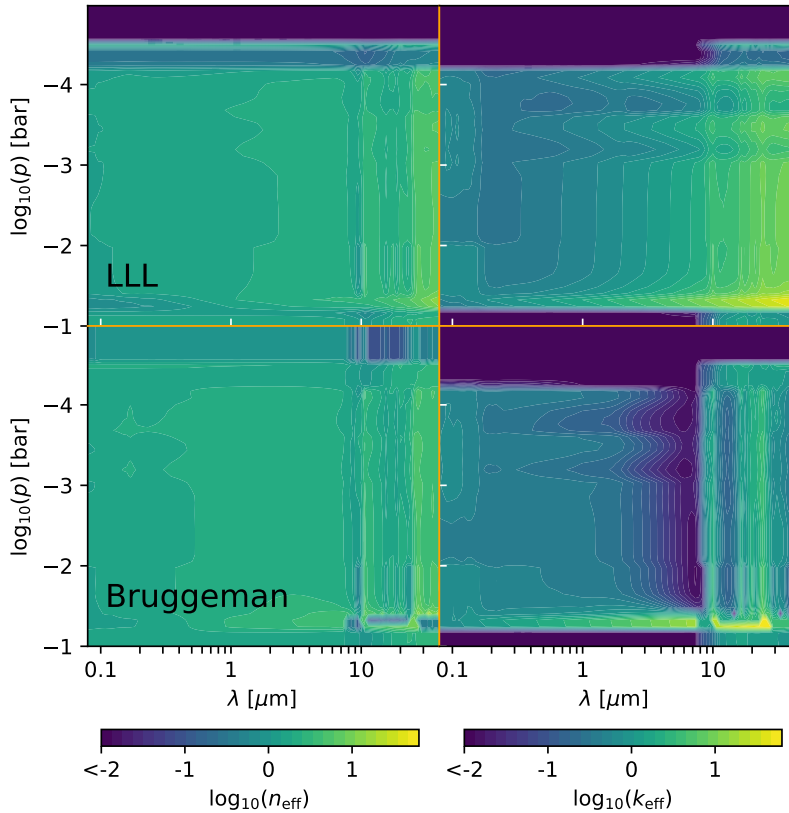


Figure C.9: Pressure dependent effective refractive index at the equator of the morning terminator of WASP-76b.

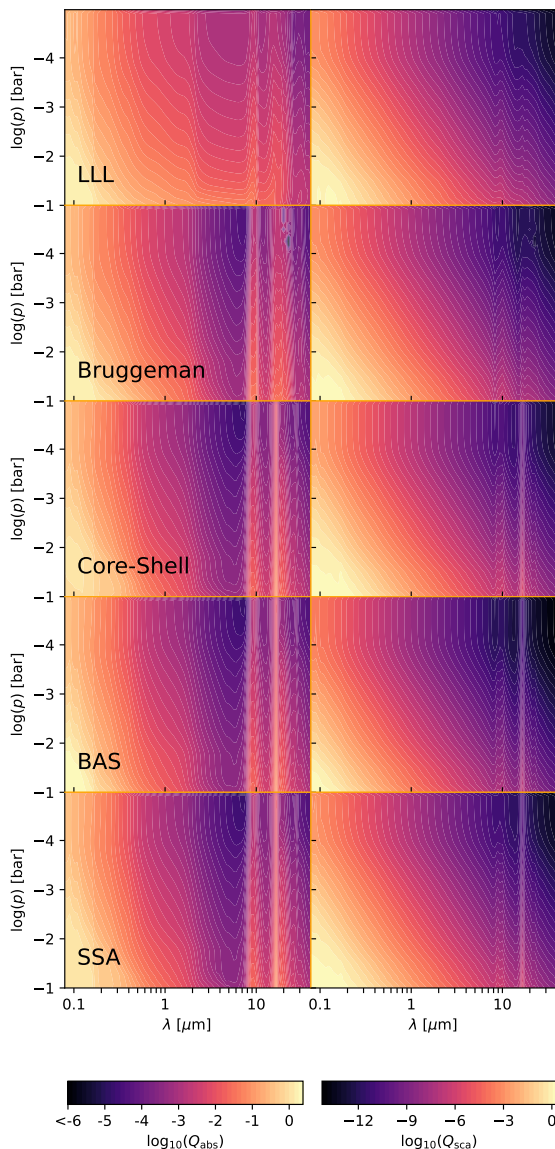


Figure C.10: Pressure dependent absorption and scattering efficiency at the equator of the morning terminator of HATS-6b.

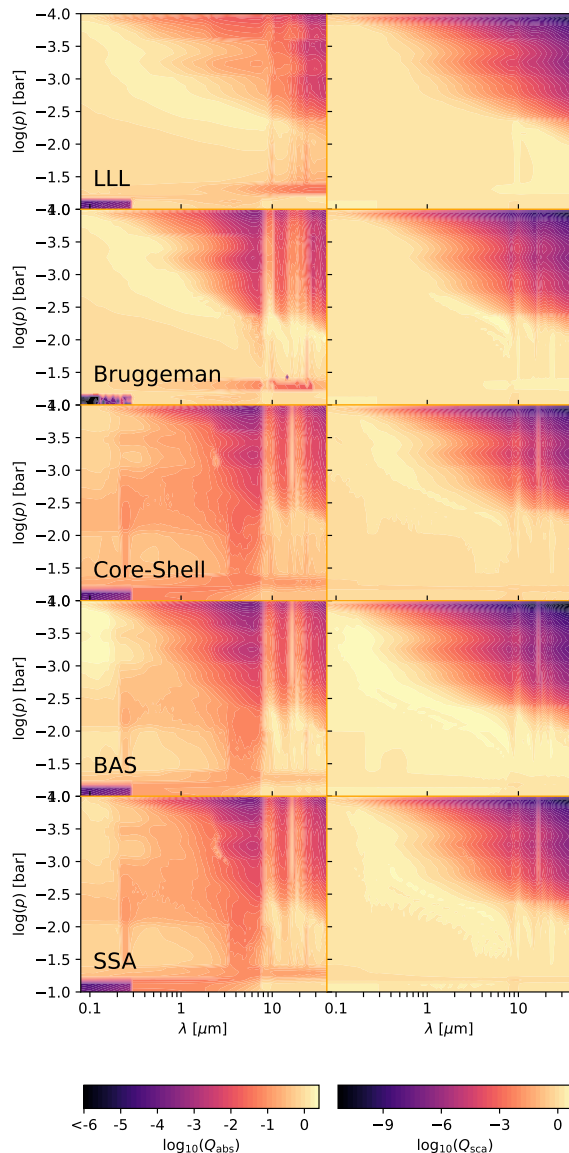


Figure C.11: Pressure dependent absorption and scattering efficiency at the equator of the morning terminator of WASP-76b.

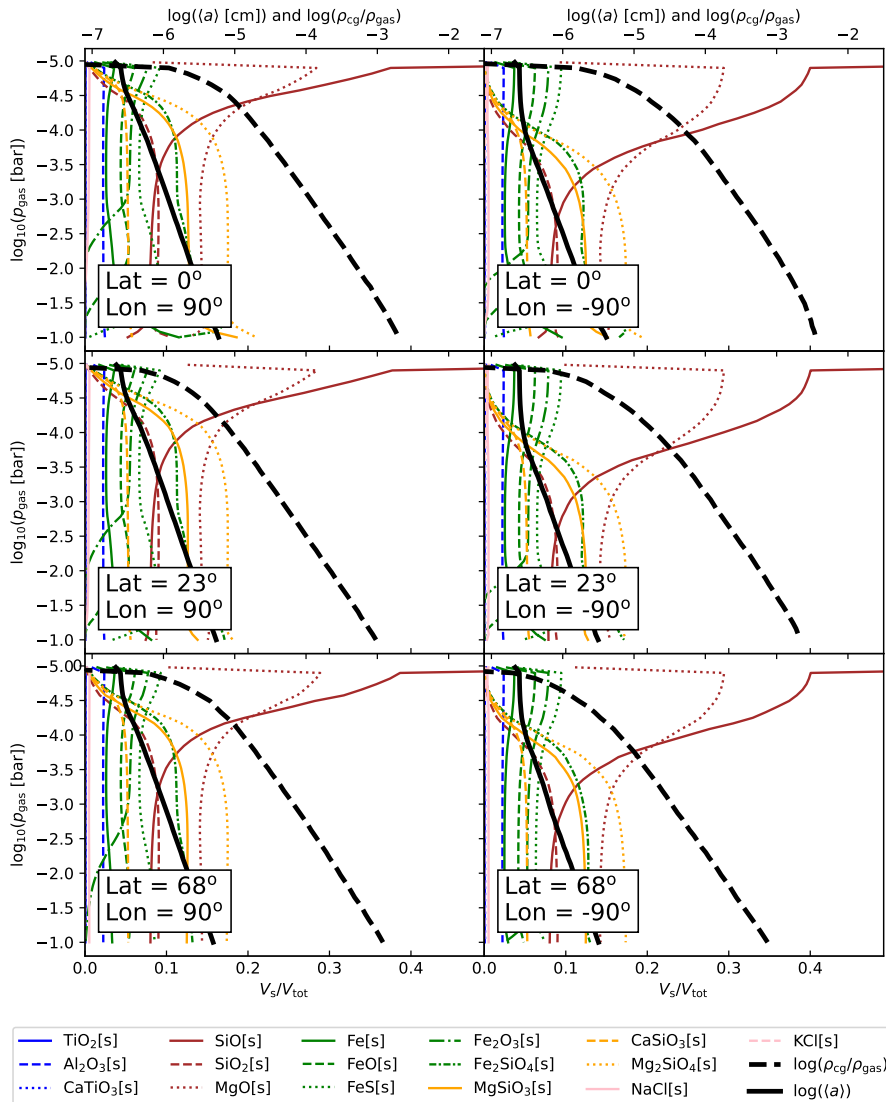


Figure C.12: Volume fractions V_s/V_{tot} of each cloud particle species considered (coloured lines), average cloud particle radius $\langle a \rangle$ of all cloud particles, and the total cloud mass fraction $\rho_{\text{cloud}}/\rho_{\text{gas}}$ for HATS-6b. Data taken from Kiefer et al. subm.

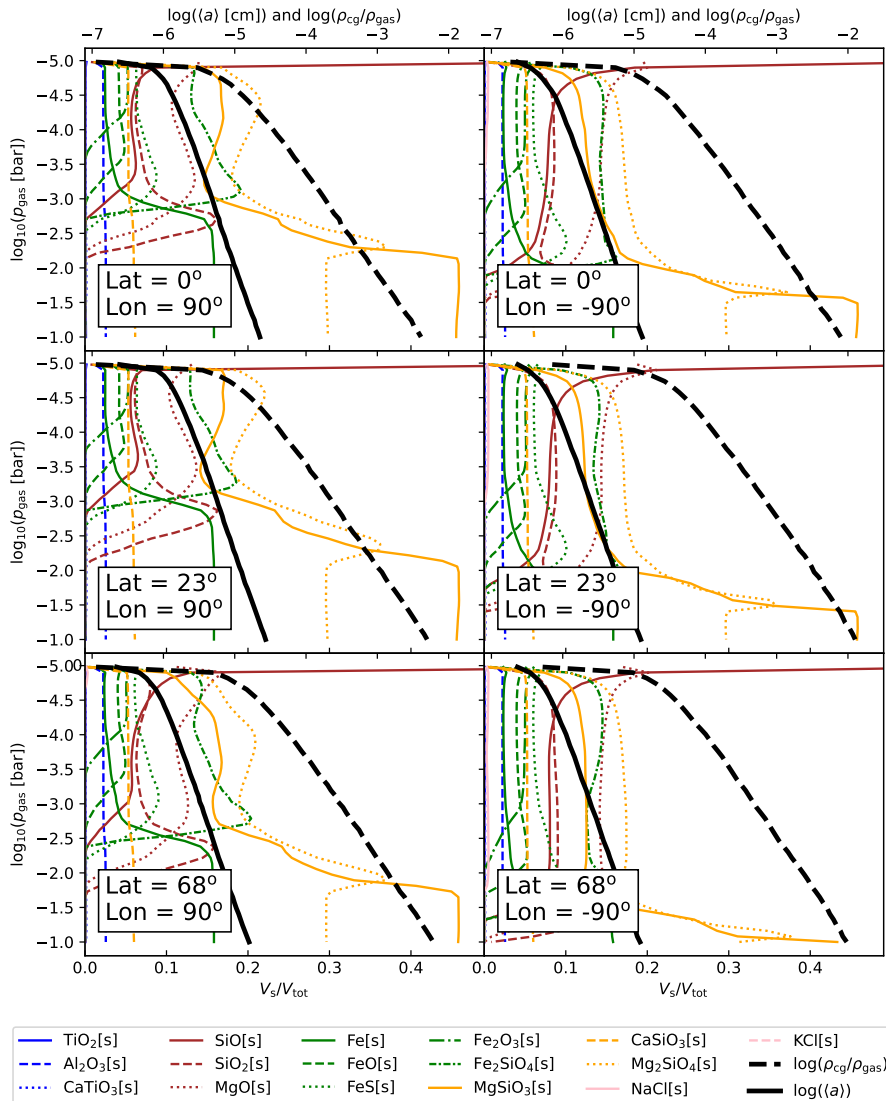


Figure C.13: Volume fractions V_s/V_{tot} of each cloud particle species considered (coloured lines), average cloud particle radius $\langle a \rangle$ of all cloud particles, and the total cloud mass fraction $\rho_{\text{cloud}}/\rho_{\text{gas}}$ for WASP-39b. Data taken from Carone et al. (2023).

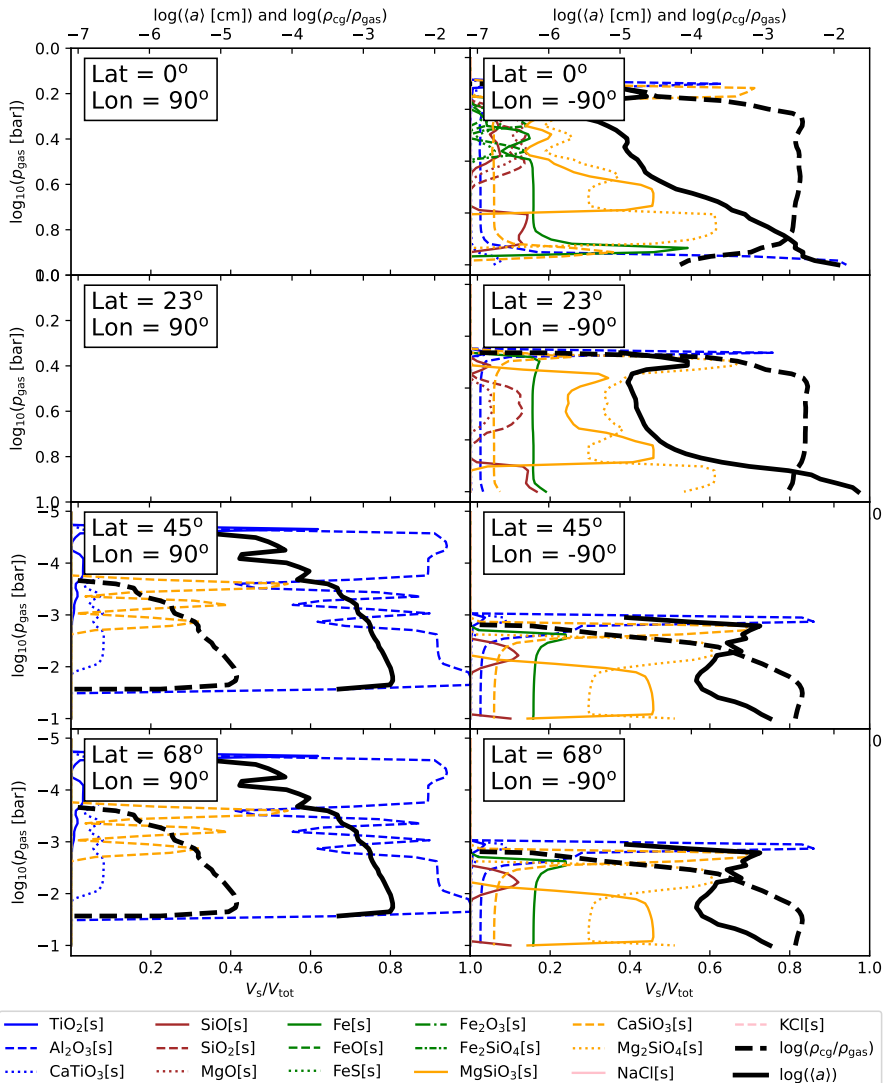


Figure C.14: Volume fractions V_s/V_{tot} of each cloud particle species considered (coloured lines), average cloud particle radius $\langle a \rangle$ of all cloud particles, and the total cloud mass fraction $\rho_{\text{cloud}}/\rho_{\text{gas}}$ for WASP-76b. The evening terminator ($\text{lon} = 90^\circ$) around the equator ($\text{lat} = 0^\circ$ and 23°) is cloud free.

Appendix D

HATS-6b

D.1 Additional cloud structure plots

The cloud particle properties of the sub-stellar and anti-stellar point for all iterations are shown in Fig. D.1. Additionally for iteration 5, the cloud particle material composition of the sub-stellar point, anti-stellar point, morning terminator and evening terminator are shown in Fig. D.2. Lastly, the transmission spectrum of each terminator grid cell ($\text{lat} = \{-68, -23, 0, 23, 68\}$) of iteration 5 before averaging is shown in Fig. D.3.

D.2 GCM convergence tests

To test the convergence of the `expeRT/MITgcm` runs, we analyse the time dependent temperature evolution of the GCM. The results can be seen in Fig. D.4. The results show that the temperature structure of all three runs are reasonably converged in the upper layers of the GCM.

D.3 Input SED for ARGO

The input SED used for the photo-chemistry of ARGO is shown in Fig. D.5. The SED is obtained from the MUSCLES survey where the star GJ667C is chosen as the closest analogue to HATS-6. The SED is combined from different

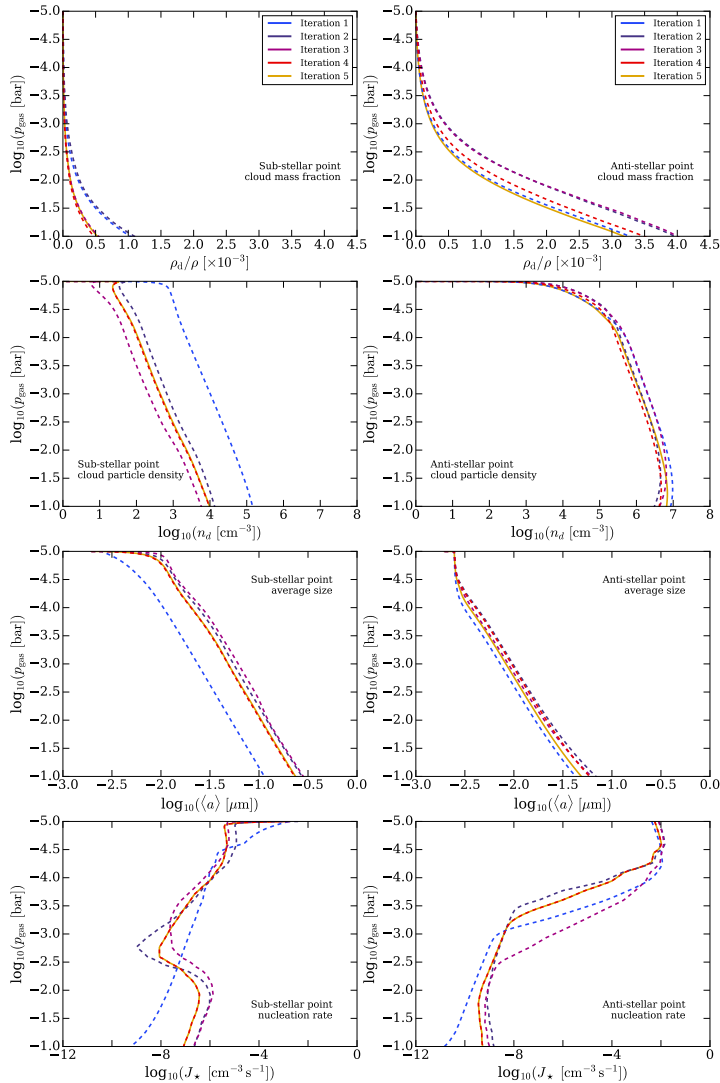


Figure D.1: Cloud particle properties of the step-wise iterated cloud structure for the warm Saturn example HATS-6b. Iteration 5 is shown as a solid line to highlight the final result. **Left:** sub-stellar point. **Right:** anti-stellar point. **Top:** cloud mass fraction ρ_d/ρ . **Upper middle:** cloud particle number density n_d . **Lower middle:** average cloud particle size $\langle a \rangle$. **Bottom:** Nucleation rate J_* . The morning and evening terminator can be found in Fig 6.5.

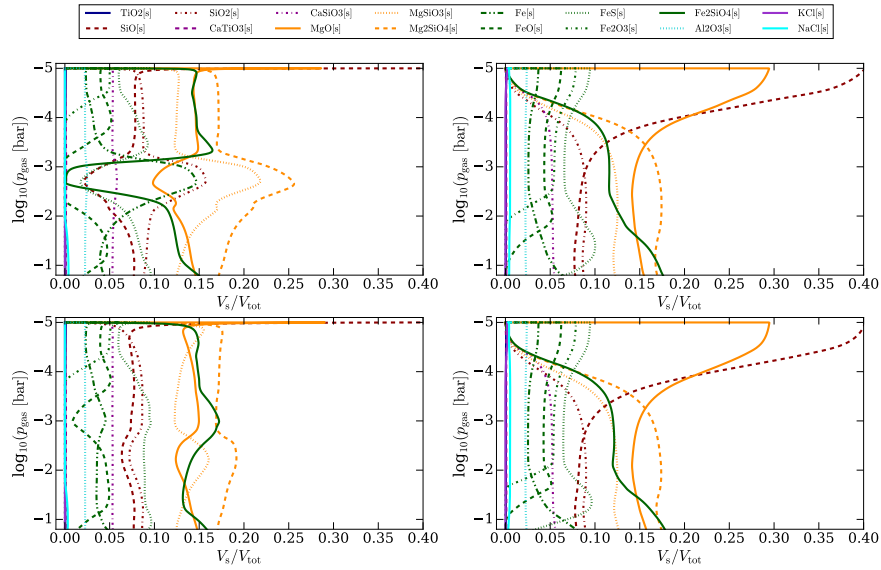


Figure D.2: Cloud particle material composition of iteration 5. **1st row:** Sub-stellar point. **2nd row:** Anti-stellar point. **3rd row:** Evening terminator. **4th row:** Morning terminator. Here the cloud profiles only reach down to 0.3 bar.

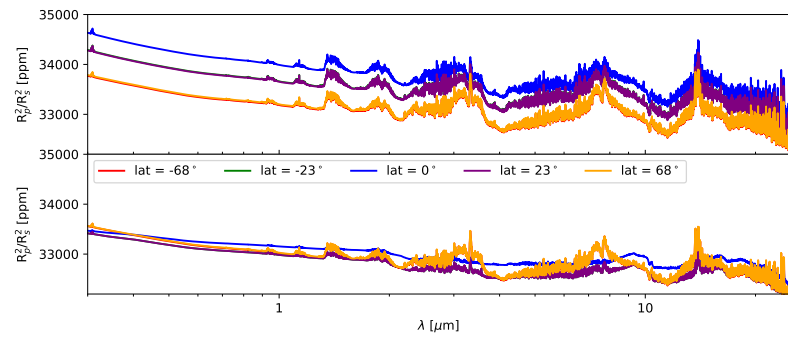


Figure D.3: Transmission spectrum for each terminator grid cell. **Top:** evening terminator. **Bottom:** morning terminator.

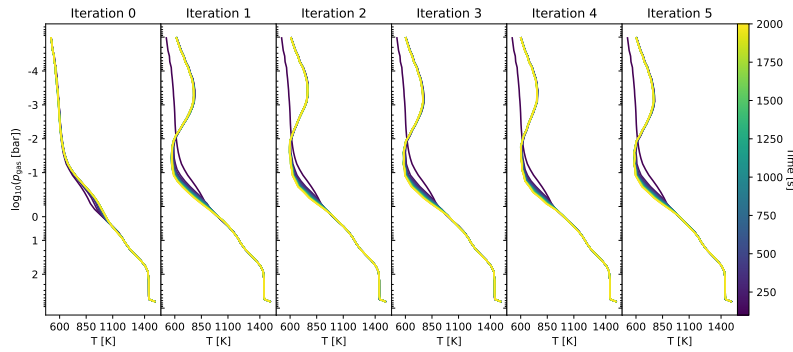


Figure D.4: Temperature evolution for every 100 days of the `expeRT/MITgcm` runs.

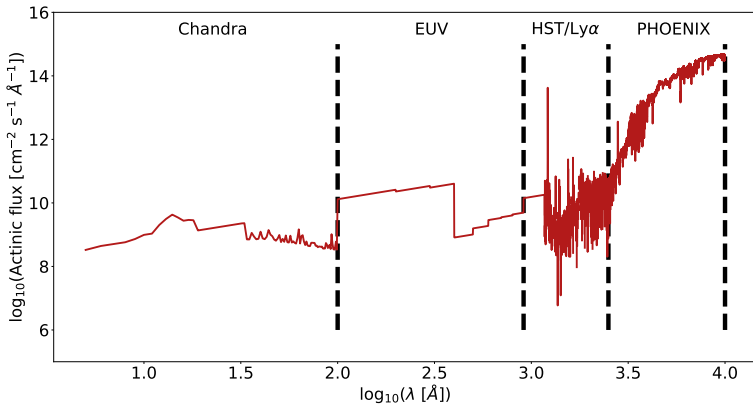


Figure D.5: Input spectral energy distribution (SED) for host star expressed in actinic flux.

spectra achieved through observations and models, as indicated in the sections separated by the dashed lines (see e.g. France et al. (2016) for details). The spectrum has been binned and adapted to the desired wavelength range 1-10,000 nm.

Bibliography

- Ackerman, A. S., Hobbs, P. V., & Toon, O. B. 1995, *J. Atmos. Sci.*, 52, 1204
- Ackerman, A. S. & Marley, M. S. 2001, *ApJ*, 556, 872
- Adcroft, A., Campin, J.-M., Hill, C., & Marshall, J. 2004a, *Mon. Weather Rev.*, 132, 2845
- Adcroft, A., Hill, C., Campin, J.-M., Marshall, J., & Heimbach, P. 2004b, overview of the formulation and numerics of the MIT GCM
- Agundez, M., Parmentier, V., Venot, O., Hersant, F., & Selsis, F. 2014, *A&A*, 564, A73
- Ahrer, E.-M., Stevenson, K. B., Mansfield, M., et al. 2023, *Nature*, 614, 653
- Airy, G. B. 1846, *MNRAS*, 7, 121
- Alderson, L., Wakeford, H. R., Alam, M. K., et al. 2023, *Nature*, 614, 664
- Alei, E., Konrad, B. S., Angerhausen, D., et al. 2022, *A&A*, 665, A106
- Allard, F., Guillot, T., Ludwig, H.-G., et al. 2003, *Proceedings of IAUS*, 211, 325
- Allard, F., Hauschildt, P. H., Alexander, D. R., Tamai, A., & Schweitzer, A. 2001, *ApJ*, 556, 357
- Amara, A. & Quanz, S. P. 2012, *Monthly Notices of the Royal Astronomical Society*, 427, 948
- Amara, A., Quanz, S. P., & Akeret, J. 2015, *Astronomy and Computing*, 10, 107
- Amundsen, D. S., Mayne, N. J., Baraffe, I., et al. 2016, *A&A*, 595, A36
- Anderson, D. R., Cameron, A. C., Delrez, L., et al. 2017, *A&A*, 604, A110

- Andersson, S., Gobrecht, D., & Valero, R. 2023, *Front. astron. space sci.*, 10
- Arakawa, A. & Lamb, V. R. 1977, in *General Circulation Models of the Atmosphere*, Vol. 17, *Methods in Computational Physics: Advances in Research and Applications*, ed. J. Chang (Elsevier), 173–265
- Arfau, A. & Lavvas, P. 2024, *MNRAS*, 530, 482
- Arrhenius, S. 1889, *Zeitschrift für Physikalische Chemie*, 4U, 226
- Asplund, M., Grevesse, N., Sauval, A. J., & Scott, P. 2009, *ARA&A*, 47, 481
- Atreya, S. K., Hofstadter, M. H., In, J. H., et al. 2020, *Space Science Reviews*, 216, 18
- Azzam, A. A. A., Tennyson, J., Yurchenko, S. N., & Naumenko, O. V. 2016, *MNRAS*, 460, 4063
- Baeyens, R. 2021, PhD thesis, book Title: On the Climate and Chemistry of Irradiated Exoplanet Atmospheres
- Baeyens, R., Decin, L., Carone, L., et al. 2021, *MNRAS*, 505, 5603
- Baeyens, R., Konings, T., Venot, O., Carone, L., & Decin, L. 2022, *MNRAS*, 512, 4877
- Bakes, E. L. O., Lebonnois, S., Bauschlicher, C. W., & McKay, C. P. 2003, *Icarus*, 161, 468
- Ball, J. M. & Carr, J. 1990, *J. Stat. Phys.*, 61, 203
- Ballerini, P., Micela, G., Lanza, A. F., & Pagano, I. 2012, *A&A*, 539, A140
- Barber, R. J., Strange, J. K., Hill, C., et al. 2014, *MNRAS*, 437, 1828
- Bardeen, C. G., Toon, O. B., Jensen, E. J., Marsh, D. R., & Harvey, V. L. 2008, *J. Geophys. Res. Atmos.*, 113
- Barman, T. S., Konopacky, Q. M., Macintosh, B., & Marois, C. 2015, *ApJ*, 804, 61
- Barth, P., Helling, C., Stüeken, E. E., et al. 2021, *MNRAS*, 502, 6201
- Barth, P., Stüeken, E. E., Helling, C., Schwieterman, E. W., & Telling, J. 2024, *A&A*, 686, A58
- Barton, E. J., Yurchenko, S. N., & Tennyson, J. 2013, *MNRAS*, 434, 1469
- Batalha, N. E., Mandell, A., Pontoppidan, K., et al. 2017, *PASP*, 129, 064501

- Batalha, N. M., Rowe, J. F., Bryson, S. T., et al. 2013, *ApJS*, 204, 24
- Batygin, K., Adams, F. C., Brown, M. E., & Becker, J. C. 2019, *Physics Reports*, 805, 1
- Baulch, D. L., Cobos, C. J., Cox, R. A., et al. 1992, *JPCRD*, 21, 411
- Baxter, C., Désert, J.-M., Tsai, S.-M., et al. 2021, *A&A*, 648, A127
- Bean, J. L., Miller-Ricci Kempton, E., & Homeier, D. 2010, *Nature*, 468, 669
- Beatty, T. G. & Seager, S. 2010, *ApJ*, 712, 1433
- Becke, A. D. 1993, *J. Chem. Phys.*, 98, 5648
- Becker, R. & Döring, W. 1935, *Annalen der Physik*, 416, 719
- Begemann, B., Dorschner, J., Henning, T., et al. 1997, *ApJ*, 476, 199
- Beleznay, M. & Kunimoto, M. 2022, *MNRAS*, 516, 75
- Bell, T. J., Crouzet, N., Cubillos, P. E., et al. 2024, *Nature Astronomy*
- Belyaev, B. A. & Tyurnev, V. V. 2018, *JETP*, 127, 608
- Benneke, B., Knutson, H. A., Lothringer, J., et al. 2019, *Nat. Astron.*, 3, 813
- Birkmann, S. M., Ferruit, P., Giardino, G., et al. 2022, *A&A*, 661, A83
- Bloot, S., Miguel, Y., Bazot, M., & Howard, S. 2023, *MNRAS*, 523, 6282
- Bohren, C. F. & Huffman, D. R. 1983, *Absorption and scattering of light by small particles*
- Bohren, C. F. & Huffman, D. R. 2008, *Absorption and Scattering of Light by Small Particles* (John Wiley & Sons)
- Boisse, I., Bouchy, F., Hébrard, G., et al. 2011, *A&A*, 528, A4
- Borsa, F., Fossati, L., Koskinen, T., Young, M. E., & Shulyak, D. 2022, *Nat Astron*, 6, 226
- Borucki, W. J. 2016, *Reports on Progress in Physics*, 79, 036901
- Borysow, A. 2002, *A&A*, 390, 779
- Borysow, A. & Frommhold, L. 1989, *ApJ*, 341, 549
- Borysow, A., Frommhold, L., & Moraldi, M. 1989, *ApJ*, 336, 495
- Borysow, A., Jorgensen, U. G., & Fu, Y. 2001, *JQSRT*, 68, 235

- Borysow, J., Frommhold, L., & Birnbaum, G. 1988, ApJ, 326, 509
- Boucher, O. 2015, in Atmospheric Aerosols: Properties and Climate Impacts, ed. O. Boucher (Dordrecht: Springer Netherlands), 9–24
- Boulanger, J., Clementel, N., van Marle, A. J., Decin, L., & de Koter, A. 2019a, MNRAS, 482, 5052
- Boulanger, J., Gobrecht, D., Decin, L., de Koter, A., & Yates, J. 2019b, MNRAS, 489, 4890
- Broeg, C., Fortier, A., Ehrenreich, D., et al. 2013, EPJ Web of Conferences, 47, 03005
- Bromley, S. T., Martín, J. C. G., & C. Plane, J. M. 2016, PCCP, 18, 26913
- Bromley, S. T. & Zwijnenburg, M. A. 2016, Computational Modeling of Inorganic Nanomaterials (CRC Press)
- Bruggeman, D. a. G. 1935, Annalen der Physik, 416, 636
- Buchhave, L. A., Bitsch, B., Johansen, A., et al. 2018, ApJ, 856, 37
- Burke, J. R. & Hollenbach, D. J. 1983, ApJ, 265, 223
- Burrows, A. & Orton, G. 2009, Giant Planet Atmospheres and Spectra, arXiv:0910.0248 [astro-ph]
- Burrows, A. & Volobuyev, M. 2003, ApJ, 583, 985
- Burton, J. J. 1977, in Nucleation Theory. In: Berne, B.J. (eds) Statistical Mechanics. Modern Theoretical Chemistry, vol 5. Springer, Boston
- Campbell, M. L. & McClean, R. E. 1993, J. Phys. Chem., 97, 7942
- Carone, L., Baeyens, R., Mollière, P., et al. 2020, MNRAS, 496, 3582
- Carone, L., Keppens, R., & Decin, L. 2014, MNRAS, 445, 930
- Carone, L., Lewis, D. A., Samra, D., Schneider, A. D., & Helling, C. 2023, ArXiv, 2301.08492
- Carone, L., Mollière, P., Zhou, Y., et al. 2021, A&A, 646, A168
- Carr, J. 1992, Proceedings of the Royal Society of Edinburgh Section A: Mathematics, 121, 231
- Carr, J. & da Costa, F. P. 1994, J. Stat. Phys., 77, 89
- Catoire, L., Legendre, J.-F., & Giraud, M. 2003, J. Propuls. Power, 19, 196

- Cañas, C. I., Kanodia, S., Bender, C. F., et al. 2022, AJ, 164, 50
- Chadney, J. M., Koskinen, T. T., Galand, M., Unruh, Y. C., & Sanz-Forcada, J. 2017, A&A, 608, A75
- Chan, Y. M. & Dalgarno, A. 1965, Proc. Phys. Soc., 85, 227
- Chang, C., Patzer, A. B. C., Kegel, W. H., & Chandra, S. 2013, Astrophys Space Sci, 347, 315
- Chang, C., Patzer, A. B. C., Sedlmayr, E., & Sülzle, D. 2005, Phys. Rev. B, 72, 235402
- Chapman, S. 1930, A Theory of Upper-atmospheric Ozone (Edward Stanford)
- Charbonneau, D., Brown, T. M., Latham, D. W., & Mayor, M. 2000, ApJ, 529, L45
- Charnay, B., Meadows, V., & Leconte, J. 2015a, ApJ, 813, 15
- Charnay, B., Meadows, V., Misra, A., Leconte, J., & Arney, G. 2015b, ApJ, 813, L1
- Chiodo, L., Salazar, M., Romero, A. H., et al. 2011, J. Chem. Phys., 135, 244704
- Christie, D. A., Mayne, N. J., Gillard, R. M., et al. 2022, MNRAS, 517, 1407
- Christie, D. A., Mayne, N. J., Lines, S., et al. 2021, MNRAS, 506, 4500
- Chubb, K. L. & Min, M. 2022, A&A, 665, A2
- Chubb, K. L., Stam, D. M., Helling, C., Samra, D., & Carone, L. 2024, MNRAS, 527, 4955
- Chubb, K. L., Tennyson, J., & Yurchenko, S. N. 2020, MNRAS, 493, 1531
- Chýlek, P., Srivastava, V., Pinnick, R. G., & Wang, R. T. 1988, Applied Optics, 27, 2396
- Coles, P. A., Yurchenko, S. N., & Tennyson, J. 2019, MNRAS, 490, 4638
- Cooke, G. J., Marsh, D. R., Walsh, C., Rugheimer, S., & Villanueva, G. L. 2023, MNRAS, 518, 206
- Cooper, C. S. & Showman, A. P. 2006, ApJ, 649, 1048
- Coppola, C. M., Lodi, L., & Tennyson, J. 2011, MNRAS, 415, 487
- Courtin, R., Wagener, R., McKay, C. P., et al. 1991, Icarus, 90, 43

- Cowan, N. B., Machalek, P., Croll, B., et al. 2012, *ApJ*, 747, 82
- Crossfield, I. J. M. 2015, *PASP*, 127, 941
- Crossfield, I. J. M., Barman, T., Hansen, B. M. S., & Howard, A. W. 2013, *A&A*, 559, A33
- Crowther, P. A. 2003, *Ap&SS*, 285, 677
- Czesla, S., Huber, K. F., Wolter, U., Schröter, S., & Schmitt, J. H. M. M. 2009, *A&A*, 505, 1277
- Dalgarno, A. & Williams, D. A. 1962, *ApJ*, 136, 690
- Dang, L., Cowan, N. B., Schwartz, J. C., et al. 2018, *Nat. Astron.*, 2, 220
- Debrecht, A., Carroll-Nellenback, J., Frank, A., et al. 2022, *Monthly Notices of the Royal Astronomical Society*, 517, 1724
- Decin, L., Cherchneff, I., Hony, S., et al. 2008, *A&A*, 480, 431
- Decin, L., Danilovich, T., Gobrecht, D., et al. 2018, *ApJ*, 855, 113
- Decin, L., Richards, A. M. S., Waters, L. B. F. M., et al. 2017, *A&A*, 608, A55
- Deitrick, R., Mendonça, J. M., Schroffenegger, U., et al. 2020, *ApJS*, 248, 30
- Demangeon, O. D. S., Cubillos, P. E., Singh, V., et al. 2024, *A&A*, 684, A27
- Deming, D. & Knutson, H. A. 2020, *Nat. Astron.*, 4, 453
- Demory, B.-O., Wit, J. d., Lewis, N., et al. 2013, *ApJL*, 776, L25
- Dishoeck, E. F. v. 2014, *Faraday Discuss.*, 168, 9
- Dobrijevic, M., Ollivier, J. L., Billebaud, F., Brillet, J., & Parisot, J. P. 2003, *A&A*, 398, 335
- Dobrijevic, M. & Parisot, J. P. 1998, *P&SS*, 46, 491
- Dominik, C., Sedlmayr, E., & Gail, H.-P. 1993, *A&A*, 277, 578
- Donn, B. 1978, Condensation Processes and the Formation of Cosmic Grains, conference Name: IAU Colloq. 52: Protostars and Planets
- Donn, B. & Nuth, J. A. 1985, *ApJ*, 288, 187
- Dorschner, J., Begemann, B., Henning, T., Jaeger, C., & Mutschke, H. 1995, *A&A*, 300, 503

- Doye, J. P. K. & Wales, D. J. 1996, *J. Chem. Phys.*, 105, 8428
- Draine, B. T. 2024, *ApJ*, 961, 103
- Draine, B. T. & Flatau, P. J. 1994, *J. Opt. Soc. Am. A*, 11, 1491
- Draine, B. T. & Salpeter, E. E. 1977, *J. Chem. Phys.*, 67, 2230
- Drummond, B., Mayne, N. J., Manners, J., et al. 2018, *ApJL*, 855, L31
- Du, H., Chen, H., Gong, J., et al. 2004, *Applied Surface Science*, 233, 99
- Dyreka, A., Min, M., Decin, L., et al. 2023, *Nature*, 625, 51
- Ehrenreich, D., Lovis, C., Allart, R., et al. 2020, *Nature*, 580, 597
- Espinoza, N., Rackham, B. V., Jordán, A., et al. 2019, *MNRAS*, 482, 2065
- Espinoza, N., Steinrueck, M. E., Kirk, J., et al. 2024, *Nature*, 632, 1017, publisher: Nature Publishing Group
- Estrela, R., Swain, M. R., & Roudier, G. M. 2022, *ApJL*, 941, L5
- Faedi, F., Barros, S. C. C., Anderson, D. R., et al. 2011, *A&A*, 531, A40
- Feautrier, P. 1964, *Comptes Rendus Academie des Sciences Paris*, 258, 3189
- Feinstein, A. D., Radica, M., Welbanks, L., et al. 2023, *Nature*, 614, 670
- Ferrari, P., Janssens, E., Lievens, P., & Hansen, K. 2019, *Int Rev Phys Chem*, 38, 405
- Ferrarotti, A. S. & Gail, H.-P. 2002, *A&A*, 382, 256
- Ferrarotti, A. S. & Gail, H.-P. 2006, *A&A*, 447, 553
- Ferruit, P., Jakobsen, P., Giardino, G., et al. 2022, *A&A*, 661, A81
- Fischer, P. D., Knutson, H. A., Sing, D. K., et al. 2016, *ApJ*, 827, 19
- Fleischer, A. J., Winters, J. M., & Sedlmayr, E. 1999, *Asymptotic Giant Branch Stars, IAU Symposium #191*, 191, 187
- Follette, K. B. 2023, *PASP*, 135, 093001
- Fonfría, J. P., Cernicharo, J., Richter, M. J., & Lacy, J. H. 2008, *ApJ*, 673, 445
- Fonfría, J. P., Hinkle, K. H., Cernicharo, J., et al. 2017, *ApJ*, 835, 196
- Fonfría, J. P., Montiel, E. J., Cernicharo, J., et al. 2021, *A&A*, 651, A8

- Forget, F. & Leconte, J. 2014, Philosophical Transactions of the Royal Society A: Mathematical, Physical and Engineering Sciences, 372, 20130084
- Fortier, A., Beck, T., Benz, W., et al. 2014, in Space Telescopes and Instrumentation 2014: Optical, Infrared, and Millimeter Wave, Vol. 9143 (International Society for Optics and Photonics), 91432J
- Fortney, J. J., Lodders, K., Marley, M. S., & Freedman, R. S. 2008, ApJ, 678, 1419
- Fortney, J. J., Visscher, C., Marley, M. S., et al. 2020, AJ, 160, 288
- France, K., Loyd, R. O. P., Youngblood, A., et al. 2016, ApJ, 820, 89
- Franta, D. & Ohlídal, I. 2005, Optics Communications, 248, 459
- Fraschetti, F., Drake, J. J., Alvarado-Gómez, J. D., et al. 2019, ApJ, 874, 21
- Frese, M. H. 1987, Defense Technical Information Center, ADA192285
- Frisch, M. J., Trucks, G. W., Schlegel, H. B., et al. 2016, Gaussian~16 Revision C.01
- Gail, H.-P. 2010, in Astromineralogy, ed. T. Henning, Lecture Notes in Physics (Berlin, Heidelberg: Springer), 61–141
- Gail, H.-P., Keller, R., & Sedlmayr, E. 1984, A&A, 133, 320
- Gail, H.-P. & Sedlmayr, E. 1986, A&A, 166, 225
- Gail, H.-P. & Sedlmayr, E. 1988, A&A, 206, 153
- Gail, H.-P. & Sedlmayr, E. 1998, Faraday Discuss., 109, 303
- Gail, H.-P. & Sedlmayr, E. 1999, A&A, 347, 594
- Gail, H.-P. & Sedlmayr, E. 2013, Physics and Chemistry of Circumstellar Dust Shells
- Galicher, R. & Mazoyer, J. 2023, Comptes Rendus. Physique, 24, 1
- Gandhi, S., Kesseli, A., Zhang, Y., et al. 2023, Astron. J., 165, 242
- Gandhi, S. & Madhusudhan, N. 2019, MNRAS, 485, 5817
- Gao, P. & Benneke, B. 2018, ApJ, 863, 165
- Gao, P. & Powell, D. 2021, ApJ, 918, L7
- Gao, P., Thorngren, D. P., Lee, E. K. H., et al. 2020, Nat. Astron., 4, 951

- Gao, P., Wakeford, H. R., Moran, S. E., & Parmentier, V. 2021, *J. Geophys. Res. Planets*, 126, e2020JE006655
- Garnett, J. C. M. & Larmor, J. 1904, *Philosophical Transactions of the Royal Society of London. Series A, Containing Papers of a Mathematical or Physical Character*, 203, 385
- Gauger, A., Gail, H. P., & Sedlmayr, E. 1990, *A&A*, 235, 345
- Genest, F., Lafrenière, D., Boucher, A., et al. 2022, *Astron. J.*, 163, 231
- Ghanbarian, B. & Daigle, H. 2016, *VZJ*, 15, vzj2015.05.0071
- Gilbert, R. G., Luther, K., & Troe, J. 1983, *Berichte der Bunsengesellschaft für physikalische Chemie*, 87, 169
- Gillon, M., Triaud, A. H. M. J., Demory, B.-O., et al. 2017, *Nature*, 542, 456, publisher: Nature Publishing Group
- Girshick, S. L. & Chiu, C. 1990, *J. Chem. Phys.*, 93, 1273
- Gobrecht, D., Cherchneff, I., Sarangi, A., Plane, J. M. C., & Bromley, S. T. 2016, *A&A*, 585, A6
- Gobrecht, D., Hashemi, S. R., Plane, J. M. C., et al. 2023, *A&A*, 680, A18
- Gobrecht, D., Plane, J. M. C., Bromley, S. T., et al. 2022, *A&A*, 658, A167
- Goeres, A. 1996, *Proceedings of the ASP Conference Series, Hydrogen Deficient Stars*, ed. C. S. Jeffery and U. Heber, 96, 69
- Goosse, H., Barriat, P.-Y., Loutre, M.-F., & Zunz, V. 2010, *Introduction to climate dynamics and climate modeling (Centre de recherche sur la Terre et le climat Georges Lemaître - UCLouvain)*
- Goumans, T. P. M. & Bromley, S. T. 2013, *Phil. Trans. R. Soc. A*, 371, 20110580
- Grant, D., Lewis, N. K., Wakeford, H. R., et al. 2023, *ApJL*, 956, L29
- Grassi, T., Bovino, S., Schleicher, D. R. G., et al. 2014, *MNRAS*, 439, 2386
- Gray, D. F. 2008, *The Observation and Analysis of Stellar Photospheres* (Cambridge University Press)
- Green, D. W. E. 2006, *IAU Circular*, 8747, 1
- Greene, T. P., Bell, T. J., Ducrot, E., et al. 2023, *Nature*, 618, 39
- Guillot, T., Fletcher, L. N., Helled, R., et al. 2022, *Giant Planets from the Inside-Out*, chapter submitted to *Protostars and Planets VII*

- Guilluy, G., Giacobbe, P., Carleo, I., et al. 2022, A&A, 665, A104
- Guilluy, G., Sozzetti, A., Brogi, M., et al. 2019, A&A, 625, A107
- Guiu, J. M., Escatllar, A. M., & Bromley, S. T. 2021, ACS Earth Space Chem., 5, 812
- Gunde, M. K. 2000, Physica B: Condensed Matter, 292, 286
- Gupta, A. & Sahijpal, S. 2020, MNRAS, 492, 2058
- Guyon, O., Pluzhnik, E. A., Kuchner, M. J., Collins, B., & Ridgway, S. T. 2006, The Astrophysical Journal Supplement Series, 167, 81
- Hammond, M., Bell, T. J., Challener, R. C., et al. 2024, Astron. J., 168, 4
- Hansen, B. M. S. 2008, The Astrophysical Journal Supplement Series, 179, 484
- Harada, C. K., Kempton, E. M.-R., Rauscher, E., et al. 2021, ApJ, 909, 85
- Harris, C. R., Millman, K. J., van der Walt, S. J., et al. 2020, Nature, 585, 357
- Hartman, J. D., Bayliss, D., Brahm, R., et al. 2015, ApJ, 149, 166
- Haynes, K., Mandell, A. M., Madhusudhan, N., Deming, D., & Knutson, H. 2015, ApJ, 806, 146
- Helling, C., Dehn, M., Woitke, P., & Hauschildt, P. H. 2008a, ApJ, 675, L105
- Helling, C. & Fomins, A. 2013, Phil. Trans. R. Soc. A, 371, 20110581
- Helling, C., Gourbin, P., Woitke, P., & Parmentier, V. 2019a, A&A, 626, A133
- Helling, C., Iro, N., Corrales, L., et al. 2019b, A&A, 631, A79
- Helling, C., Kawashima, Y., Graham, V., et al. 2020, A&A, 641, A178
- Helling, C., Klein, R., Woitke, P., Nowak, U., & Sedlmayr, E. 2004, A&A, 423, 657
- Helling, C., Lee, E., Dobbs-Dixon, I., et al. 2016, MNRAS, 460, 855
- Helling, C., Lewis, D., Samra, D., et al. 2021, A&A, 649, A44
- Helling, C., Oevermann, M., Lüttke, M. J. H., Klein, R., & Sedlmayr, E. 2001, A&A, 376, 194
- Helling, C. & Rimmer, P. B. 2019, Philosophical Transactions of the Royal Society A: Mathematical, Physical and Engineering Sciences, 377, 20180398

- Helling, C., Samra, D., Lewis, D., et al. 2023, A&A, 671, A122
- Helling, C., Thi, W. F., Woitke, P., & Fridlund, M. 2006, A&A, 451, L9
- Helling, C., Tootill, D., Woitke, P., & Lee, E. K. H. 2017, A&A, 603, A123
- Helling, C. & Woitke, P. 2006, A&A, 455, 325
- Helling, C., Woitke, P., Rimmer, P. B., et al. 2014, Life, 4, 142
- Helling, C., Woitke, P., & Thi, W.-F. 2008b, A&A, 485, 547
- Hendrix, J. L. A. M., Louca, A. J., & Miguel, Y. 2023, MNRAS, 524, 643
- Heng, K., Hayek, W., Pont, F., & Sing, D. K. 2012, MNRAS, 420, 20
- Henning, T., Begemann, B., Mutschke, H., & Dorschner, J. 1995, A&A Supplement Series, 112, 143
- Henry, G. W., Marcy, G. W., Butler, R. P., & Vogt, S. S. 2000, ApJ, 529, L41
- Herbst, E. 2014, Phys. Chem. Chem. Phys., 16, 3344
- Herbst, E. 2017, International Reviews in Physical Chemistry, 36, 287
- Hergert, W. & Wriedt, T. 2012, The Mie Theory: Basics and Applications
- Herschel, W. & Watson, D. 1781, Philosophical Transactions of the Royal Society of London Series I, 71, 492
- Highberger, J. L., Savage, C., Biegling, J. H., & Ziurys, L. M. 2001, ApJ, 562, 790
- Higuchi, Y., Fukuda, Y., Fujita, Y., Yamakita, N., & Imajo, T. 2008, Chemical Physics Letters, 452, 245
- Hindmarsh, A. C. 1983, Scientific Computing, 55
- Hobbs, R., Rimmer, P. B., Shorttle, O., & Madhusudhan, N. 2021, MNRAS, 506, 3186
- Hobbs, R., Shorttle, O., & Madhusudhan, N. 2022, MNRAS, 516, 1032
- Hobbs, R., Shorttle, O., Madhusudhan, N., & Rimmer, P. 2019, MNRAS, 487, 2242
- Hoeijmakers, H. J., Ehrenreich, D., Heng, K., et al. 2018a, Nature, 560, 453
- Hoeijmakers, H. J., Schwarz, H., Snellen, I. A. G., et al. 2018b, A&A, 617, A144

- Hoeijmakers, H. J., Seidel, J. V., Pino, L., et al. 2020, A&A, 641, A123
- Hollenbach, D. & Salpeter, E. E. 1971, ApJ, 163, 155
- Holton, J. R. & Hakim, G. J. 2013, An introduction to dynamic meteorology, fifth edition edn. (Amsterdam: Academic Press)
- Hood, T., Debras, F., Moutou, C., et al. 2024, A&A, 687, A119
- Hu, R. 2021, ApJ, 921, 27
- Hu, Y. & Ding, F. 2011, A&A, 526, A135
- Huang, J., Seager, S., Petkowski, J. J., Zhan, Z., & Ranjan, S. 2022, ApJ, 933, 6
- Hubeny, I., Burrows, A., & Sudarsky, D. 2003, ApJ, 594, 1011
- Hueso, R. & Sánchez-Lavega, A. 2019, Space Science Reviews, 215, 52
- Huffman, D. R. & Wild, R. L. 1967, Physical Review, 156, 989
- Hunter, J. D. 2007, Computing in Science and Engineering, 9, 90
- Hébrard, E., Dobrijevic, M., Bénilan, Y., & Raulin, F. 2006, J. Photochem. Photobiol. B, 7, 211
- Hébrard, E., Tomlin, A. S., Bounaceur, R., & Battin-Leclerc, F. 2015, Proceedings of the Combustion Institute, 35, 607
- Höfner, S. 2009, Proceedings of the ASP Conference Series, Cosmic Dust - Near and Far ed Th. Henning, E. Gruen, J. Steinacker, 414, 3
- Hünsch, M., Weidner, C., & Schmitt, J. H. M. M. 2003, A&A, 402, 571
- Ih, J., Kempton, E. M.-R., Whittaker, E. A., & Lessard, M. 2023, ApJL, 952, L4
- Innes, H., Tsai, S.-M., & Pierrehumbert, R. T. 2023, ApJ, 953, 168
- Jacobson, M. Z., Turco, R. P., Jensen, E. J., & Toon, O. B. 1994, Atmos. Environ., 28, 1327
- Jaiswal, B. & Robinson, T. D. 2023, MNRAS, 523, 2809
- Javoy, S., Naudet, V., Abid, S., & Paillard, C. E. 2003, Exp. Therm. Fluid Sci, 27, 371
- Juncker, D., Jørgensen, U. G., & Helling, C. 2017, A&A, 608, A70

- JWST Transiting Exoplanet Community Early Release Science-Team, Ahrer, E.-M., Alderson, L., et al. 2023, *Nature*, 614, 649
- Kahnert, M. 2015, *JQSRT*, 152, 16
- Kalikmanov, V. I. & van Dongen, M. E. H. 1993, *Physical Review E*, 47, 3532
- Kaltenegger, L., Selsis, F., Fridlund, M., et al. 2010, *Astrobiology*, 10, 89
- Kammerer, J., Lacour, S., Stolker, T., et al. 2021, *A&A*, 652, A57
- Karovicova, I., Wittkowski, M., Ohnaka, K., et al. 2013, *A&A*, 560, A75
- Kasper, D., Bean, J. L., Line, M. R., et al. 2021, *ApJL*, 921, L18
- Kataria, T., Showman, A. P., Fortney, J. J., et al. 2015, *ApJ*, 801, 86
- Kataria, T., Sing, D. K., Lewis, N. K., et al. 2016, *ApJ*, 821, 9
- Katrib, Y., Martin, S. T., Hung, H.-M., et al. 2004, *J. Phys. Chem. A*, 108, 6686
- Kawashima, Y. & Min, M. 2021, *A&A*, 656, A90
- Kempton, E. M.-R., Bean, J. L., & Parmentier, V. 2017, *ApJL*, 845, L20
- Kempton, E. M.-R., Zhang, M., Bean, J. L., et al. 2023, *Nature*, 620, 67
- Kendrew, S., Scheithauer, S., Bouchet, P., et al. 2016, *Proceedings of the SPIE*, 9904, 990443
- Kendrew, S., Scheithauer, S., Bouchet, P., et al. 2015, *PASP*, 127, 623
- Khachai, H., Khenata, R., Bouhemadou, A., et al. 2009, *Journal of Physics: Condensed Matter*, 21, 095404
- Khouri, T., Maercker, M., Waters, L. B. F. M., et al. 2016, *A&A*, 591, A70
- Kiefer, S., Bohn, A. J., Quanz, S. P., Kenworthy, M., & Stolker, T. 2021, *A&A*, 652, A33
- Kiefer, S., Gobrecht, D., Decin, L., & Helling, C. 2023, *A&A*, 671, A169
- Kiefer, S., Lecoq-Molinos, H., Helling, C., Bangera, N., & Decin, L. 2024, *A&A*, 682, A150
- Kitzmann, D. & Heng, K. 2018, *MNRAS*, 475, 94
- Knutson, H. A., Charbonneau, D., Allen, L. E., et al. 2007, *Nature*, 447, 183

- Knutson, H. A., Dragomir, D., Kreidberg, L., et al. 2014, *ApJ*, 794, 155
- Kok, R. J. d., Brogi, M., Snellen, I. a. G., et al. 2013, *A&A*, 554, A82
- Kolokolova, L. & Gustafson, B. A. S. 2001, *JQSRT*, 70, 611
- Komacek, T. D., Fauchez, T. J., Wolf, E. T., & Abbot, D. S. 2020, *ApJ*, 888, L20
- Komacek, T. D. & Showman, A. P. 2016, *ApJ*, 821, 16
- Komacek, T. D., Showman, A. P., & Parmentier, V. 2019, *ApJ*, 881, 152
- Komacek, T. D., Showman, A. P., & Tan, X. 2017, *ApJ*, 835, 198
- Komacek, T. D., Tan, X., Gao, P., & Lee, E. K. H. 2022, *ApJ*, 934, 79
- Konings, T., Baeyens, R., & Decin, L. 2022, *A&A*, 667, A15
- Kreidberg, L., Bean, J. L., Désert, J.-M., et al. 2014, *Nature*, 505, 69
- Kumar, A., Kumar, M., & Singh, R. P. 2021, *Optik*, 241, 167064
- Kusakabe, M., Kajino, T., Mathews, G. J., & Luo, Y. 2019, *Physical Review D*, 99, 043505
- Köhn, C., Helling, C., Enghoff, M. B., et al. 2021, *A&A*, 654, A120
- Lacy, B. I. & Burrows, A. 2020, *ApJ*, 905, 131
- Lally, M. & Vanderburg, A. 2022, *Astron. J.*, 163, 181
- Landau, L. & Lifshitz, E. 1960, *Electrodynamics of Continuous Media* (Internet Archive)
- Lasserus, M., Schnedlitz, M., Messner, R., et al. 2019, *Chem. Sci.*, 10, 3473
- Lau, R. M., Hankins, M. J., Han, Y., et al. 2022, *Nat Astron*, 6, 1308
- Lazzati, D. 2008, *MNRAS*, 384, 165
- Lebonnois, S., Bakes, E. L. O., & McKay, C. P. 2003, *Icarus*, 161, 474
- Lecoq-Molinos, H., Gobrecht, D., Sindel, J. P., Helling, C., & Decin, L. 2024, arXiv, 2401.02784, accepted by *A&A*.
- Lee, E., Casewell, S. L., Chubb, K. L., et al. 2020a, *MNRAS*, 496, 4674
- Lee, E., Taylor, J., Grimm, S. L., et al. 2019, *MNRAS*, 487, 2082
- Lee, E. K. H. 2023, *MNRAS*, stad2037

- Lee, E. K. H., Bleicic, J., & Helling, C. 2018, A&A, 614, A126
- Lee, E. K. H., Dobbs-Dixon, I., Helling, C., Bognar, K., & Woitke, P. 2016, A&A, 594, A48
- Lee, E. K. H., Helling, C., Giles, H., & Bromley, S. T. 2015, A&A, 575, A11
- Lee, E. K. H., Parmentier, V., Hammond, M., et al. 2021, MNRAS, 506, 2695
- Lee, E. K. H., Tan, X., & Tsai, S.-M. 2024, MNRAS, 529, 2686
- Lee, E. K. H., Tsai, S.-M., Hammond, M., & Tan, X. 2023, A&A, 672, A110
- Lee, E. K. H., Wood, K., Dobbs-Dixon, I., Rice, A., & Helling, C. 2017, A&A, 601, A22
- Lee, H. D., Morris, H. S., Laskina, O., et al. 2020b, ACS Earth Space Chem., 4, 650
- Lentz, W. 1973, A Method of Computing Spherical Bessel Functions of Complex Argument with Tables, Tech. rep.
- Leonardi, P., Nascimbeni, V., Granata, V., et al. 2024, Astronomy & Astrophysics, 686, A84
- Li, G., Gordon, I. E., Rothman, L. S., et al. 2015, ApJ Supplement Series, 216, 15
- Libby-Roberts, J. E., Berta-Thompson, Z. K., Diamond-Lowe, H., et al. 2022, AJ, 164, 59
- Lieshout, R. v., Min, M., & Dominik, C. 2014, A&A, 572, A76
- Lin, A. S. J., Libby-Roberts, J. E., Alvarado-Montes, J. A., et al. 2023, AJ, 166, 90
- Lindemann, F. A., Arrhenius, S., Langmuir, I., et al. 1922, Transactions of the Faraday Society, 17, 598
- Line, M. R. & Parmentier, V. 2016, ApJ, 820, 78
- Line, M. R., Vasisht, G., Chen, P., Angerhausen, D., & Yung, Y. L. 2011, ApJ, 738, 32
- Lines, S., Manners, J., Mayne, N. J., et al. 2018a, MNRAS, 481, 194
- Lines, S., Mayne, N. J., Boutle, I. A., et al. 2018b, A&A, 615, A97
- Liu, C., Lee Panetta, R., & Yang, P. 2014, JQSRT, 146, 331

- Lodders, K. & Fegley, B. 2002, Icarus, 155, 393
- Loe, M. G., Wakeford, H. R., & Leinhardt, Z. M. 2023, MNRAS, stad3743
- Looyenga, H. 1965, Physica, 31, 401
- Loskutov, V. M. 1971, Trudy Astronomiceskoy Observatorii Leningrad, 28, 14
- Lothringer, J. D. & Barman, T. 2019, ApJ, 876, 69
- Louca, A. J., Miguel, Y., Tsai, S.-M., et al. 2022, MNRAS, stac1220
- Lovis, C., Pepe, F., Bouchy, F., et al. 2006, Ground-based and Airborne Instrumentation for Astronomy, 6269, 249
- Loyd, R. O. P., France, K., Youngblood, A., et al. 2016, ApJ, 824, 102
- Loyd, R. O. P., France, K., Youngblood, A., et al. 2018, ApJ, 867, 71
- Lundqvist, M. J., Nilsing, M., Persson, P., & Lunell, S. 2006, Int. J. Quantum Chem., 106, 3214
- Lustig-Yaeger, J., Fu, G., May, E. M., et al. 2023, Nat. Astron., 7, 1317
- Mackowski, D. W. & Mishchenko, M. I. 1996, JOSA A, 13, 2266
- Mackwell, S. J., Simon-Miller, A. A., Harder, J. W., & Bullock, M. A. 2014, Comparative Climatology of Terrestrial Planets (University of Arizona Press)
- Maes, S., Ceuster, F. D., Sande, M. V. d., & Decin, L. 2024, The Astrophysical Journal, 969, 79
- Maguire, C., Gibson, N. P., Nugroho, S. K., et al. 2024, A&A, 687, A49
- Mai, C. & Line, M. R. 2019, ApJ, 883, 144
- Maire, A.-L., Baudino, J.-L., Desidera, S., et al. 2020, A&A, 633, L2
- Manabe, S. & Wetherald, R. T. 1967, Journal of the Atmospheric Sciences, 24, 241, publisher: American Meteorological Society Section: Journal of the Atmospheric Sciences
- Marcq, E., Mills, F. P., Parkinson, C. D., & Vandaele, A. C. 2017, Space Science Reviews, 214, 10
- Markel, V. A. 2016, J. Opt. Soc. Am. A, JOSAA, 33, 1244
- Marois, C., Lafreniere, D., Doyon, R., Macintosh, B., & Nadeau, D. 2006, ApJ, 641, 556

- Marois, C., Macintosh, B., Barman, T., et al. 2008, *Science*, 322, 1348
- Marois, C., Zuckerman, B., Konopacky, Q. M., Macintosh, B., & Barman, T. 2010, *Nature*, 468, 1080
- Marshall, J., Adcroft, A., Hill, C., Perelman, L., & Heisey, C. 1997a, *J. Geophys. Res. Oceans*, 102, 5753
- Marshall, J., Hill, C., Perelman, L., & Adcroft, A. 1997b, *J. Geophys. Res. Oceans*, 102, 5733
- Marshall, J. & Plumb, A. 2007, *Atmosphere, Ocean and Climate Dynamics - 1st Edition* | Elsevier Shop
- Matsakos, T. & Königl, A. 2016, *ApJL*, 820, L8
- Matsuura, M., Barlow, M. J., Zijlstra, A. A., et al. 2009, *MNRAS*, 396, 918
- Maxwell, J. C. 1865, *Philosophical Transactions of the Royal Society of London*
- Mayne, N. J., Baraffe, I., Acreman, D. M., et al. 2014, *A&A*, 561, A1
- Mayne, N. J., Drummond, B., Debras, F., et al. 2019, *ApJ*, 871, 56
- Mayor, M., Pepe, F., Queloz, D., et al. 2003, *The Messenger*, 114, 20
- Mayor, M. & Queloz, D. 1995, *Nature*, 378, 355
- Mbarek, R. & Kempton, E. M.-R. 2016, *ApJ*, 827, 121
- McElroy, D., Walsh, C., Markwick, A. J., et al. 2013, *A&A*, 550, A36
- McGrory, M. R., H. Shepherd, R. H., King, M. D., et al. 2022, *PCCP*, 24, 5813
- McKay, C. P., Pollack, J. B., & Courtin, R. 1991, *Science*, 253, 1118
- McKemmish, L. K., Masseron, T., Hoeijmakers, H. J., et al. 2019, *MNRAS*, 488, 2836
- McKemmish, L. K., Yurchenko, S. N., & Tennyson, J. 2016, *MNRAS*, 463, 771
- McWilliams, J. C. 1996, *Annual Review of Fluid Mechanics*, 28, 215
- Meehl, G. A. 1984, *Climatic Change*, 6, 259
- Mendonça, J. M., Tsai, S.-m., Malik, M., Grimm, S. L., & Heng, K. 2018, *ApJ*, 869, 107

- Mie, G. 1908, Annalen der Physik, 330, 377
- Mignon, L., Meunier, N., Delfosse, X., et al. 2023, A&A, 675, A168
- Miguel, Y., Guillot, T., & Fayon, L. 2016, A&A, 596, A114
- Miller, N. & Fortney, J. J. 2011, ApJ, 736, L29
- Min, M., Hovenier, J. W., & de Koter, A. 2003, JQSRT, 79-80, 939
- Min, M., Hovenier, J. W., Dominik, C., de Koter, A., & Yurkin, M. A. 2006, JQSRT, 97, 161
- Min, M., Hovenier, J. W., & Koter, A. d. 2005, A&A, 432, 909
- Min, M., Ormel, C. W., Chubb, K., Helling, C., & Kawashima, Y. 2020, A&A, 642, A28
- Mishchenko, M. I., Dlugach, J. M., & Liu, L. 2016, JQSRT, 178, 284
- Mol Lous, M., Helled, R., & Mordasini, C. 2022, Nat. Astron., 6, 819
- Molaverdikhani, K., Henning, T., & Mollière, P. 2019, ApJ, 883, 194
- Molaverdikhani, K., Henning, T., & Mollière, P. 2020, ApJ, 899, 53
- Mollière, P., Molyarova, T., Bitsch, B., et al. 2022, ApJ, 934, 74
- Mollière, P., Stolk, T., Lacour, S., et al. 2020, A&A, 640, A131
- Mollière, P., Wardenier, J. P., Boekel, R. v., et al. 2019, A&A, 627, A67
- Montaner, A., Galtier, M., Benoit, C., & Bill, H. 1979, Physica Status Solidi Applied Research, 52, 597
- Mordasini, C., Boekel, R. v., Mollière, P., Henning, T., & Benneke, B. 2016, ApJ, 832, 41
- Morley, C. V., Fortney, J. J., Marley, M. S., et al. 2012, ApJ, 756, 172
- Morton, T. D. & Swift, J. 2014, ApJ, 791, 10
- Moses, J. I. 2014, Philos. Trans. Royal Soc. A PHILOS T R SOC A, 372, 20130073
- Moses, J. I., Fouchet, T., Bézard, B., et al. 2005, J. Geophys. Res. Planets, 110
- Moses, J. I., Visscher, C., Fortney, J. J., et al. 2011, ApJ, 737, 15
- Mukherjee, S., Batalha, N. E., & Marley, M. S. 2021, ApJ, 910, 158

- Müller, S., Ben-Yami, M., & Helled, R. 2020, *ApJ*, 903, 147
- Namekata, K., Maehara, H., Sasaki, R., et al. 2020, *PASJ*, 72, 68
- Nasedkin, E., Mollière, P., Lacour, S., et al. 2024, arXiv, 240403776N
- Neil, A. R. & Rogers, L. A. 2020, *ApJ*, 891, 12
- Niculescu-Duvaz, M., Barlow, M. J., Bevan, A., et al. 2022, *MNRAS*, 515, 4302
- Nikolov, N., Sing, D. K., Fortney, J. J., et al. 2018, *Nature*, 557, 526
- Nikolov, N., Sing, D. K., Gibson, N. P., et al. 2016, *ApJ*, 832, 191
- Nixon, M. C. & Madhusudhan, N. 2022, *ApJ*, 935, 73
- Noti, P. A., Lee, E. K. H., Deitrick, R., & Hammond, M. 2023, *MNRAS*, 524, 3396
- Nuth, J. A., Allen, Jr., J. E., & Wiant, M. 1985, *ApJ*, 293, 463
- Nuth, J. A. & Donn, B. 1981, *ApJ*, 247, 925
- Nuth, J. A. & Ferguson, F. T. 2006, *ApJ*, 649, 1178
- Ohno, K., Okuzumi, S., & Tazaki, R. 2020, *ApJ*, 891, 131
- Olson, G. L., Auer, L. H., & Buchler, J. R. 1986, *JQSRT*, 35, 431
- Ormel, C. W. & Min, M. 2019, *A&A*, 622, A121
- Owen, J. E. & Lai, D. 2018, *MNRAS*, 479, 5012
- Owens, A., Conway, E. K., Tennyson, J., & Yurchenko, S. N. 2020, *MNRAS*, 495, 1927
- Palik, E. D. 1985, Academic Press Handbook Series, New York: Academic Press, 1985, edited by Palik, Edward D.
- Paris, P. v., Gratier, P., Bordé, P., Leconte, J., & Selsis, F. 2016, *A&A*, 589, A52
- Parmentier, V., Fortney, J. J., Showman, A. P., Morley, C., & Marley, M. S. 2016, *ApJ*, 828, 22
- Parmentier, V., Line, M. R., Bean, J. L., et al. 2018, *A&A*, 617, A110
- Parmentier, V., Showman, A. P., & Fortney, J. J. 2021, *MNRAS*, 501, 78
- Parmentier, V., Showman, A. P., & Lian, Y. 2013, *A&A*, 558, A91

- Pascucci, I., Testi, L., Herczeg, G. J., et al. 2016, ApJ, 831, 125
- Patzer, A. B. C., Chang, C., & Sülzle, D. 2014, Chemical Physics Letters, 612, 39
- Patzer, A. B. C., Gauger, A., & Sedlmayr, E. 1998, A&A, 337, 847
- Pelletier, S., Benneke, B., Ali-Dib, M., et al. 2023, Nature, 1
- Penrose, O. & Lebowitz, J. L. 1979, in Fluctuation Phenomena, ed. E. W. Montroll & J. L. Lebowitz (Elsevier), 293–340
- Perez-Becker, D. & Showman, A. P. 2013, ApJ, 776, 134
- Peskin, C. S. 1972, Journal of Computational Physics, 10, 252
- Peters, B. 2017, in Reaction Rate Theory and Rare Events Simulations, ed. B. Peters (Amsterdam: Elsevier), 147–156
- Petigura, E. A., Marcy, G. W., Winn, J. N., et al. 2018, Astron. J., 155, 89
- Phillips, N. A. 1956, Quarterly Journal of the Royal Meteorological Society, 82, 123, eprint: <https://onlinelibrary.wiley.com/doi/pdf/10.1002/qj.49708235202>
- Piette, A. A. A., Madhusudhan, N., McKemmish, L. K., et al. 2020, MNRAS, 496, 3870
- Pinilla, P., Garufi, A., & Gárate, M. 2022, A&A, 662, L8
- Piskunov, N. E., Kupka, F., Ryabchikova, T. A., Weiss, W. W., & Jeffery, C. S. 1995, A&A Supplement Series, 112, 525
- Plane, J. M. C. 2013, Philos. Trans. Royal Soc. A PHILOS T R SOC A, 371, 20120335
- Plane, J. M. C. & Robertson, S. 2022, Faraday Discuss., 238, 461
- Polman, J., Waters, L. B. F. M., Min, M., Miguel, Y., & Khorshid, N. 2023, A&A, 670, A161
- Polyansky, O. L., Kyuberis, A. A., Zobov, N. F., et al. 2018, MNRAS, 480, 2597
- Pont, F., Knutson, H., Gilliland, R. L., Moutou, C., & Charbonneau, D. 2008, MNRAS, 385, 109
- Pont, F., Sing, D. K., Gibson, N. P., et al. 2013, MNRAS, 432, 2917
- Posch, T., Kerschbaum, F., Fabian, D., et al. 2003, ApJ Supplement Series, 149, 437

- Potapov, A. & Bouwman, J. 2022, *Front. astron. space sci.*, 9
- Powell, D., Louden, T., Kreidberg, L., et al. 2019, *ApJ*, 887, 170
- Powell, D., Zhang, X., Gao, P., & Parmentier, V. 2018, *ApJ*, 860, 18
- Prahl, S. 2023, 10.5281/zenodo.8218010
- Prinoth, B., Hoeijmakers, H. J., Kitzmann, D., et al. 2022, *Nat Astron*, 6, 449
- Qu, Z.-w. & Kroes, G.-J. 2006, *J. Phys. Chem. B*, 110, 8998
- Querry, M. R. 1998, Optical Constants of Minerals and Other Materials from the Millimeter to the Ultraviolet (Chemical Research, Development & Engineering Center, U.S. Army Armament Munitions Chemical Command)
- Radhakrishnan, K. & Hindmarsh, A. C. 1993, NASA Reference Publication, 19940030753
- Ragent, B., Colburn, D. S., Rages, K. A., et al. 1998, *J. Geophys. Res. Planets*, 103, 22891
- Rauer, H., Catala, C., Aerts, C., et al. 2014, *Experimental Astronomy*, 38, 249
- Rauscher, E. & Menou, K. 2010, *ApJ*, 714, 1334
- Richard, C., Gordon, I. E., Rothman, L. S., et al. 2012, *JQSRT*, 113, 1276
- Ricker, G. R., Latham, D. W., Vanderspek, R. K., et al. 2010, 215, 450.06, conference Name: Bulletin of the American Astronomical Society
- Ridden-Harper, A., Nugroho, S. K., Flagg, L., et al. 2023, *Astron. J.*, 165, 170
- Rimmer, P. B. & Helling, C. 2013, *ApJ*, 774, 108
- Rimmer, P. B. & Helling, C. 2016, *ApJS*, 224, 9
- Rimmer, P. B. & Helling, C. 2019, *ApJS*, 245, 20
- Rimmer, P. B. & Rugheimer, S. 2019, *Icarus*, 329, 124
- Ritter, D. & Weisshaar, J. C. 2002, ACS Publications, 93, 1576
- Robbins-Blanch, N., Kataria, T., Batalha, N. E., & Adams, D. J. 2022, *ApJ*, 930, 93
- Rodgers-Lee, D., Rimmer, P. B., Vidotto, A. A., et al. 2023, *MNRAS*, 521, 5880
- Roman, M. & Rauscher, E. 2017, *ApJ*, 850, 17

- Roman, M. & Rauscher, E. 2019, ApJ, 872, 1
- Roman, M. T., Kempton, E. M.-R., Rauscher, E., et al. 2021, ApJ, 908, 101
- Roth, A., Parmentier, V., & Hammond, M. 2024, MNRAS, stae984
- Rowe, J. F., Matthews, J. M., Seager, S., et al. 2008, ApJ, 689, 1345
- Rupprecht, G., Pepe, F., Mayor, M., et al. 2004, Ground-based Instrumentation for Astronomy, 5492, 148
- Russell, B. 2004, History of Western Philosophy (London: Routledge)
- Rustamkulov, Z., Sing, D. K., Mukherjee, S., et al. 2023, Nature, 614, 659
- Sabotta, S., Kabath, P., Korth, J., et al. 2019, MNRAS, 489, 2069
- Sabri, T., Gavilan, L., Jäger, C., et al. 2013, ApJ, 780, 180
- Sachs, A. 1974, Phil. Trans. R. Soc. A, Mathematical and Physical Sciences, 276, 43
- Sainsbury-Martinez, F., Tremblin, P., Mancip, M., et al. 2023, The Astrophysical Journal, 958, 68, publisher: The American Astronomical Society
- Samland, M., Mollière, P., Bonnefoy, M., et al. 2017, A&A, 603, A57
- Samra, D., Helling, C., Chubb, K. L., et al. 2022, A&A
- Samra, D., Helling, C., & Min, M. 2020, A&A, 639, A107
- Sande, M. V. d. & Millar, T. J. 2019, ApJ, 873, 36
- Sanghavi, S., West, R., & Jiang, J. 2021, ApJ, 907, 30
- Savel, A. B., Kempton, E. M.-R., Malik, M., et al. 2022, ApJ, 926, 85
- Savel, A. B., Kempton, E. M.-R., Rauscher, E., et al. 2023, ApJ, 944, 99
- Schneider, A. D. 2024, PhD thesis, book Title: Bridging atmospheres and interiors: Exploring exoplanetary gas giants
- Schneider, A. D., Baeyens, R., & Kiefer, S. 2022a, gcm_toolkit, DOI: 10.5281/zenodo.7116787
- Schneider, A. D., Carone, L., Decin, L., Jørgensen, U. G., & Helling, C. 2022b, A&A, 666, L11
- Schneider, A. D., Carone, L., Decin, L., et al. 2022c, A&A, 664, A56

- Schraper, R. & Henning, T. 2004, ApJ, 614, 960
- Schubert, G. & Walterscheid, R. L. 2002, in Allen's Astrophysical Quantities, ed. A. N. Cox (New York, NY: Springer), 239–292
- Schwierman, E. W., Kiang, N. Y., Parenteau, M. N., et al. 2018, Astrobiology, 18, 663, publisher: Mary Ann Liebert, Inc., publishers
- Seager, S. 2011, Exoplanets (University of Arizona Press)
- Sears, F. W. & Salinger, G. L. 1975, Thermodynamics, Kinetic Theory, and Statistical Thermodynamics, 3rd Edition
- Sedlmayr, E. & Krüger, D. 1997, AIP Conference Proceedings, 402, 425
- Sekine, Y., Imanaka, H., Matsui, T., et al. 2008, Icarus, 194, 186
- Shapiro, R. 1970, Reviews of Geophysics, 8, 359
- Showman, A. P., Fortney, J. J., Lian, Y., et al. 2009, ApJ, 699, 564
- Showman, A. P. & Guillot, T. 2002, A&A, 385, 166
- Showman, A. P. & Polvani, L. M. 2011, ApJ, 738, 71
- Showman, A. P., Tan, X., & Parmentier, V. 2020, Space Science Reviews, 216, 139
- Simon, A. A., Tabataba-Vakili, F., Cosentino, R., et al. 2018, Astron. J., 155, 151
- Sindel, J. P., Gobrecht, D., Helling, C., & Decin, L. 2022, A&A, 668, A35
- Sing, D. K., Désert, J.-M., Fortney, J. J., et al. 2011, A&A, 527, A73
- Sing, D. K., Fortney, J. J., Nikolov, N., et al. 2016, Nature, 529, 59
- Sing, D. K., Wakeford, H. R., Showman, A. P., et al. 2015, MNRAS, 446, 2428
- Skinner, J. W. & Cho, J. Y.-K. 2022, MNRAS, 511, 3584
- Smith, M. D. 1998, Icarus, 132, 176
- Smolders, K., Acke, B., Verhoelst, T., et al. 2010, A&A, 514, L1
- Sogawa, H., Koike, C., Chihara, H., et al. 2006, A&A, 451, 357
- Sousa-Silva, C., Al-Refaie, A. F., Tennyson, J., & Yurchenko, S. N. 2015, MNRAS, 446, 2337

- Spake, J. J., Sing, D. K., Wakeford, H. R., et al. 2021, MNRAS, 500, 4042
- Spiegel, D. S., Fortney, J. J., & Sotin, C. 2014, PNAS, 111, 12622
- Spyratos, P., Nikolov, N., Southworth, J., et al. 2021, MNRAS, 506, 2853
- Stangret, M., Casasayas-Barris, N., Pallé, E., et al. 2022, A&A, 662, A101
- Staniforth, A. & Wood, N. 2003, MWR, 131, 1931
- Staniforth, A. & Wood, N. 2008, Journal of Computational Physics, 227, 3445
- Stegmann, P. G. & Yang, P. 2017, J. Aerosol Sci., 114, 327
- Steinrueck, M. E., Koskinen, T., Lavvas, P., et al. 2023, ApJ, 951, 117
- Steinrueck, M. E., Parmentier, V., Showman, A. P., Lothringer, J. D., & Lupu, R. E. 2019, ApJ, 880, 14
- Steinrueck, M. E., Showman, A. P., Lavvas, P., et al. 2021, MNRAS, 504, 2783
- Stevenson, D. J. 1982, Annual Review of Earth and Planetary Sciences, 10, 257
- Stock, J. W., Kitzmann, D., & Patzer, A. B. C. 2022, MNRAS, 517, 4070
- Stock, J. W., Kitzmann, D., Patzer, A. B. C., & Sedlmayr, E. 2018, MNRAS, 479, 865
- Stolker, T., Bonse, M. J., Quanz, S. P., et al. 2019, A&A, 621, A59
- Sumlin, B. J., Heinson, W. R., & Chakrabarty, R. K. 2018, JQSRT, 205, 127
- Suto, H., Sogawa, H., Tachibana, S., et al. 2006, MNRAS, 370, 1599
- Swain, M. R., Tinetti, G., Vasish, G., et al. 2009, ApJ, 704, 1616
- Tabone, B., Bettoni, G., van Dishoeck, E. F., et al. 2023, Nat. Astron., 7, 805
- Tan, X., Komacek, T. D., Batalha, N. E., et al. 2024, MNRAS, 528, 1016
- Tan, X. & Showman, A. P. 2017, ApJ, 835, 186
- Tan, X. & Showman, A. P. 2021, MNRAS, 502, 2198
- Tazaki, R. & Tanaka, H. 2018, ApJ, 860, 79
- Tazaki, R., Tanaka, H., Okuzumi, S., Kataoka, A., & Nomura, H. 2016, ApJ, 823, 70
- Tennyson, J. & Yurchenko, S. N. 2012, MNRAS, 425, 21

- Thomas, M. & Gautier, C. 2009, *J. Geophys. Res. Atmos.*, 114
- Thompson, M. A., Krissansen-Totton, J., Wogan, N., Telus, M., & Fortney, J. J. 2022, *Proceedings of the National Academy of Sciences*, 119, e2117933119
- Thorngren, D., Gao, P., & Fortney, J. J. 2019, *ApJ*, 884, L6
- Thorngren, D. P., Fortney, J. J., Murray-Clay, R. A., & Lopez, E. D. 2016, *ApJ*, 831, 64
- Tielens, A. 2022, *Frontiers in Astronomy and Space Sciences*, 9
- Tilley, M. A., Segura, A., Meadows, V. S., Hawley, S., & Davenport, J. 2019, *Astrobiology*, 19, 64
- Tinyanont, S., Kasliwal, M. M., Krafton, K., et al. 2019, *ApJ*, 873, 127
- Tipler, P. A. & Mosca, G. 2015, *Physik für Wissenschaftler und Ingenieure*, 7. Auflage, by P.A. Tipler and G. Mosca
- Titov, D. V., Ignatiev, N. I., McGouldrick, K., Wilquet, V., & Wilson, C. F. 2018, *Space Science Reviews*, 214, 126
- Tokano, T. 2013, *Geophys. Res. Lett.*, 40, 4538
- Tombaugh, C. W. 1946, *Leaflet of the Astronomical Society of the Pacific*, 5, 73
- Toon, O. B. & Ackerman, T. P. 1981, *Appl. Opt.*, 20, 3657
- Toon, O. B., Turco, R. P., Westphal, D., Malone, R., & Liu, M. 1988, *Int. J. Atmos. Sci.*, 45, 2123
- Toublanc, D., Parisot, J. P., Brillet, J., et al. 1995, *Icarus*, 113, 2
- Trainer, M. G., Wong, M. H., McConnochie, T. H., et al. 2019, *J. Geophys. Res. Planets*, 124, 3000
- Tsai, S.-M., Kitzmann, D., Lyons, J. R., et al. 2018, *ApJ*, 862, 31
- Tsai, S.-M., Lee, E. K. H., & Pierrehumbert, R. 2022, *A&A*, 664, A82
- Tsai, S.-M., Lee, E. K. H., Powell, D., et al. 2023, *Nature*, 617, 483
- Tsai, S.-M., Lyons, J. R., Grosheintz, L., et al. 2017, *ApJS*, 228, 20
- Tsai, S.-M., Malik, M., Kitzmann, D., et al. 2021, *ApJ*, 923, 264
- Tsai, S.-M., Parmentier, V., Mendonça, J. M., et al. 2024, *ApJ*, 963, 41
- Tsuji, T. 2002, *ApJ*, 575, 264

- Tsuji, T. 2005, *Apj*, 621, 1033
- Tsuji, T., Ohnaka, K., Aoki, W., & Nakajima, T. 1996, *A&A*, 308, L29
- Turbet, M., Bolmont, E., Chaverot, G., et al. 2021, *Nature*, 598, 276
- Turco, R. P., Hamill, P., Toon, O. B., Whitten, R. C., & Kiang, C. S. 1979, *Int. J. Atmos. Sci.*, 36, 699
- Turrini, D., Nelson, R. P., & Barbieri, M. 2015, *Experimental Astronomy*, 40, 501
- Underwood, D. S., Tennyson, J., Yurchenko, S. N., et al. 2016, *MNRAS*, 459, 3890
- Unga, F., Choël, M., Derimian, Y., et al. 2018, *J. Geophys. Res. Atmos.*, 123, 13,944
- Vallis, G. K. 2017, *Atmospheric and Oceanic Fluid Dynamics: Fundamentals and Large-Scale Circulation*, 2nd edn. (Cambridge: Cambridge University Press)
- Vehkämäki, H., Määttänen, A., Lauri, A., Napari, I., & Kulmala, M. 2007, *Atmos. Chem. Phys.*, 7, 309
- Venot, O. & Agúndez, M. 2015, *Exp Astron*, 40, 469
- Venot, O., Bounaceur, R., Dobrijevic, M., et al. 2019, *A&A*, 624, A58
- Venot, O., Cavalié, T., Bounaceur, R., et al. 2020, *A&A*, 634, A78
- Venot, O., Drummond, B., Miguel, Y., et al. 2018, *Exp Astron*, 46, 101
- Venot, O., Hébrard, E., Agúndez, M., et al. 2012, *A&A*, 546, A43
- Venot, O., Rocchetto, M., Carl, S., Roshni Hashim, A., & Decin, L. 2016, *ApJ*, 830, 77
- Ventura, P., Dell'Agli, F., Lugaro, M., et al. 2020, *A&A*, 641, A103
- Voshchinnikov, N. V., Videen, G., & Henning, T. 2007, *Appl. Opt.*, AO, 46, 4065
- Vuitton, V. 2021, in *Encyclopedia of Geology* (Elsevier), 217–230
- Wakeford, H. R. & Sing, D. K. 2015, *A&A*, 573, A122
- Wakeford, H. R., Sing, D. K., Deming, D., et al. 2018, *ApJ*, 155, 29
- Wakeford, H. R., Visscher, C., Lewis, N. K., et al. 2017, *MNRAS*, 464, 4247

- Wang, H. & Wordsworth, R. 2020, ApJ, 891, 7
- Ward-Duong, K., Patience, J., Follette, K., et al. 2020, ApJ, 161, 5
- Waters, L. B. F. M., Molster, F. J., de Jong, T., et al. 1996, A&A, 315, L361
- Way, M. J., Aleinov, I., Amundsen, D. S., et al. 2017, ApJS, 231, 12
- Weart, S. 2010, Studies in History and Philosophy of Science Part B: Studies in History and Philosophy of Modern Physics, 41, 208
- Webber, M. W., Lewis, N. K., Marley, M., et al. 2015, ApJ, 804, 94
- Wende, S., Reiners, A., Seifahrt, A., & Bernath, P. F. 2010, A&A, 523, A58
- West, R. G., Hellier, C., Almenara, J. M., et al. 2016, A&A, 585, A126
- Whiteway, J. A., Komguem, L., Dickinson, C., et al. 2009, Science, 325, 68
- Williams, D. A. 2005, Journal of Physics: Conference Series, 6, 1
- Williams, P. M., van der Hucht, K. A., & The, P. S. 1987, A&A, 182, 91
- Winters, J. M., Fleischer, A. J., Gauger, A., & Sedlmayr, E. 1994, A&A, 290, 623
- Winters, J. M., Fleischer, A. J., Gauger, A., & Sedlmayr, E. 1995, A&A, 302, 483
- Wiscombe, J. 1979, University Corporation for Atmospheric Research, No. NCAR/TN-140+STR
- Witte, S., Helling, C., Barman, T., Heidrich, N., & Hauschildt, P. H. 2011, A&A, 529, A44
- Woitke, P., Goeres, A., & Sedlmayr, E. 1996, A&A, 313, 217
- Woitke, P. & Helling, C. 2003, A&A, 399, 297
- Woitke, P. & Helling, C. 2004, A&A, 414, 335
- Woitke, P. & Helling, C. 2021, Astrophysics Source Code Library, ascl:2104.018
- Woitke, P., Helling, C., & Gunn, O. 2020, A&A, 634, A23
- Woitke, P., Helling, C., Hunter, G. H., et al. 2018, A&A, 614, A1
- Woitke, P., Kamp, I., & Thi, W.-F. 2009, A&A, 501, 383
- Woitke, P., Sedlmayr, E., & Lopez, B. 2000, A&A, 358, 665

- Wolf, S. & Voshchinnikov, N. V. 2004, Computer Physics Communications, 162, 113
- Wolszczan, A. & Frail, D. A. 1992, Nature, 355, 145
- Wong, I., Benneke, B., Gao, P., et al. 2020, ApJ, 159, 234
- Wong, I., Chachan, Y., Knutson, H. A., et al. 2022, Astron. J., 164, 30
- Wong, M. H., Bjoraker, G. L., Goulaud, C., et al. 2023, Remote Sensing, 15, 702
- Yan, F., Pallé, E., Reiners, A., et al. 2020, A&A, 640, L5
- Yan, F., Reiners, A., Pallé, E., et al. 2022, A&A, 659, A7
- Yang, J., Boué, G., Fabrycky, D. C., & Abbot, D. S. 2014, ApJ, 787, L2
- Young, R. M. B., Read, P. L., & Wang, Y. 2019, Icarus, 326, 225
- Youngblood, A., France, K., Loyd, R. O. P., et al. 2017, ApJ, 843, 31
- Youngblood, A., France, K., Loyd, R. O. P., et al. 2016, ApJ, 824, 101
- Yung, Y. L., Allen, M., & Pinto, J. P. 1984, ApJS, 55, 465
- Yurchenko, S. N., Amundsen, D. S., Tennyson, J., & Waldmann, I. P. 2017, A&A, 605, A95
- Yurchenko, S. N., Mellor, T. M., Freedman, R. S., & Tennyson, J. 2020, MNRAS, 496, 5282
- Yurchenko, S. N. & Tennyson, J. 2014, MNRAS, 440, 1649
- Yurchenko, S. N., Tennyson, J., Syme, A.-M., et al. 2022, MNRAS, 510, 903
- Zalucha, A. M., Michaels, T. I., & Madhusudhan, N. 2013, Icarus, 226, 1743
- Zamyatina, M., Hébrard, E., Drummond, B., et al. 2022, MNRAS, stac3432
- Zeidler, S., Posch, T., & Mutschke, H. 2013, A&A, 553, A81
- Zeidler, S., Posch, T., Mutschke, H., Richter, H., & Wehrhan, O. 2011, A&A, 526, A68
- Zhai, H.-J. & Wang, L.-S. 2007, J. Am. Chem. Soc., 129, 3022
- Zhang, X., Wang, X., Sai, H., et al. 2022, MNRAS, 509, 2013
- Zhu, W. & Dong, S. 2021, ARA&A, 59, 291

- Zieba, S., Kreidberg, L., Ducrot, E., et al. 2023, *Nature*, 620, 746
- Zsigmondy, R. 1898, *Justus Liebigs Annalen der Chemie*, 301, 29
- Zubko, V. G., Mennella, V., Colangeli, L., & Bussoletti, E. 1996, *MNRAS*, 282, 1321
- Öberg, K. I. & Bergin, E. A. 2016, *ApJ*, 831, L19
- Öberg, K. I., Murray-Clay, R., & Bergin, E. A. 2011, *ApJ*, 743, L16
- Žák, J., Kabáth, P., Boffin, H. M. J., Ivanov, V. D., & Skarka, M. 2019, *Astron. J.*, 158, 120

List of Publications

1. Espinoza, N., Steinrueck, M. E., Kirk, J., MacDonald, R. J., Savel, A. B., Arnold, K., Kempton, E. M.-R., Murphy, M. M., Carone, L., Zamyatina, M., Lewis, D. A., Samra, D., **Kiefer, S.**, Rauscher, E., Christie, D., Mayne, N., Helling, Ch., Rustamkulov, Z., Parmentier, V., May, E. M., Carter, A. L., Zhang, X., López-Morales, M., Allen, N., Blecic, J., Decin, L., Mancini, L., Molaverdikhani, K., Rackham, B. V., Palle, E., Tsai, S.-M., Ahrer, E.-M., Bean, J. L., Crossfield, I. J. M., Haegele, D., Hébrard, E., Kreidberg, L., Powell, D., Schneider, A. D., Welbanks, L., Wheatley, P., Brahm, R., Crouzet, N. (2024). Inhomogeneous terminators on the exoplanet WASP-39 b. *Nature*, 632, 1017–1020.
2. **Kiefer, S.**, Bach-Møller, N., Samra, D., Lewis, D. A., Schneider, A. D., Amadio, F., Lecoq-Molinos H., Carone, L., Decin, L., Jørgensen, U. G., and Helling, Ch. Under the magnifying glass: A combined 3D model applied to cloudy warm Saturn type exoplanets around M-dwarfs *Astronomy & Astrophysics*, submitted.
3. **Kiefer, S.**, Samra, D., Lewis, D. A., Schneider, A. D., Min, M., Carone, L., Decin, L., Helling, Ch. Why heterogeneous cloud particles matter: Iron-bearing species and cloud particle morphology affects exoplanet transmission spectra. *Astronomy & Astrophysics*, submitted.
4. **Kiefer, S.**, Lecoq-Molinos, H., Helling, Ch., Bangera, N., Decin L. (2024). Fully time-dependent cloud formation from a non-equilibrium gas-phase in exoplanetary atmospheres. *Astronomy & Astrophysics*, 682, A150.
5. **Kiefer, S.**, Gobrecht, D., Decin, L., Helling, Ch. (2023). The effect of thermal non-equilibrium on kinetic nucleation. *Astronomy & Astrophysics*, 671, A169.

6. Tayar, J., Moyano, F. D., Soares-Furtado, M., Escorza, A., Joyce, M., Martell, S. L., García, R. A., Breton, S. N., Mathis, S., Mathur, S., Delsanti, V., **Kiefer, S.**, Reffert, S., Bowman, D. M., Van Reeth, T., Shetye, S., Gehan, C., Grunblatt, S. K. (2022). Spinning up the Surface: Evidence for Planetary Engulfment or Unexpected Angular Momentum Transport? *The Astrophysical Journal*, 940, 23.
7. Schneider, A. D., Carone, L., Decin, L., Jørgensen, U. G., Mollière, P., Baeyens, R., **Kiefer, S.**, Helling, Ch (2022). Exploring the deep atmospheres of HD 209458b and WASP-43b using a non-gray general circulation model. *Astronomy & Astrophysics*, 664, A56.

FACULTY OF SCIENCE
DEPARTMENT OF PHYSICS AND ASTRONOMY
Celestijnenlaan 200A box 2402
B-3001 Leuven

